THE UNIVERSITY *of* LIVERPOOL

Electrical and Optical Properties of Nitrogenated : Hydrogenated : Amorphous Carbon Thin Films

Thesis submitted in accordance with the requirements of the University of Liverpool for the degree of Doctor in Philosophy

by

Dedimuni Amith Indika Munindradasa

Department of Electrical Engineering and Electronics

June 1999

Abstract

The electronic and optical properties of hydrogenated amorphous carbon (a-C:H) and nitrogenated : hydrogenated amorphous carbon (a-C:H:N), deposited using inductively coupled plasma enhanced chemical vapour deposition (ICPECVD) and helicon wave excited plasma enhanced chemical vapour deposition (HWPECVD) are discussed in this thesis. The design and the implementation of the helicon wave excited plasma system is also presented.

The capacitance voltage (C-V) characteristics of heterojunctions formed by depositing a-C:H:N on Si, show that almost ideal interface behaviour can be accomplished using ICPECVD for optimised plasma conditions. The highest frequency response, known to date for a-C, 13MHz, is also reported. The photoluminescence (PL) studies are carried out to investigate the influence of nitrogen in a-C:H:N. The nitrogen and the optical band gap dependencies of PL indicated the existence of N associated recombination centres. A twin recombination mechanism at localised tails and N associated centres is suggested to describe the observed behaviour. The capability of selective energy transitions in a helicon wave plasma as predicted theoretically is successfully demonstrated for N_2 plasma. The passivation of high power electronic devices and the electron field emission are presented as potential areas where a-C:H and a-C:H:N perform successfully.

To My Parents

Acknowledgements

It would be far too long to mention them all who have taught and inspired me in their own unique way throughout the history of mankind. My unsung gratitude goes to all of them.

First and foremost, I am indebted to Professor Gehan Amaratunga, my supervisor for his ever present guidance, encouragement, generous support and constructive criticism, without whom this work would never have been a reality.

The author is most grateful to Kevin Molloy, Peter Storey and other technical staff members for their support rendered throughout the whole process. The University of Liverpool and The Committee of Vice-Chancellors and Principles are acknowledged for the financial assistance provided, allowing me to undertake this study. University of Moratuwa is acknowledged for providing me with study leave from work and travel grants.

I would like to thank my tutor Professor M.T.C.Fang, thesis advisor Dr.S.Taylor and Professor W.Eccleston for their guidance and for creating a cordial environment which made my studies in Liverpool enjoyable. Thank you very much; Ioannis Alexandrou, Magdalene Goh, Guan Lim, Ismail Musa and Nalin Rupesinghe (also for FTIR and field emission measurements) for giving me a family away from home. The excitement Dr. Manish Chhowalla gets for every *pigeon-drop* result always led to warm and lengthy discussions. He is specially thanked for stimulating enthusiastic discussions and for proof reading this thesis.

Very special thanks go to Pani and Damayanthi Dharmawardana for being my *foster-parents* in England. All the other seen and unseen friends are acknowledged for their limitless sharing and deep understanding. I would like to extend my warmest appreciation to my sisters for their invaluable encouragement and tolerance. At last but not least I would like to offer my *big thank you* to my mother and late father - who always encouraged free thinking, for what was the beginning of it all.

Glossary of Abbreviations

a-C	=	Amorphous carbon
a-C:H	=	Hydrogenated amorphous carbon
a-C:H:N	=	Nitrogenated : hydrogenated amorphous carbon
a-Si	=	Amorphous silicon
a-Si:H	=	Hydrogenated amorphous silicon
CVD	=	Chemical vapour deposition
PVD	=	Physical vapour deposition
ICPECVD	=	Inductively coupled plasma enhanced chemical vapour deposition
HWPECVD	=	Helicon wave excited plasma enhanced chemical vapour deposition
I-V	=	Current-voltage
C-V	=	Capacitance-voltage
RF	=	Radio frequency
PL	=	Photoluminescence
ITO	=	Indium tin oxide
SNMS	=	Scanning neutral mass spectroscopy
AMLCD	=	Active matrix liquid crystal display
XTEM	=	Cross-sectional transmission electron microscopy
PEELS	=	Parallel electron energy loss spectroscopy
E_{mode}	=	Capacitively coupled mode of plasma
H_{mode}	=	Inductively coupled mode of plasma
DOS	=	Density of states
IR	=	Infrared
UV	=	Ultraviolet
FWHM	=	Full width at half maximum
MCS	=	Metal-carbon-silicon
OES	=	Optical emission spectroscopy
CCD	=	Charge coupled device

Contents

List of Figures

List of Tables

Chapter 1

Introduction

1.1 Motivation and Scope

After the invention of the bipolar transistor in 1947 [1], the interest in semiconductor devices grew exponentially. New semiconductor materials were also investigated and at the same time, the observations that had been made previously and reported in a scattered manner, re-examined in a different perspective. Early work during 1950s and 1960s about insulating oxide glasses - chalcogenides, materials containing the elements sulphur, selenium and tellurium (*eg.* As_2Se_3, GeS_2 etc.) led to the classification of a different and new form of semiconductor material, amorphous semiconductors [2].

In microscopic terms, the *amorphous* concept describes, materials having short range order, *i.e.* no long range order as in a crystalline counterpart. This lack of long range order leads to *localised* behaviour, unlike in crystalline lattices in which properties can be generalised without specific consideration of spatial variations. The main practical advantage of amorphous materials is that they can be synthesised at low temperature, making them suitable for large area electronics, for example displays where the substrate is glass or plastic.

When it comes to electronic properties of amorphous materials, the most important question to be addressed is how the long range disorder of the material affects the electronic transport mechanism, and as far as optical properties are concerned, how the localised states contribute to the absorption and re-

emission processes. Since a-Si:H was first synthesised in the late 1960s, a new era of amorphous semiconductors has developed. The significance of this step was recognized in 1977 when Sir Nevill Mott and P.W. Anderson were awarded the Nobel Prize in physics, for their work which paved the way towards understanding amorphous materials. The key to understanding amorphous materials is the concept of localised electronic states, which is succinctly covered in their lectures [3, 4] delivered on the occasion of the presentation of the Nobel Prize. A whole new technology has evolved, based on a-Si:H - the basic electronic material for Active Matrix Liquid Crystal Displays (AMLCDs) [5, 6, 7] and large area thin film solar cells [8, 9, 10].

Carbon being the smallest element in group-IV of the periodic table, where all elementary semiconductors (Si, Ge and gray-Sn) are also grouped, makes it interesting to investigate its capability as a semiconductor. The crystalline form of carbon, diamond, has extreme hardness, good heat conductivity, wide electronic band gap material with high carrier mobilities (the highest hole mobility and the second highest mobility for electrons among known materials) and a high break down electric field. However, the rarity of natural diamond and the high temperatures involved in synthetic diamond processing makes it impractical to develop it for electronics. The amorphous analogy of C to Si, can however be readily synthesised in the laboratory using similar methods.This makes the study of a-C as a complementary material to a-Si in an interesting proposition.

The presence of both σ and π bonds in the same structure makes a-C markedly different from a-Si. Several theoretical attempts have been made to explain the experimental observations made, and to predict certain properties. A model comprised of several elementary blocks in a random structure has been developed to understand the nature of a-C, and shown to be consistent with a-C grown by sublimation of graphite targets [11]. The theoretical importance of σ and π bonds in carbon to explain the electronic behaviour of a-C structure has been discussed at length [12, 13] with respect to the Wang and Ho model [14]. Drabold *et. al.* have interpreted the defect free optical band gap in a-C, based on pair formation in three fold coordinated bonds in the amorphous network [15]. Even though macroscopic models could be consistent with most

generalised structural aspects, as far as electronic properties are concerned, it is very important to understand the basic atomic level interactions in a-C.

Materials for electronics applications are generally characterised by their electrical and optical (electromagnetic) properties. Even though crystalline materials could be described adequately with isotropic models, when it comes to amorphous materials such interpretations would be unrealistic. Alternatively anisotropic models have been proposed and analysed critically [16] against conventional models, taking into account the properties of samples made from several independent techniques, such as DC plasma, microwave plasma, RF sputtering. Among those, the behaviour of RF sputtered films have been explained with a simple model based on layer arrangement with polymeric components embedded in a graphitic bulk. This has been further established with XTEM investigations. Photoconductivity [17], high voltage heterojunction fabrication [18], quantum size effects [19], have all been demonstrated in amorphous carbon, and is indicative of it's continuing development as a semiconductor.

With the general aim of developing a-C as an electronic material, the main scope of the present work is,

- To investigate the electronic and optical properties of a-C:H and a-C:H:N grown in an inductively coupled PECVD,
- To design and implement the helicon wave excited plasma system to,
  - Resonant excite a N_2 plasma to obtain continuous excitations at $X^1\Sigma_g^+ \rightarrow C^3\Pi_u$ energies.
  - Adopt the concept of helicon wave excitation for amorphous carbon deposition.
- To identify potential applications of these materials.

In the rest of this chapter, the main features of carbon in terms of its bonding and related electronics properties are introduced. An introduction is also given to the main features of the deposition methods and processes used. In chapter 2 electronic properties of a-C:H:N films are discussed in terms of I-V and

C-V characteristics. The behaviour of heterojunctions with Si are looked at to understand the nature of a-C:H:N/Si interface. With temperature dependence of conductivity, evidence to suggest localised state conduction at low temperatures and transition to extended-like state conduction at high temperatures is established. It is shown from the C-V behaviour that by optimisation of plasma conditions almost ideal interfaces can be obtained. The frequency response reported here is thought to be the highest observed for these materials to date. It was established that the heterostructure behaves according to existing MCS models with slight modifications.

Optical and PL properties are looked at in chapter 3. Evidence for optically inactive DOS in the band gap are investigated by analysing the low absorption region. The activation of extended states at high temperatures is further established through the temperature dependence of the optical absorption. Evidence for localised N associated states are seen in the PL behaviour. A twin recombination mechanism, in tail states and in N associated states is identified from the N and band gap dependencies of PL. PL is identified as a powerful technique to get an insight about localised states compared to other optical measurements.

Design of the helicon system and the properties of the films deposited are discussed in chapter 4. The feasibility of continuous excitation of N_2 at $X^1\Sigma_g^+ \rightarrow C^3\Pi_u$ energies is demonstrated. The effect of resonant excitation on deposited films are discussed and compared with ICPECVD.

Semiconductor device passivation and electron field emission are identified as potential applications of amorphous carbon in chapter 5. A mechanism to describe the strong passivation capability shown is suggested. The field emission measurements are compared with proposed models, and it is shown that the dominant barrier for field emission exists at the a-C:H:N/n-Si interface for the films studied.

The key features of the present work as the author sees it, and suggestions for continuation of this work are given in chapter 6.

1.2 Amorphous Carbon Materials

1.2.1 Introduction

The quest of mankind to convert *ordinary* materials into *precious* ones led to alchemy. In a similar vein, the synthesis of diamond has also been a continuing quest over many centuries, one which persuaded Sir Isaac Newton to an attempt to convert powder graphite into diamond by applying extreme pressure and temperature. Results were never known. Present day science enables the fabrication of crystalline diamond by bringing carbon into an appropriate metastable phase described in Berman-Simon diagram (Pressure-Temperature phase diagram) using high temperature and high pressure processes. In the last 15 years lower temperature and low pressure plasma processes have also been used to synthesise diamond from the vapour phase [20]. The extreme pressures and temperatures required to attain the stable sp^3 phase are overcome at atomic level by balance of chemical attachment (deposition) and abstraction (etching) process. Net growth of crystalline diamond grains on nucleating sites is enabled in such a process.

1.2.2 Different Bonding Configurations in Carbon and Physical Properties

The carbon atom possesses six electrons, out of which four are valence electrons in 2s and 2p orbitals capable of forming a variety of bond configurations. The combination of four valence electrons can hybridise into sp^3, sp^2 and sp metastable energy configurations, as shown in Fig. 1.1.

The bond arrangement resulting from sp^3 hybridisation consists of four homogeneously spaced (109^0 bond angle) and tetrahedrally oriented bonds. The orbital overlap is longitudinal. Such an orbital overlap is referred to as a σ bond. In sp^2 bonding, there are three equally spaced σ bonds in a single plane. In addition there is another *dumb-bell* shaped p-orbital oriented orthogonally to the plane in which the 3 σ-bonds overlap. The bond formed by the overlap of these p-orbitals is referred to as a π bond. The sp hybridisation describes two

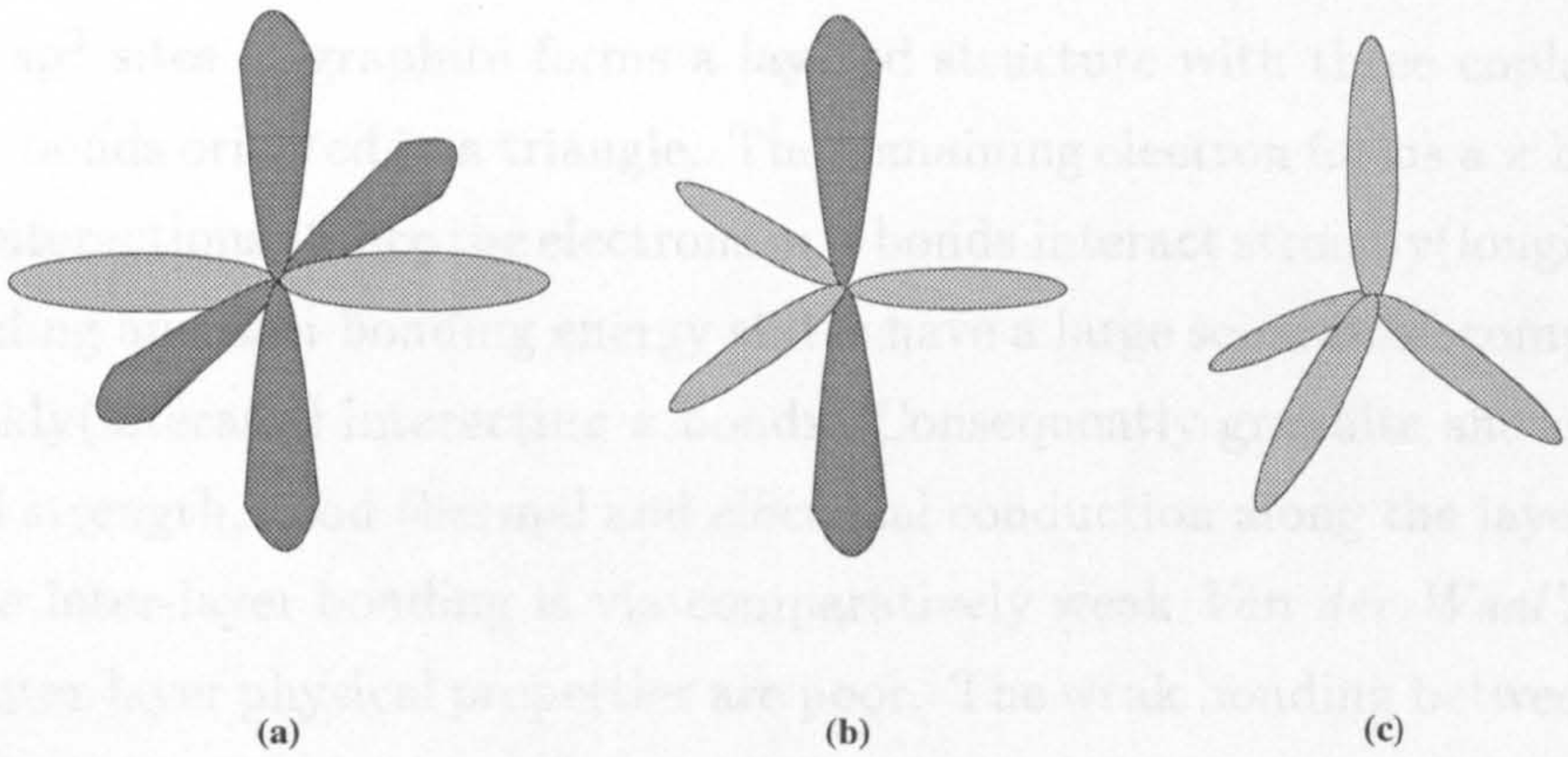

Figure 1.1: The orbital spread of (a) sp, (b) sp^2 and (c) sp^3 hybridised carbon atoms are illustrated.

π bonds in two orthogonal axes and two σ bonds in the other axis.

The interaction of neighbouring sp^3 hybridised atoms forms a tetrahedrally bonded three dimensional structure, of which diamond is a good example. A similar interaction in sp^2 hybridised atoms forms a planar structure as in crystalline graphite while sp atoms form linear bonding, typically in C-H chains. The sp^3 and sp^2 bonding structure can also be present in non-crystalline amorphous carbon (a-C), where the local order is preserved without any long range order.

The ability of carbon to form a mixture of bond types, namely sp^3, sp^2 and sp, in the same environment allows for a degree of *bond-wise* saturation in the structure in the amorphous state, unlike in a-Si where the singular sp^3 hybridisation must lead to dangling bonds. This makes a-C chemically inert within relative terms. The reduction in mid-gap electronic states leads to a well defined optical band-gap [21, 22, 23, 24].

An abundance of tetrahedrally bonded regions in a-C film can make it hard,

electrically resistive and dielectrically strong [25, 26, 27, 28, 29]. However, large number of sp^3 sites in the film leads to high internal stress, leading to poor adhesion as the layer becomes thicker [30].

The sp^2 sites in graphite forms a layered structure with three coplanar covalent σ bonds oriented in a triangle. The remaining electron forms a π bond via lateral interactions. Since the electrons in σ bonds interact strongly(longitudinally), the bonding and anti-bonding energy states have a large separation compared to the weakly(laterally) interacting π bonds. Consequently graphite shows strong physical strength, good thermal and electrical conduction along the layer. However, the inter-layer bonding is via comparatively weak *Van der Waal's* forces. Hence inter-layer physical properties are poor. The weak bonding between layers allows them to slide freely, giving graphite good lubricant properties.

In general, amorphous carbon contains both sp^3 and sp^2 hybridised carbon atoms in varying proportions. The proportion of the type of bonding can be controlled by varying the parameters of the film deposition process [31]. As the sp^3 to sp^2 content becomes small, most of the physical properties move towards those associated with graphite [32].

It has been suggested in literature that the sp^2 hybridised carbon atoms tend to cluster into small domains embedded in an sp^3 bonded carbon matrix [33, 34]. This aspect of bond distribution results in two major features observed in amorphous carbon. First of all the bulk properties are a combination of those due to two markedly different *materials.* Second, the resulting inhomogeneity induced by the presence of clusters is off set to some extent by the greater interaction ability within the sp^2 bonded cluster itself.

A sheet of sp^2 hybridised carbon atoms can curl up when there are rings of atoms which are five membered or less [35]. The close structure thus formed by 60 sp^2 bonded atoms is known as the *fullerene molecule.* Rolling up of larger sheets forms tubular structures known as *nanotubes.* These structures taken individually show strong mechanical properties due to the enclosed structure, while strong interaction of π bonds along the surface gives *metallic-like* electrical properties. Contrary to the conventional concept that the three dimensional structures of sp^3 bonds form hard material, it has been shown that three dimen-

sionally interlinked *graphitic* planes also form hard material [36]. The initial formation of closed sp^2 bonded structures has been observed both in solid [37] and also in plasma phase [38].

The use of precursor gases as the source is common practice for most CVD processes [39]. In the deposition of carbon, these precursor gases are hydrocarbons such as CH_4 and C_2H_2. Inevitably this leads to the presence of hydrogen in the resulting material [40]. Vainonen*et. al.* have found that the H associated bond migration upon annealing can cause macroscopic changes in the physical properties of a-C films [41]. Introduction of H passivates dangling bonds in a-Si. However in a-C the dangling bond passivation which can be achieved by introducing H is not significant owing to the variety of bond hybridisations [42, 43, 44].

The electronic and optical properties of a material are largely affected by the bonding and anti-bonding energy states which lie closest to each other. This means that the π and π^* which result from sp^2 and sp bond hybridisations control the electronic and optical properties in a-C. The clustering of such sites causes a greater degree of delocalisation within the cluster. Additionally if the cluster separation is smaller than the Bohr radius (the representative parameter of electrostatic interactions), then the inter-cluster interactions are considerable, leading to the possibility of delocalised π-π^* electronic states. The nearest analogy to such states is the *extended* states of a system such as a-Si with only sp^3 hybridised bonds. However, due to the polar nature of π bonds, compared to sp hybridised bonds, delocalisation of π electrons in an amorphous system is drastically reduced. The small degree of delocalisation in sp^2 clusters results largely in localised deep π states, analogous to *tail* states in a-Si. The effect of such localisation is reflected in the electrical properties discussed in chapter 2 and in the PL behaviour discussed in chapter 3.

1.2.3 Nitrogen Containing Amorphous Carbon

The solid solutions containing elements from immediately neighbouring positions in the periodic table cause least disturbance in the bonding environment

due to the smallest possible differences in atomic radii and in electro-negativity. In carbon, boron and nitrogen are the most promising elements to form electro-positive and electro-negative solid solutions (doping), respectively. There have been a number of attempts to incorporate boron and nitrogen in tetrahedrally bonded amorphous carbon [45, 46]. A successful solution of either element should lead to a movement in the Fermi energy of the a-C without any reduction in band-gap from its intrinsic value. Introduction of dopants such as N into the C structure, makes it relax, leading to a modification in overall properties corresponding to the presence of additional π bonding [46, 47, 48, 49, 50].

N too can contribute both σ and π bonds at sp^3 and sp^2 hybridised sites [51, 52]. There are a variety of bonding possibilities for N in a-C. If N is to act as an electronic dopant, then it should be bonded in such a way that a donor electron in a non-bonded orbital is available. One possibility is the substitution of a C atom with an N forming four σ bonds with adjacent C atoms, leaving one electron in an un-bonded state. The non-doping configurations are, the formation of three σ bonds and a *lone-pair* or the formation of four σ bonds, but passing the remaining electron to a lone-pair in C resulting in a C-N *compensating* site. Another possibility is the formation of three σ bonds and a π bond leaving the other electron in an atomic N p-orbital. A π bond and two σ bonds with a lone-pair is the another non-doping configuration. The other unique linear non-doping configuration is having, two π bonds, a σ bond and a lone-pair. The orbital orientations of these conditions are schematically illustrated in Fig. 1.2.

Bursill *et. al.* showed in their PEELS observations that N is bonded predominantly in trigonal sp^2 sites, both in nanocrystalline and amorphous phases [53]. The presence of N in the C matrix has significantly modified the infrared response of the material [54]. It has been suggested that alloying N in a-C to form a-C:H:N reduces the defect electronic states in the band-gap. This effect has been observed in the optical extinction coefficient and also the optical band gap of the material [55]. The influence of N upon electronic states and the Fermi level in a-C has been investigated theoretically by Stumm *et. al.* [56]. They suggest that the N at tetrahedral sites or at sites in chains of an even number of

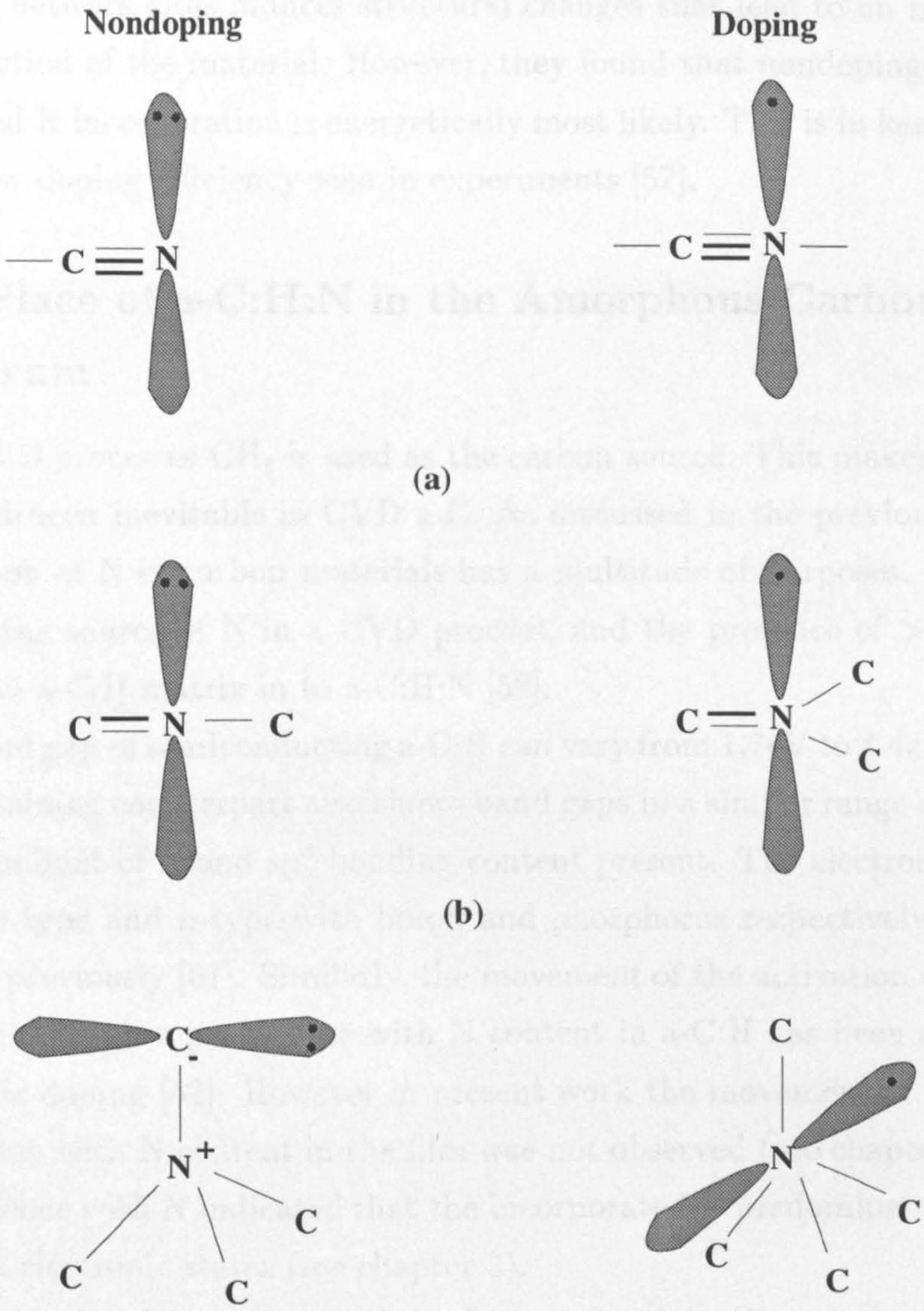

Figure 1.2: The orbital spread of (a) sp, (b) sp^2 and (c) sp^3 hybridised nitrogen atoms and the doping variant of the corresponding hybridisations are illustrated. The lone-paired electron orbitals are denoted by a set of two dots.

π bonded sites results in an increase of the Fermi energy, while N incorporation in strained network sites induces structural changes that lead to an increase in the sp^2 fraction of the material. However, they found that nondoping threefold co-ordinated N incorporation is energetically most likely. This is in keeping with the very low doping efficiency seen in experiments [57].

1.2.4 Place of a-C:H:N in the Amorphous Carbon Spectrum

In most CVD processes CH_4 is used as the carbon source. This makes the presence of hydrogen inevitable in CVD a-C. As discussed in the previous section, incorporation of N in carbon materials has a multitude of purposes. When N_2 is used as the source of N in a CVD process, and the presence of >2atm% N modifies the a-C:H matrix in to a-C:H:N [58].

The band gap of semiconducting a-C:H can vary from 1.7eV to 4.4eV [59, 60]. The N containing counterpart also shows band gaps in a similar range depending upon the amount of N and sp^3 bonding content present. The electronic doping of a-C:H, *p*-type and *n*-type with boron and phosphorus respectively has been attempted previously [61]. Similarly, the movement of the activation energy for conduction through a peak value with N content in a-C:H has been attributed to electronic doping [52]. However in present work the movement of activation in conduction with N content in the film was not observed (see chapter 2). The PL dependence with N indicated that the incorporated N predominantly resides in localised electronic states (see chapter 3).

A concept of a planar ternary phase diagram is adopted to represent the a-C material spectrum containing H and C [62, 63]. This can be modified in the third dimension to include the presence of N in the H and C environment as illustrated in Fig. 1.3.

- The five corners of the pyramid represent,
  - Solid phases
    - entirely sp^3 bonded diamond and

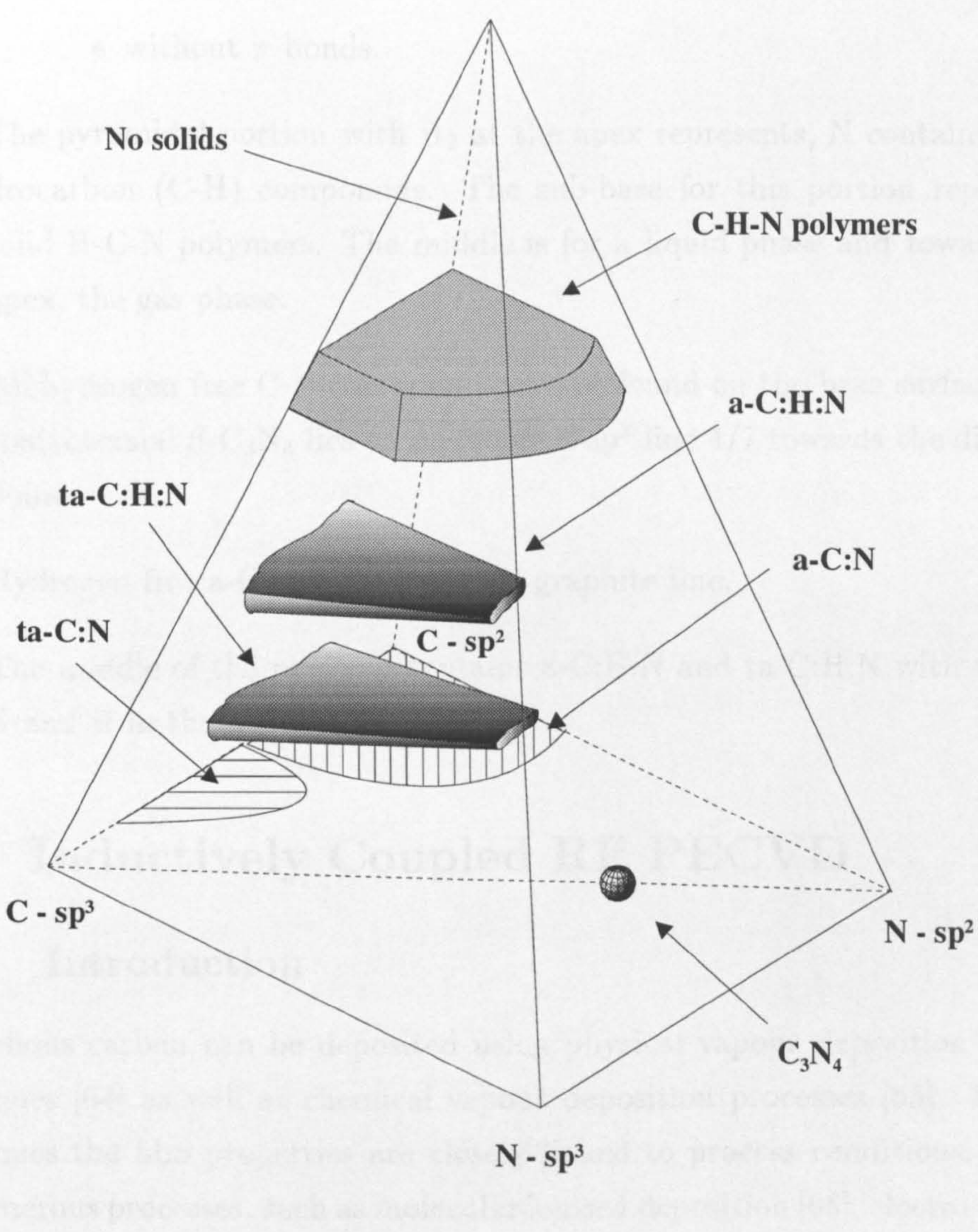

Figure 1.3: Pyramidal phase diagram of H, N and C compounds.

        * entirely sp^2 bonded crystalline graphite, and

  - Gaseous phase H_2 and

  - The incorporated N bonded

        * with associated π bonds

        * without π bonds.

- The pyramidal portion with H_2 at the apex represents, N containing hydrocarbon (C-H) compounds. The sub-base for this portion represents solid H-C-N polymers. The middle is for a liquid phase and towards the apex, the gas phase.

- All hydrogen free C-N compounds can be found on the base surface. The controversial β-C_3N_4 lies on diamond-N-sp^2 line 4/7 towards the diamond point.

- Hydrogen free a-C in is on diamond-graphite line.

- The middle of the pyramid contains a-C:H:N and ta-C:H:N with varying N and H in them.

1.3 Inductively Coupled RF PECVD

1.3.1 Introduction

Amorphous carbon can be deposited using physical vapour deposition (PVD) techniques [64] as well as chemical vapour deposition processes [65]. In both techniques the film properties are closely linked to process conditions. There are numerous processes, such as molecular ionised deposition [66], electro-plating [67], DC glow discharge [68], magnetron sputtering [69], mass selected ion beam [70], cathodic vacuum arc [71] and plasma enhanced CVD [72] etc. which can be used for a-C film formation.

In PECVD processes, the chemically active vapour phase agent is generated via a plasma activity. RF plasma enhanced CVD (RF PECVD) is a common

technique used for depositing a-C:H and a-C:H:N due to stable plasma conditions and the ability to use hydrocarbon gases for source materials.

1.3.2 Inductively Coupled RF Plasma

In *reactively* coupled RF plasma systems, the source of energy for plasma generation comes from an RF power supply. The overall load offered to the RF supply is a combination of the *antenna* reactance and the impedance related to the plasma column. Depending upon the condition of the plasma column, the load seen by the RF source varies [73]. The resultant field acting upon the plasma has two components, *i.e.* the electric field originating from the potential drop across the plasma due to the potential difference between the antenna and the ground, and the field induced by the oscillating RF field. At low power inputs, irrespective of the geometry of the RF *antenna*, the electric field due to the potential drop dominates. At higher RF power inputs, the type of the reactance offered by the plasma is determined by whether it is an oscillatory electric field or magnetic field. The system couples capacitively at low RF powers, which is referred to as E_{mode} operation and with increased power coupling transfers either to inductive coupled (H_{mode}) or remains capacitively coupled depending upon the dominant field type [74].

The antenna geometry of parallel plates offers dominant electric fields in the high power regime and continues to be *capacitively coupled* even after mode transition. In this type of arrangement, the feed electrode develops a *DC self bias* potential owing to differential mobilities of electrons and ions. The sign of the bias potential is determined by the relative size of electrodes, and in most cases it is negative [75]. The DC electric field due to self bias induces a potential energy upon ionised species which, in turn causes them to drift along in the DC field. An ion reaching the feed electrode carries a kinetic energy determined by the self bias, *i.e.* in capacitively coupled plasmas the ion energy is predominantly kinetic and the impinging velocity on the substrate depends upon the DC self bias.

The coil type antenna arrangement as seen in Fig. 1.4, applies an induced

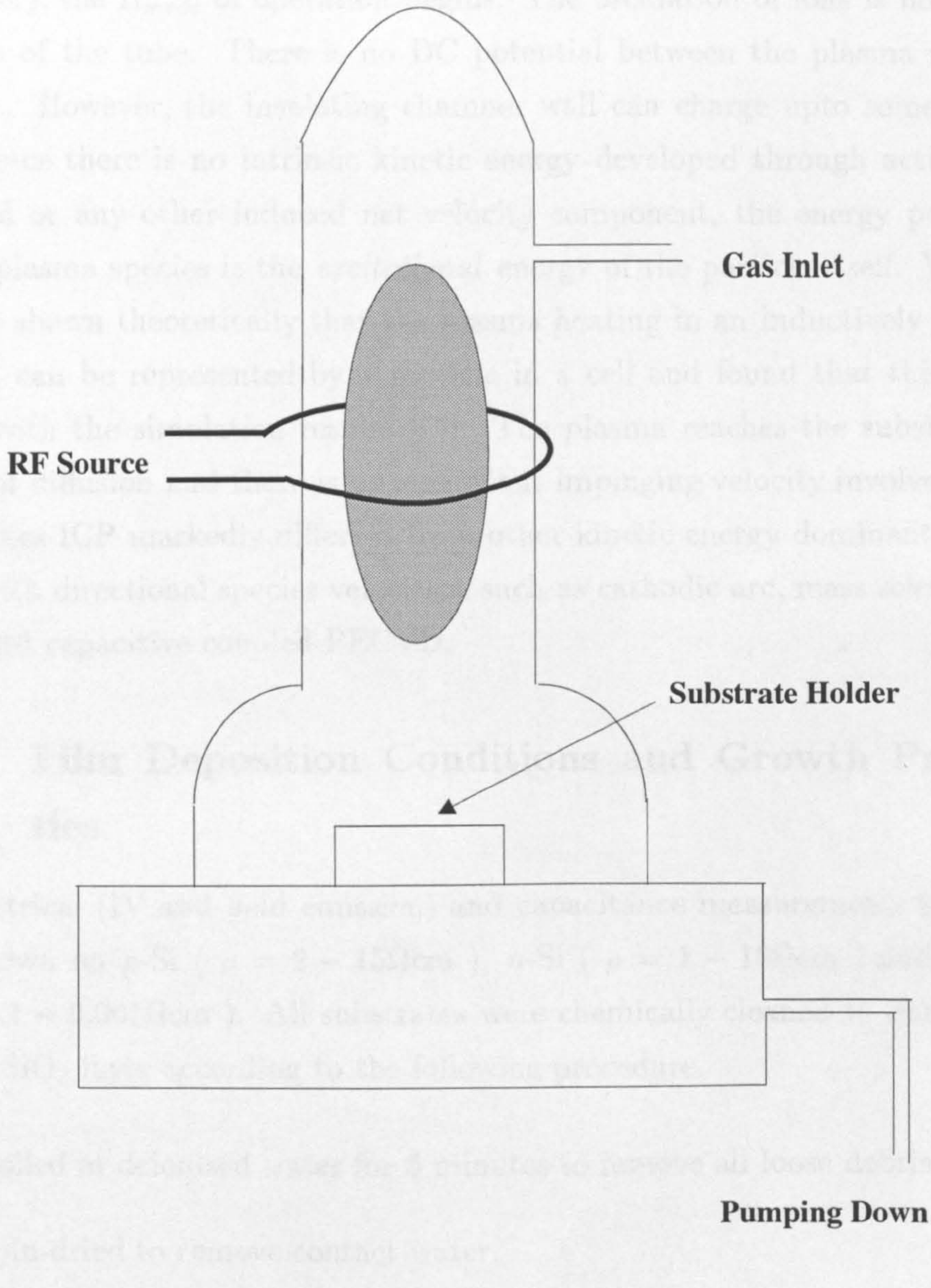

Figure 1.4: The schematic diagram of the inductively coupled PECVD system.

oscillatory magnetic field along the axis of the plasma tube. When the electric field associated with the magnetic field is large enough to overcome the electrostatic field due to potential difference between the antenna and the ground (chamber), the H_{mode} of operation begins. The oscillation of ions is normal to the axis of the tube. There is no DC potential between the plasma and the antenna. However, the insulating chamber wall can charge upto some degree [76]. Since there is no intrinsic kinetic energy developed through action of a DC field or any other induced net velocity component, the energy possessed by the plasma species is the *excitational* energy of the particle itself. Yoon *et. al.* have shown theoretically that the plasma heating in an inductively coupled plasma, can be represented by a particle in a cell and found that this model agrees with the simulation results [77]. The plasma reaches the substrate by means of diffusion and there is no significant impinging velocity involved. This fact makes ICP markedly different from other kinetic energy dominant plasma types with directional species velocities, such as cathodic arc, mass selected ion beam and capacitive coupled PECVD.

1.3.3 Film Deposition Conditions and Growth Properties

For electrical (IV and field emission) and capacitance measurements the films were grown on p-Si ($\rho = 2 - 15\Omega$cm), n-Si ($\rho = 1 - 10\Omega$cm) and n^{++}-Si ($\rho = 0.1 - 0.001\Omega$cm). All substrates were chemically cleaned to remove the surface SiO_2 layer according to the following procedure.

- Boiled in deionised water for 5 minutes to remove all loose debris.
- Spin-dried to remove contact water.
- Heated in trichloro ethylene at 60^0C for 10 minutes to degrease.
- Rinsed in 2-propanol.
- Washed in deionised water to remove degreasing agent.

- Heated in deionised water, hydrogen peroxide and ammonium hydroxide in the ratio 5:1:1 at 60^0C for 10 minutes. This oxidising mixture grows a thin SiO_2 on the Si surface which is subsequently etched off.
- Washed in deionised water.
- Heated in deionised water, hydrogen peroxide and hydrochloric acid in the ratio 5:1:1 at 60^0C for 10 minutes. The oxide layer grown above is dissolved and a fresh oxide free Si surface results.
- Washed in running deionised water for 5 minutes to remove any contamination.
- Spin-dried.

For optical experiments samples were deposited either on glass substrates or on fused quartz disks. Glass and quartz were cleaned using the first five steps of the above procedure or by ultrasound cleaning in acetone. All substrates were given an in-situ He plasma preclean at 600W RF power for 30-60s in order to sputter clean any impurities.

Precursor Ratio CH_4 : N_2 (sccm)	**N Content** N at. %	**Deposition Rate** nm/min
5 : 0	0	7.3
7 : 3	3.6	5.0
5 : 5	9.0	25.5
2.5 : 7.5	27	35.6
1 : 9	30	47.9

Table 1.1: The precursor ratio, the corresponding N content in the film and the deposition rate at 600W of RF power and ≈900mtorr deposition pressure are summarised. The N content in the films were determined by Scanning Neutral Mass Spectroscopy (SNMS) carried out at MATS UK.

In table 1.1, typical deposition parameters for films having varying N content are summarised. Generally a base pressure of $\approx 10^{-3}$mbar was used with a

deposition pressure of ≈0.9mbar and 600W of RF power input. For electrical and optical measurements film thickness of 100-500nm was maintained while the field emission measurements were performed with films ≈30nm thick.

The RF power dependency of deposition rate in the power range 600W to 1050W is shown in Fig. 1.5 for CH_4:N_2 = 1:1 ratio. Deposition rate reaches a peak value of 74nmmin^{-1} for RF power input of ≈900W. The film deposition process is the net result of competing growth and an etching reactions. At low RF power inputs the reactive species production is not efficient, and the net deposition rate is low. At high RF powers, etching species are in abundance, and the deposition rate is again low. The mid power range (900W in the present case) is a compromise between deposition and etching.

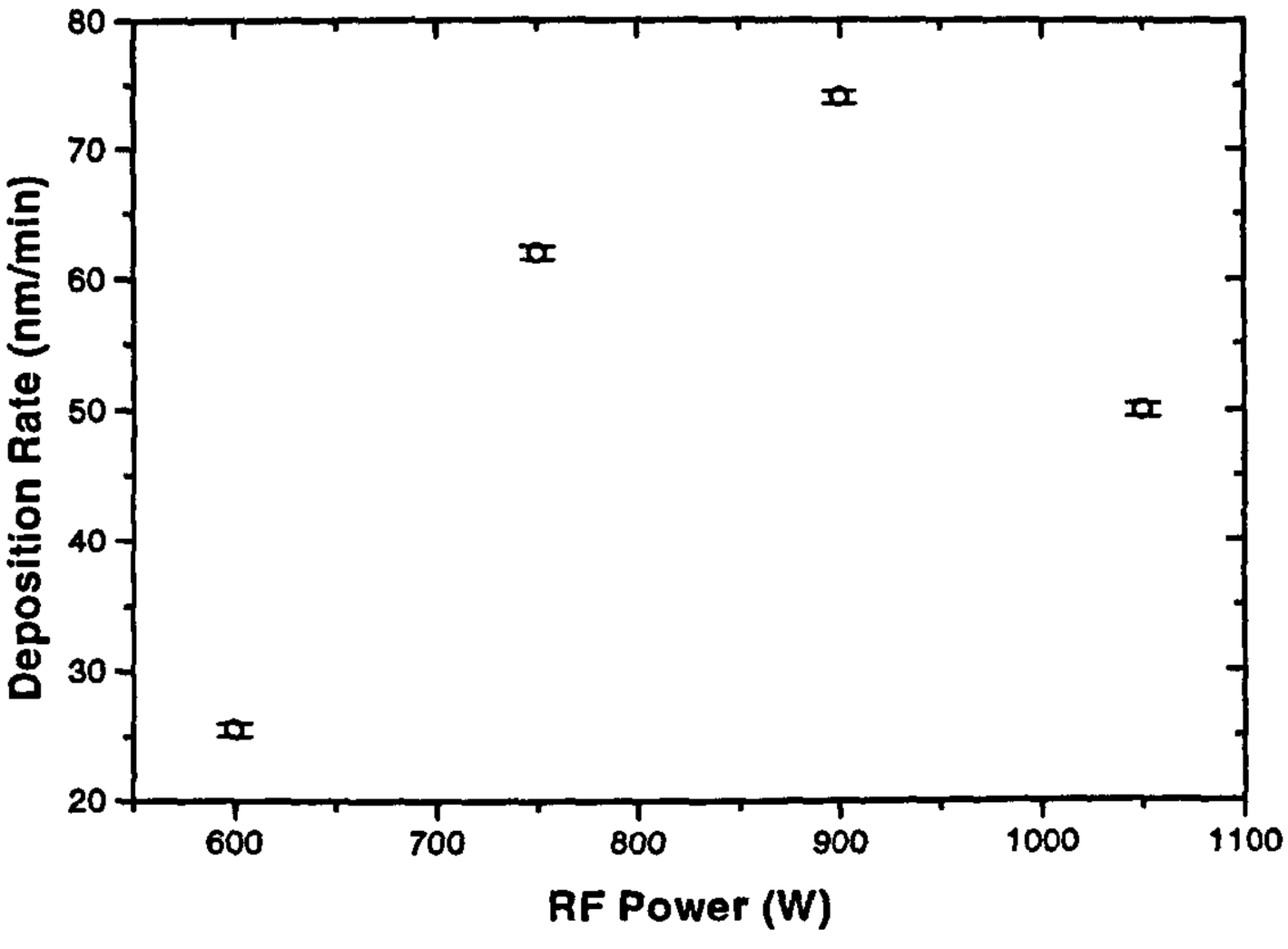

Figure 1.5: The plot of rate of deposition against RF power applied. Deposition rate goes through a peak around 900W.

1.3.4 Film Properties

In Fig. 1.6 the FTIR absorption spectra of films deposited in the ICPECVD system are illustrated. When there is no intentional inclusion of N in the film, only peaks associated with C-C and C-H are present. Such peaks can be seen in all spectra below 1700 cm^{-1}, and also from 2700 to 3100 cm^{-1} wave numbers.

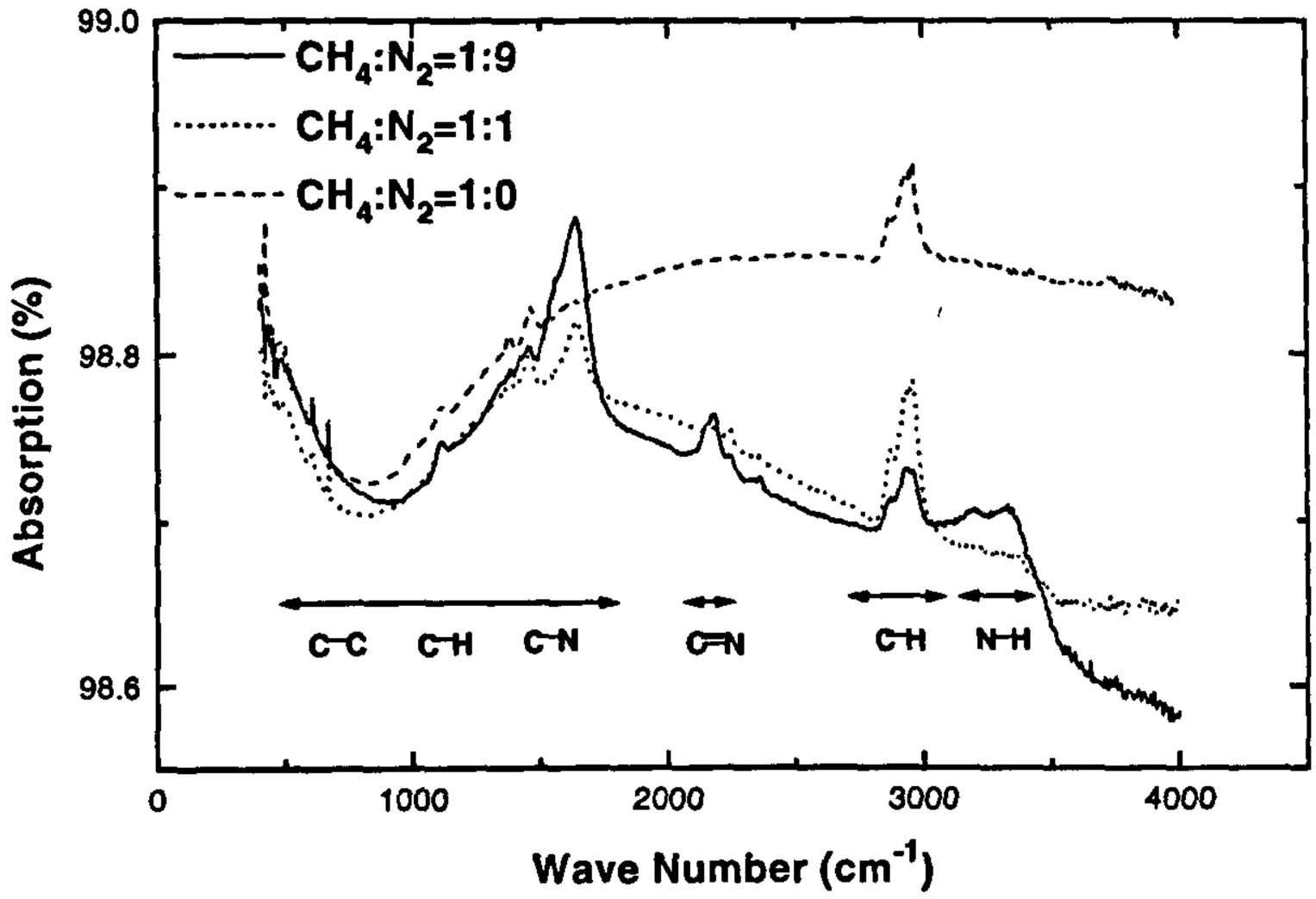

Figure 1.6: The IR absorption spectra of a-C:H and a-C:H:N films containing different N content. The peak associated with C-H stretching modes from 2700 to 3100 cm^{-1} wave numbers is common for all films. The C-N peak towards 1700 cm^{-1} wave numbers is present only in N containing films. The triple bonded C-N from 2065 to 2260 cm^{-1} and N-H from 3150 to 3400 cm^{-1} appear only in the film with the highest N content.

The N associated modes are dominated by the peak seen in the region of 1700 cm^{-1} wave numbers. Though this range is characterised by C-C, and C-H as well as C-N modes, the clear peak seen only in N containing films at 1700cm^{-1} can be unambiguously ascribed to C-N [78]. The triple bonded N stretching mode from 2065 to 2260 cm^{-1} wave numbers is seen only when the film with

the highest (30%) N content. The range from 3150 to 3400 cm^{-1} wave numbers is associated with N-H stretching modes and also with modes originating from sp C≡C-H sites around 3300 cm^{-1} wave numbers. The absence of such a peak in the film with no N suggests that the peak in the film containing highest N content is an N-H stretching mode [79].

1.4 Helicon Wave Excited PECVD

1.4.1 Introduction

The existence of helicon mode electromagnetic waves in the natural environment and under certain experimental conditions in laboratory plasmas has been well known for a long time (see chapter 4). The practical usage of helicon waves to generate laboratory plasma sources has been pursued since it was shown that there is evidence of electron acceleration in such sources [80]. With the commercial development on the plasma dynamics in such sources, they have applied in materials processing, advanced accelerators and radiation sources [81]. The initial usage of helicon plasma sources in materials processing was for etching, owing to the higher plasma densities which can be achieved [82, 83]. Subsequently helicon plasmas were used in deposition processes. Koike *et. al.* demonstrated the use of a helicon plasma in the production of multilayered X-ray mirrors [84]. There are further reports of high quality SiO_2 growth at low temperatures [85] and the deposition of fluorinated amorphous carbon [86]. In the present work a helicon wave plasma is used to generate nitrogen plasma and also to deposit a-C:H and a-C:H:N.

1.4.2 Plasma Generation

In general the excitation of plasma species takes place through collisional energy transfers between particles. When an electro-magnetic wave is launched in to a plasma in the presence of a static magnetic field, the right hand circular polarised component propagates along the magnetic axis for angular frequencies less than

the cyclotron frequency, while the left hand circular polarised component gets attenuated, as discussed in chapter 4.

When there is a particle having a velocity slightly lower than that of the phase velocity of the electro-magnetic wave, then the particle gains energy from the wave, and this phenomenon is known as *Landau damping* (or *inverse Cerenkov radiation*). This process allows the plasma excitations to take place via collisionless energy transfer between the wave and the particle. In the literature there are reports, modelling the Landau damping effect with finite element analysis [87], and theoretical studies of the influence of RF antenna types [88] and the practical regime necessary to sustain such plasmas [89].

The phase velocity of the propagating wave is a function of the DC magnetic field and the RF antenna length. Hence the energy transfer can be tailored externally, unlike in conventional plasmas. This fact allows resonant type tunable plasma excitations with narrow energy distributions.

1.4.3 Deposition Conditions

The substrate cleaning procedure was similar to that used in ICPECVD. The base pressure reached prior to deposition was $\approx 2\times10^{-5}$mbar and the deposition pressure was ≈1mbar. During deposition substrates were held parallel to the DC magnetic axis.

The RF power is fed through a *double loop* helicon antenna and can be varied up to 3kW. Films were deposited from 50W to 500W. As shown in Fig. 4.10 deposition rate goes through a peak for ≈150W due to the same reason as described in ICPECVD case, when no magnetic field is applied. Fig. 4.12 illustrates the magnetic field dependency of the film deposition rate. The maximum value of 6nmmin^{-1} goes through a step change at ≈40mT which is the magnetic field at which preferred N excitations take place. Additional excitation of N has made the etching process more efficient.

Chapter 2

Electrical Characterisation of a-C:H:N

2.1 Introduction

In this chapter the basic electrical properties of inductively coupled PECVD deposited a-C:H and a-C:H:N are analysed. By looking at the temperature dependence of the conductivity, the conduction mechanism in the bulk is selected among possible processes in amorphous materials. The heterostructures of Au/a-C:H:N/Si are examined in order to the understand the barriers associated with interfaces. The nature of Au contacts on a-C:H:N is also discussed.

The capacitance-voltage (C-V) characteristics can be used to identify the charge present at the interface and in the bulk material. The frequency response of the C-V characteristics can be used to determine the polarity and location of the charge.

2.2 IV Characteristics

2.2.1 Conduction Mechanisms

In a crystalline semiconductor the conduction process at any given temperature is mainly determined by the sharp energy levels which form the band-gap, and

the relative position of the Fermi energy with respect to these energy levels. The relative position of the Fermi energy in turn reflects the number of mobile charge carriers (electrons and holes) in the conduction and valence bands. The conduction of charge carriers in an insulator at low electric fields is mainly associated with inter-band-gap energy states termed *traps.*

For amorphous materials, the concept of distinct band-gap energy levels breaks down. It is replaced by the density of states associated with *delocalised* energy states and *localised* energy states. In addition there can be inter-band-gap defect states as well, as in an insulator. In this scenario the conduction mechanism in an amorphous material has to be understood in terms of a combination of delocalised, localised and trap states. There are several possible bulk dominated conduction processes that can be identified in amorphous semiconductor materials.

- Extended state conduction :

  In the density of states distribution, the energy levels away from mid-gap are relatively more delocalised. Carriers excited in to these or higher states are delocalised and thus are the most mobile. The lowest energy of such a delocalised state is referred to as the *mobility edge* in an amorphous semiconductor. Hence, *extended states* are those which have energies above the mobility edge. One form of conduction in amorphous semiconductors can occur when carriers are thermally activated above the mobility edge, E_m. This can be expressed as :

$$\sigma_{ext} = \sigma_m \exp\left[-\frac{E_m - E_F}{kT}\right] \tag{2.1}$$

  Where the terms in expression 2.1 are, σ_m - the average conductivity above the mobility edge, E_m - the energy at the mobility edge, E_F - Fermi energy, k - Boltzmann constant, and T - absolute temperature. The concept of the Fermi energy is carried over from classical crystalline semiconductors to express the population probability of a given energy level. In amorphous carbon the deep π states are highly localised and can be considered as tail

states (see next section). The π states lying close to the σ states can in some cases have an *extended-like* nature. Hence, for amorphous carbon the analogous extended state conduction takes place by activation of carriers into shallow π states.

- Band tail conduction :

The *band tails* denote the localised states situated closer to mid-gap which originate from bond disorder (variations in bond angle and bond length). At absolute zero these states are inactive for carrier transport. However at elevated temperatures there can be conduction which arises from hopping between localised tail states. Even though the wave-function associated with localised states does not strongly interact between neighbouring sites, at elevated temperatures the spatial extent of the wave function makes tunnelling type transitions more probable. Tail state conductivity can be expressed as :

$$\sigma_{tail} = \sigma_t \exp\left[-\frac{E_t - E_F}{kT}\right] \tag{2.2}$$

where E_t - the average energy shown by the tail state conduction path and σ_t - the average conductivity in tail states. This parameter depends upon the density of tail states and on the degree of wave-function overlap in neighbouring localised states. The σ_t is expected to be lower than σ_m due to the high degree of localisation of the tail states in contrast to states near the mobility edge. However, since E_t lies closer to the Fermi energy than E_m, the exponential term in 2.2 compensates for the lowering of the prefactor σ_t for tail conduction, especially at low temperatures where it is the most prominent.

The above mentioned band tail conduction mechanism can be used to describe the conduction via localised tail states associated with deep level π states in a-C. The sp^2 sites, which give rise to the π states have been shown to cluster together via energy calculations [90]. The degree of overlap of π states within the cluster can be large, allowing the possibility of

local delocalisation. However, it has been shown that if the Bohr radius of the cluster is not larger than the cluster radius then the inter-cluster interactions are very weak [91]. Also, the possibility of local delocalisation is limited due to the polar nature of p-orbitals which form the π bonds. Unlike amorphous Si where all bonds have the σ character, proximity of π bonds alone is not sufficient to allow delocalisation. The bond angles must also be closely aligned to allow overlap of the π states. This has been found (by atomic level simulations) to localise the π states in a-C even above the percolation limit. That is, when all the sp^2 clusters have merged into each other [90]. Therefore the deep π states in a-C are strongly localised.

- Hopping conduction at the Fermi energy :

  When the density of states at the Fermi energy is very large, the tunnelling between such states becomes prominent. The primary conduction occurs at the Fermi energy and is usually related to the defect density within the material. Since this is a tunnelling process, it is weakly temperature dependent. The conductivity arising from this process is weak when the defect density is low so that it can only be observed at low temperatures [2]. The hopping conduction is given by :

$$\sigma_{hop} \propto \exp\left[-\frac{1}{T^{1/4}}\right] \tag{2.3}$$

- Space charge limited conduction (SCLC) :

  A space charge region is generally associated with a region within a material which has a net negative or positive charge. This can readily occur in a semiconductor or in an insulator. Such regions arise due to several reasons, such as fixed or polarised charge at the interface or in the bulk, depleted regions, the charging up of traps and excess injection of carriers into a space which can be centralised. The common feature associated with SCLC is the presence of a local electric field which affects the propagation of carriers across the material. The current through the material scales

with the *effective thickness* of the space charge layer [92]. The current density in SCLC is given by :

$$J = \frac{8\epsilon\mu}{9}\frac{V^n}{d^3} \tag{2.4}$$

where ϵ - permittivity of the space charge region, μ - carrier mobility, V - voltage and d - effective thickness of the space charge region.

In addition to the macroscopic properties which reflect the bulk conduction process, there can be barrier limited properties originating either at interfaces with metal contacts or different material regions, or microscopic barriers within the material. There are two main mechanisms which describe current flow across such barriers.

- Poole-Frenkel conduction.

  The Poole-Frenkel effect is sometimes called the *internal Schottky effect* because the *local thermal excitation* of carriers is very similar to the thermionic emission of a bulk barrier in the Schottky effect. The conduction is via the detrapped electrons or holes generated by field- enhanced thermal excitations. Both, the Pool-Frenkel and Schottky effect are due to the Coulombic interaction between the escaped carrier and the opposite charge. However they differ in that the opposing charge in the Poole-Frenkel effect is fixed while in the Schottky effect it is the mobile image of the escaped carrier. Therefore, the barrier in the Poole-Frenkel effect is two times lower than in the Schottky effect [93]. The current density is then given by :

$$J \approx \vec{E}\exp\left[-\frac{q}{kT}\left(\phi_B - \sqrt{\frac{q\vec{E}}{\pi\epsilon}}\right)\right] \tag{2.5}$$

  where $\vec{E}$ - local electric field and ϕ_B - local barrier seen by carriers.

- Fowler-Nordheim tunnelling :

This is another barrier limited type conduction mechanism in semiconductors associated with interface barriers. The concept is treated in length in chapter 5. The current through such an interface is given by,

$$J \propto \vec{E}^2 \exp\left[-\frac{4}{3\hbar}\sqrt{2m^* q}\ \phi_B^{3/2}\frac{1}{\vec{E}}\right] \tag{2.6}$$

where all notations are described in detail in chapter 5.

2.2.2 Heterojunctions on Si

Although electronic tail states and defect states exist across the gap, they are low enough so that a well defined optical band-gap (Tauc and E_{04} in chapter 3) approaching 2.7-3.4eV, for the experimental films studied in this work, can be measured. When a-C:H or a-C:H:N is deposited on crystalline Si, an amorphous/crystalline semiconductor heterojunction can be formed. It has been demonstrated that incorporation of N into the a-C:H matrix leads to dramatic variation in its properties. a-C:H:N has been shown to have lower compressive stress as well as a lower defect concentration [52]. There is also the possibility that nitrogen gives rise to electronic doping in a-C:H. The heterostructures were fabricated by depositing a-C:H:N films using an inductively coupled plasma system with CH_4 and N_2 as the source gases. The films were deposited on p (2-15Ωcm) and n-type (1-10Ωcm) Si wafers (330-420μm thick). The films thickness obtained using profilometry was from 100nm-500nm. All Si substrates were wet chemically cleaned prior to deposition using the standard process described in chapter 1, and also sputter cleaned insitu with a He plasma. Subsequent to deposition Au metal contacts ranging from 0.25-2mm in diameter and $\approx 0.7\mu$m were thermally evaporated at a vacuum better than $\approx 10^{-6}$mbar. The I-V data were collected using a programmable electro-meter (Keithley 617) and a programmable voltage source (Keithley 230). The back contact to Si was obtained by either evaporating 2μm of Al or via large area pressure contacts on Al.

Au/a-C:H:N/*p*-Si Structure

Typical I-V characteristics of the Au/a-C:H:N/*p*-Si structure are shown in Fig. 2.1. The voltage indicated is the value applied to the Si substrate via the Al contact with respect to that applied to a-C:H:N via the Au contact. The forward to backward rectifying current ratio is ≈4 orders of magnitude and the forward turn on onset shows an *ideality* factor of ≈3. I-V properties were repeatable with negligible hysteresis within the detectable limit of the instrument (±0.01V). Similar behaviour from a-C/a-C:H films on Si has also been reported in the literature [94, 95]. In some reports the observed behaviour is attributed to heterojunction properties between a-C and Si owing to different band gaps and Fermi level positions [94], while in others the doping effect was also considered [95].

The deviation of the ideality factor η given by,

$$I_F = I_0 \exp\left[\frac{qV_F}{\eta kT}\right]$$

where I_F - forward conduction current and V_F - forward bias voltage,

towards a large value suggests that the carrier transport through the structure is not dominated by purely diffusion $\eta \rightarrow 1$ or recombination $\eta \rightarrow 2$ [96]. The free carrier density in a-C:H:N is expected to be much smaller than in *p*-Si due to a large number of possible bond configurations in which the N sites are either inactive or compensated [51]. This feature rules out the possibility of significant carrier recombination at the junction through the classical diffusion of carriers from either side of the junction to the depletion region.

To understand the rectifying nature of the heterostructure we shall look at the band alignment at the interface between a-C:H:N and *p*-Si. The position of the Fermi level with respect to band edges can be found by measuring the conductivity as a function of temperature. As investigated further in detail in the next section, the activation energy of this material was found to be ≈0.7eV, which did not vary significantly with the N content in the film. This can be understood in terms of a highly localised N related DOS which do not participate significantly in the electrical conduction process [97].

The influence of nitrogen on PL properties investigated in chapter 3 suggests

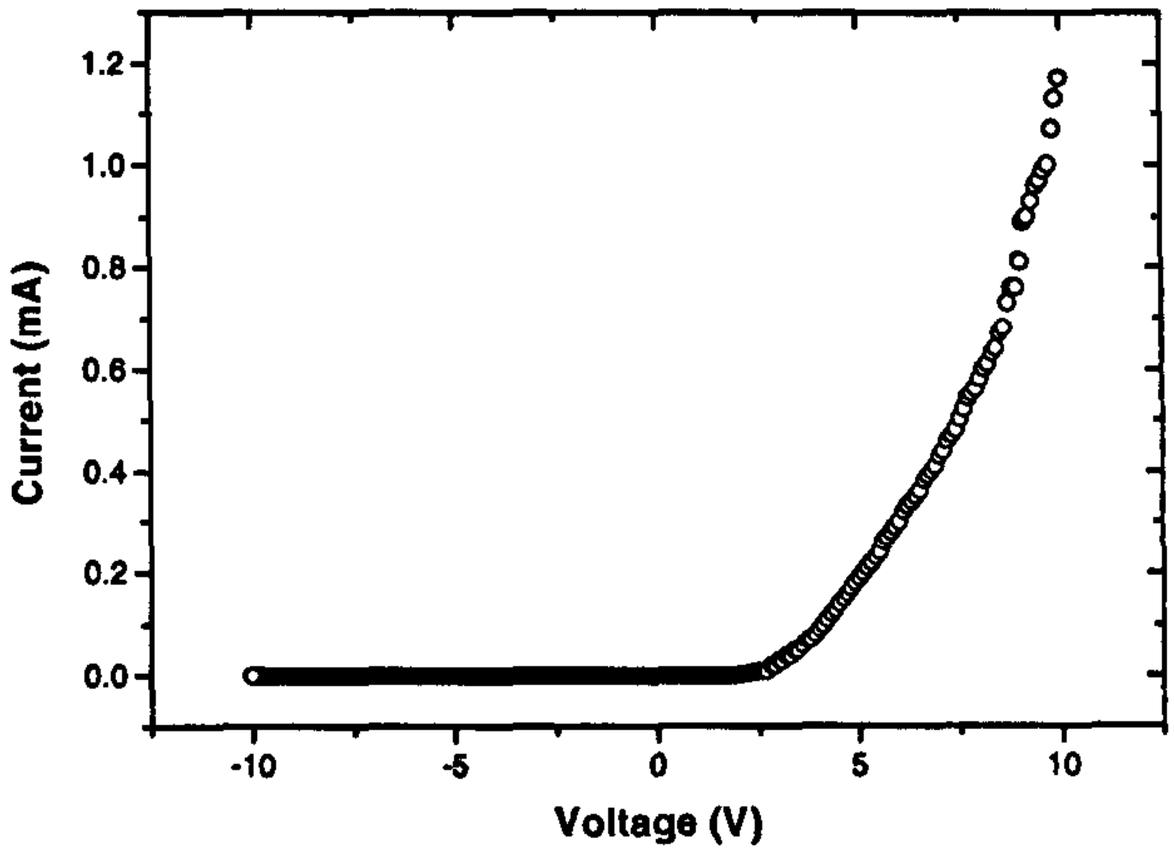

(a) I-V characteristics in linear plot.

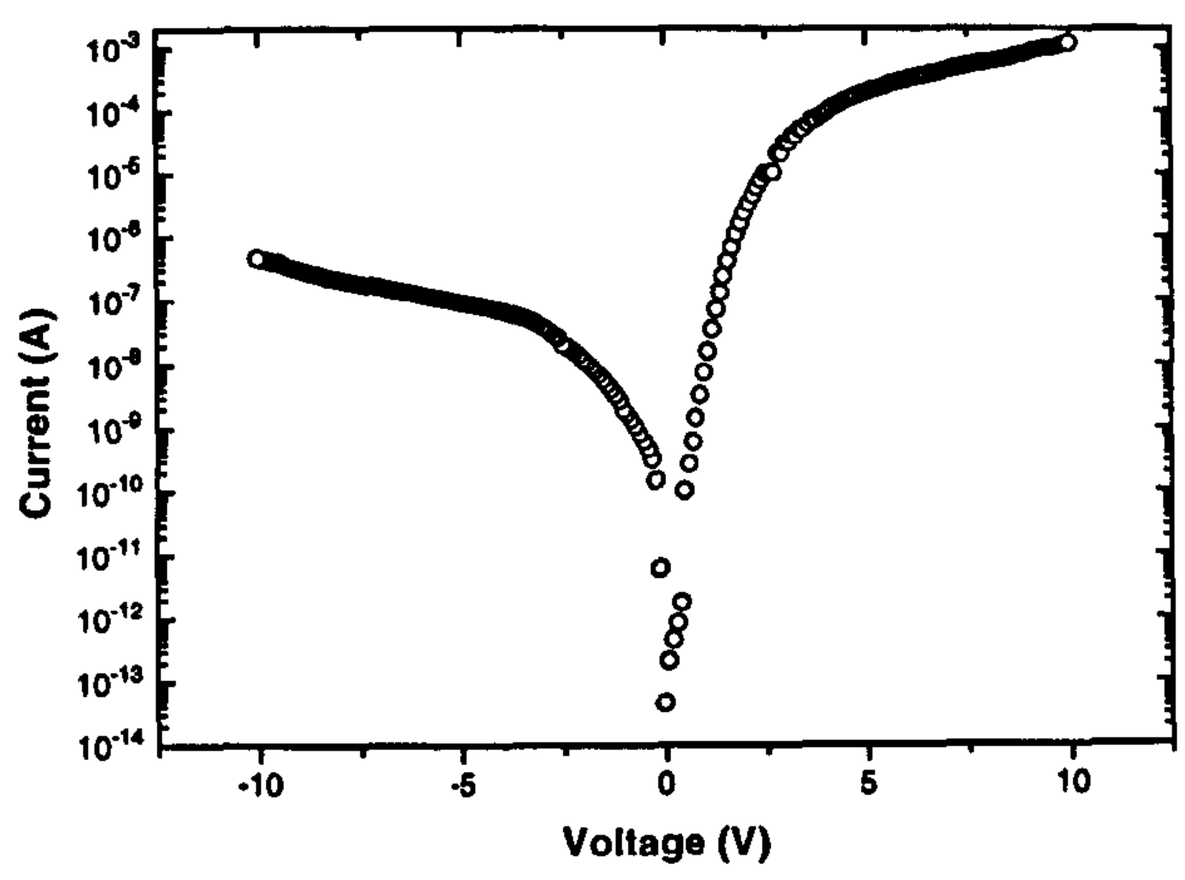

(b) I-V characteristics in log plot.

Figure 2.1: Typical I-V characteristics of a Au/a-C:H:N/*p*-Si heterostructure. Forward turn-on onset current shows an equivalent ideality factor of ≈3. The rectifying current ratio of 3-4 orders of magnitude can be seen in the log plot.

that the activation energy measured is in fact the Fermi level separation from the optical band edge. The moderately doped *p*-Si has a Fermi level separation of 0.2eV from the valence band edge. When the electron affinity of a-C:H:N is taken to be ≈2.5eV [98], an ≈1.3eV barrier for transfer of electrons from a-C:H:N to Si and an ≈0.4eV barrier for transfer of holes from the Si to the a-C:H:N are formed as illustrated in Fig. 2.2(a). As the level of positive bias on the Si with respect to the a-C:H:N increases the barrier for holes becomes smaller while that for electrons from the a-C:H:N becomes larger. That is the hole injection from *p*-Si into a-C:H:N is promoted over electron injection across the junction due to both reduction in barrier height and ready availability of holes in the *p*-Si. The valence band discontinuity of ≈+0.1eV was not found to be significant as seen by others in the literature [99].

When the bias is in the reverse direction, the barrier seen by electrons does not reduce significantly due to large conduction band offset (≈-1.5eV). Hole injection from the a-C:H:N is also poor due to the weak *n*-type behaviour of the material. The end result is low conduction in the reverse direction, suggesting that the rectifying nature is a combination of both barrier effects and carrier densities.

If the current in the a-C:H:N/*p*-Si heterostructure is limited by tunnelling, then it should follow the reduced form of Fowler-Nordheim expression eqn2.6. The tunnelling current density in the equation 2.6 through a triangular barrier, J is $a \exp\left(\frac{-b\phi^{3/2}}{E}\right)$, where ϕ is the barrier to tunnelling and E is the electric field. The forward current of the Au/a-C:H:N/*p*-Si structure plotted on the Fowler-Nordheim axes is illustrated in Fig. 2.3 (electric field was derived assuming the applied voltage is dropped over the a-C:H:N layer linearly). The figure shows typical carrier tunnelling through a barrier characteristics. The barrier height extracted from the slope of the graph was found to be 0.05eV for high bias voltages, when the effective mass (m*) of the carrier is taken to be 0.1 of the rest mass. Given that the metal contacts are ohmic with low contact resistance as discussed in section 2.2.4, the linear characteristic of Fig. 2.3 in the electric field range of ≈3-13Vμm^{-1} indicates that the injected holes from *p*-Si tunnel through the reduced barrier at the valence band.

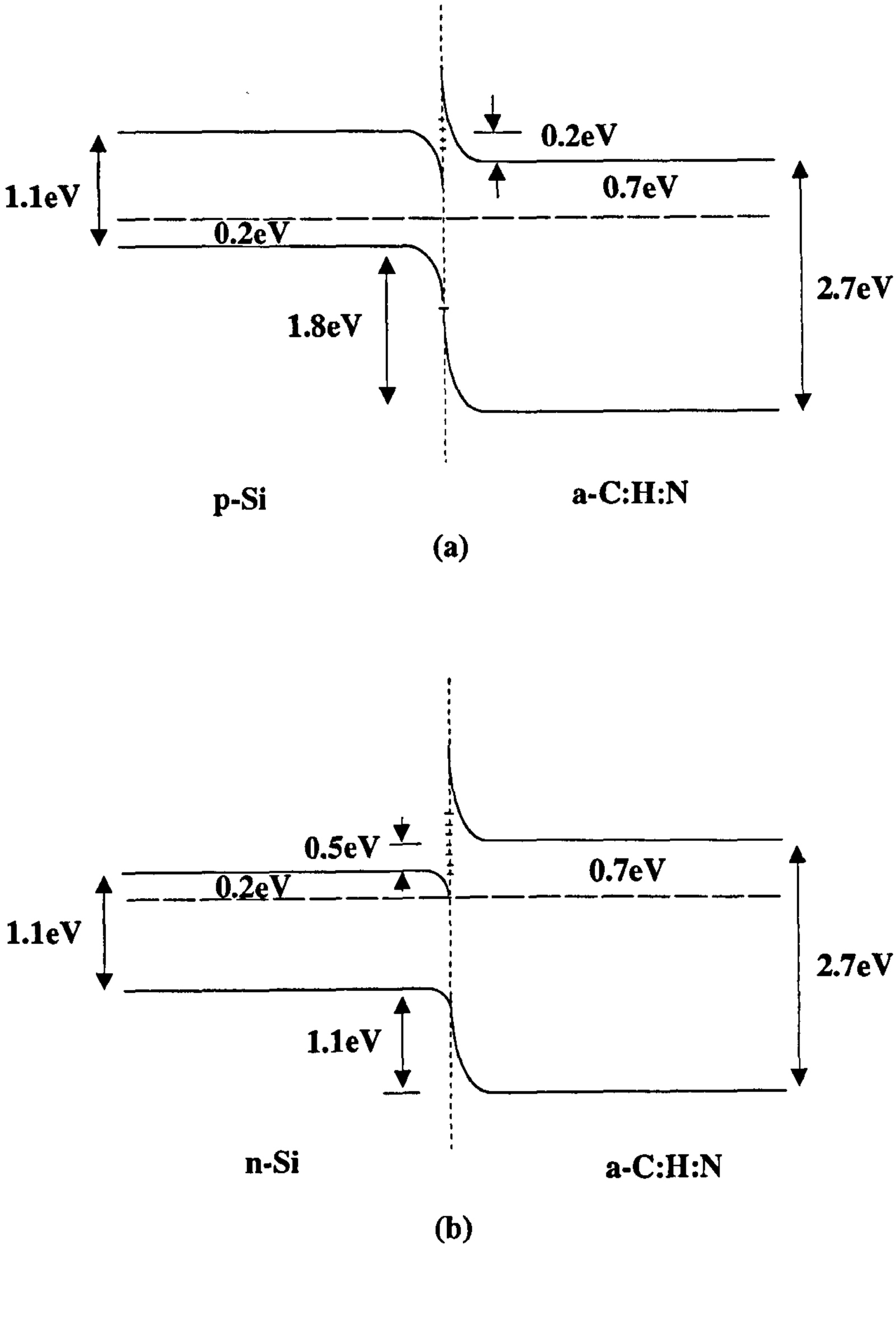

Figure 2.2: (a) : The energy band diagram of a-C:H:N/p-Si heterojunction is illustrated, that of a-C:H:N/n-Si structure is in (b). The continuity of vacuum energy level is assumed. The electron affinity of a-C:H:N is taken to be $\approx$2.5eV.

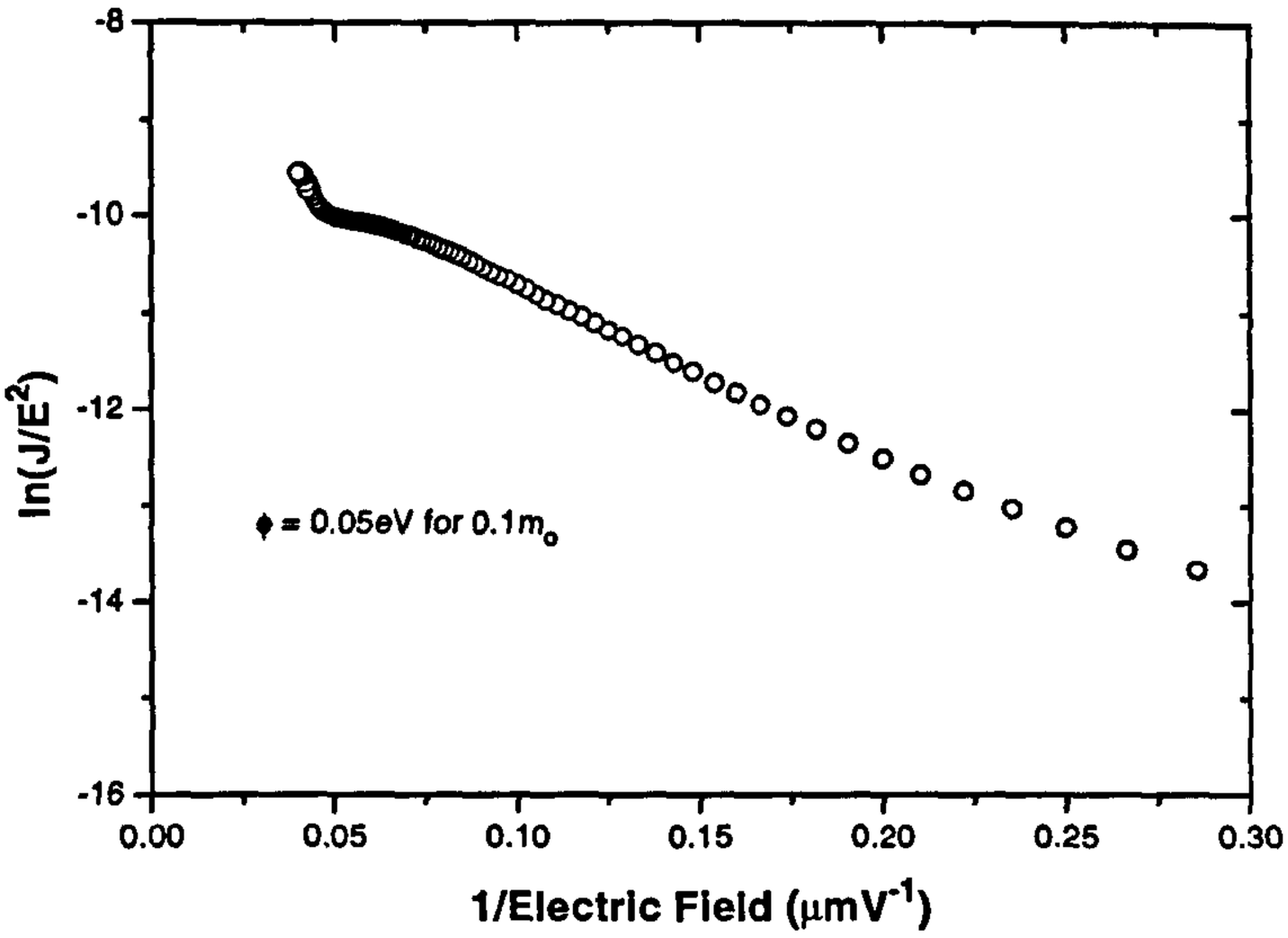

Figure 2.3: Fowler-Nordheim plot for Au/a-C:H:N/p-Si structure. A barrier height of 0.05eV can be extracted from the slope of the curve assuming an effective mass of $0.1m_o$.

Au/a-C:H:N/n-Si Structure

Results from a-C:H:N on n-Si heterojunctions are plotted in Fig. 2.4. The polarity of rectification is reverse of that shown with p-Si heterojunctions. The forward to backward rectification ratio and the *ideality factor* (2-3) are of the same order as those obtained for p-Si structures, indicating similar mechanisms may also govern the current flow in these heterojunctions.

When n-Si is negatively biased the barrier seen by injected electrons is $\approx$0.8eV and is less than that on p-Si (see the band diagram in Fig. 2.2(b)) so that the tunnelling probability increases at higher bias levels. Even though no barrier or valence band offset is seen by holes from the a-C:H:N to the n-Si, the relatively low density of holes prevents significant carrier recombination at the junction. Applying negative bias on the Si with respect to the a-C:H:N, barrier lowering at the conduction band causes electron injection from a-C:H:N.

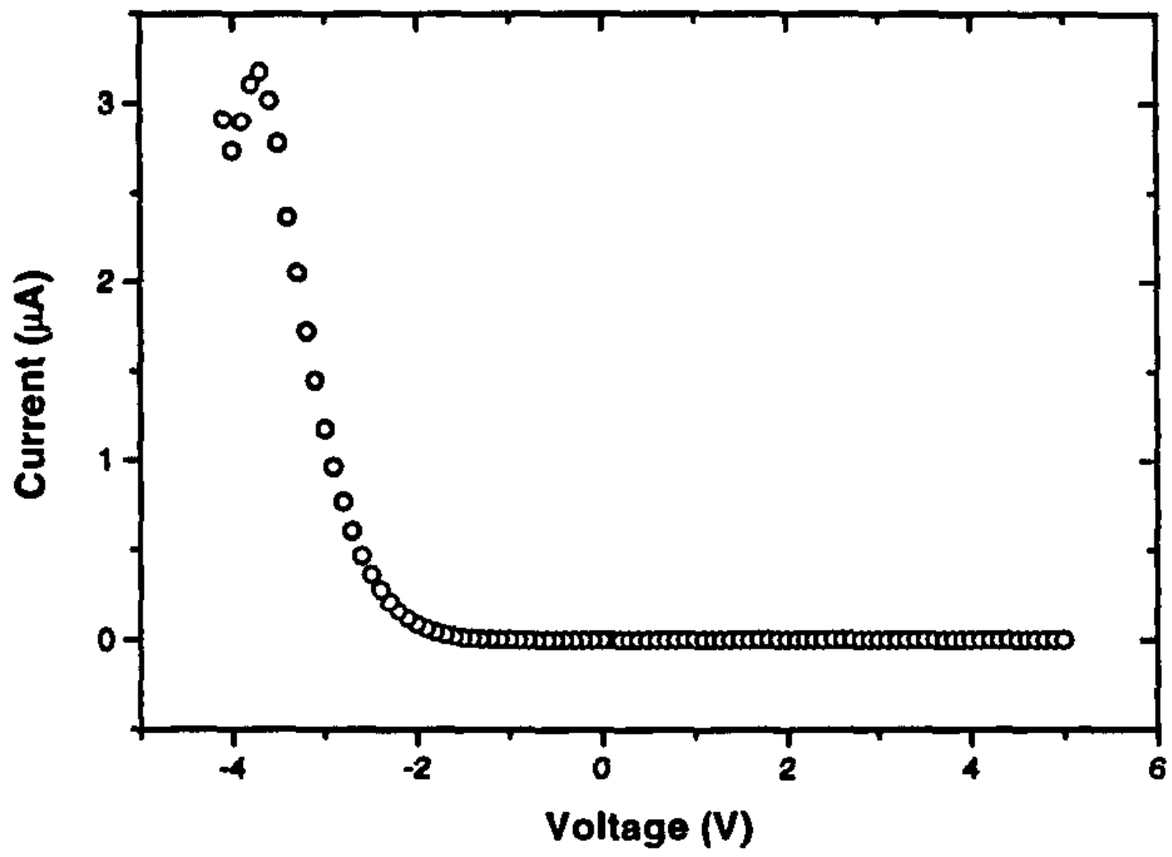

(a) I-V characteristics in linear plot.

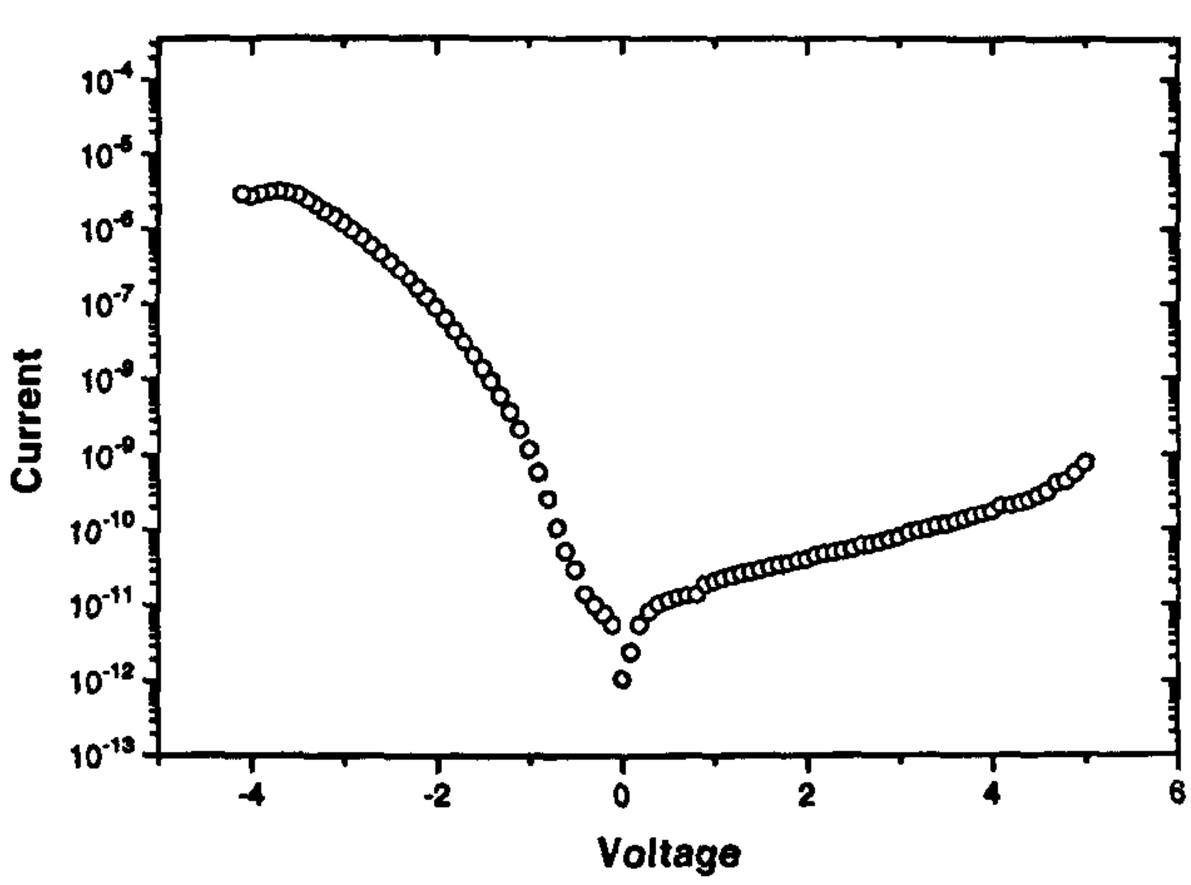

(b) I-V characteristics in log plot.

Figure 2.4: Typical I-V characteristics of a Au/a-C:H:N/*n*-Si heterostructures. The rectifying current ratio of more than 3 orders of magnitude is seen even with *n*-Si.

Due to relatively low hole concentration in n-Si, significant hole injection is not expected even though barrier lowering is present at the valence band.

The Fowler-Nordheim plot for Au/a-C:H:N/n-Si structure shown in Fig. 5.9 yields an extracted barrier height of 0.07eV for an effective mass of $0.1m_o$. The origin of this characteristic behaviour is due to tunnelling of electrons from n-Si to a-C:H:N through the barrier in the conduction band. The barrier related conduction limits seen at room temperature in both Au/a-C:H:N/p-Si and in Au/a-C:H:N/n-Si are due to hole and electron tunnelling at valence and conduction bands, respectively, in accordance with Fowler-Nordheim type behaviour described by equation 2.6. The fact that, the data plotted in ln(I/V) vs. $V^{\frac{1}{2}}$ axes as illustrated in Fig. 2.5 was not linear , rules out the possibility of dominance of the Poole-Frenkel conduction described in equation 2.5.

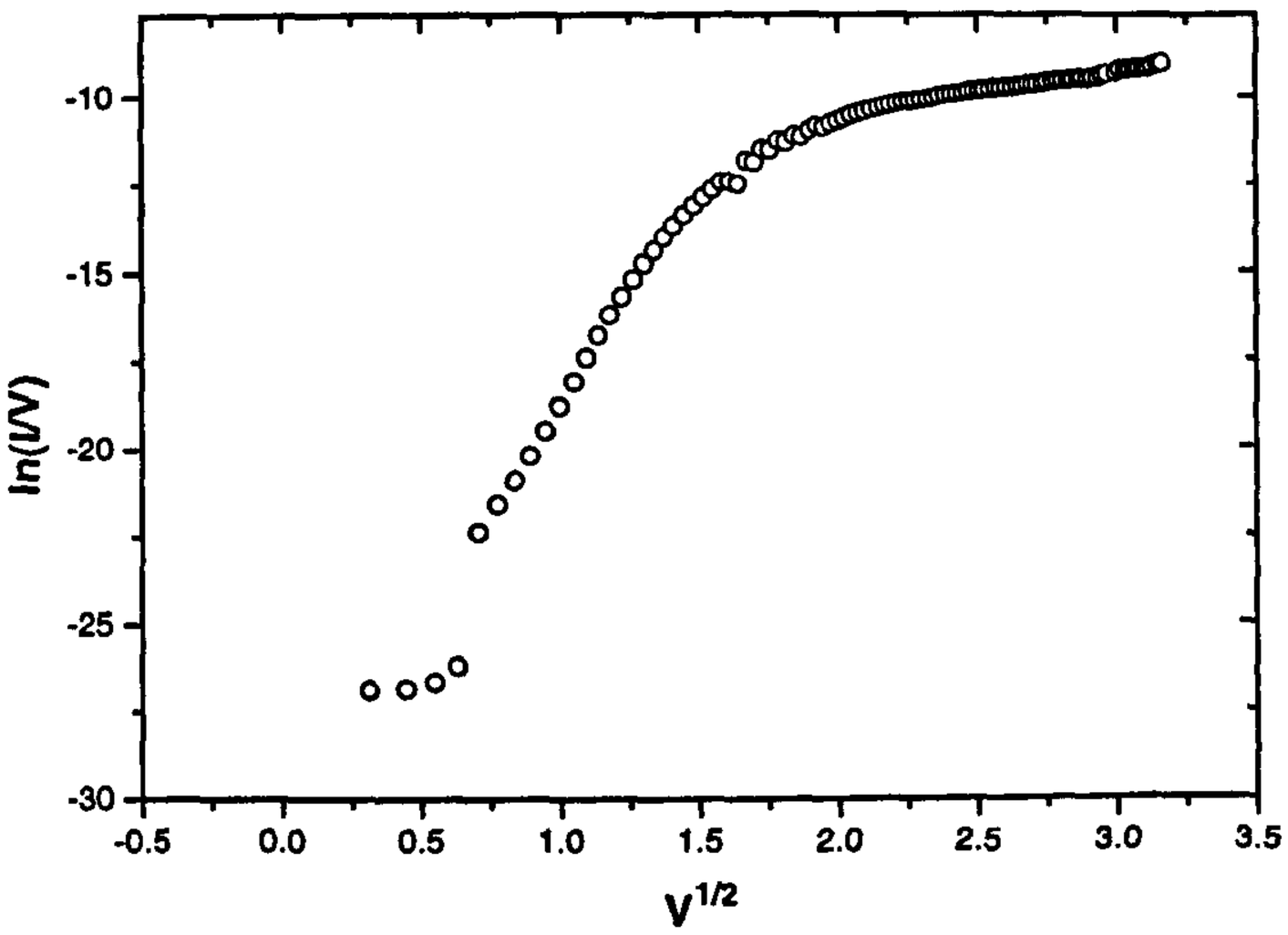

Figure 2.5: The I-V data plotted in Poole-Frenkel type axes are not linear.

2.2.3 Temperature Dependence of Conductivity and the Conduction Mechanism

To perform conductivity measurements at different temperatures, Au *gap cells* with dimensions 50μm×2mm×0.5μm were thermally evaporated at pressures lower than 10^{-6}mbar. The Au contacts were evaporated onto a-C:H and a-C:H:N films deposited on 0.5mm thick fused quartz substrates. The I-V data were collected using the apparatus described in the previous section. The conductivity of a-C:H:N was found to remain constant at $\approx 10^8 \Omega$cm for all CH_4:N_2 ratios ranging from 1:9.0 to 1:0.1 investigated in this study. However, the temperature dependence of conductivity showed two distinct activation regions, one at low temperature and the other at higher temperatures. The temperature dependence of the conduction was studied to investigate the various activated modes of conduction. The data was fitted using the characteristic Arrhenius relationship :

$$\sigma = \sigma_* \exp\left[-\frac{E_* - E_F}{kT}\right] \tag{2.7}$$

where σ_* - the prefactor which describes the average conductivity associated with the activation process, E_* - the energy level that participates in the activation process and E_F - Fermi level of the material [100]. The ln(σ) vs. 1000/T data plotted in Fig. 2.6 clearly shows two distinct regions of activated conduction. Interestingly a similar two stage activation process has also been reported for hydrogen free a-C:N in the literature [101]. By comparing the respective activation energies obtained from slopes of the plot and the average conductivity given by the intercept (σ_*), a conduction mechanism can be inferred.

Initially, the conductivity for temperatures close to room temperature are considered. The slope and the intercept for the lower part of the curve (25-80^{0}C) were found to be -5.37×10^3K and -12.8, respectively. The corresponding activation energy E_l and the average conductivity σ_l were found to be 0.46eV and 2.76×$10^{-6}\Omega^{-1}$cm^{-1}, respectively. In the high temperature regime (80-250^{0}C), a slope of -9.88×10^3K and the intercept of -8.0 were found, giving an E_h of 0.85eV and a σ_h of 3.35×$10^{-4}\Omega^{-1}$cm^{-1}.

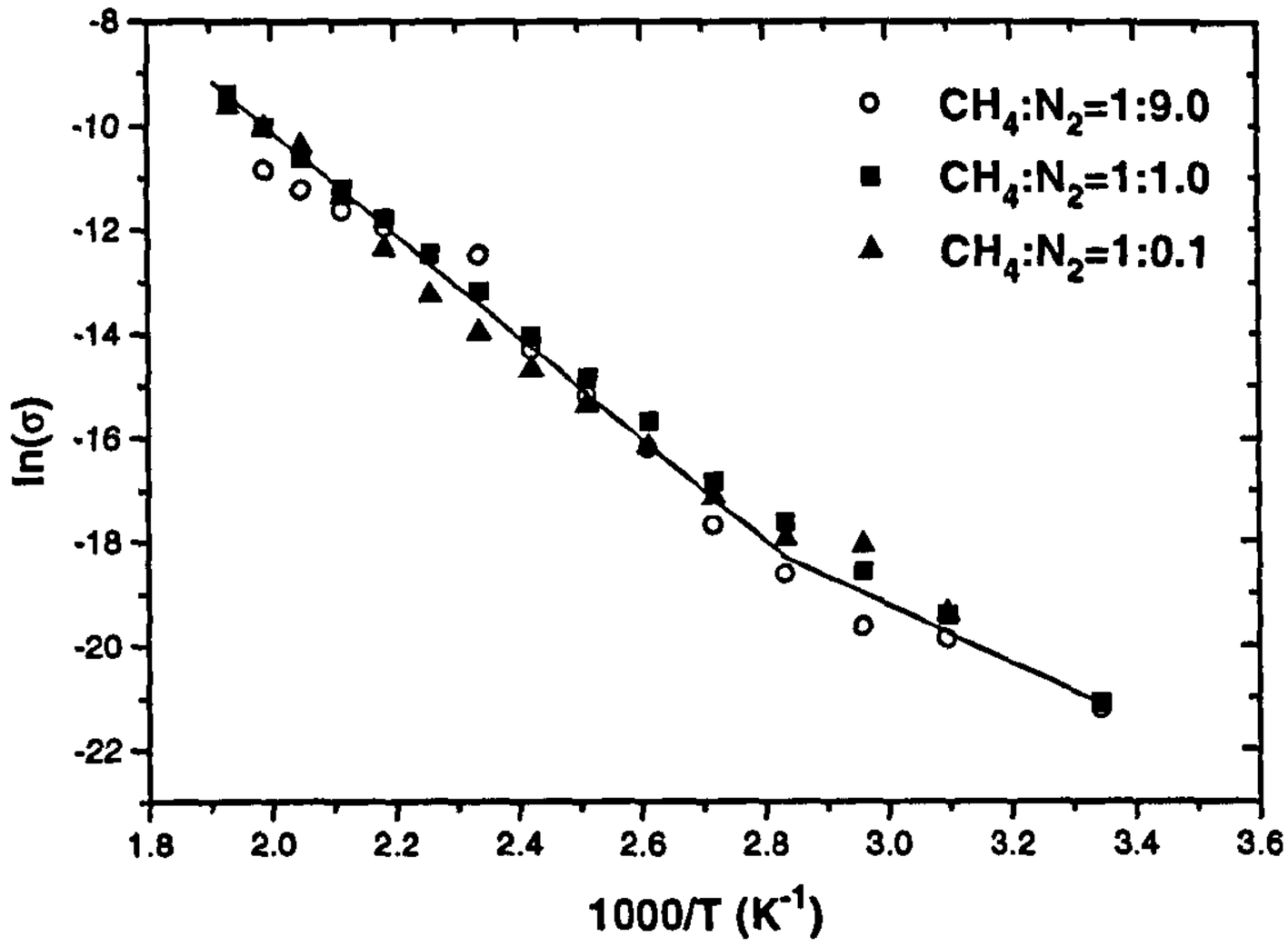

Figure 2.6: The conductivity of a-C:H:N remains the same for three ratios of CH_4:N_2 shown above. The temperature dependence shows two activation regions for all films.

Hopping conduction at mid-gap energies [102] (see expression 2.3), space charge limited conduction [103] (see expression 2.4) and variable range hopping at Fermi energy [104] have been reported as possible conduction mechanisms in amorphous carbon thin films. The fact that the conductivity is strongly dependent on temperature as indicated by the steep slopes in figure 2.6 , rules out the possibility of hopping dominated conduction at the Fermi level for the temperature range considered here. In fact hopping at the Fermi energy is weakly temperature dependent and is readily seen only at low temperatures [2]. However, for the I-V characteristics of heterojunctions, the plot ln(I) vs. ln(V) showed a super-linear region (only at large bias voltages) with n=2.64 as illustrated in Fig. 2.7, indicating space charge effects under high bias conditions.

Since both σ_l and E_l are smaller than σ_h and E_h, it can be concluded that the average conductivity associated with the low activation energy process is smaller than that associated with the high activation process. This indicates

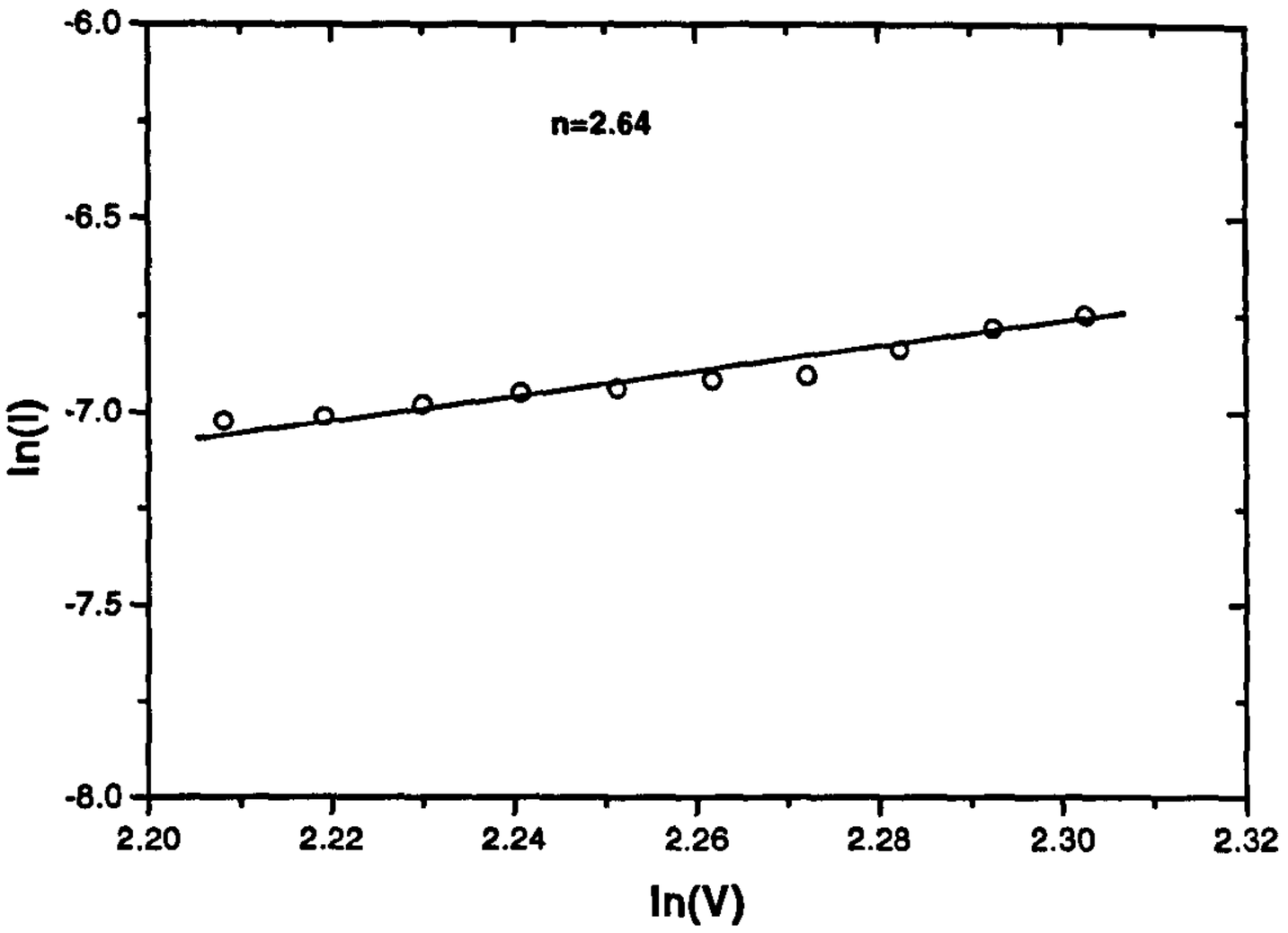

Figure 2.7: The I-V data plotted in ln(I) vs. ln(V) axes indicate a super-linear region with n=2.64 at high bias voltages.

that the low energy activation process is associated with *tail-like* conduction observable at low temperatures, and a high activation energy *extended-like* conduction process, which dominates at high temperatures. In a-C:H:N, tail-like states are mainly deep π^*_C and localised π^*_N states. The smaller σ_l and E_l seen in the low temperature regime is in good agreement with this kind of process, with electrons being activated into localised states 0.46eV above the Fermi level (assuming the a-C:H:N to be weakly *n*-type) and inter-cluster tunnelling due to spatial overlap of the wave functions above absolute zero at the localised tail (π^*_N) energies initiating conduction at low temperatures. At elevated temperatures above $\approx 80^0$C, carriers can be activated into π^*_C states situated 0.85eV away from the Fermi energy. The higher delocalisation of these states compared to π^*_N is indicated by the larger σ_h. The assumption of the Fermi level being closer to the conduction band edge is justified from the PL observations reported in the next chapter. In order to derive an activation energy to represent both mechanisms in band diagrams, an average conduction band edge, 0.7eV above

the Fermi energy (assuming 15% N states conduction) is taken (see Fig. 2.8).

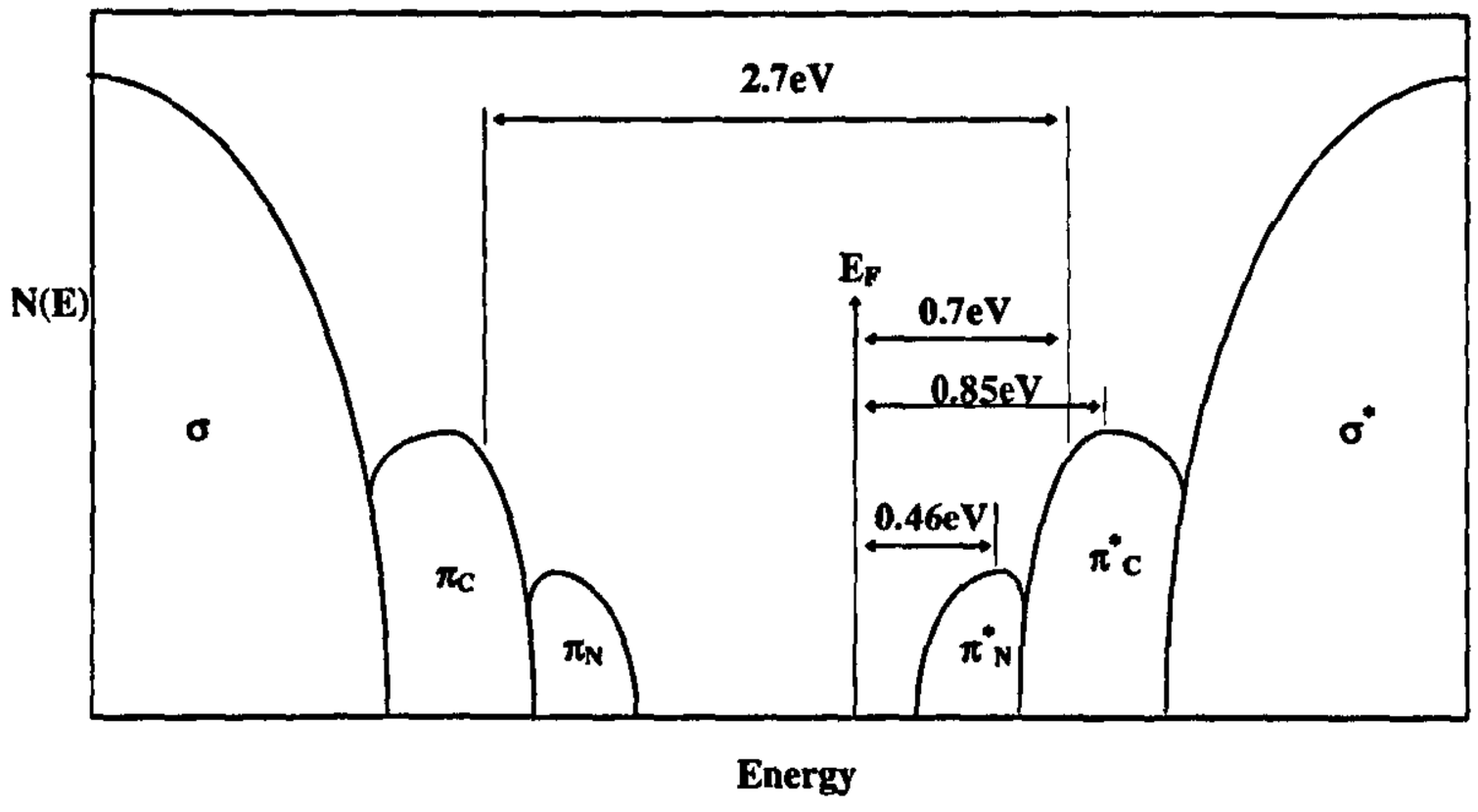

Figure 2.8: Schematic diagram of N and C associated σ and π states in a-C:H:N.

The effect of annealing on Au/a-C:H:N/*p*-Si structures with different N content in the film is illustrated in Fig. 2.9. For the highest N content film (Fig. 2.9(a)) the rectifying nature was lost after annealing. In contrast the lowest N content film is not affected by annealing upto 250°C. For the moderate N concentration film (Fig. 2.9(c)), the reverse conduction was found to increase. The volatility of N upon annealing has been reported in the literature [105, 106]. The results for the moderate-content film indicate that the annealing process has activated inactive N sites and has reduced the barrier at the conduction band by the movement of the Fermi level with activated N. At low N concentration in the film, the annealing process has no significant effect due to an inadequate number of nitrogen sites.

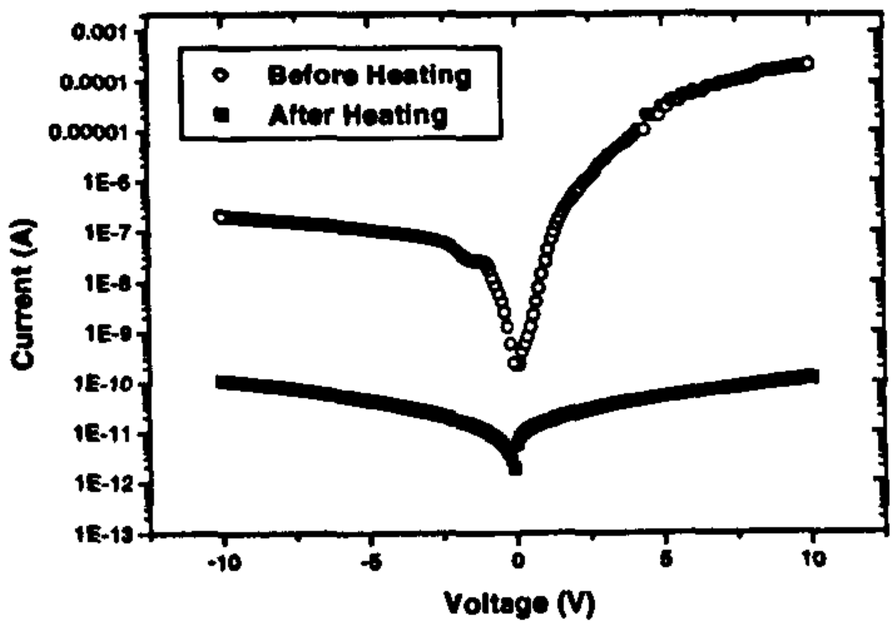

(a)

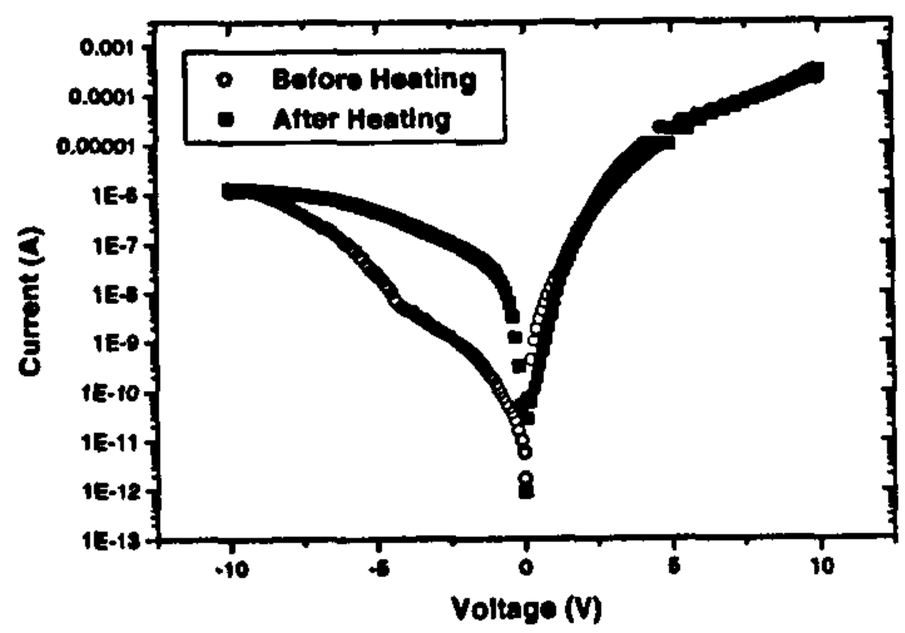

(b)

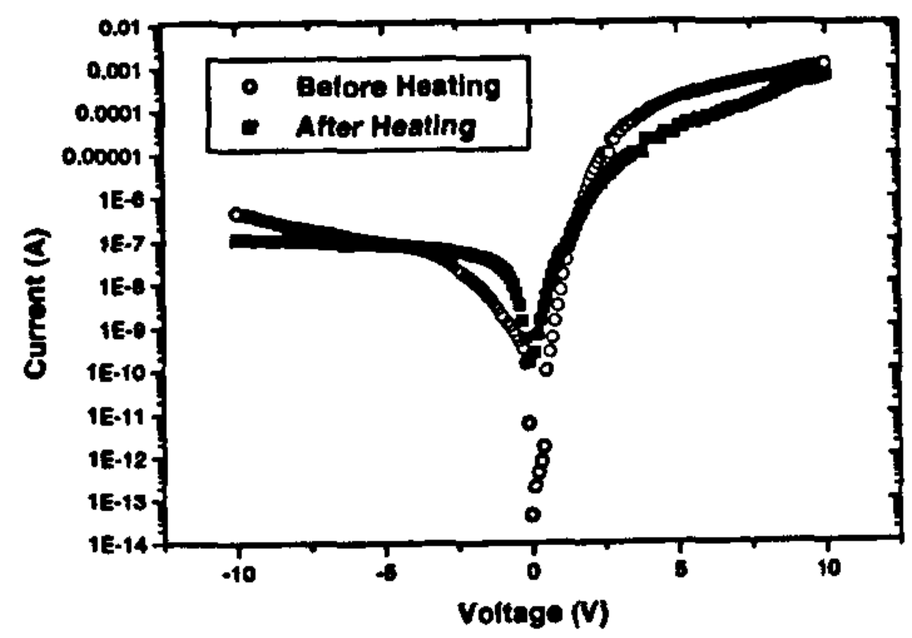

(c)

Figure 2.9: The I-V characteristics of Au/a-C:H:N/*p*-Si heterostructure showing loss of rectifying nature when heated beyond 250°C for films deposited with the CH_4:N_2 ratio of 1:9.0 (a). For the ratio of CH_4:N_2=1:1.0 in (b), the rectifying ratio is also affected with heating, but to a lesser degree. With a low ratio of CH_4:N_2=1:0.1 in (c), the original rectifying current ratio is retained even after heating.

2.2.4 Behaviour of Gold Contacts on a-C:H:N

The metal contact on a semiconductor is the link to external electrical connections and should not influence the measurement by introducing additional effects. The *contact resistance* and the *edge effects* are the most common by-products associated with non-ideal metal contacts. It is found that gold on a-C:H:N or a-C:H behaves as a barrier free (ohmic) contact material. Now we shall compare the contact resistance to the bulk resistance of the material (a-C:H:N is more *insulator like*, having a resistivity of $\approx 10^8 \Omega$cm due to charge carriers being localised as discussed in the previous section) of such an electrode. When the junction is in reverse bias the average current density (assuming drift of carriers) through the structure is given by,

$$\vec{J} = \frac{qp'W}{\tau} \tag{2.8}$$

where q - the charge, p' - carrier density, W - width of the layer and τ - carrier life time.

If we assume that the carrier distribution in the a-C:H:N is uniform and low at equilibrium then the carrier concentration across the layer becomes approximately constant. If the a-C:H:N layer is taken to be thin ($\approx 0.3\mu$m) and completely depleted at 0V bias due to built in potential alone, the diffusion current can be neglected. The drift current density is,

$$\begin{aligned} \vec{J} &= q(\mu_n + \mu_p)p'\vec{E} \\ &= \frac{q}{kT}\frac{(b+1)^2}{2b}qDp'\vec{E} \end{aligned} \tag{2.9}$$

where $b = \mu_n/\mu_p$, $D' = \mu_n kT/q$, the ambipolar diffusion coefficient of injected carriers $D = 2D'/(1+b)$ and $\vec{E}$ - average electric field across the depletion layer.

Since a-C:H:N is very lightly n-type at high electric fields the entire layer is depleted. Now the potential drop across the film is,

$$V_C = \vec{E}W \tag{2.10}$$

From the above equations V_C can be obtained,

$$V_C = \frac{kT}{q}\frac{2b}{(1+b)^2}\frac{W^2}{D\tau} \tag{2.11}$$

The resistance of the bulk and the junction is then given by,

$$R_B \equiv \frac{V_C}{I_F} = \underbrace{\frac{kT}{q}\frac{2b}{(1+b)^2}\frac{W^2}{D\tau}}_{a}\frac{1}{I_F} \tag{2.12}$$

$$R_B = a\frac{1}{I_F}$$

where I_F - the current through the junction. Now the total series resistance R_s of the structure becomes the addition of the contact resistance R_c and the bulk resistance R_B. Hence R_s is given by,

$$R_s = R_B + R_c \tag{2.13}$$

$$R_s = a\frac{1}{I_F} + R_c$$

Expression 2.13 suggests that the intercept of the plot R_s versus $1/I_F$ should give the contact resistance of the structure. A plot of R_s vs. $1/I_F$ is shown in Fig. 2.10. Two linear regions having different slopes can readily be seen. At low applied fields when the current through the structure is small, the influence of the contact was found to be considerable and the contact resistance extracted from this region shows a large value ($\approx$75kΩ), comparable with the bulk resistance. However when the applied electric field is increased and there is a large current flow through the structure, the effect of the contact is less significant, so $R_c \rightarrow 0$. The resistance at the metal contact is negligible compared to that of the bulk.

The reverse current measured using four different electrode diameters are shown in Fig. 2.11. The current through the device scales with the area of the

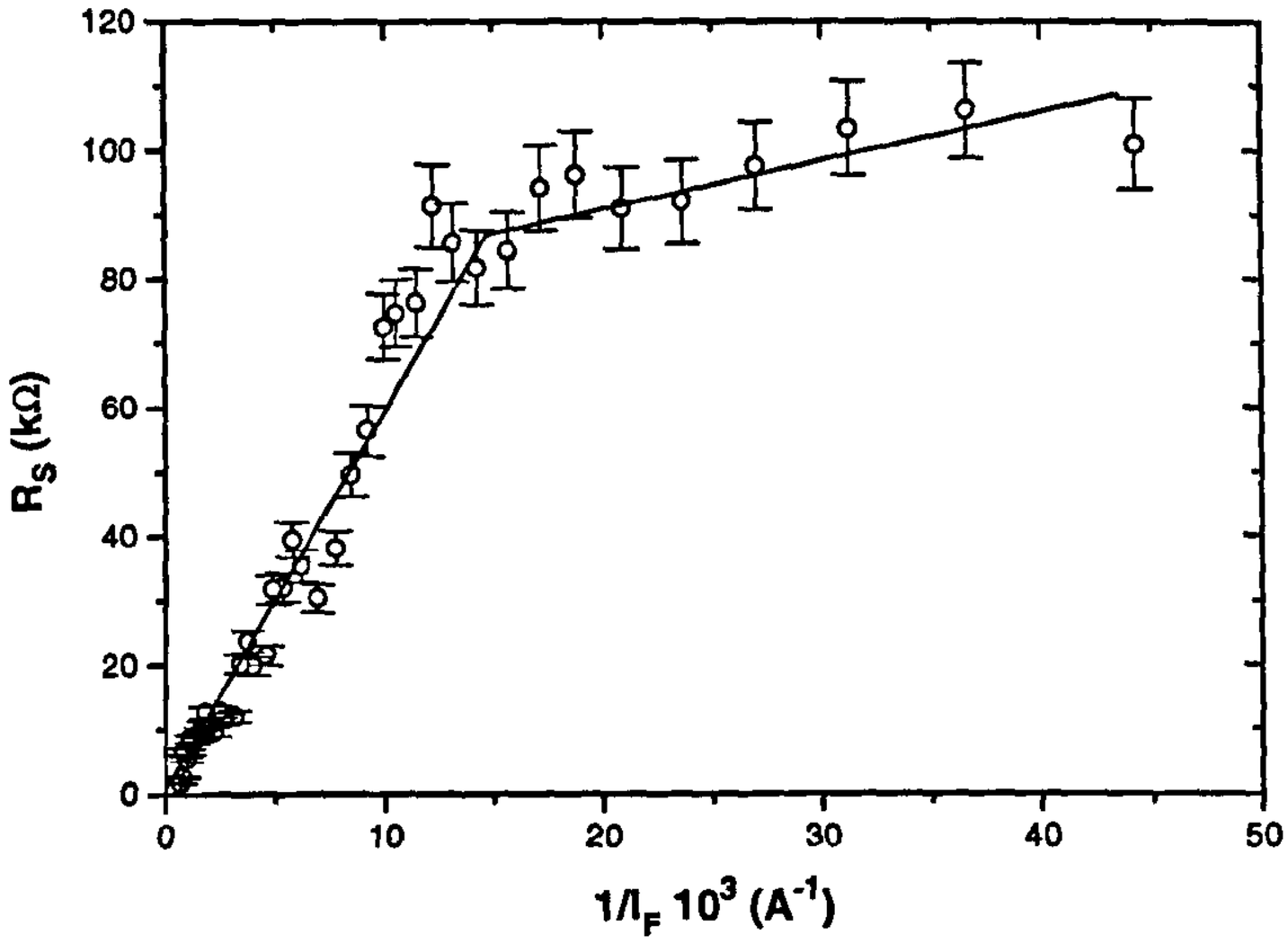

Figure 2.10: The series resistance R_s Vs. $1/I_F$ is plotted. It shows contact resistance is negligible compared to bulk resistance.

top metal contact when it is in reverse bias. This is an indication of efficient carrier transport through Au/a-C:H:N interface. The relationship of the current to the square of the electrode diameter is illustrated in Fig. 2.12. The reverse current is linearly proportional to the square of the diameter of the top electrode. This indicates that the Au/a-C:H:N interface is free of electrode edge effect. A linear dependence with electrode diameter is expected when edge effects are absent in an interface. In an edge effect free electrode the current through the electrode should scale with the electrode area[1].

2.3 Capacitance-Voltage (C-V) Characteristics

2.3.1 Introduction

The bias voltage dependence of capacitance gives an insight primarily into electrostatic nature of the bulk and the interfaces involved. The hysteresis asso-

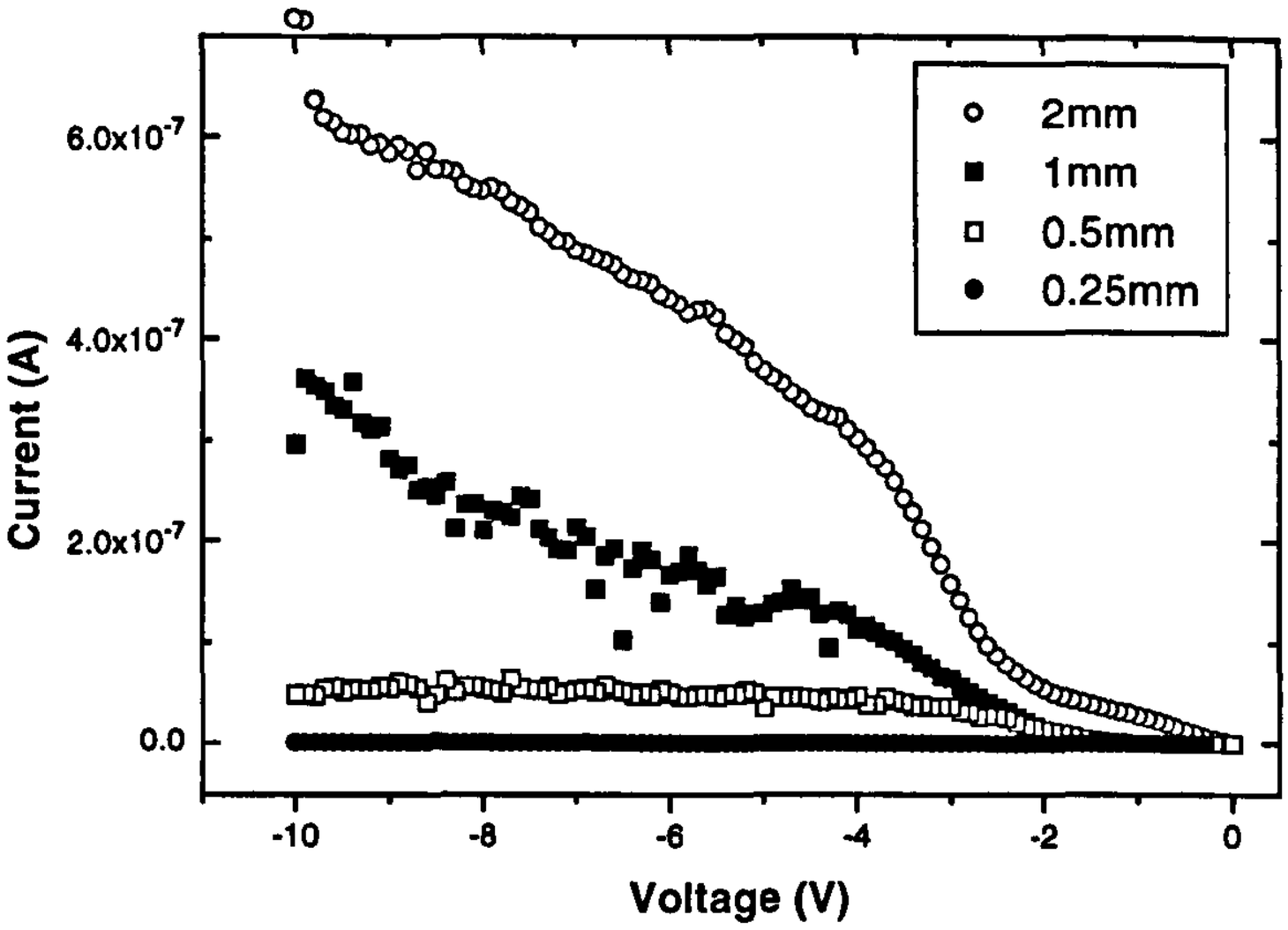

Figure 2.11: The current scaling with top contact area for four different Au electrode diameters ranging from 0. 25mm to 2mm is illustrated.

ciated with consecutive forward and reverse scans of the bias voltage gives a measure of the type and the stability of the charges present. The frequency dependence of the C-V characteristics indicates the polarisability of interface charge domains. The C-V measurements were performed on the Au/a-C:H:N/*p*-Si structures. C-V The measurements were made using an impedance analyser (Hewlett Packard 4192A). The frequency effects were monitored using an AC voltage with variable amplitude ranging from 5-1100mV with frequencies within 5Hz-13MHz superimposed on DC bias.

2.3.2 C-V Properties of Heterojunctions on Si

Au/a-C:H:N/*p*-Si (the a-C:H:N layer with CH_4:N_2 = 1:1) heterostructures were found to show a typical transition from a state of depletion, corresponding to low capacitance, to that of accumulation with a relatively large capacitance, when the bias voltage on *p*-Si was scanned from negative to positive with respect to

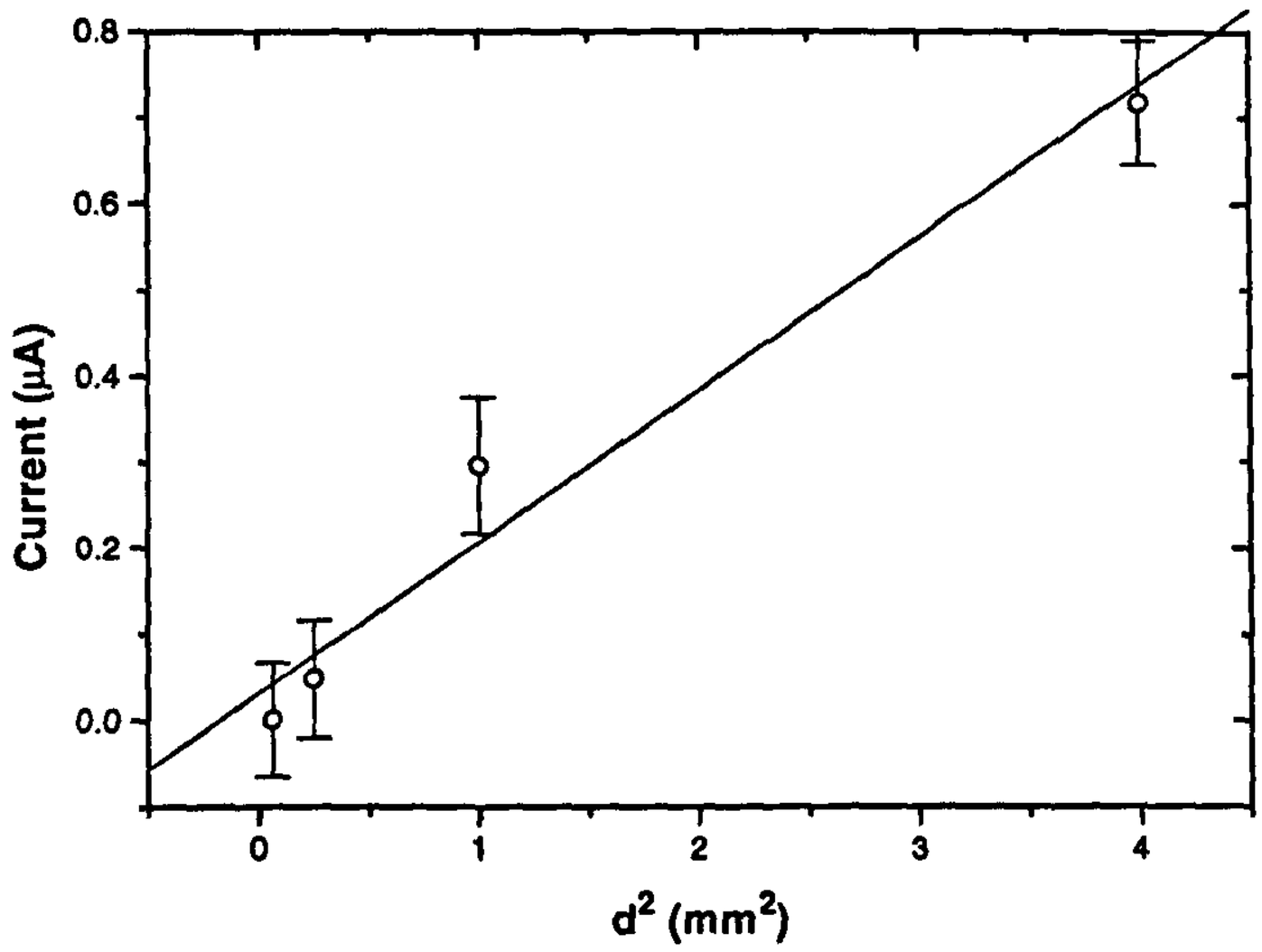

Figure 2.12: The reverse current versus the square of the electrode diameter. The linear relationship shown indicates the absence of *edge-effects* in Au/a-C:H:N interface.

the gold contact. Given that the there is a large carrier density in *p*-Si compared to a-C:H:N, the accumulation type of behaviour is expected at the junction when the *p*-Si is biased positive. The depletion layer at the junction is expected to be in the a-C:H:N layer due to its much lower charge (doping) concentration.

As the frequency of modulation is varied, the capacitance in accumulation is found to be significantly affected compared to that in depletion. The capacitance in accumulation was found to increase in the high frequency regime as shown in Fig. 2.13. In contrast, at low frequencies (in kHz range) the accumulation capacitance decreases with frequency as indicated by figure 2.14. Similar behaviour of capacitance can be found in the literature [107]. However, the highest frequency at which the transition from depletion to accumulation has been limited to frequencies lower than 1MHz in other reports, contrary to present work where a top frequency of 13MHz was only limited by the capability of the instrument [107, 108, 109]. The large variation of accumulation capacitance compared to

that in depletion, suggests that the concentration of polarisable charge domain are in *p*-Si/a-C:H:N interface and the bulk material contains only small amount of such domains. Seth *et. al.* have proposed that large variations of depletion capacitance indicate polarisable domains in the bulk [108].

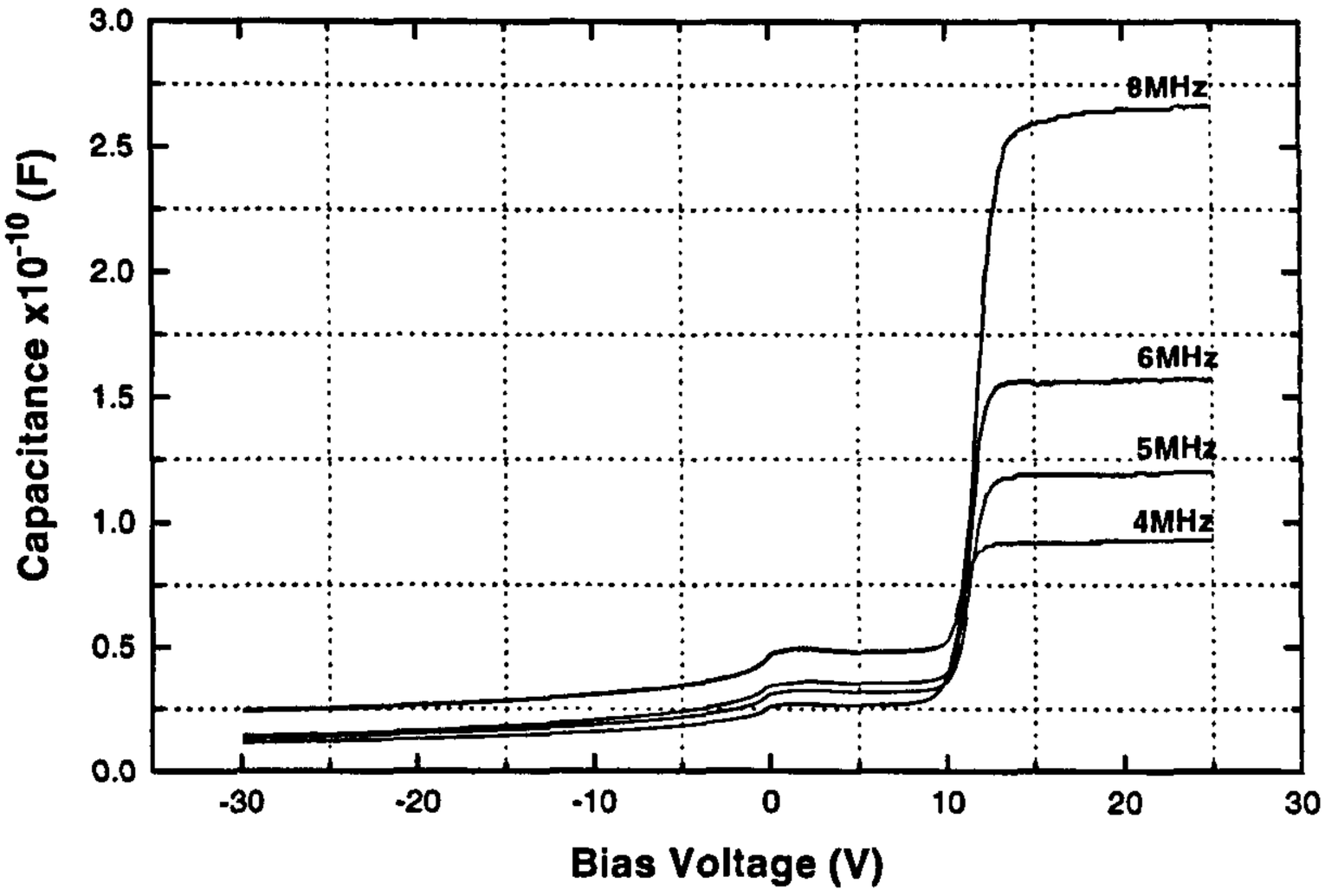

Figure 2.13: Voltage dependence of Capacitance at different frequencies in MHz range (*p*-Si/a-C:H:N/Au structure). As frequency increases capacitance in accumulation becomes larger while it remains relatively unchanged in depletion.

2.3.3 Quality in a-C:H:N films via C-V Hysteresis

The characteristic C-V transition from depletion to accumulation state in a Au/a-C:H:N/*p*-Si structure, would not necessarily follow the same path in the reverse scan of the bias voltage. This phenomenon gives rise to a hysteresis in the C-V behaviour. As the bias voltage decreases from a large negative value on *p*-Si, the external electric field can cause any mobile (loose) charge to drift. The drift in mobile charges generates an internal electric field which opposes the applied electric field. As a result the flat-band transition is seen to increase to an elevated

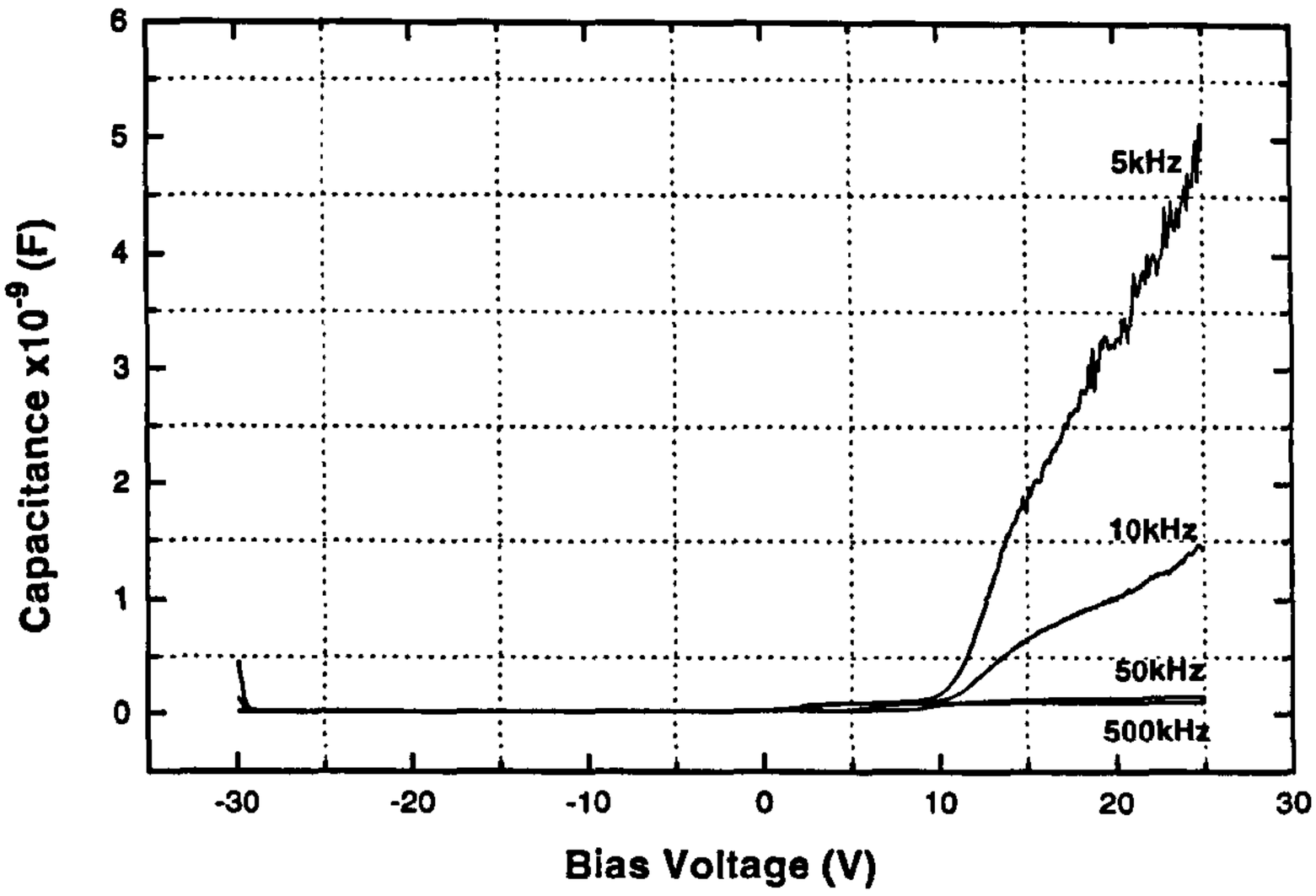

Figure 2.14: Low frequency dependence (in kHz range) of Capacitance with bias voltage shows opposite variation to that seen in Fig. 2.13, as frequency increases the capacitance in accumulation decreases.

bias voltage in order to compensate for the internal electric field associated with the drift charges (see the forward runs of Fig. 2.15(a) and Fig. 2.15(b)). With the reverse run the opposite happens. If only a small amount of fixed charges are present, no hysteresis is observed as shown in Fig. 2.15(c). However, a shift in flat-band voltage corresponding to the additional external field required to overcome the opposing internal field associated with fixed charges is needed. Absence of charges in the heterostructure yields *ideal-like* C-V characteristics (Fig. 2.15(d)). The highest amount of charge is present in the film deposited at the lowest RF power of 50W, with a ratio of CH_4:N_2 = 1:1 (see Fig. 2.15(a)). For the film deposited at 1025W (with the same conditions), residual charges are almost eliminated (Fig. 2.15(d)). Fig. 2.15(b) shows the situation at 600W and the Fig. 2.15(c) is the film deposited at the same power with a gas ratio of CH_4:N_2:He = 1:1:1. At the highest RF power, the greater excitation of reactive species leads to charge free film deposition. In addition, He dilution also

increases the degree of ionisation of species eliminating mobile charge domains.

The charges associated with the hysteresis can be found by looking at the offset in flat-band voltage. The expression $\Delta Q = C\ \Delta V$ relates the shift in voltage to the associated charges involved. Table 2.1 summarises the associated charges from Fig. 2.15.

	Charge Density ($cm^{-2}eV^{-1}$)	
	Fixed	**Mobile**
Fig. 2.15(a)	-3.9×10^{11}	$+3.9\times10^{11}$
Fig. 2.15(b)	-9.2×10^{10}	$+9.2\times10^{10}$
Fig. 2.15(c)	-3.9×10^{10}	-
Fig. 2.15(d)	-3.9×10^{9}	$+3.9\times10^{9}$

Table 2.1: Fixed and mobile charges responsible for hysteresis and the flat-band shift in C-V response.

2.3.4 Frequency dependence of C-V reviewed in accordance with existing models

The frequency dependence of capacitance in accumulation from 1kHz to 8MHz is shown in Fig. 2.17. Capacitance in accumulation starts from the large value of 105pF at 1kHz and decreases to a minimum at around 3MHz and begins to increase again at higher frequencies in accordance with the metal/carbon/silicon model proposed by Chan *et. al.*[107]. In this model, parameters such as R_C - the bulk resistance and C_i - the layer capacitance, in parallel to represent the amorphous carbon layer, are used as shown in Fig. 2.16. To represent the junction, C_d - depletion capacitance, R_j - junction resistance, C_p - capacitance to represent polarisation effect and a unit comprised R_s and C_s to recognise trap response, are employed in parallel. The junction and bulk are taken to be in series to describe the Au/a-C:H:N/*p*-Si structure. In this work a C-V response up to 13MHz (the frequency limit of the instrument used here) was observed,

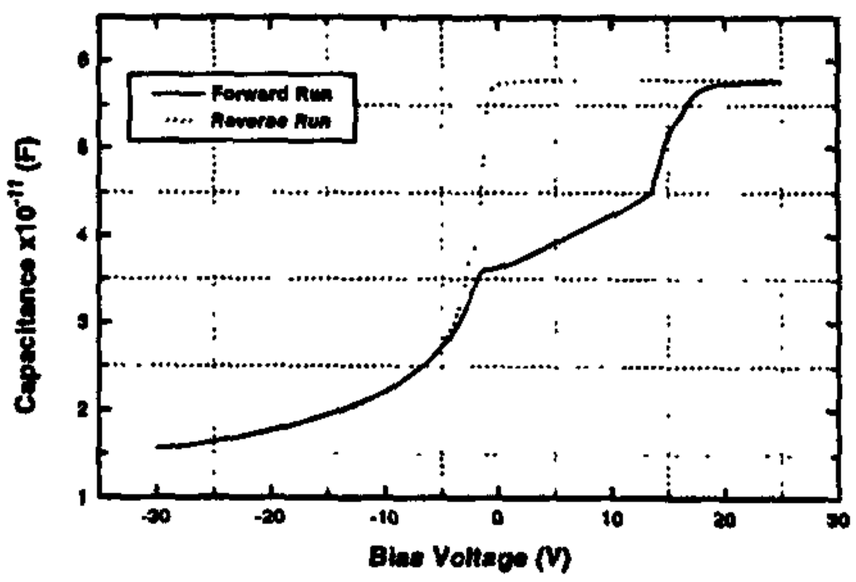

(a) The transition from depletion to accumulation state is separated from the transition of accumulation to depletion state by a bias voltage of 20V indicating a large hysteresis in C-V behaviour.

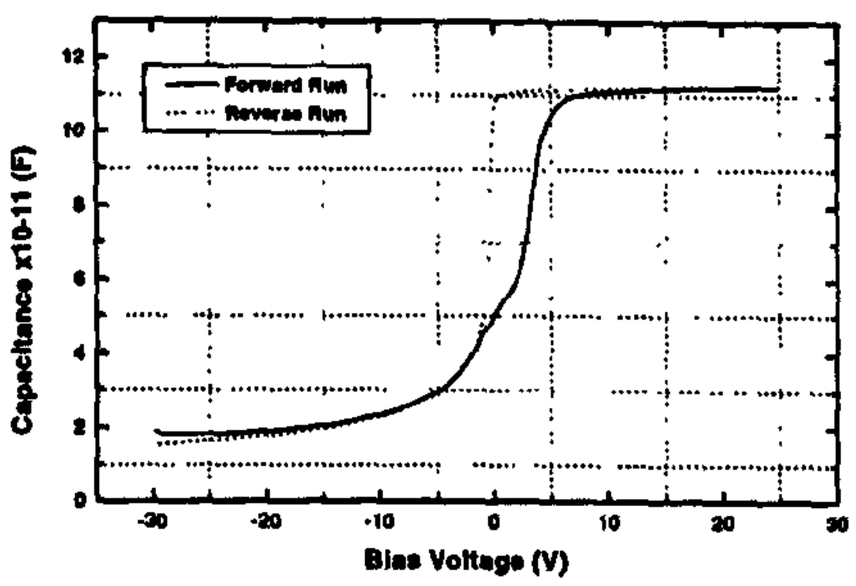

(b) C-V characteristics showing a smaller hysteresis than in (a). The flat-band voltage is positive in both cases also indicating presence of fixed charges as well.

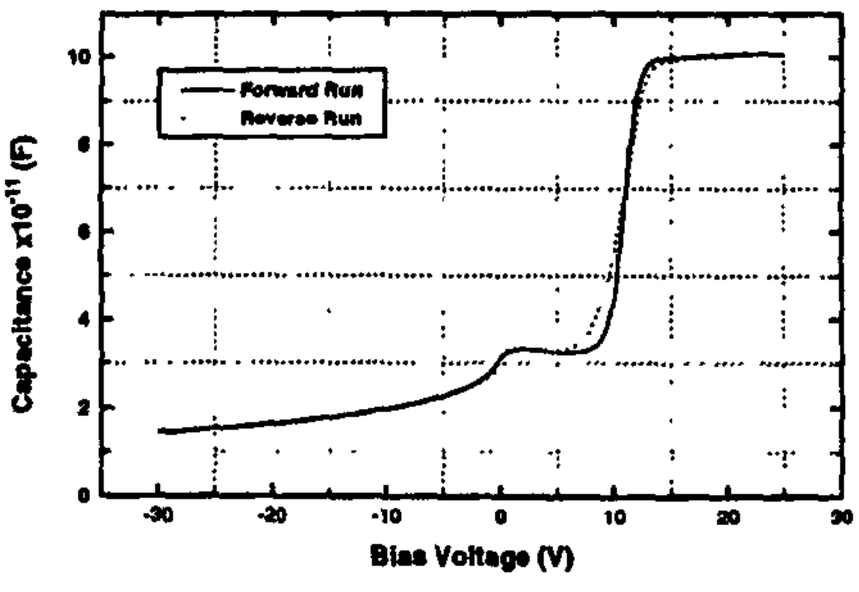

(c) The hysteresis voltage of forward and reverse scans has shrunk to a negligible value but with a 12V flat-band voltage.

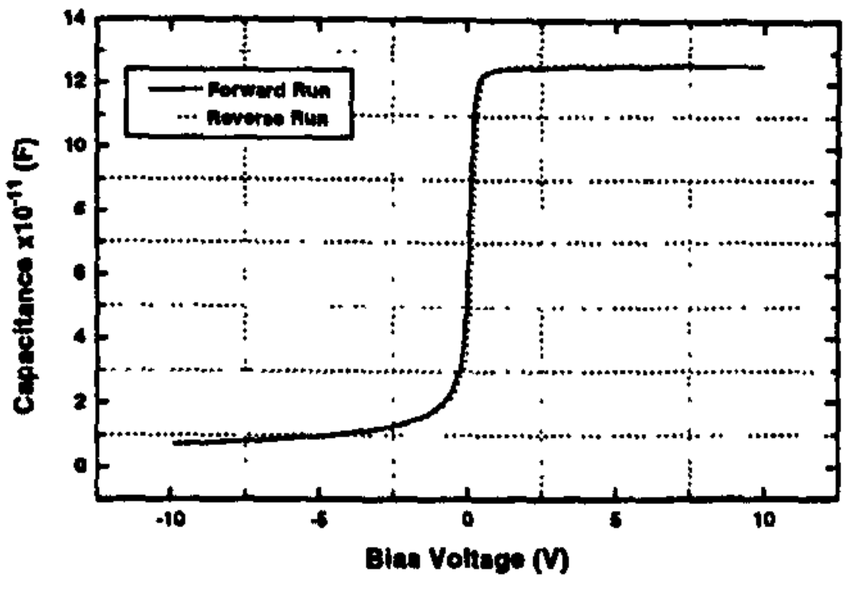

(d) C-V characteristics with a negligible hysteresis and a zero flat- band voltage.

Figure 2.15: The properties of a-C:H:N films corresponding to different deposition conditions influencing the presence of fixed and mobile charge elements in Au/a-C:H:N/*p*-Si heterojunctions. This is manifested as the changes in the flat-band voltage and hysteresis, respectively, in Capacitance-Voltage characteristics.

in contrast to previous reports where the typical depletion transition was lost at frequencies above ≈1MHz [107, 108, 109].

To accommodate increased low frequency response, the polarisation parameter, C_p, was modified to,

$$C_p = C_0 + C_l \left(\frac{\omega_0}{\omega}\right)^n + C_h \left(\frac{\omega}{\omega_0}\right)^k \tag{2.14}$$

where C_0 - DC prefactor, C_l - low frequency prefactor, C_h - high frequency prefactor and $\omega_0 = 1$ rad sec^{-1}.

The following fit parameters were obtained by the least square fit to data points. $R_C = 100k\Omega$, $C_i = 100pF$, $R_j = 100M\Omega$, $C_d = 15pF$, $C_0 = 60pF$, $C_l = 30F$, $C_h = 4\times10^{-11}pF$, n = 2 and k = $\frac{8}{5}$. The fit using the above parameters is indicated by the solid line in figure 2.17. It can be seen from 2.17 that the fit is in good agreement with the experimental results. As shown in Fig. 2.18 the capacitance in depletion of the Au/a-C:H:N/ *p*-Si heterostructure does not deviate significantly as the modulating frequency of the bias voltage is varied from 1kHz to 8MHz.

The depletion capacitance is due to charge separation across a mobile charge free area. Since it indicates there are no mobile charges present within the region where the electric field is applied, it can be inferred that the frequency of AC modulation does not change the depletion capacitance significantly.

2.3.5 Conclusions

In the beginning of the chapter, it was identified that the conduction processes such as extended state conduction, band tail conduction, hopping at Fermi energy and space charge limited conduction are possible mechanisms to describe the bulk conduction in amorphous carbon, specifically a-C:H and a-C:H:N which are relevant to the present study.

Necessary conceptual adaptations to incorporate energy levels originating from $\pi_C - \pi_C^*$, $\pi_N - \pi_N^*$, σ_C and σ_N in the above models were identified. *Tail-like* states comprising of π_N^* in a-C:H:N which lie close to the mid-gap and *extended-like* states lying away from the mid-gap attributed to π_C^* sites were

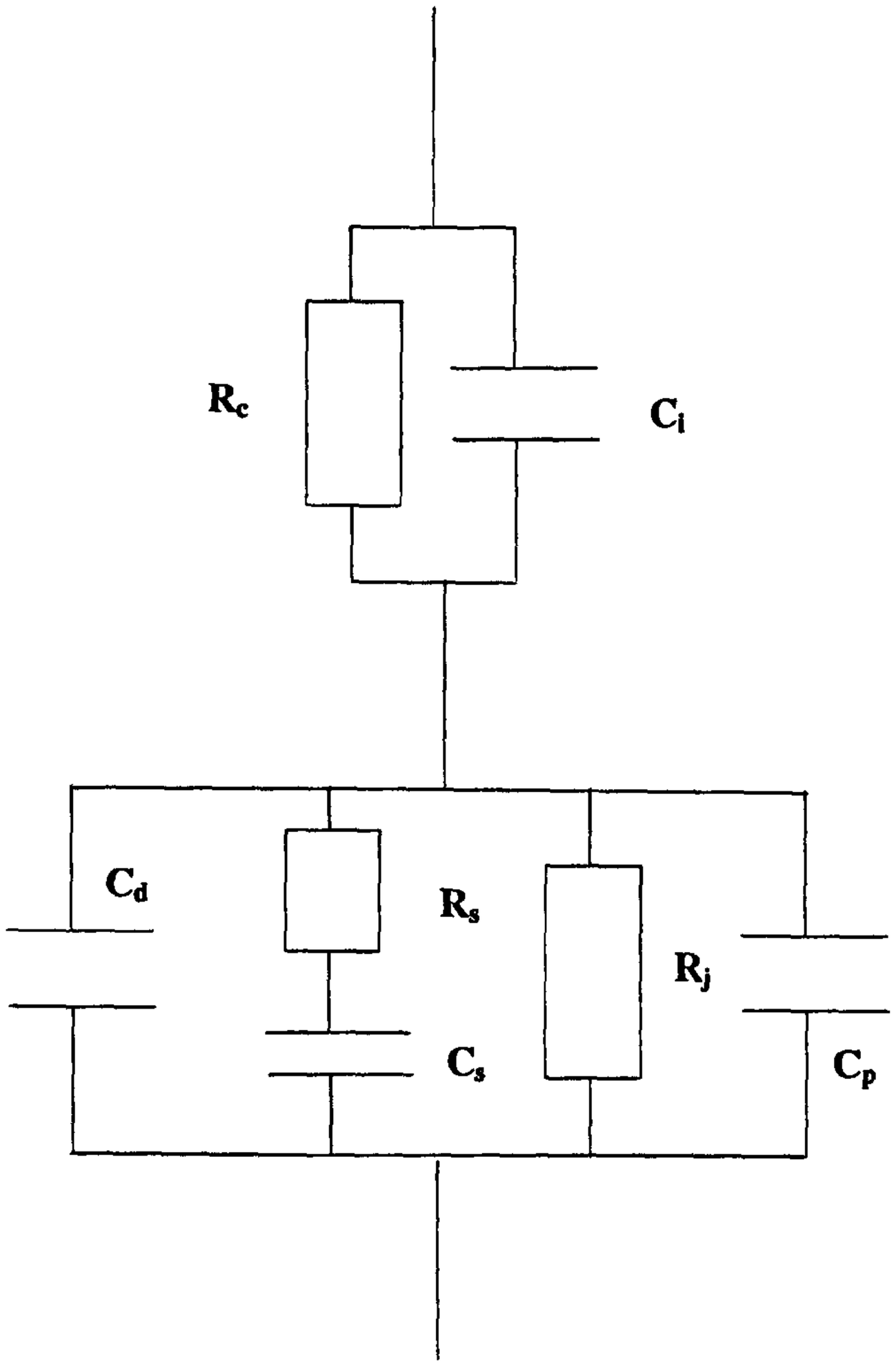

Figure 2.16: The equivalent circuit of the metal-carbon-silicon structure.

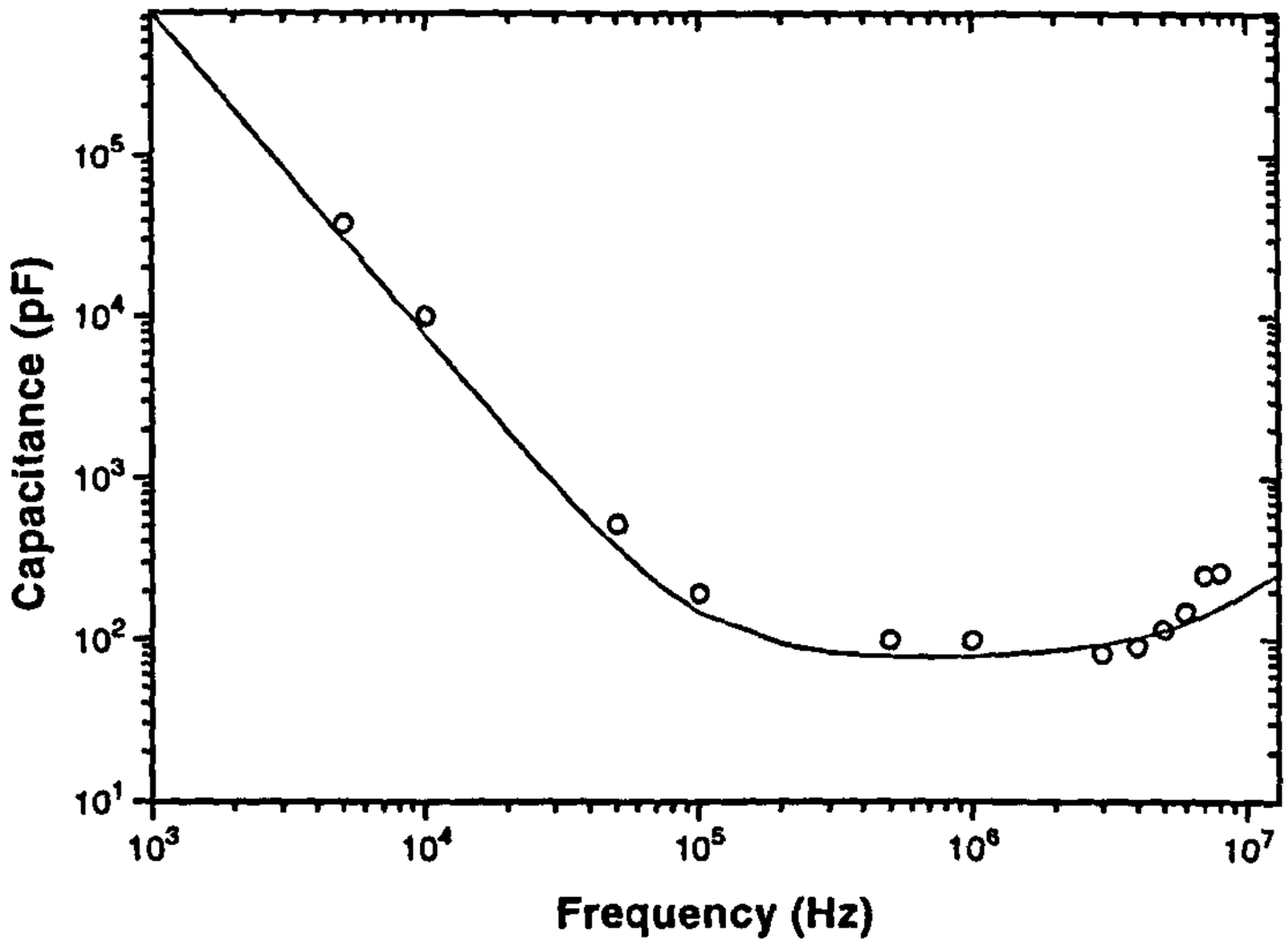

Figure 2.17: The capacitance in accumulation as a function of frequency. The dots indicate the measured value and the solid line is the model fit.

recognised.

When there are potential barriers present either at the interface, or within the bulk material in the form of distributed local barriers, the current conduction can be barrier limited. It was found that the barrier limiting process in both Au/a-C:H:N/p-Si and Au/a-C:H:N/n-Si is Fowler-Nordheim type tunnelling of holes and electrons, respectively.

The temperature dependence of conductivity showed two distinct activation regimes, one ranging from 25°C to $\approx$ 80°C and another up to 253°C. However the variation of the N content in the film did not affect the conduction mechanism. It was found that the low temperature range is best described by band tail conduction with an activation energy of 0.46eV and the average conduction prefactor of $2.76\times10^{-6}\Omega^{-1}\text{cm}^{-1}$. The mechanism responsible for the high temperature range is more extended-state-like conduction with an activation, of 0.85eV and the average conductivity prefactor of $3.35\times10^{-4}\Omega^{-1}\text{cm}^{-1}$. These results are in agreement with the theory.

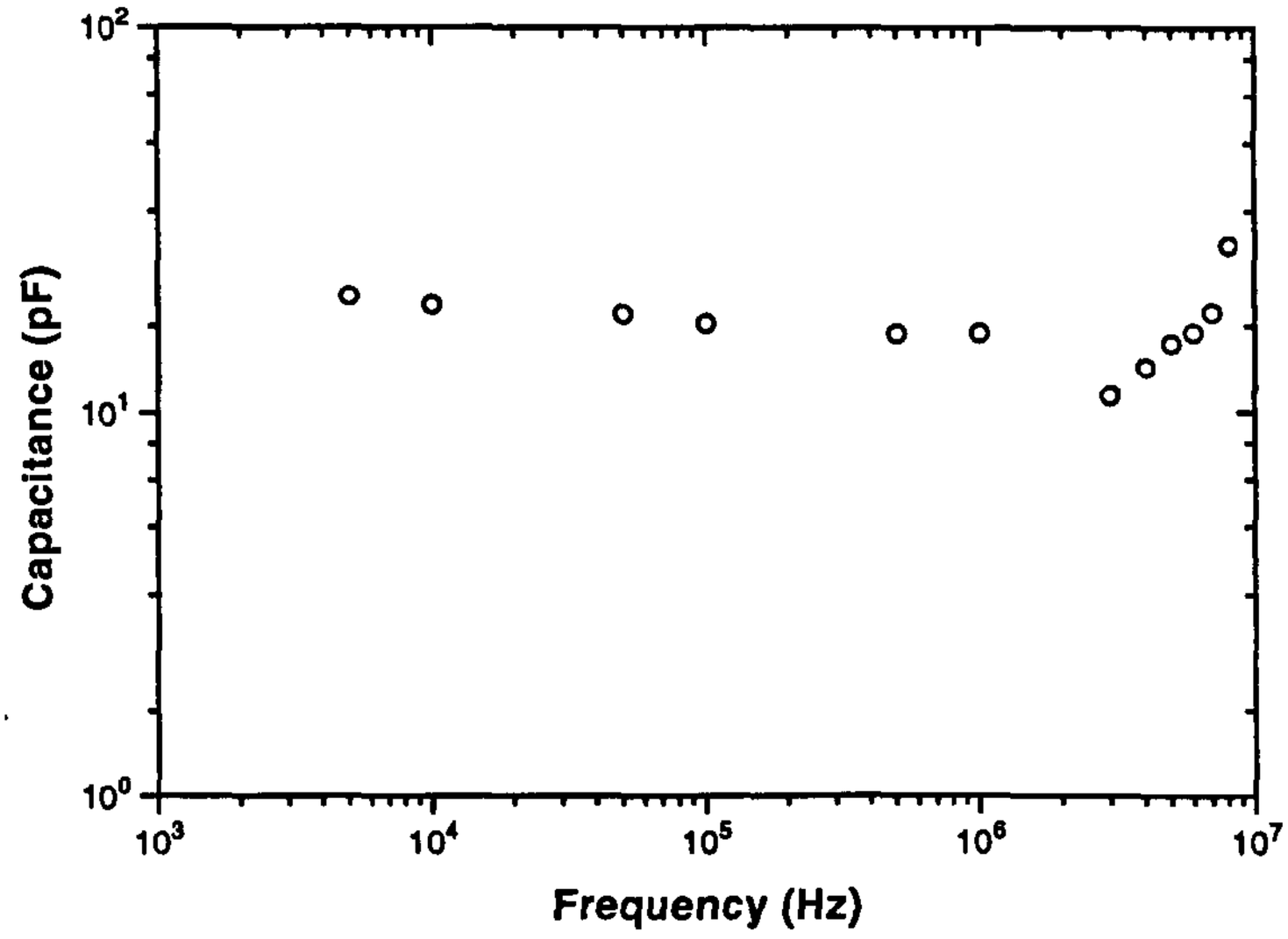

Figure 2.18: Variation of the capacitance in the depletion state as a function of the modulating frequency.

It was found that the contact resistance of Au on a-C:H:N is very small compared to the resistance of the bulk. The fact that the current through the Au contact scales with the contact area suggests that Au/a-C:H:N interface has minimum influence due to edge electric field effects.

C-V properties of the Au/a-C:H:N/*p*-Si structure were examined. The C-V plots show clear regions corresponding to depletion and accumulation in the structure. Interestingly, the material studied here displayed this behaviour up to 13MHz, which was the limit of the instrument used. The highest frequency reported to date on a-C:H was 1MHz [107, 108, 109]. The frequency dependence of capacitance in accumulation and depletion indicates that the charge domains are concentrated more at the interface compared to the bulk. It was found that interface charge densities as low as $3.9\times10^{9}\mathrm{cm}^{-2}\mathrm{eV}^{-1}$ can be achieved with a-C:H:N. The hysteresis in the C-V response can be used as a measure of the quality of the film. The C-V response was described in terms of a previously proposed model for metal-carbon-Si structures. The model was modified here

to take into account the low frequency behaviour in the depletion region. It was found that the model described the experimental results with good accuracy.

Chapter 3

Optical and PL Properties of a-C:H:N

3.1 Introduction

The photoluminescence properties and optical behaviour of amorphous carbon have been investigated by a number of researchers [110, 111, 112]. Hydrogenated amorphous carbon (a-C:H) films deposited using PECVD techniques from a hydrocarbon source gas can show a wide range of mechanical, electrical and optical properties [113, 114, 115, 79, 61, 107] due to various of bond configurations such as, tetrahedral sp^3, trigonal sp^2 and linear sp. Kruangam *et.al.*[116] and Hamakawa *et.al.* [117] have reported the use of a-C:H as the active layer in electroluminescent devices. a-C:H:N also has superior mechanical, electrical and optical properties making it useful for wear resistance applications as well as for cold cathode sources of electrons with emission at low electric fields [112, 118]. Furthermore, materials containing (C-H) bonds also show strong room temperature photoluminescence [119, 110, 120, 111]. It is thought that this behaviour is due to photo excitation resulting in generation of confined electron hole pairs in π and π^* states of a-C:H and a-C:H:N films. Since the $\pi - \pi^*$ states associated with sp^2 sites are surrounded by wider gap sp^3 sites sharp band edge fluctuations are created leading to localised band edge states [121]. In this chapter we discuss the influence of nitrogen on the room temperature photoluminescence

(PL) and optical properties of a-C:H films. And in addition to temperature effects on optical behaviour, band gap dependence of PL, PL fatigue and electric field effects on PL are also discussed.

3.2 Electromagnetic Interactions in Carbon Based Materials

3.2.1 Electromagnetic wave propagation in a conductive medium

The general wave equation in a conducting medium ($\sigma \neq 0$) has the form,

$$\vec{\nabla}^2 \vec{E} = \epsilon_r \epsilon_0 \mu_r \mu_0 \frac{\partial^2 \vec{E}}{\partial t} + \mu_r \mu_0 \sigma \frac{\partial \vec{E}}{\partial t} \tag{3.1}$$

where all notation have their usual meaning. If we assume solutions of the form

$$\vec{E} = \vec{E}_0 \exp[\, i(\vec{k} \cdot \vec{r} - \omega t)]$$

in equation 3.1, the *complex phase velocity* v^*, is given by,

$$\frac{1}{v^{*2}} = \epsilon\mu + i\frac{\mu\sigma}{\omega} \tag{3.2}$$

Now we define the *complex refractive index* n^*, and hence the *complex dielectric constant* ϵ_r^*,

$$\begin{aligned} n^* &= \frac{c}{v^*} \\ \epsilon_r^* &= n^{*2} \end{aligned} \tag{3.3}$$

Similar results are obtained by solving wave equation for magnetic field, $\vec{H}$, also. Now there is a propagating electric field wave given by,

$$\vec{E}_y = A\exp\left[\, i\omega\left(\frac{x}{v^*} - t\right)\right] = A\exp\left[\, i\omega\left(\frac{xn^*}{c} - t\right)\right] \tag{3.4}$$

where A - a constant, x - the distance variable in the direction of propagation and y - direction of electric field vector. Assuming plane wave propagation,

$$n^* = n + ik \tag{3.5}$$

From equations 3.4 and 3.5 now we have the plane wave electric field given by,

$$\vec{E}_y = \underbrace{A\exp\left(-\frac{\omega k x}{c}\right)}_{\textbf{magnitude}}\overbrace{\exp[\, i(k'x - \omega t)]}^{\textbf{phase}} \tag{3.6}$$

where k' - the propagation constant of the wave.

As seen in expression 3.6 the *phase* component suggests that the electric field wave travels forward in x-direction, but the *magnitude* component decays exponentially as the wave propagates forward. This attenuation process is characterised by the *absorption index* or the *extinction coefficient*, k. Now we are in a position to grasp the concept of complex parameters v^* , n^* and ϵ_r^*. The information regarding the magnitude variation and the phase of the wave can be found from n^* and v^*. From expressions 3.4 and 3.5 we have,

$$\epsilon_r^* = \epsilon_{r1} + i\epsilon_{r2} = n^{*2} = (n^2 - k^2) + 2ink \tag{3.7}$$

$$\Rightarrow \epsilon_{r1} = n^2 - k^2 \tag{3.8}$$

$$\Rightarrow \epsilon_{r2} = 2nk \tag{3.9}$$

The attenuation of an electromagnetic wave incident on a medium capable of optical reflection and transmission, is generally characterised by the *optical absorption coefficient* α. The *transmittance* T and the *reflectance* R of the medium are defined as,

$$T = \frac{(1 - R^2)\exp(-\alpha x)}{1 - R^2\exp(-2\alpha x)} \tag{3.10}$$

$$R^2 = \left|\frac{1-n^*}{1+n^*}\right|^2 \tag{3.11}$$

where $\alpha = \frac{4\pi k}{\lambda}$ can be obtained by comparing the attenuation constant in equation 3.6, given that the transmittance and the reflectance are defined for a given energy. The energy of the electromagnetic wave is proportional to $\vec{E} \times \vec{H}$. Since $\vec{E}$ and $\vec{H}$ have the same form, the attenuation factor for energy flow comes from squaring equation 3.6.

An optically active material is characterised mainly by the complex dielectric constant ϵ_r^*. Out of measurable quantities, transmittance T and the reflectance R, the refractive index n and the extinction coefficient k can be extracted and the components of the complex dielectric constant derived.

3.3 Optical Characterisation

3.3.1 Introduction

The interactions of a semiconductor with electro-magnetic radiation is responsible for a variety of phenomena. These can be utilised to understand the quantum level energy arrangements inside the material itself. Since most of the carbon based semiconductor materials exhibit an optical band gap in the range of ≈1eV to ≈5.4eV, it is interesting to study the optical properties of such materials in the infrared (IR) to ultraviolet (UV) wavelength range. The optical absorption is an end result of processes such as,

- Band to band transitions of electrons via energy absorption from irradiated photons, leading to excitations across the *forbidden energy gap*.
- Localised states to band transitions :
  - the transition of an electron from an inter-band localised state to the *conduction band*.
  - the transition of a *valence* electron into an empty localised state.

- Localised state to localised state transitions. In which the participating charge carriers would not be mobile due to the non-periodicity of the wave function limiting the carriers to a small spatial region.

- The generation of excitons which can later be either dissociated or ionised to produce mobile carriers.

If the photo absorption process generates mobile charge carriers, then it is reflected in properties of the material such as photoconduction and electric field quenching of PL. On the other hand the de-excitation of immobile charge carriers can lead to processes such as luminescence (emission of photons) from the material.

3.3.2 Transmittance and Reflectance of a-C:H and a-C:H:N on quartz substrates

The transmittance data collected at normal incidence and the reflectance data at near normal were corrected for the system and substrate response by taking the baseline data with the quartz substrate as the reference. Transmittance and reflectance in the wavelength range of 200nm to 900nm for a-C:H:N and a-C:H films on quartz substrates are shown in Fig. 3.1. Examination of data in figure 3.1 reveals that when there is no detectable nitrogen present in the film, the transmittance in the pass-band wavelengths is ≈90%. The presence of even a small amount of N in the film brings this figure down to ≈80% initially, however further increase in the N content does not decrease the level of transmission further. The fact that the reflectance is comparatively small (<20%) and approximately the same throughout the wavelength range of interest, irrespective of the N content, indicates that the additional *absorption* is not an artifact of the change in reflection. Given the fact that the pass-band transmittance profile is flat (*i.e.* invariant over wavelengths ranging from ≈400nm to 900nm), the increase in *absorption* with N in the film cannot be due to a scattering dominated process either, indicating that it is a phenomenon associated with N. For wavelength <300nm there is a region where absorption dominates. The reflectance

measured here is due to two reflective components. One is at the film interface and the other is at the film-quartz interface. Since the reflectance remains at a similar level to that of the pass-band even in the high absorption region, this indicates that the major reflective contribution is at the air-material interface. However, collectively it can be seen that the change in nitrogen content in the film from 9at% N to ≈30at% does not significantly influence optical properties of the films.

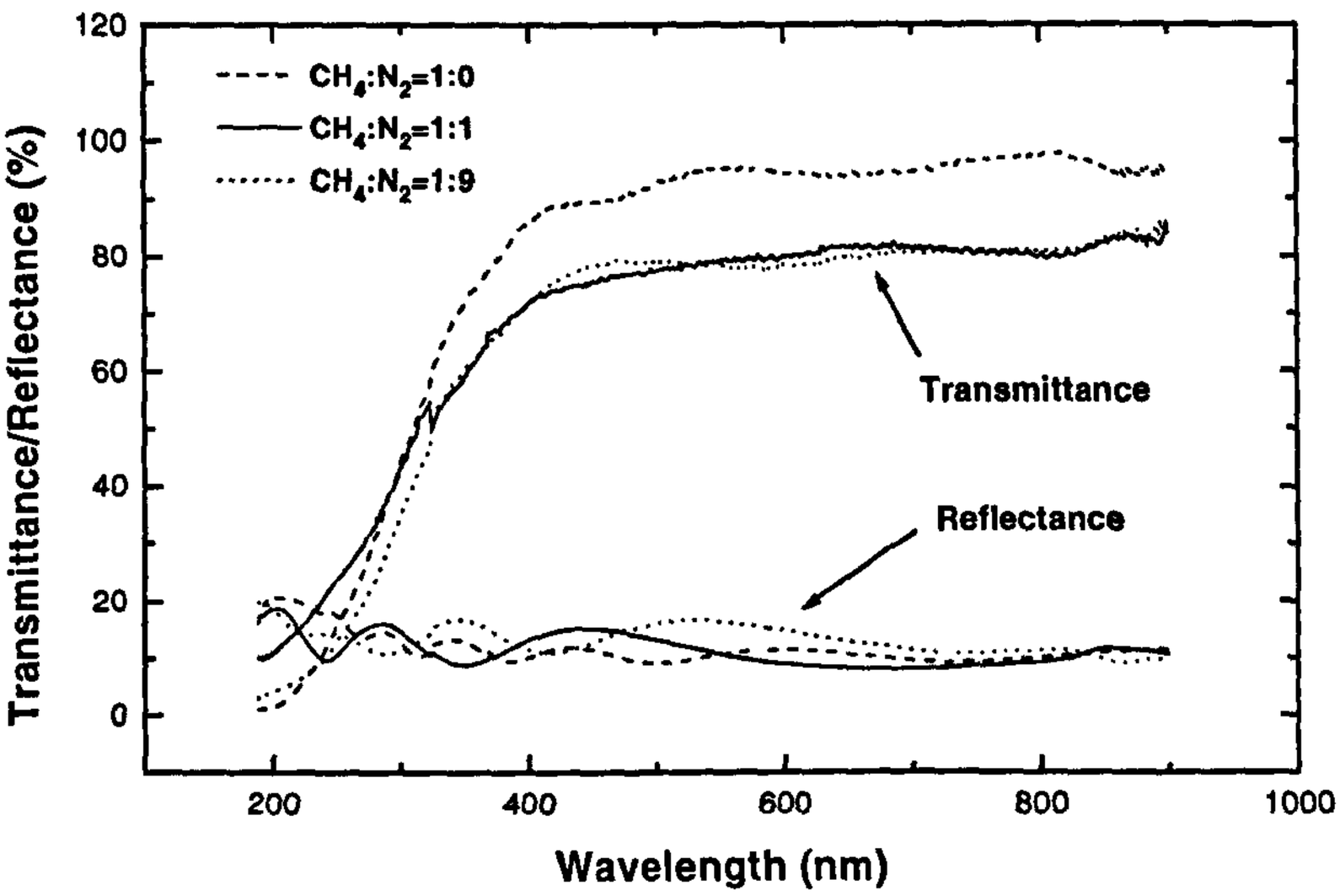

Figure 3.1: Transmittance and reflectance vs. wavelength. It can be seen that for wavelengths longer than 400nm, a-C:H:N on quartz is nearly transparent. The reflectance in the wavelength range 200nm to 900nm remains less than 20%. Also, the transmittance or reflectance is observed to be unaffected by the amount of nitrogen present in the film.

Refractive index n and extinction coefficient k were extracted from transmittance and reflectance data taken assuming a two layer system consisting of the film and and quartz. The n and k values for a-C:H:N films with three different nitrogen contents are plotted in figure 3.2. The n values were found to range from 1.5 to 3.0 suggesting a polymeric form of a-C:H:N films [122]. The

refractive index was also found to be independent of nitrogen content in the film, as indicated in figure 3.2(a). The magnitude of n is seen to rise rapidly for photon energies beyond ≈4.5eV for all films. This correlates to the energy range where transmittance decreases considerably and becomes comparable with the reflectance (see Fig. 3.1). There are two main regions in figure 3.1, the *non-absorbing* region ($T \rightarrow 1$) and where the absorption is significant ($T \ll 1$). In the former case, the real part of the refractive index is defined as $n = \frac{\sin i}{\sin r}$, where i - angle of incident and r - angle of refraction. However, the relationship for n must be modified for the case where significant absorption occurs. The rapid increase in n observed in figure 3.2(a) is attributed to the shift in transmittance.

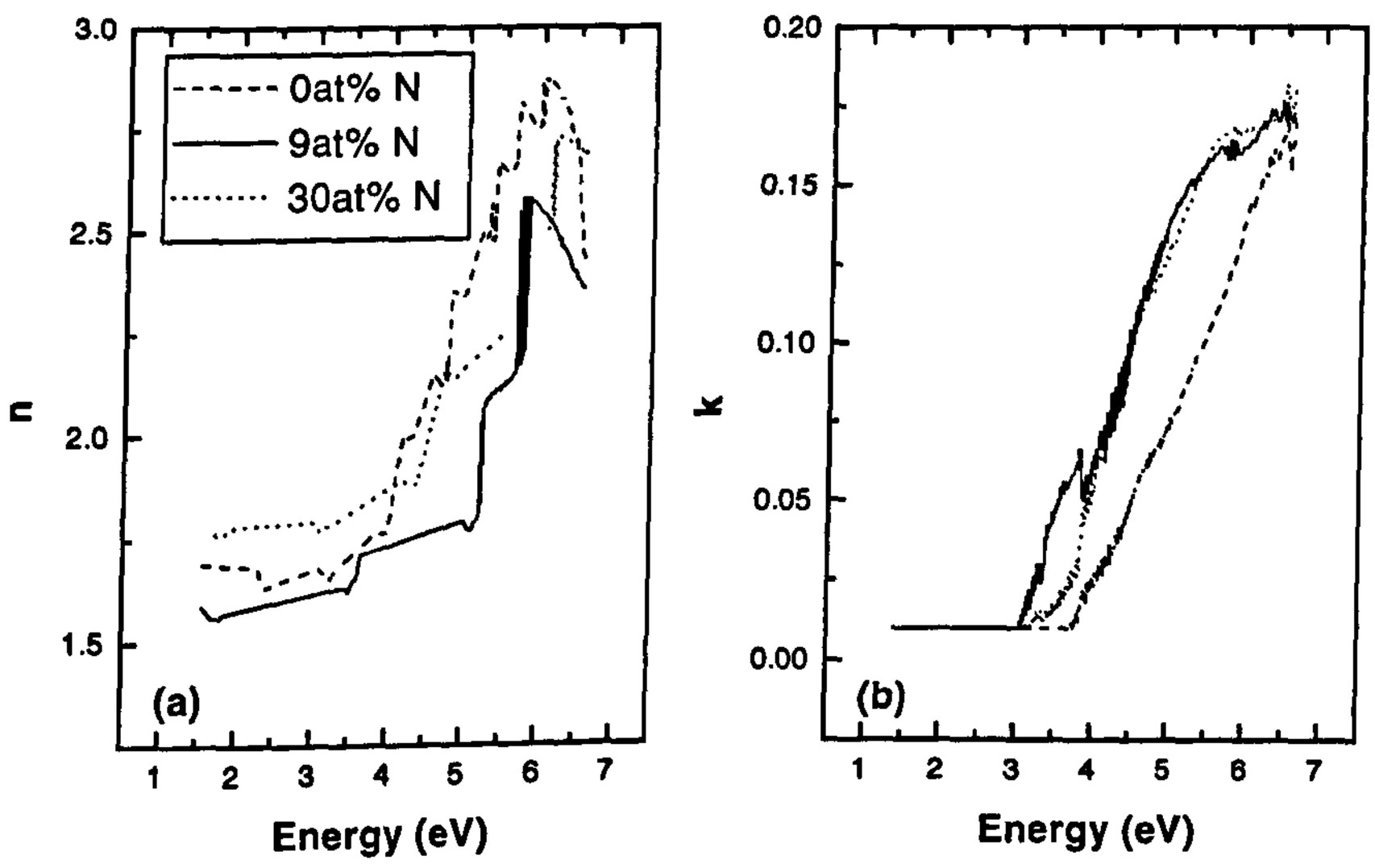

Figure 3.2: Plot of refractive index, n, and extinction coefficient, k, extracted from the reflectance and transmittance data for a-C:H:N on quartz. Similar to figure 3.1, the n and k values are seen to be unaffected significantly by the presence of N.

The extinction coefficient k versus the photon energy plotted in Fig. 3.2(b) indicates the presence of N by shifting the curve to a lower energy in transmit-

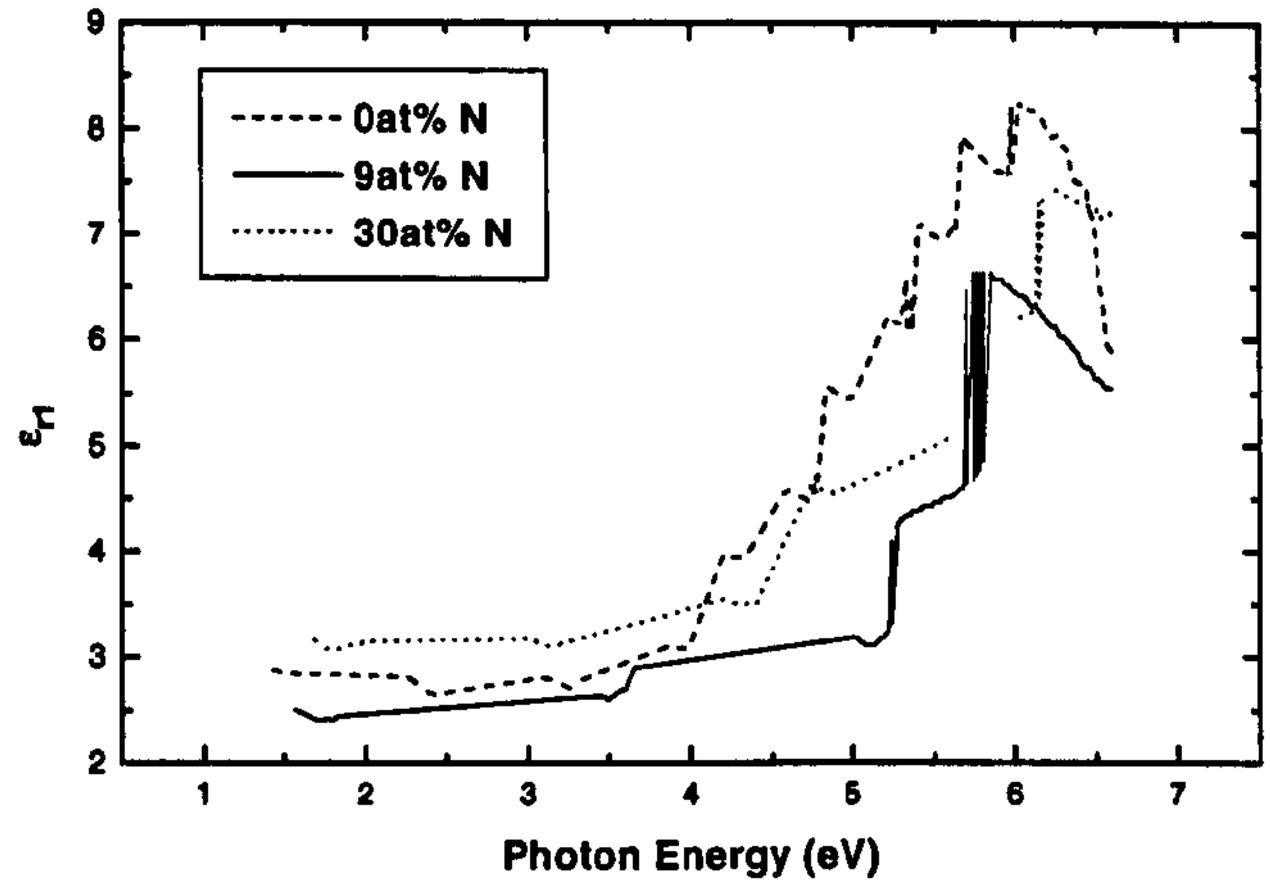

(a)

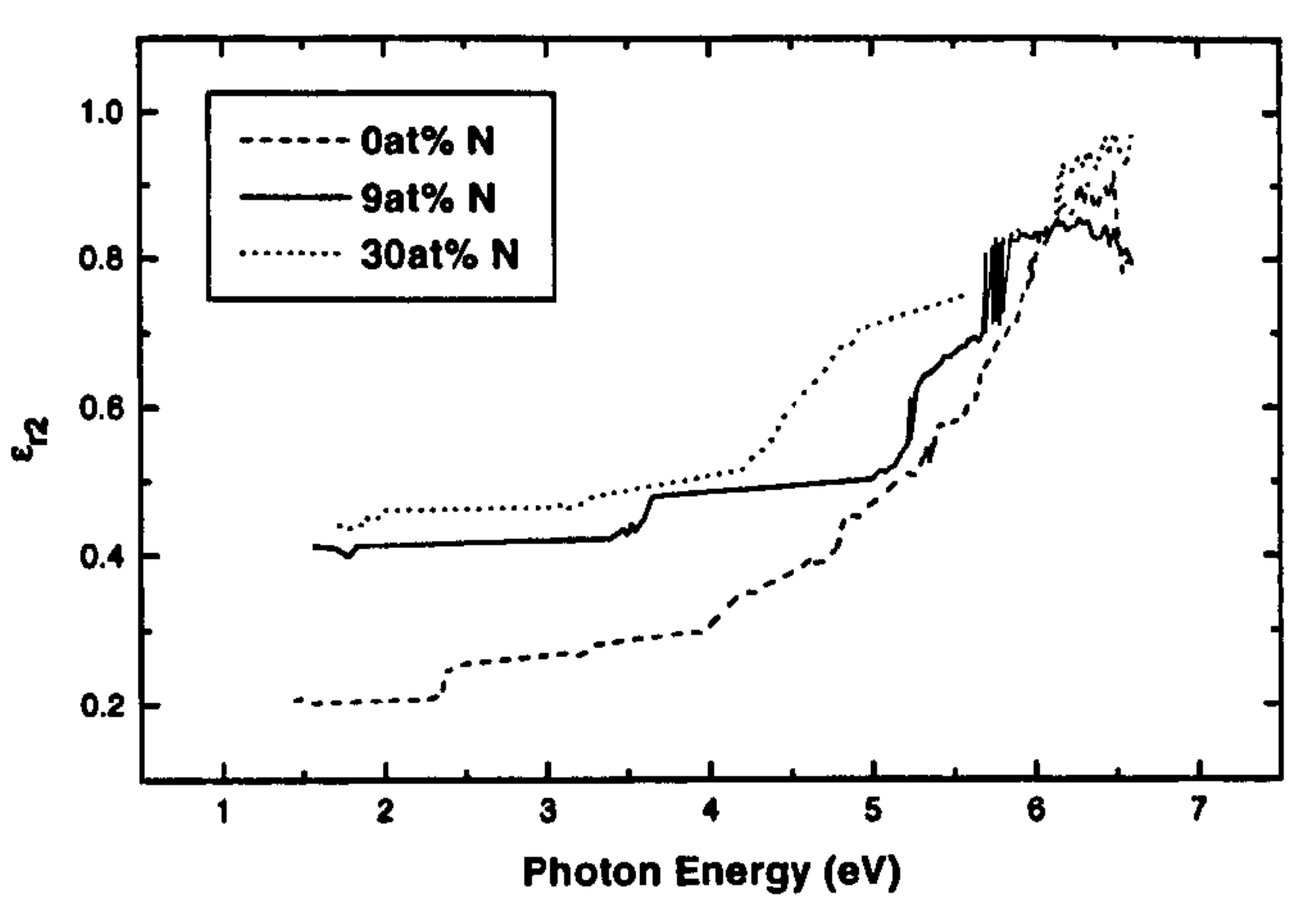

(b)

Figure 3.3: The real part of the dielectric constant (ϵ_{r1}) shown in (a) is invariant with nitrogen content in the film below 4eV, similar to figure 3.2. However the imaginary part (ϵ_{r2}) in (b) shows a shift that is also seen in the Tauc gap for a-C:H films with N and without N.

tance data. However, here again the variation in N content has not induced any significant change in the shape of the k profile. The photon energy dependence of the real and imaginary parts of the dielectric constant is illustrated in Fig. 3.3. The real part ϵ_{r1} seen in Fig. 3.3(a) shows a similar energy dependence to that for n in Fig 3.2(a). The real part of the complex dielectric constant given by $\epsilon_{r1} = n^2 - k^2$, is dominated by the n^2 portion of the function due to the fact that n is more than an order of magnitude larger than k for a-C:H:N and a-C:H, so that $\epsilon_{r1} \approx n^2$. The primary mechanism of absorption in semiconducting materials is band to band transitions. However the optical data heavily depend upon the density of states that participate in the absorption process and on the nature of energy transitions described by the *transition matrix.* To separate these two contributions to the absorption process, it is necessary to have additional data regarding density of states from independent measurements other than optical methods. However, the imaginary part of dielectric constant, ϵ_{r2}, plotted in Fig. 3.3(b) gives some insight into how such transitions are affected by the inclusion of N into the a-C:H matrix. The ϵ_{r2} can be expressed as,

$$\epsilon_{r2} = 4\pi^2 e^2 a^3 R^2 \underbrace{\int \mathrm{N_V(E)N_C(E+\hbar\omega)\,dE}}_{\textbf{joint density of states}} \tag{3.12}$$

where a - the volume parameter, R - the *dipole matrix* defined for energy separation of $\hbar\omega$ and N_V, N_C - density of states of valence and conduction bands respectively [2]. Here, it is assumed that the major optical transitions are of band to band type. However, unlike a crystalline material in which both momentum, k, and the energy E are conserved, in an amorphous material the k-conservation is relaxed. The elements of the dipole matrix R become an average over any pair of states where there is an energy separation of $\hbar\omega$. Therefore in amorphous semiconductors, the difference between *direct transition* or an *indirect transition* is not distinct since the uncertainty in the momentum is of the same order as the momentum itself. In Fig. 3.3(b), profiles are without sharp features due to the lack of k-conservation and disorder which have drowned any possible *Van Hove singularities* in ϵ_{r2} space [2]. The possible excitonic absorption near the band edges is also hidden for the same reason. Examination of Fig. 3.3(b) shows there

is a clear increase in ϵ_{r2} for a-C:H:N compared to a-C:H for low photon energies. However, the change in N content in the film does not induce a significant change in ϵ_{r2}, in accordance with the extinction coefficient and the optical band gap. It is not clear whether the increase in ϵ_{r2} with N inclusion at low energies is due to DOS modification or is indicative of an absorption selection criteria, with the optical measurements alone. Further work to determine the joint density of states is required to determine the effect of N on the imaginary portion of the dielectric function. However, this is outside the realm of the present study. The drop of transmittance seen in Fig. 3.1 for a-C:H:N is in agreement with the behaviour of ϵ_{r2}. The rapid increase in ϵ_{r2} beyond 5eV can be attributed to optical interaction associated with $\sigma - \sigma^*$ states. Even though the a-C:H:N films studied here are $\approx$50% sp^3, a similar feature corresponding to $\pi - \pi^*$ transitions is not seen. This may be an indication of better transition rules associated with σ states at higher energies due to the wide de-localisation of energy levels compared to the π states. The comparably not so rapid increase of ϵ_{r2} for the highest N content a-C:H:N indicates, either the formation of N associated DOS or the tailing of the σ band. However ϵ_{r2} is not a sensitive enough measurement to indicate the influence of nitrogen within the range (3.6% to 30%) examined here.

3.3.3 RF power dependence of optical parameters

The RF power of the plasma determines the amount of energy associated with active species that participate in the deposition process. The type of bond that forms depends upon the energy of the arriving species. The bonding in turn determines the short range order of the material. The short range order is an influential parameter which controls the *band gap* of the material. For a crystalline material the *band gap* has a precise meaning. That is since the short range order is undisturbed over large distances, the wave function is periodic and there is no bonding disorder. This feature eliminates any tailing of band edges. The DOS at the edges of the valence and conduction bands is sharp. The energy difference between these two edges is the band gap. However, for an amorphous

material, edges of the bonding and anti-bonding states tend to tail off with energy due to bonding disorder. Further in the carbon system it becomes more complex owing to the possibility of different bonding configurations that can arise. In addition to possible tailing off of σ and σ^* DOS, there can be π and $\pi*$ states from the sp^2 sites embedded in the σ and σ^* tails as well as tailing of π and π^* states. Therefore, the *band gap* is a very complex issue for the carbon system.

One of the widely used method of describing the band gap for comparison purposes is to describe the energy at which the absorption coefficient, α, is equal to $10^4 cm^{-1}$, referred to as the E_{04} gap. However, in some materials $\alpha > 10^4 cm^{-1}$ in the optical absorption regime, making E_{04} unsuitable. Another approach is via extrapolation of the bands. In 1966 Tauc *et. al.* introduced a model assuming the power law dependency of tail DOS with energy [2]. So that the extended states of *conduction* ($N_C(E)$) and *valence* ($N_V(E)$) band are given by,

$$\begin{aligned} N_C(E) &\propto (E - E_{GC})^{nc} \\ N_V(E) &\propto (-E + E_{GV})^{nv} \end{aligned} \tag{3.13}$$

where E_{GC} and E_{GV} are extrapolated conduction and valence band edges, respectively. Note that for the carbon system the *conduction band edge* and the *valence band edge* are loose terms as they can arise from a collective DOS originated from σ and π tails in anti-bonding and bonding states when they participate in optical absorption (optically active). With the assumptions that the conduction and valence band edges have similar shapes and the dipole matrix elements are independent of energy, the absorption near the gap takes the form of a joint density of states given by,

$$\hbar\omega\alpha = A(\hbar\omega - E_G)^{(n_C+n_V+1)} \tag{3.14}$$

where E_G is the band gap given by the separation of the extrapolated band edges. For parabolic band edges, $n_C = n_V = \frac{1}{2}$ and the expression 3.14 becomes,

$$\sqrt{\hbar\omega\alpha} = B(\hbar\omega - E_G) \tag{3.15}$$

The optical Tauc gap is an extrapolation of the density of states which are optically active. The band gap seen by the mobile charge carriers can, however, be different depending on the degree of de-localisation of the DOS. The band gap associated with electrical conduction is known as the mobility gap.

The RF power dependency of the Tauc plot of a-C:H:N is shown in Fig. 3.4. When the RF power input to the plasma is low, the energy associated with an active plasma species is also low. The bond type and the bond coordination of a particular site (*i.e.* the short range order of the film being deposited), is related to the average energy of the reactive species [123]. For 50W power input there is a relatively wide Tauc gap of ≈3.4eV. As the power increases there is a rapid drop in Tauc gap, initially to 2.9eV at 150W and remains close to ≈2.8eV at 500W (refer to Fig. 4.11). Depositions at higher RF powers could not be carried out due to limitations of the inductively coupled PECVD system used here.

A summary of the optical properties depending upon the RF power is listed in table 3.1. The polymeric nature of the films exhibited by the wide band gaps (≈2.7eV to 3.4eV), and the relatively small refractive indices (≈1.3 to 3.0), make it difficult to pinpoint the microstructural characteristics that may be responsible for determining optical properties. Unlike in non-polymeric materials in which the optical and electric properties are governed by the amount and the clustering of sp^2 sites, in polymeric materials the degree of polymerisation also induces an additional order parameter which adds further complexity. However the reduction in the band gap with power is consistent with a-C:H and a-C:H:N films deposited using PECVD [124, 60]. This suggests that unlike ion beam methods where the sp^3/sp^2 ratios are determined strictly by physical impingement by ions, in inductively coupled plasma there is an additional chemical process which needs to be considered in order to fully understand the microstructure of a-C:H films. In inductively coupled plasmas there is no directional kinetic energy component as in capacitively coupled and cathodic arc plasmas. Instead at higher RF powers the plasma species are in excited states so that the possessed energy can be transferred in deposition reactions on the

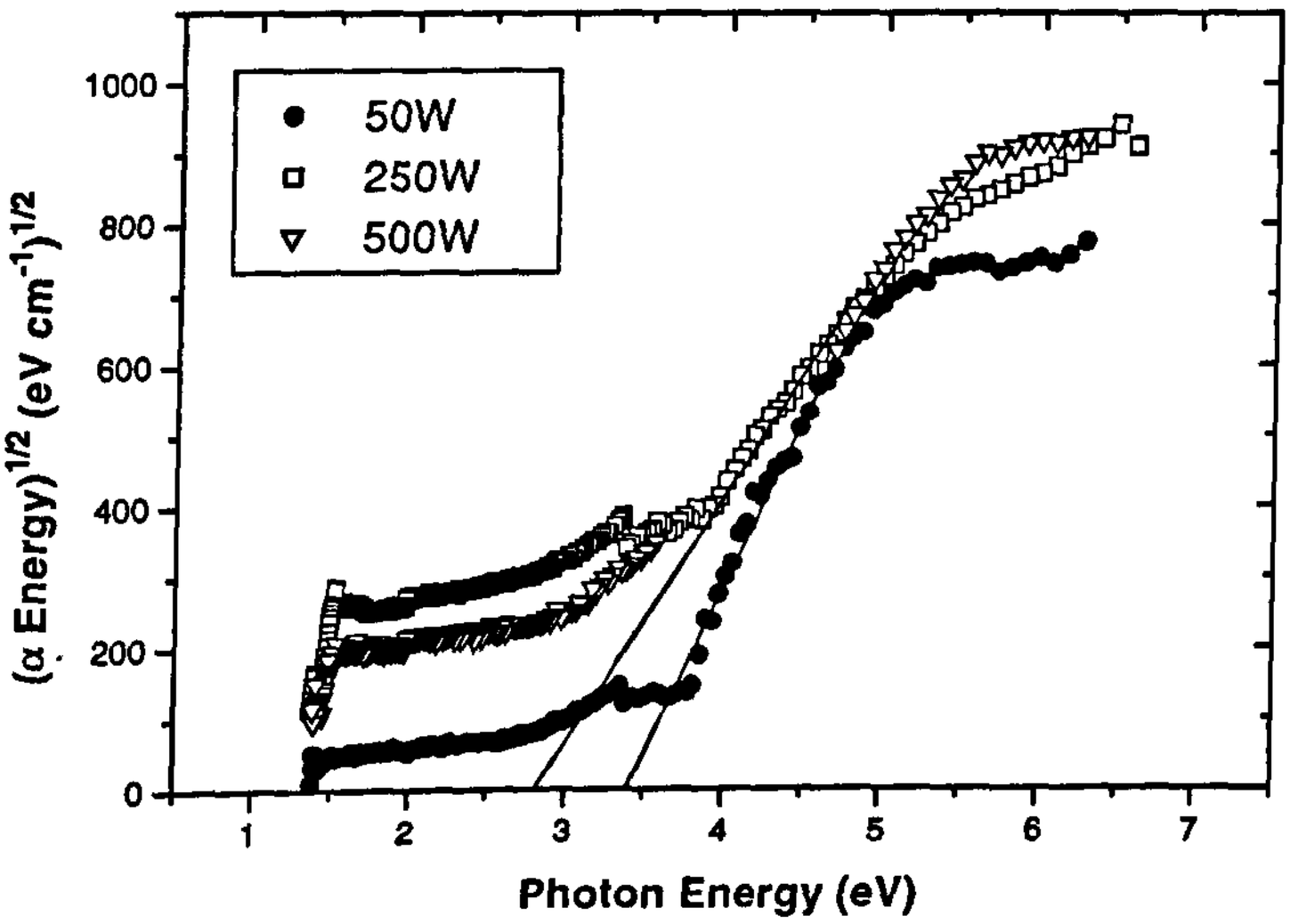

Figure 3.4: Tauc plot at three different RF powers. The Tauc gap can be extracted from the linear portion of the data by extrapolating down to energy axis as indicated by the solid line. Note that the Tauc gap decreases from 3.4eV to 2.8eV as the RF power is increased from 50W to 500W.

	RF Power		
	50W	**150W**	**500W**
n ± 0.05	1.3	1.7	1.3
k ± 0.05	0.08	0.18	0.25
ϵ_{r1} ± 0.1	1.6	3.0	1.6
ϵ_{r2} ± 0.1	0.2	0.6	0.6
Tauc Gap ± 0.05 (eV)	3.4	2.9	2.8

Table 3.1: Summary of RF power dependence of n, k, ϵ_{r1}, ϵ_{r2} (at 2.1eV) and the Tauc gap.

growing film. As indicated by ϵ_{r2} variations in table 3.1 there is an increase in n value at 150W. This suggests the rapid shrinking in band gap is due to changes in macroscopic structure. However the reduction in n while ϵ_{r2} remains constant with increase in power cannot be reconciled with structural changes.

Examination of the overall shape of the Tauc plot in Fig. 3.4 reveals that they are not completely linear, indicating that the assumption made in expression 3.14 that $n_C = n_V = \frac{1}{2}$ does not hold for a-C:H:N examined here. Similarly non-parabolic band edges have been reported previously [125, 126, 127]. As shown in Fig. 3.5, the resulting joint density of states for the assumption $n_C = n_V = 0$ gives a linear fit. Physical meaning of this assumption is rather ambiguous as it requires the extended DOS to be energy independent. It is more likely to assume that they do not participate in the optical absorption process. However for comparison purposes the Tauc gap is used in this work (since the E_{04} level in α is not applicable for certain type of films).

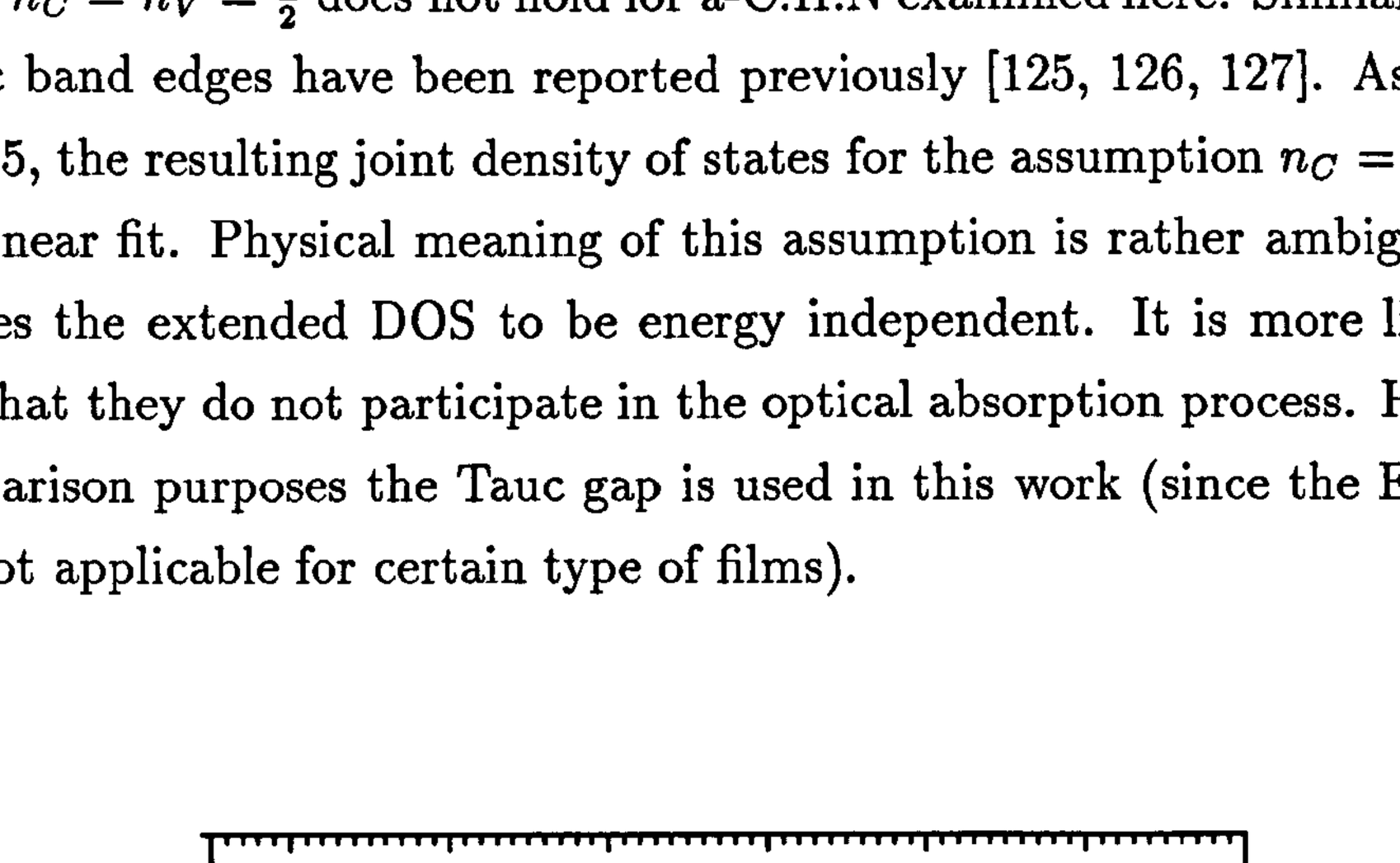

Figure 3.5: The assumption of energy independent extended states is compared with the parabolic assumption.

3.3.4 Temperature Dependence of Transmittance

The transmittance as a function of the wavelength for different temperatures is plotted in figure 3.6. No change in transmittance was detected for temperatures upto 80°C. However when the temperature was increased further, the absorption was found to increase and the absorption-edge was found to shift to longer wavelengths.

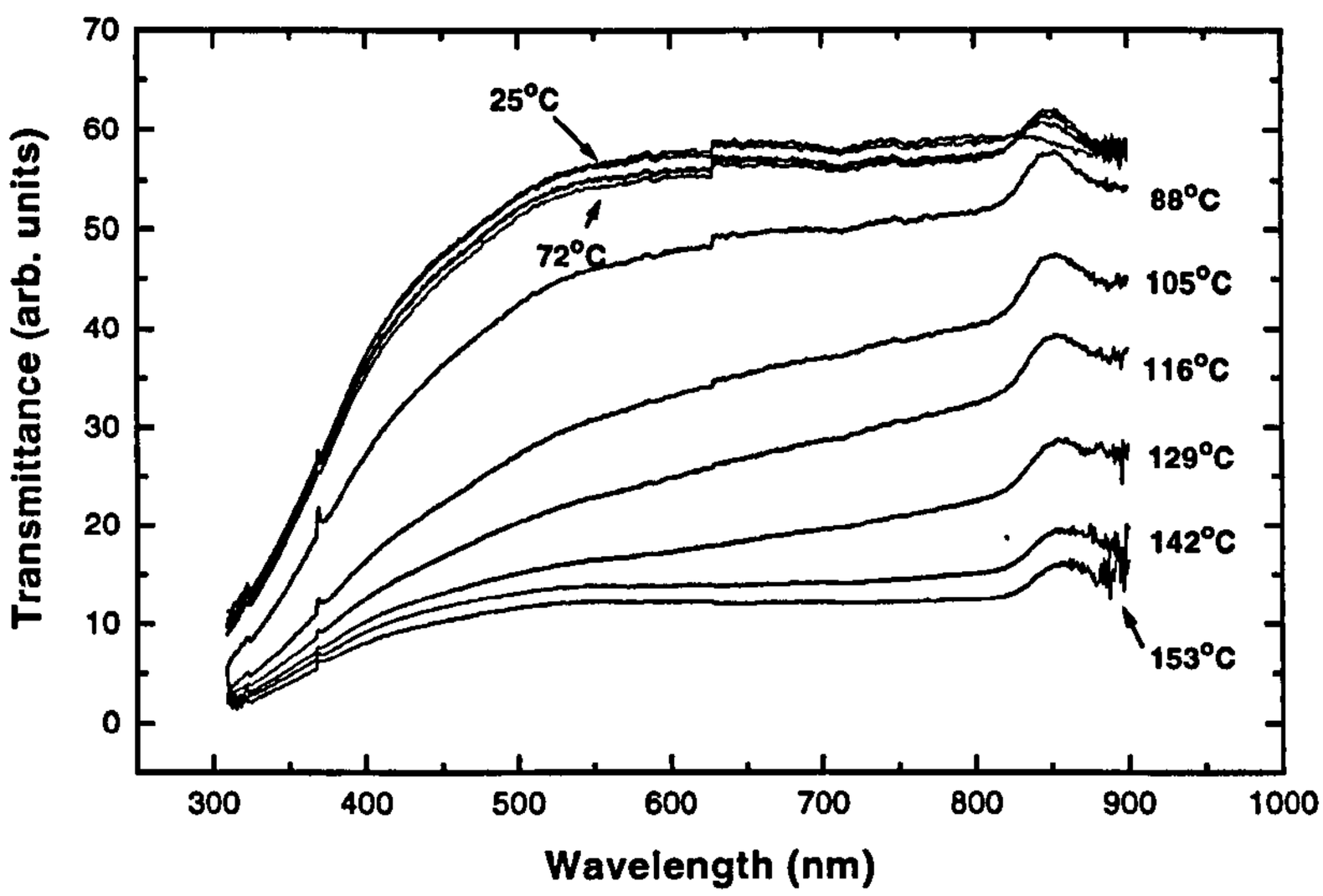

Figure 3.6: Transmittance versus wavelength. The plot shows that the transmittance is unaffected upto 80°C above which it gradually decreases.

Similar behaviour was also observed in the temperature dependence of the conductivity, as shown in Fig. 2.6. From the room temperature to ≈80°C the conductivity was found to have a less steep slope than at higher temperatures. It was concluded that two slopes of conductivity vs. temperature suggested a secondary activation beyond 80°C. The less steep slope with a smaller average conductivity originated from the activation of carriers into more localised *tail-like* states. In this region, since the tail-like states are highly localised, the activated carrier dissociation is limited, making the absorption in deep states

insignificant. Hence the participation of deep tail states in absorption process is not significant. The absorption that takes place at higher energies reflects a wider band-gap. However, the secondary activation of *extended-like* states at higher temperatures can lead to stronger absorption in deep tail states due to increased number of active carriers, as seen in Fig. 3.6 beyond 80°C. Therefore it can be concluded that the shift in absorption-edge is due to deep energy states participation in absorption process making the transmitting window narrower. This absorption edge shift consolidates the fact that the secondary activation is associated with DOS which are more de-localised than the initial activation.

3.3.5 Low Absorption Region

An exponential energy dependence of optical absorption in the low absorbing region was first observed by Urbach in alkali halide crystals [128]. The Urbach edge can be seen in all amorphous semiconductors including a-C. In the exponential region the absorption coefficient α is given by,

$$\alpha = \alpha_0 \exp\left[\frac{(E - \hbar\omega)}{E_0}\right] \tag{3.16}$$

where α_0 - a constant, $\hbar\omega$ - tail separation and E_0 - Urbach tail width.

	RF Power			**Precursor Ratio CH_4 : N_2**		
	50W	**150W**	**500W**	**1 : 0**	**1 : 1**	**1 : 9**
E_0 (eV)	0.65	1.18	0.87	0.86	0.81	0.77
$\frac{d\alpha}{dE} \times 10^4 (eV^{-1}cm^{-1})$	7.8	4.1	8.2	3.9	1.0	0.5

Table 3.2: Urbach tail width E_0 and the absorption slope $\frac{d\alpha}{dE}$ in the low absorption region are listed for different RF powers and for varying N content in the film.

The real origin of this behaviour is still in debate. The similarity seen in the slope of all amorphous semiconductors led to the original view that it reflects the energy dependence of the matrix elements, contrary to the nature of joint

density of states. Dow *et. al.* suggested an excitonic origin [129]. However currently it is thought that the Urbach tail represents the disorder broadening of the joint density of states. This view is easily applicable to singular bond type materials. When it comes to the carbon system the effects originating from multiple bond types make it more complex. The *tail region* can comprise of σ tails, π and π tails. The inclusion of N can make the situation even more complex because N too can form separate σ and π bonds having different states of energies to that of C-C.

In table 3.2 the Urbach tail width and the slope of α in the low absorption region are listed. The RF power dependency is shown for a-C:H:N deposited with a CH_4:N_2 = 1:1. It can be seen that as the N content in the film increases the Urbach tail width decreases indicating confinement of optically active exponential region. The slope of α also decreases with N. Collectively the N inclusion in the a-C:H matrix reduces the density of optically active states in the Urbach region. If the real origin of Urbach tail is disorder broadening then the experimental results indicate that the inclusion of N has reduced the bond disorder generated states in the vicinity of the band edge. However the behaviour of E_0 and $\frac{d\alpha}{dE}$ with RF power does not give a firm insight into the nature of the Urbach edge.

3.3.6 Conclusions

The electromagnetic wave interactions in semiconductors having finite conductivity result in absorption and reflection of the incoming energy. Since the absorption process is associated with the energy transition of charge carries inside the material, it can be used to get an insight into the nature of the electronic density of states in a semiconductor. Generally, optical transitions are characterised by the complex dielectric constant. This can be found from the measurable quantities of transmittance and reflectance. The investigation of the a-C:H:N films revealed that the presence of N in the films leads to a relative reduction in transmittance. However the variation in N content, does not lead any measurable change in transmittance. The reflectance is invariant for all the

N concentrations once it is introduced in the film. By comparing the heavily absorbing region with the *transparent* region, it was found that reflectance in a-C:H and a-C:H:N occurs mainly at the air-material interface.

The real part of the refractive index n was found to be invariant with N content in the film. The values of n, ranging from ≈1.3 to 3.0 indicate polymeric type films [60]. The extinction coefficient k shows the presence of N as a shift towards lower photon energies, but further increase in N content does not lead to any measurable effect. The Tauc gap of a-C:H is ≈3.0eV which reduces to 2.7eV on incorporation of N. The real part of the dielectric constant is dominated by n since k is smaller by an order of magnitude. The imaginary part of the dielectric constant ϵ_{r2} is a measure of the joint density of states and the dipole matrix. It was seen that ϵ_{r2} did not show any sharp features in contrast to a crystalline material, due to momentum relaxation. There was a rapid increase in ϵ_{r2} beyond ≈5eV due to σ-σ^* transitions.

A reduction in Tauc gap from ≈3.4eV to ≈2.8eV with increase in RF power from 50W to 500W has observed. This behaviour cannot be simply explained by the cluster model [98] alone due to the fact that the polymeric nature of the film can introduce an additional degree of order with polymerisation. It was also seen that the parabolic energy dependency of the DOS at the high absorption edge (Tauc assumption) is not the most appropriate one for films under current investigation. Further it was found that the energy independent edges (*i.e.* n_V=n_C=0 in the power law) gives a better linear fit. However, the Tauc gap was monitored for comparison purposes.

The temperature dependence of transmittance showed an activation of deep states for ≈80°C and above. This is in keeping with the second activation region also seen at 80°C in the conductivity vs. 1/T data in chapter 2.

The low absorption region characterised by an exponential dependency of the absorption coefficient was also observed. The Urbach tail width was found to reduce with the N content in the film. The slope of α in the Urbach region also decreased with increasing N. If the origin of the Urbach tail is bond disorder, then it can be inferred that N inclusion has reduced the disorder broadening in a-C:H. However, as an overall measurement, optical parameters are not sufficient

to gain a clear insight into the impact of nitrogen introduction on the DOS of a-C:H.

3.4 Photoluminescence Properties

3.4.1 Introduction

For the photoluminescence (PL) study a tunable Ar ion laser operated between 514nm and 458nm, (laser emissions at 501nm, 496nm, 488nm, 476nm, 472nm and 465nm) was used as the excitation source. The power available for excitation depended upon the wavelength of the laser line and can be varied from 600mW for the 514nm line to 35mW for the 458nm line. The sample was excited at a glancing angle by a modulated laser beam (≈450Hz) so that the reflected residual beam component offered minimal additions to the collected PL signal. The PL emission was dispersed by a ruled grating type monochromator having a maximum resolution of 4.5nm/mm and detected by a photomultiplier placed normal to the sample as shown in Fig. 3.7. The amplifier was locked-in for synchronous detection by taking the reference frequency as that of the laser beam modulation, in order to remove the possible DC bias induced on the detector by the scattered ambient. A low pass optical filter in front of the detector was used to prevent the exciting laser line from saturating the detector. All PL spectra were corrected for the system response by taking into account the base line generated by a known tungsten source spectrum.

For PL measurements, a-C:H and a-C:H:N films of 100nm-400nm thick were deposited on Si substrate. All spectra gathered were corrected for film thickness variations. For electric field quenching studies an ITO/a-C:H:N/Au sandwich structure was used. Excitation was coupled through the transparent ITO electrode at a glancing angle. The PL emission was collected normal to the device and the electric field was applied between ITO and Au electrodes. The fatigue measurements were performed on films deposited on Si substrates.

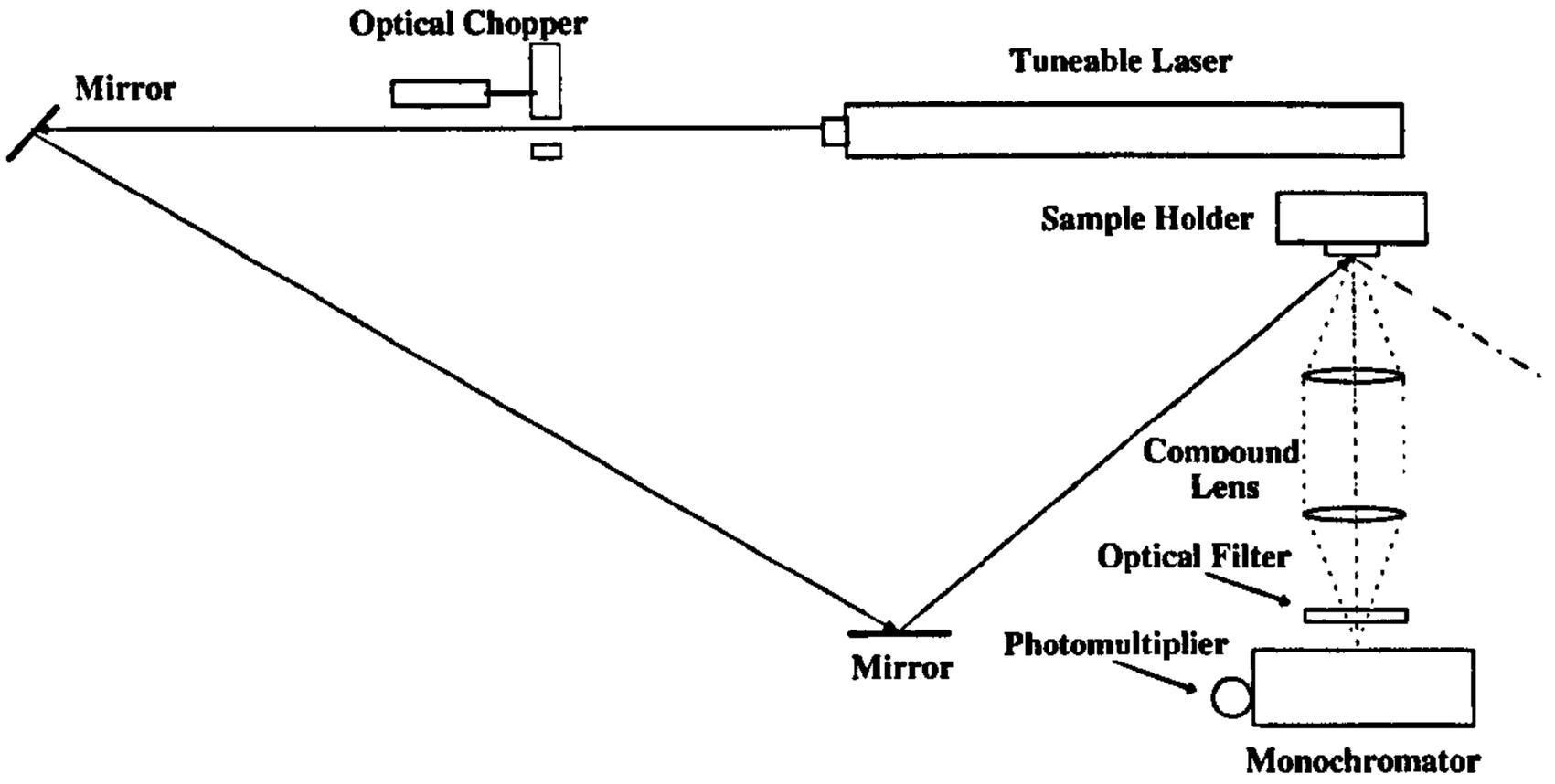

Figure 3.7: The schematic diagram of the PL measurement set up. The photomultiplier output is fed into a lock-in amplifier having a demodulation reference frequency of 450Hz derived from the optical chopper. A low pass optical filter in front of the monocromater is used to exclude the exciting laser line.

3.4.2 Apparent shifts in PL parameters with varying nitrogen content in films

The PL spectra from a-C:H:N films with nitrogen content varying from 0-30at% are shown in Figure 3.8. The PL peak energy position was found to shift from 2.23eV for the film containing no nitrogen to 2.12eV for the film with the maximum nitrogen content. Several models have been proposed in the literature to describe the photoluminescence observed in amorphous materials [2].

- Band to mid-gap recombinations : In this model, electron transitions from the conduction band tails to mid-gap states and hole transitions from the valence band tails to mid-gap states are considered [130]. The requirement of active recombination centres at mid-gap necessitates two main features for this model to be applicable :

1) The DOS have to be large enough with optically active deep states in the middle of the forbidden gap, so that the effect is manifested as a pinned Fermi level at mid-gap energies (*i.e.* the activation energy is half that of band-gap).

2) The radiative transition occurs with mid-gap states either from conduction or from valence band edges so that the energy of the emitted radiation is half of the band gap energy (*i.e.* the PL peaks from the emitted spectra lie at energies equal to half the optical band-gap).

Other implications of the model are that the electron-phonon interactions are weak, the broadening of the spectral line-width arises from the energy distribution of the deep recombination centres and from disorder broadening of tail states, and that there must be an equivalent absorption band at similar energies to the luminescence band.

- Band-tail to band-tail recombinations : With these types of recombinations weak electron-phonon interactions are also taken into account. This model suggests that photo-excited carriers are either thermalised down the broad tail states and relax or recombine radiatively[131, 132]. The thermalised relaxation process is expected to dominate close to the band edges where the DOS is high and the excited carriers are thought to relax with phonon interactions. In contrast the low DOS associated with deeper tail states reduces the possibility of thermalised relaxation and radiative recombination is expected to be more likely. The features inherent to this model are :

  - The PL peak energy indicates the separation of the two recombination edges. If there is a deviation of PL peak energy from of the optical band-gap, the difference corresponds to twice the tail width.

  - As the energy of excitation increases the PL peak energy shifts to higher energies (*i.e.* shows a blue-shift). At higher energies of excitation the recombination process takes place via shallow tail states

so that the separation of the recombination edges are wider, causing the blue-shift in PL peak energy.

Initially it was thought that the broad tail widths must correspond with the absorption bands. Later, however, it was understood broad tail widths could be obtained without optical absorption if the electron and hole states were separated by large enough band edge fluctuations [133].

- Transitions with strong phonon coupling : In such transitions, the PL peak energy and the spectral line width are mainly determined by the strength of the phonon coupling [134]. The main features are :

  - The absorption spectrum is Gaussian at low temperatures and at high temperatures the higher *vibrionic* levels cause modifications to the spectrum beyond the peak energy.
  - The PL spectrum is also Gaussian and red-shifted by an amount known as the *Stokes shift*. At high temperatures the emission spectrum resembles the lower energy portion (below the low temperature peak) of the absorption spectrum [135].

When the above models are examined in the context of a-C:H, the *band-tails* are comprised of a combination of σ-tails originating from bond disorder in σ and σ^* states at sp^3, sp^2 and possible sp sites while the π-tail states similarly originate from disorder of π and π^* states at sp^2 and sp sites, together with the ordered π and π^* sites. The sp^2 sites in a-C and a-C:H are thought to segregate into clusters within the sp^3 matrix to reduce the over all energy [136]. The π-π^* state band tails lying closer to mid-gap can be highly localised, leading to large disorder potential fluctuations. The fact that the carbon system can have a variety of bond types leads to very broad tails ($\approx$0.2-0.5eV) compared to a-Si ($\approx$0.1-0.2eV) where only σ bonds are present [137]. This is manifested as a broad Urbach tail width for a-C:H and a-C:H:N as observed here (see Table 3.2) and also reported in the literature [60, 121]. In this frame work, the deep band-tail states in a-C:H can be of the non-absorbing type while the shallow

states have more *extended-like* characteristics. The heavy localisation of the π-π^* states giving rise to closely coupled photo-excited electron-hole pairs has been used to describe room temperature PL observed in a-C:H films [111]. In a-C:H:N the additional role of σ_N and π_N states must also be considered.

The normalised PL intensity versus the photon energy for a-C:H and a-C:H:N films is plotted in figure 3.8. Given that a-C:H:N films have an optical Tauc gap of ≈2.7eV, compared to ≈3.0eV for a-C:H, and that the measured PL peak lies at 2.1-2.2eV (from figure 3.8) for all films, an energy difference of 0.6-0.8eV is obtained between the absorption edge and the PL peak. These values are inconsistent with the band to mid-gap recombination model mentioned above in which the PL peak should lie at energies equal to half the band gap (≈1.3eV in this case). Furthermore the typical activation energy of conduction for a-C:H:N is ≈0.7eV, indicating that the Fermi level is not pinned at mid-gap. Similarly, with the model associated with strong phonon coupling, a relatively large shift in PL peak energy from absorption edge is inferred. However comparison of the spectral shape of the PL in Fig. 3.8 with the absorption spectra shown in Fig. 3.2(b), does not show any resemblance associated with a typical Stokes-shift, even if the low absorption region is taken to correspond to states where high temperature PL occurs. This incompatibility rules out the description of PL from a Stokes-shift in a-C:H:N.

The band tail to band tail recombinations, taken together with broad tails in a-C:H can give some insight into the origin of PL in a-C:H:N, as proposed by others [111, 121, 138]. It can be seen that as the N content in the film increases the PL peak shifts to lower energies (red-shift) and the spectral line-width increases (see Fig. 3.8). However, the optical absorption data in Table 3.2 indicates that as N increases the Urbach tail width decreases [52]. In general, as the Urbach tail width increases (>0.5eV), the PL spectral width also increases [121]. This is contrary to observations made for a-C:H:N in this work. The shift in PL peak position and the behaviour of spectral line width with N content indicates that the model for PL from a-C:H is inadequate for a-C:H:N. Similar PL peaks at ≈2.1eV and wide Urbach tails (>0.4eV) for a-C:H:N can be found in literature[139]. In this report, the Urbach tail width and the optical band-gap

were found to decrease with introduction of N into the films.

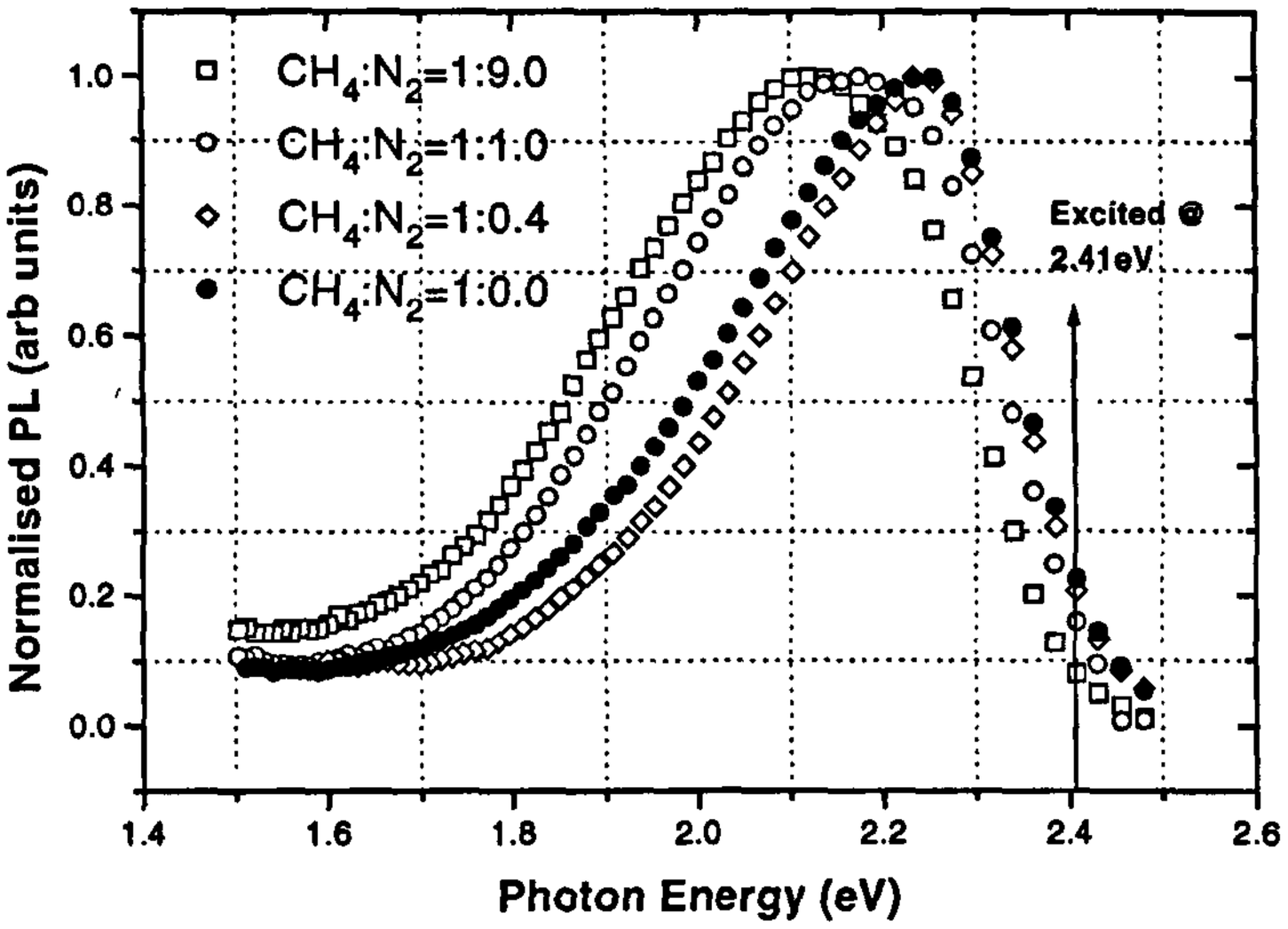

Figure 3.8: PL spectra of a-C:H:N with varying N contents from no detectable N to 30% N. Excitation energy used was the 2.41eV Ar ion laser line. As N content in the film increases the PL peak position shifts from higher photon energy of 2.23eV to 2.12eV. The spectral width of the spectra also broadens with N content in the film.

Now we shall look at the problem in context of recombination centres associated with N in conjunction with the $\pi - \pi^*$ centres. The PL spectra obtained by excitations at 2.41eV, seen in Fig. 3.8, can be decomposed into three Gaussian sub-peaks, two major peaks at ≈2.2eV and ≈2.1eV together with another broad sub-peak at ≈1.7-1.8eV as illustrated in Fig. 3.9.

The relative intensities of the sub-peaks in Fig. 3.9(a), show the largest at ≈2.1eV, the next at ≈2.2eV and the smallest at ≈1.7eV. The largest N content of ≈30at. % ($CH_4 : N_2 = 1 : 9$), is expected to be the saturation level of N in a-C:H:N [52]. The PL of the film with 9at. % N ($CH_4 : N_2 = 1 : 1$) also reveals similar sub-peaks. But, interestingly the sub-peak at 2.1eV, though still the largest, is now lower in intensity relative to the 2.2eV peak [see Fig. 3.9(b)].

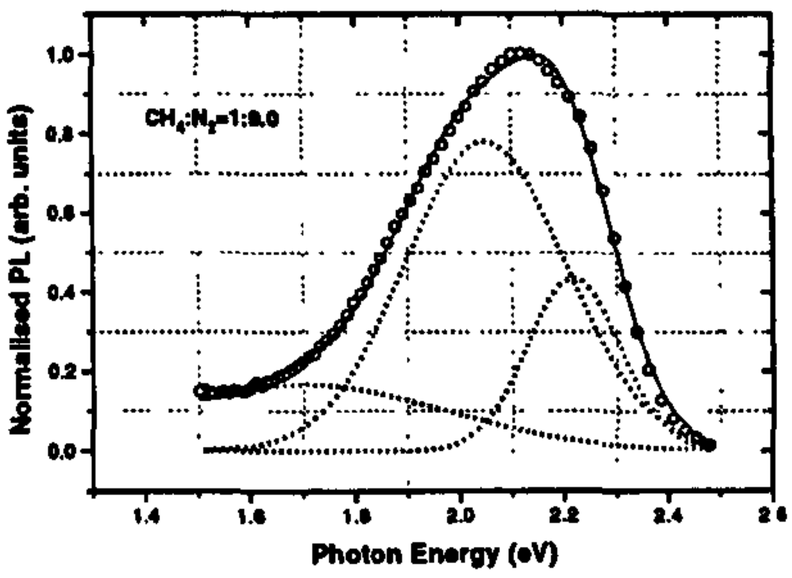

(a) The PL spectrum at the highest N content. The intensity ratio of two major sub-peaks, 2.1eV to 2.2eV is 1.79.

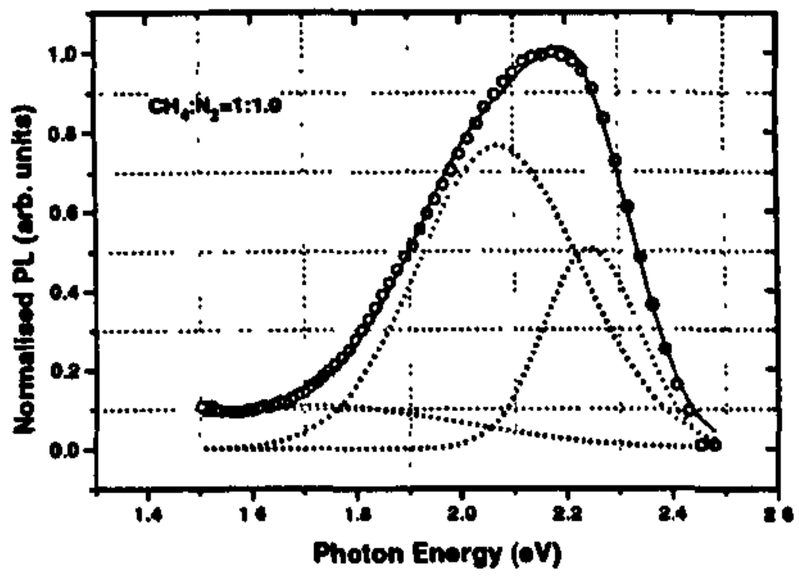

(b) The deconvolution shows similar sub-peaks as in (a). But as N content goes down, major sub-peak ratio also goes down to 1.5.

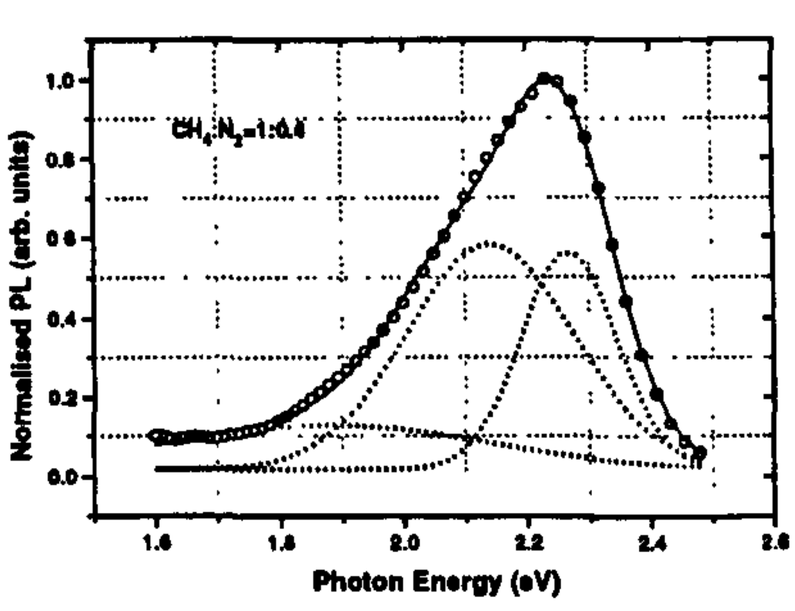

(c) Further reduction in N content brings the deconvolved major sub-peak ratio down to 1.03.

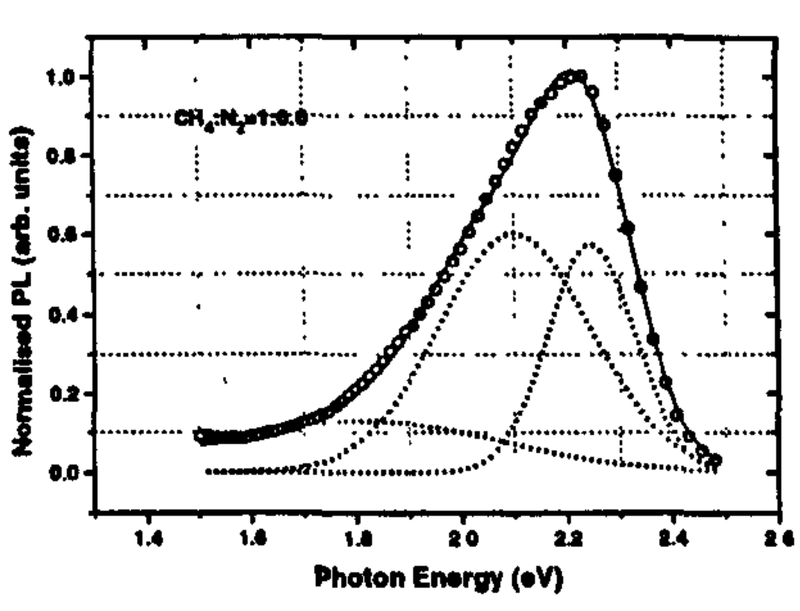

(d) Deconvolved spectrum of the film containing no detectable N. The major sub-peak ratio is 1.04.

Figure 3.9: The deconvolution of PL spectra yields three Gaussian sub-peaks. The effect of nitrogen content over the intensity ratio of two major sub-peaks at 2.1eV to 2.2eV is shown.

As seen in figures 3.9(c) for 3.6at. % N, and 3.9(d) for no detectable N in the sample, the relative intensities of the 2.1eV sub-peak has become comparable with that of 2.2eV. The change in intensity of these two sub-peaks at 2.1eV and 2.2eV (here after denoted by $P_{2.1}$ and $P_{2.2}$ respectively) with varying N content in the film, suggests that the apparent red-shift of PL with N, and the accompanying spectral line width broadening are an outcome of this relative intensity change.

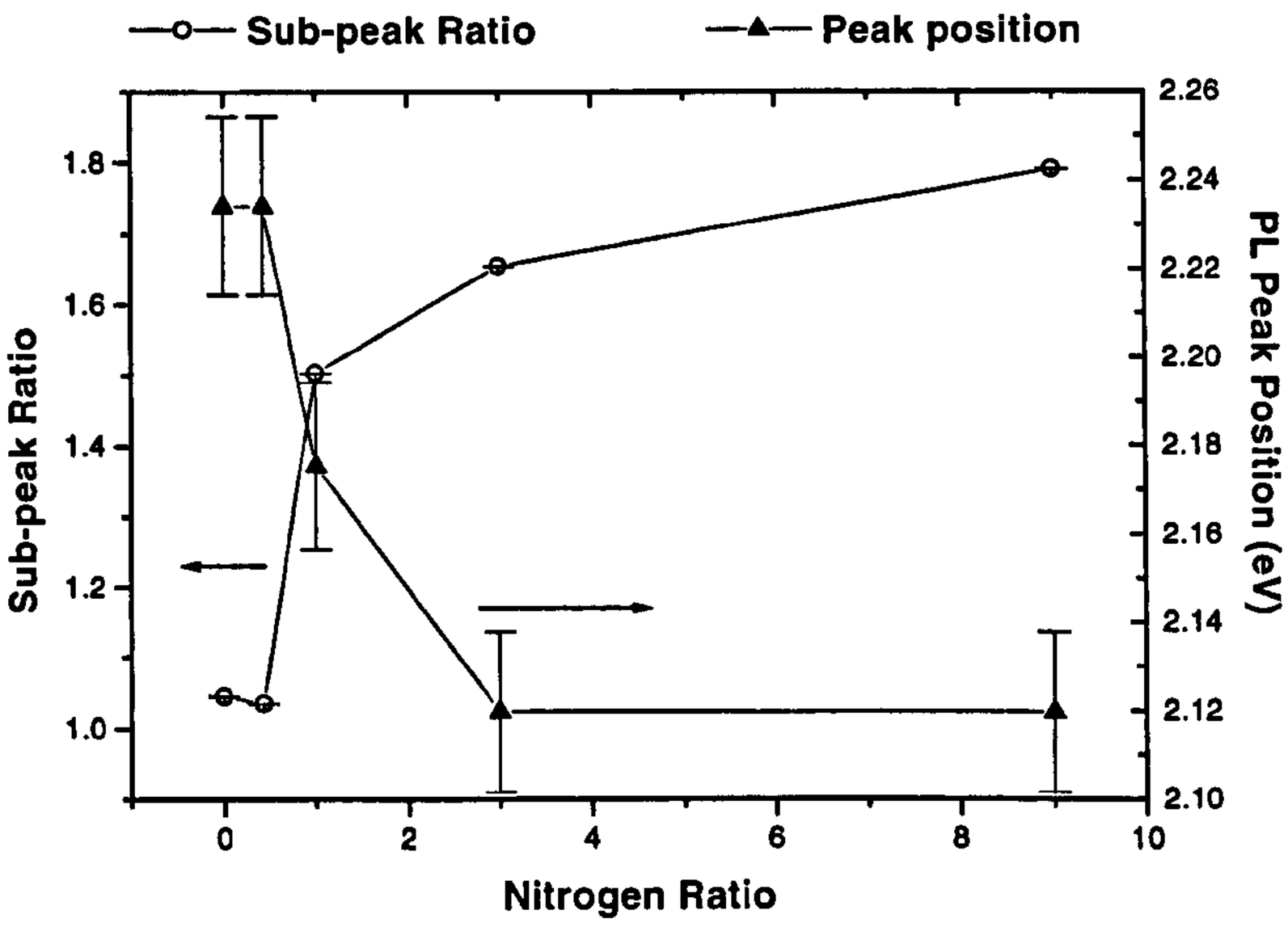

Figure 3.10: The peak position of the composite PL envelope is plotted against nitrogen flow ratio. As the N ratio increases the energy of the peak position reduces. The deconvolved major sub-peak ratio of the PL spectra shows an inverse behaviour and increases from 1.04 to 1.79 with N content.

In Fig. 3.10, the sub-peak ratio $P_{2.1}/P_{2.2}$ and the shift in PL peak of the composite envelope are plotted against the N_2/CH_4 ratio, denoted as the *nitrogen ratio*. As N ratio increases the sub-peak ratio was found to increase from 1.04 to 1.79. The corresponding PL peak position movement was from 2.23eV to 2.12eV. The trend shown by the sub-peak ratio closely resembles the inverse change of the PL peak shift (red-shift) with N content in the film. Given the

fact that the band-gap does not change with varying N as seen in Fig. 3.2(b), this is strong evidence for the apparent shift in peak position of the composite envelope being due to intensity competition between these two sub-peaks. It is not due to any movement of the recombination centre within the band-gap as the N content increases. We shall later find more evidence which supports this concept by looking at the band-gap dependence of PL, excited at different energies.

With N modification of a-C:H to form a-C:H:N, there are $\pi_N - \pi_N^*$ states closer to mid-gap surrounded by $\pi_C - \pi_C^*$ states, in certain configurations of N bonding [51]. Generally, these deep states are localised, forming strong correlation between photo-generated electrons and holes. The photon absorption in surrounding *extended like* states generates excited carriers which thermalise down to $\pi_C - \pi_C^*$ and $\pi_N - \pi_N^*$ states lying deeper via inter-cluster interactions[91], where they radiatively recombine or relax down non-radiatively in defect states. This can give rise to two types of origin to PL, namely π_N associated which is lower in energy and π_C associated, higher in energy.

The nitrogen dependence of the full width half maximum (FWHM) of the normalised PL spectra is illustrated in Fig. 3.11. The spectral line width increases rapidly for a small increase in N ratio and then after following a gradual increase tends to saturate. The spectral widths are comparable with those reported previously for similar materials[140]. Similar behavior of FWHM with N content can be found in literature [139]. Given that the Urbach tail width decreases with N as in table 3.2, and also the tail widths are >0.5eV, if the PL peak shift were tail dominated then the FWHM should also be decreased [121].

The spectral line-width widening seen with increasing N content can also be understood within the same context of there being two dominant recombination centres giving rise to relative PL intensity competition between π_N associated emissions and π_C associated emissions. As the N content increases the π_N DOS also increases making the probability of recombinations at N sites higher, relative to that at C cites resulting in an increased $P_{2.1}/P_{2.2}$ ratio. The width of the two sub-peaks remains unchanged with changing N content, with 0.18eV for the sub-peak at 2.2eV and 0.31eV for the sub-peak at 2.1eV. This shows that

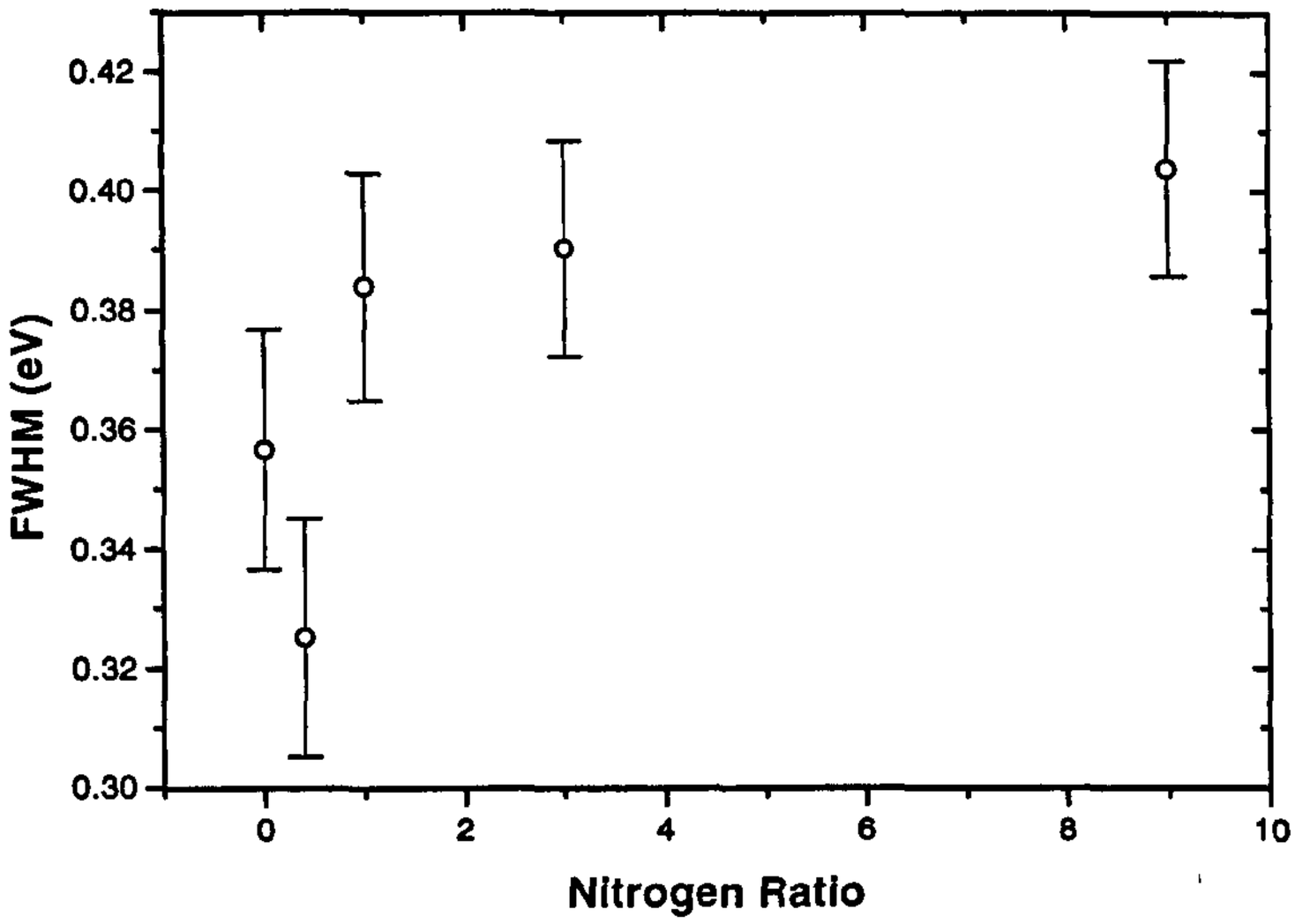

Figure 3.11: The spectral width of the composite PL envelope as N content increases.

inclusion of nitrogen does not influence the line shape. Rather, nitrogenation leads to a higher intensity of the PL sub-peak at 2.1eV. Although the width of the sub-peaks remains unchanged with N content the intensity increases, the intensity level at which the half maximum occurs goes up. This is reflected as a broadening in the composite PL profile.

3.4.3 Effect of different excitation energies

The excitation energy dependence of PL in a-C:H and a-C:H:N is shown in Fig. 3.12. As the energy of excitation increases in the sub band gap region from 2.41eV to 2.71eV, the PL spectra show a blue shift, as expected. For both a-C:H and a-C:H:N, as excitation energy increases, the probability of reaching energy states situated away from mid-gap increases. The excited carriers from these states thermalise down to more localised states deeper in band tails and recombine. Now the destination energy reached after similar number of thermalising

steps is higher in energy. This effect is reflected as a blue-shift in the PL peak with increased excitation energy [see Fig. 3.12(a)].

The presence of N in the film does not alter the above process. As a result a similar trend in PL is expected for a-C:H:N also. Nevertheless the PL associated with π_N states are not affected by the increase in excitation energy. But the relative intensity increament at π_C can induce a blue-shift in composite envelope as seen in Fig. 3.12(b).

3.4.4 Band-gap dependence of PL properties

The PL spectra obtained from films having varying band gaps from 2.9eV to 3.2eV ($CH_4 : N_2 = 1 : 1$) excited at different sub band gap energies are plotted in Fig. 3.14. In similar materials, no changes in PL peak for a-C:H:N [139] or blue-shifts for a-C:H with increasing band-gaps [141, 60] were reported. However, the composite PL peak position is found to red-shift with band gap widening for a-C:H:N in this case.

In Fig. 3.13 the PL peak energy excited at 2.5eV is compared with similar observations reported in the literature. It is seen that the PL peak is sub-band gap almost in every case. In the present work the PL peak energy decreases with increased band gap contrary to linear dependence of PL peak position with band gap seen in capacitively coupled PECVD deposited films [139, 140, 121, 138, 142].

Comparing PL originating from deep tail states in a-C:H, in a-C:H:N the PL arising from π_N states deeper in the band gap can be unaffected by the widening of the band gap. *i.e.* the band gap widening process can be a *bulk* property keeping N containing clusters still intact. As band gap widens the energy of π_C recombination centres move away from the mid-gap. When these are excited by sub band gap energies, as the band gap widens the DOS states participating in the excitation reduces. The lesser excitations in π_C reduce the PL resulting from those states. Since the relative intensity associated with lower energy π_N remains the same, the composite peak apparently red-shifts.

In Fig. 3.15 the PL peak position of the composite envelope is plotted against

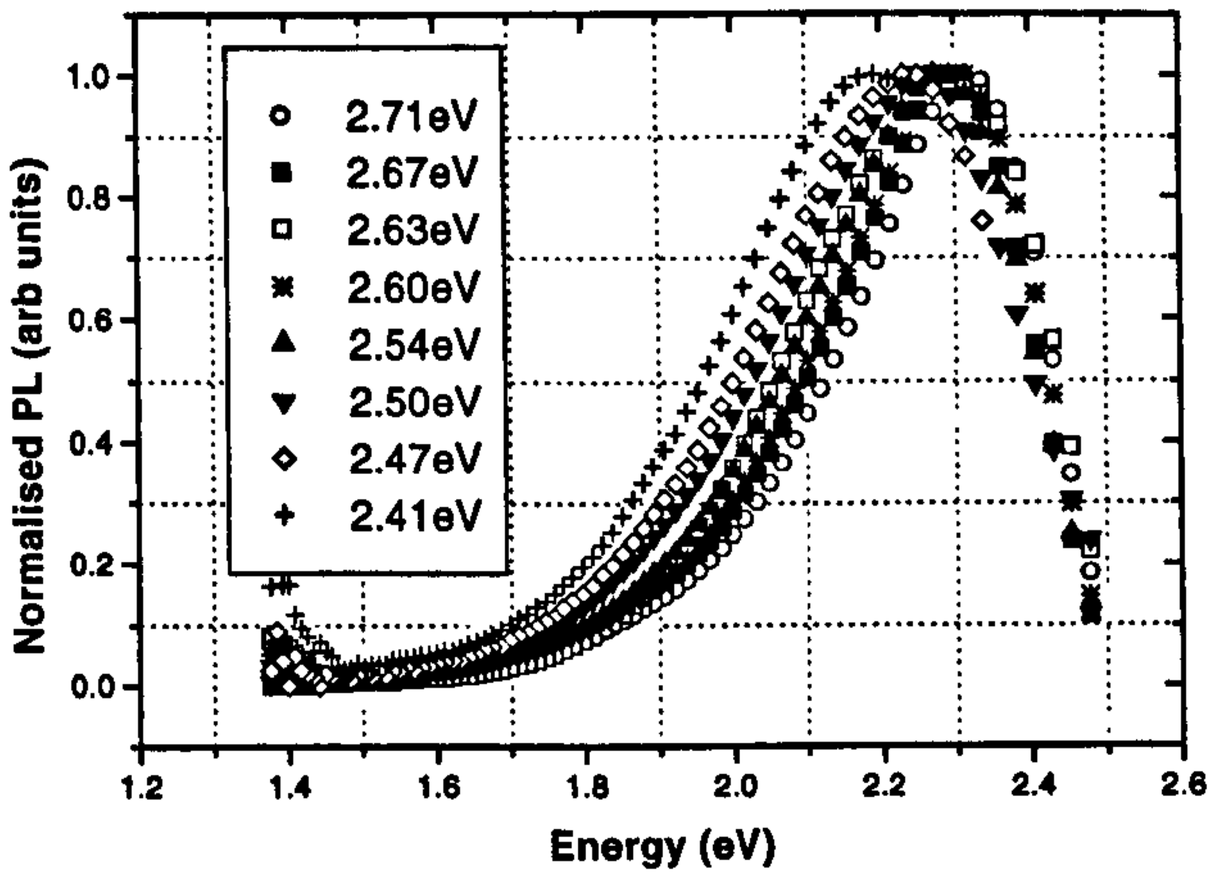

(a) PL spectra of a-C:H for different excitations energies.

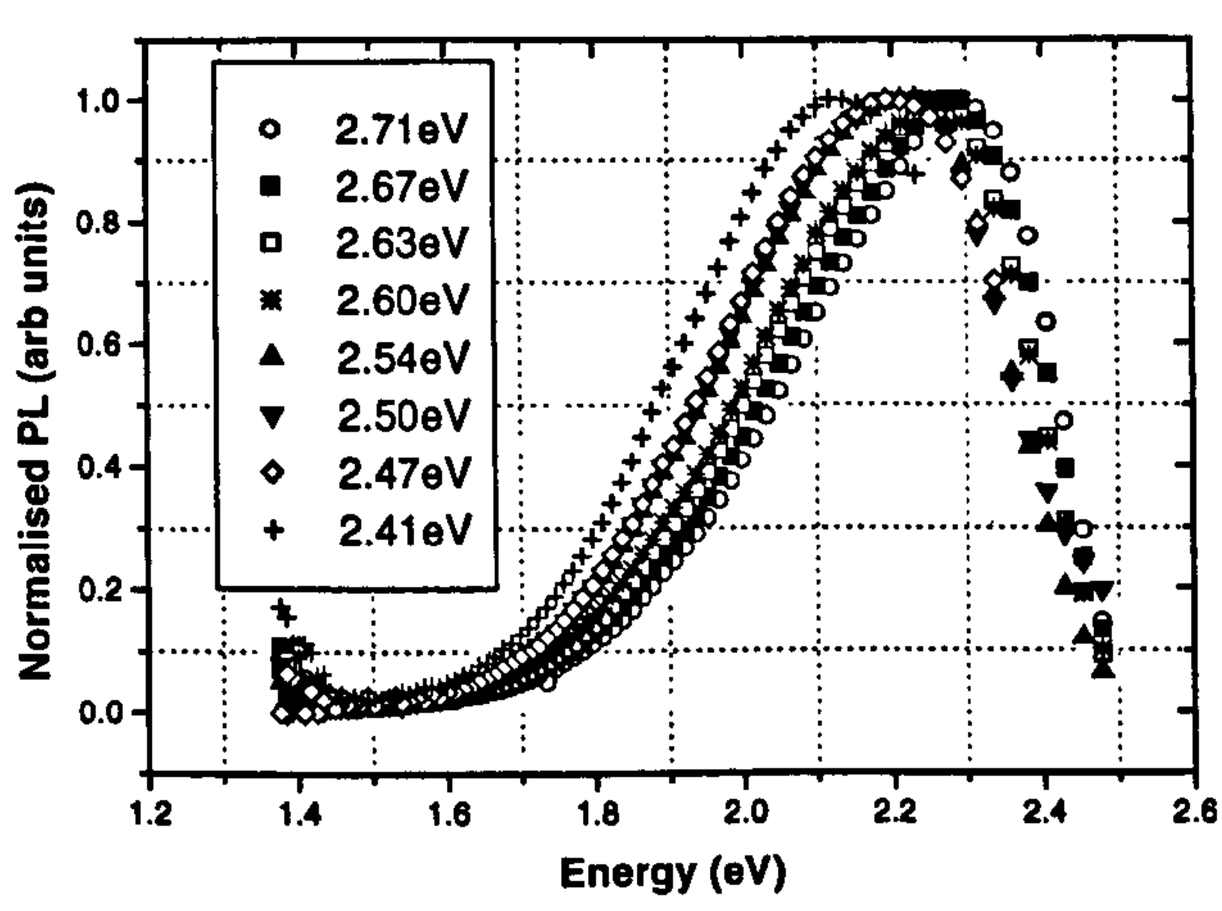

(b) PL spectra of CH_4:N_2=1:1 for different excitation energies.

Figure 3.12: The normalised PL spectra of a film having no detectable N are in (a) and CH_4:N_2=1:1 in (b). In both cases as excitation energy increases the composite PL peak moves towards higher energies indicating an additional tail state recombinations.

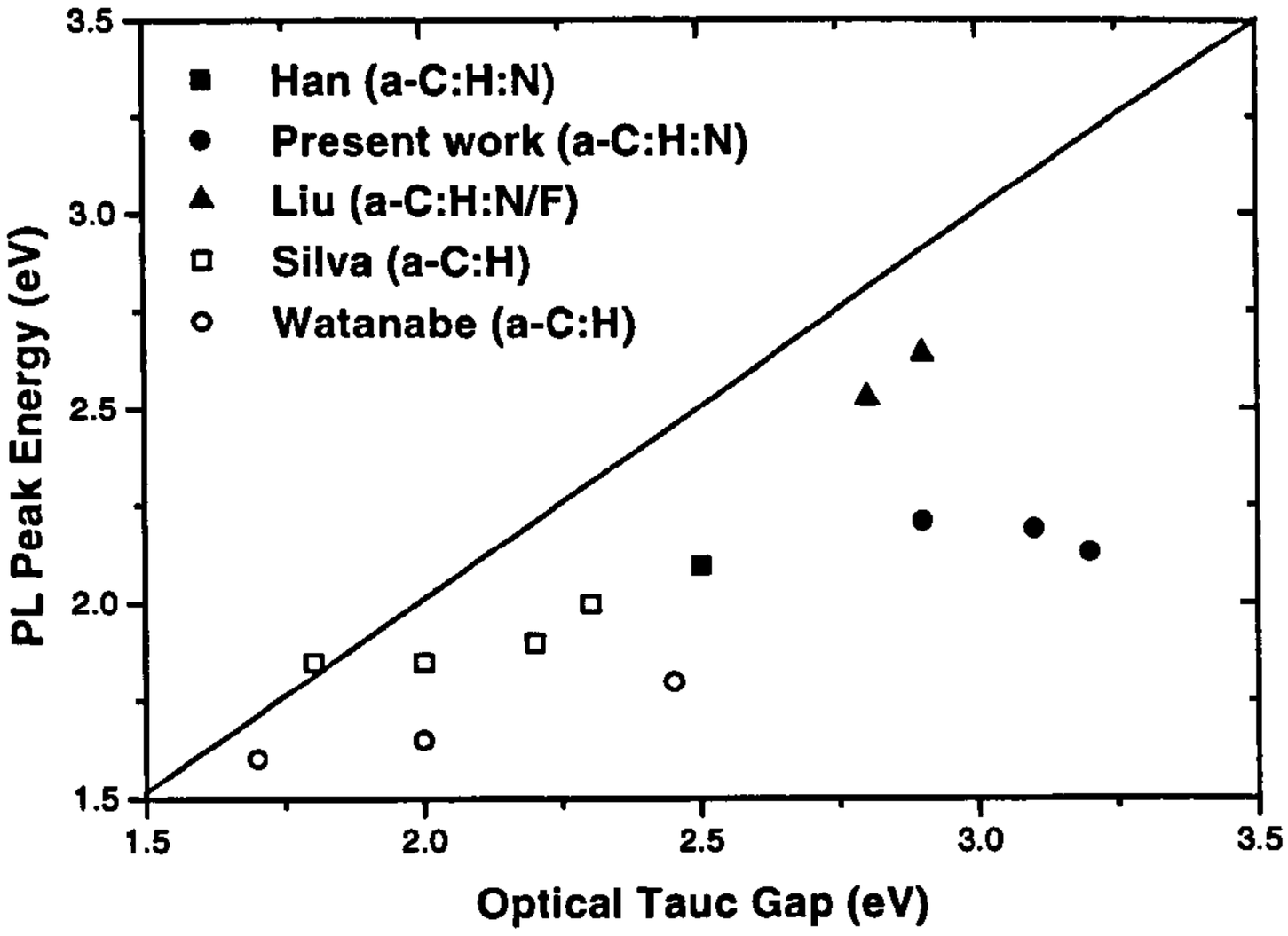

Figure 3.13: The peak position of the composite PL envelope versus optical Tauc gap of a-C:H:N, a-C:H:N/F and a-C:H. The sub-band gap PL is observed almost in every case.

the excitation energy for different band gaps. With increasing excitation energy, the PL peak position also increases for all the band gaps. This is in accordance with the mechanism described in the previous section. Moreover for all energies of excitation the peak positions of the widest band gap lies below that of the narrower. Given that the PL peak of a-C:H with higher band-gap of 3.0eV was at higher energy (see Fig. 3.8), the above results strong indicated that the apparent red-shift seen in Fig. 3.9 is in fact due to intensity competition between two sub-peaks associated with π_C and π_N.

3.4.5 PL Fatigue

The PL spectra collected under prolonged exposure of the sample ($CH_4 : N_2 = 1 : 1$) to an exciting laser beam at 2.41eV showed a reduction in intensity with time. Similar behaviour has been reported previously for a-C:H [143, 144, 60, 145].

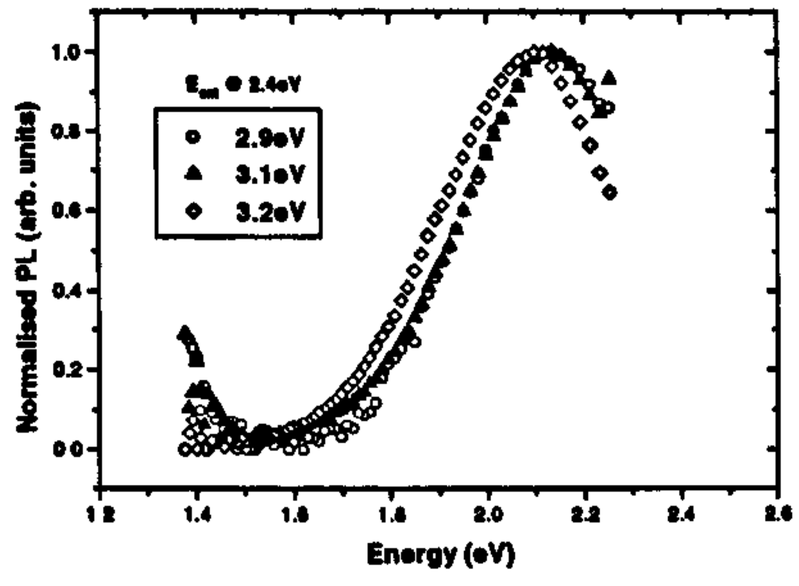

(a) The PL spectra collected for 2.4eV excitations.

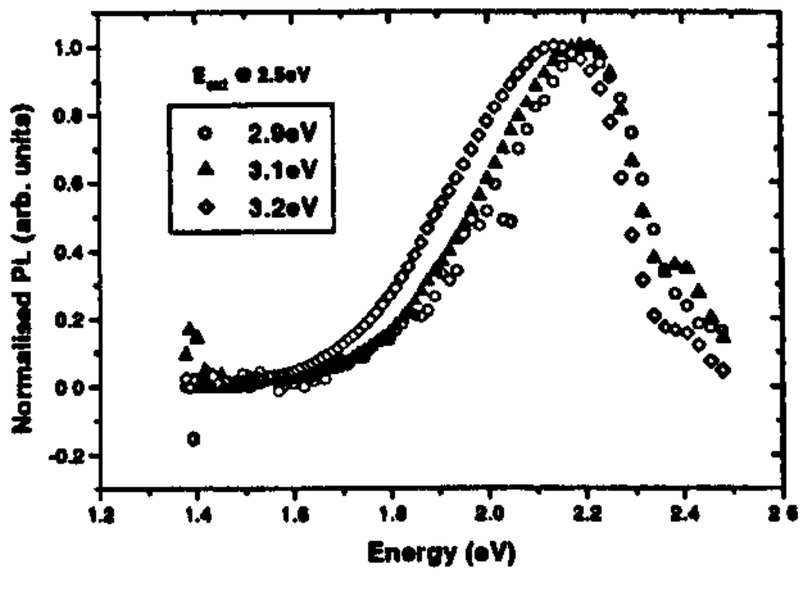

(b) The PL spectra collected for 2.5eV excitations.

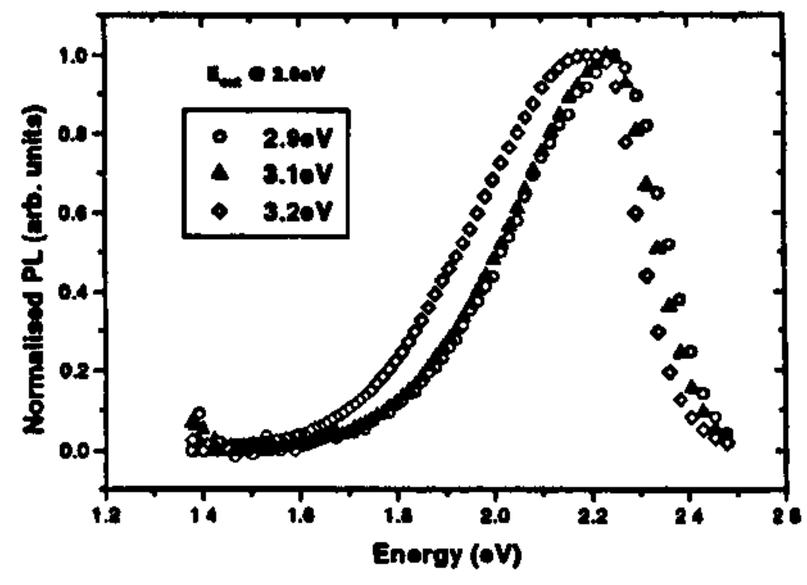

(c) The PL spectra collected for 2.6eV excitations.

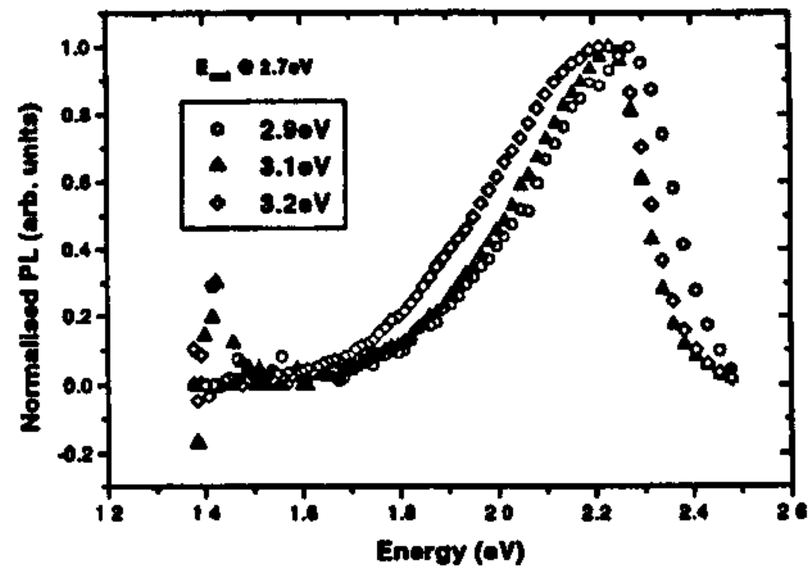

(d) The PL spectra collected for 2.7eV excitations.

Figure 3.14: The normalised PL spectra collected from films having varying band gaps, for different excitation energies are plotted. Interestingly, as the band gap of the film increases the peak energy of the spectrum moves towards lower energies for the same energy of excitation.

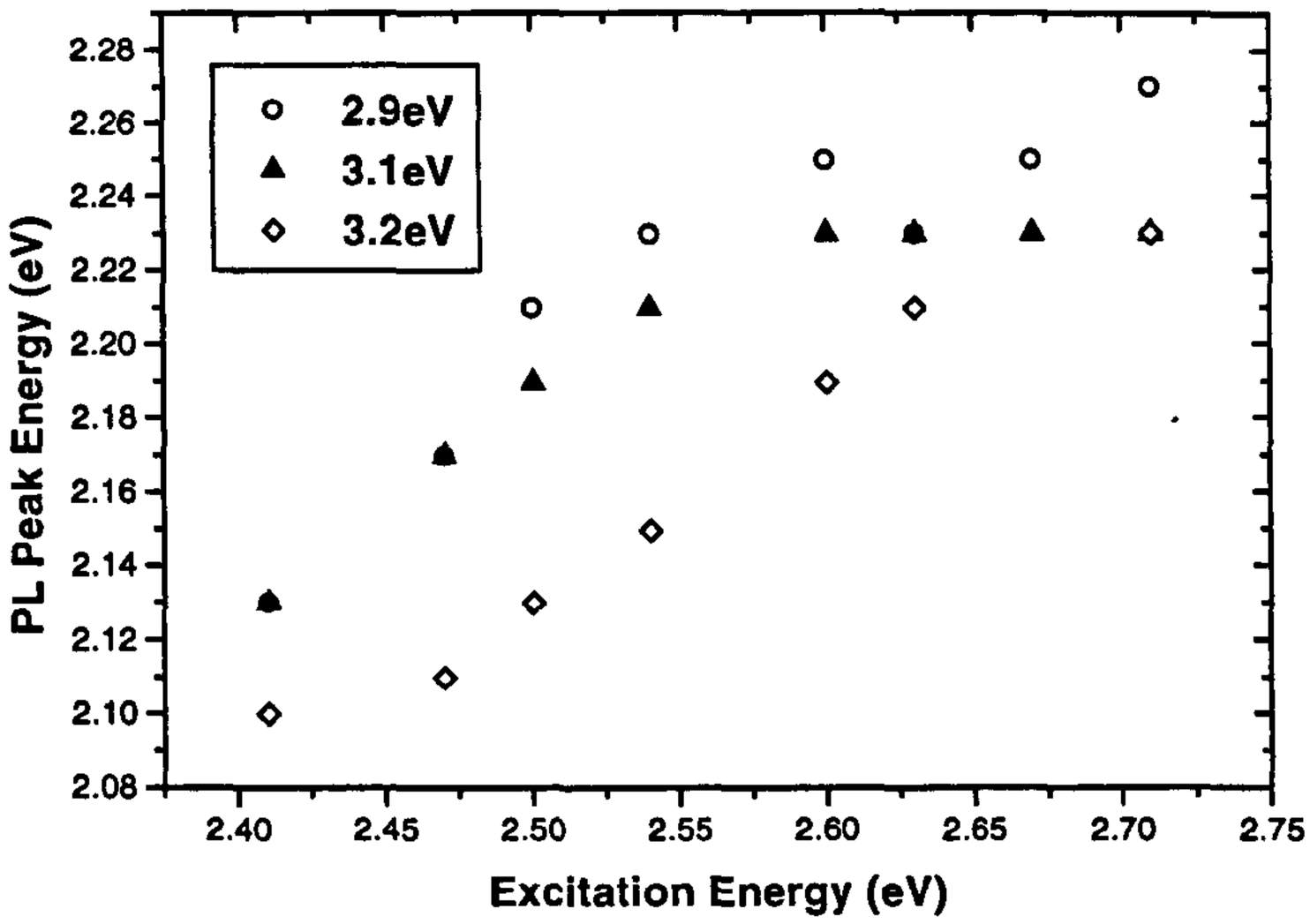

Figure 3.15: The peak position of the composite PL envelope is plotted against the energy of excitation for different Tauc gaps. As expected the peak energy moves towards higher values as the excitation energy is increased. However as the Tauc gap of the film increases the energy at which peak occurs becomes smaller at the same energy of excitation.

The peak intensity decay over time can be fitted into the expression,

$$I = I_\infty + I_0 \exp\left(-\frac{t}{t_0}\right) \tag{3.17}$$

where I_∞ - steady state intensity, I_0 - decay height and t_0 - decay time constant, and gives an exponential decay with a decay factor of 15.77 as shown in Fig. 3.16. The real origin of this phenomenon is not known yet. Nevertheless the information gathered is useful in assessing the long term reliability of a-C:H:N as an optical material.

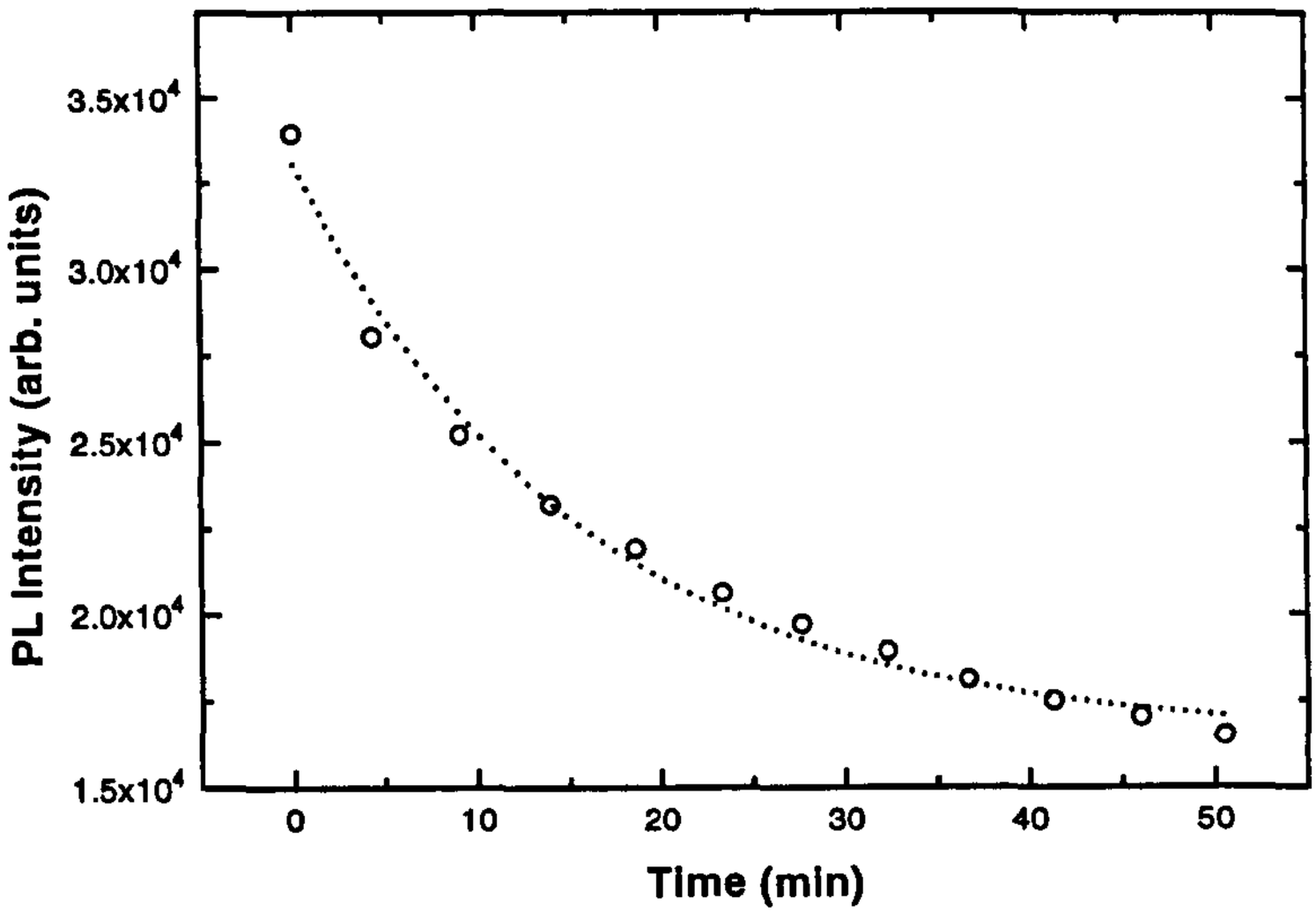

Figure 3.16: The PL intensity decays exponentially with time under prolong exposure to exciting laser beam.

3.4.6 Electric-Field Quenching of PL

An electric field was applied across an Au/a-C:H:N/ITO structure while the PL spectra were collected. The excitation was coupled through the ITO electrode which is transparent to excitation wavelengths. As applied electric field decreases from $7.5\text{V}\mu\text{m}^{-1}$ to no applied electric field, the PL intensity also reduces as seen in Fig. 3.17. However the plot of PL intensity vs. time shows that the decay rate is slower (Fig. 3.18) with applied electric field.

A decay in PL intensity was seen for both incremental and decremental applied electric fields. This observation can be attributed to the PL fatigue in the film. The absence of significant electric field quenching indicates that the origin of PL in a-C:H:N is from bound carriers (excitonic type) and that the photo excited carriers do not dissociate easily even at electric fields as high as $7.5\text{V}\mu\text{m}^{-1}$. The absence of photo-conductivity also confirms this.

Taking the change in PL peak intensity to be fatigue dominated, the curve

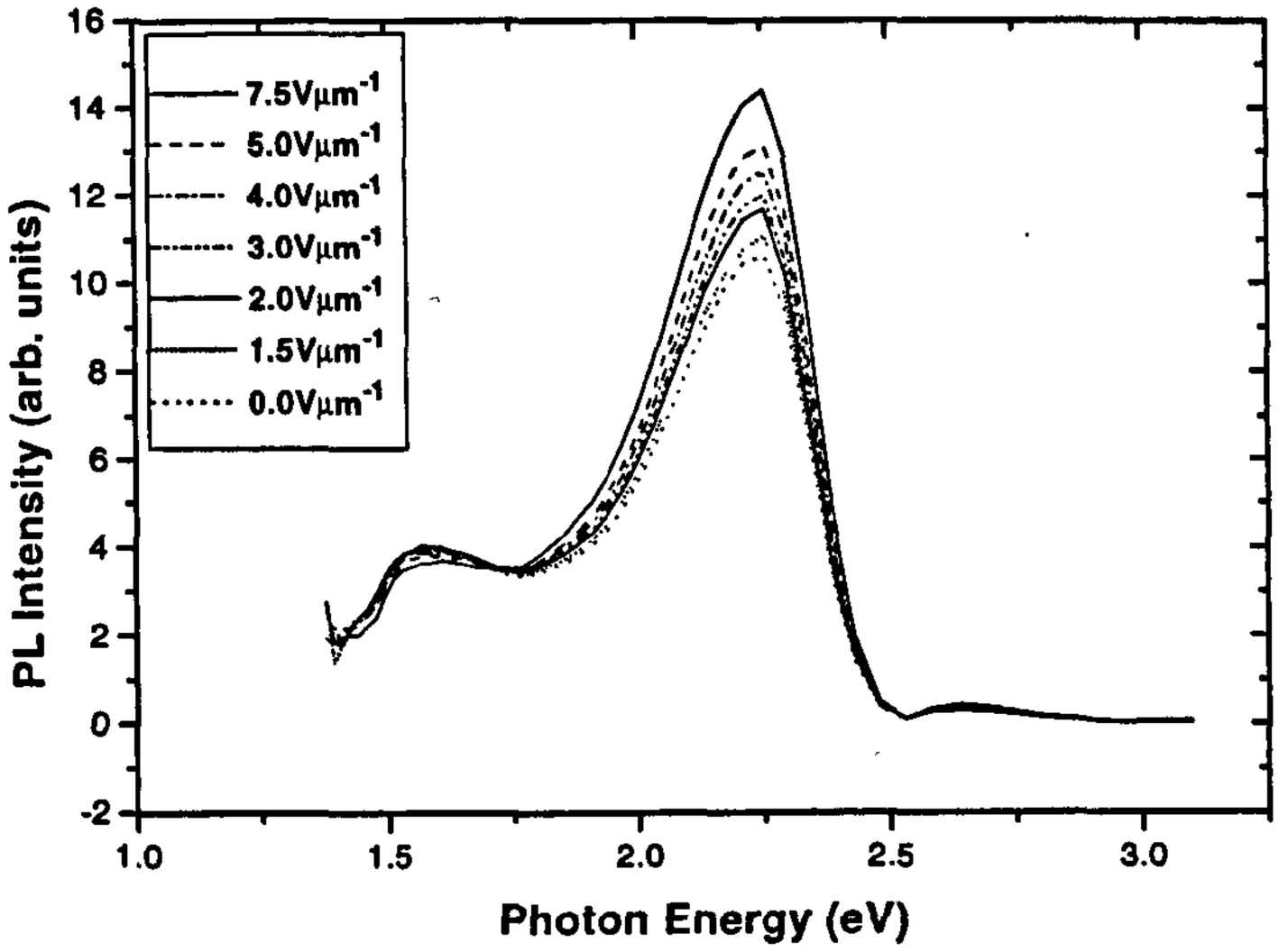

Figure 3.17: As the electric field applied across Au/a-C:H:N/ITO structure reduces, the intensity of the PL spectra decreases.

fitted to expression 3.17 is shown in Fig. 3.18. Here the rate of decay has dropped as indicated by a larger time constant (72.98) compared to 15.77 in Fig. 3.16 for the case with no applied field.

3.4.7 Conclusions

In this section we have studied the effect of nitrogen on photoluminescence in a-C:H:N. In particular it is suggested that the apparent shift in the PL peak and the broadening of the PL peak with nitrogen content is due to increased intensity from nitrogen associated recombination centres lying deeper in the band-gap. The red-shift of the PL peak seen with increasing band gap also supports this view. The fact that the spectral width of the PL sub-peak associated with N does not change as the N content is increased up to the saturation value, also points to the N states associated with this centre being very strongly localised. We conclude that PL is a very sensitive measurement of the relative changes in DOS

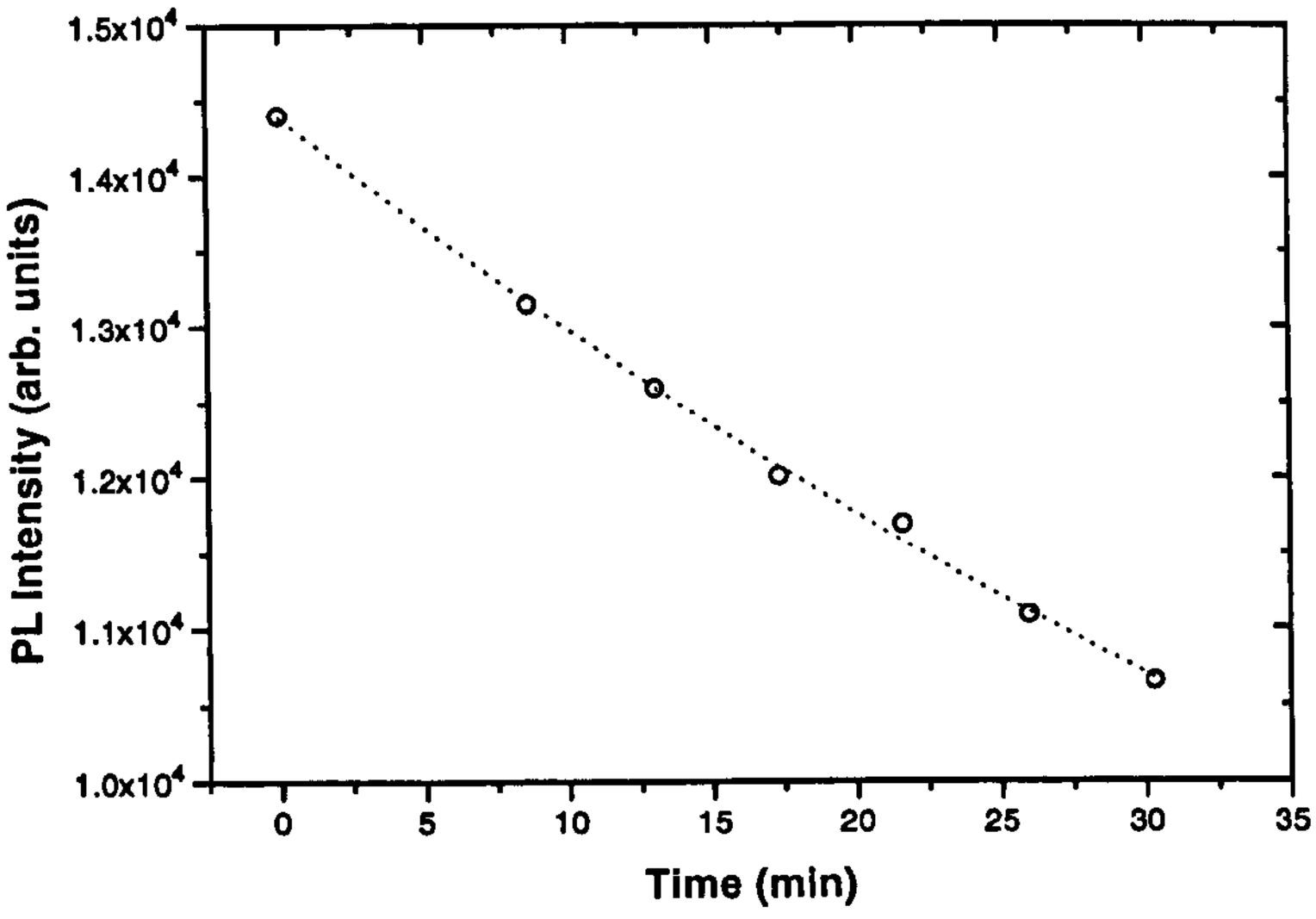

Figure 3.18: The decay of PL intensity with reduction in applied electric field is at a slower rate (a decay rate of 72.98) than in Fig. 3.16.

of a-C:H due to inclusion of N compared to conventional optical absorption.

Chapter 4

Helicon System

4.1 Introduction

Plasma processes play a major role in industrial applications such as thin film deposition, etching and laser generation. In general such processes involve the collision between energetic ions or electrons with neutral particles to form reactive chemical species. To obtain desired results from plasma processing, careful control of parameters such as particle energy, impinging velocity and flux density etc. at the substrate is necessary. Unfortunately most plasma reactors are prone to instabilities if not monitored properly. Radio Frequency (RF) gas discharges are popular where the stability of the plasma is important. In general such reactors are either capacitively coupled or inductively coupled, resulting in rather broad ion energy distribution. Resonant excitations formed by launching of circular polarised electro-magnetic waves into the plasma via a specially designed antenna in the presence of an axial magnetic field, produces energetic plasma species with a selective narrow energy distribution. Such excitations are due to attenuation of helicon waves by Landau damping in the plasma [146, 147, 148]. Landau damping has been used for Ar ion laser excitation [148] and for silicon plasma excitation [149]. Ganguli *et. al.* have reported Ar plasma generated in a microwave discharge by Landau damping [150].

Nitrogen plasma is commonly generated by passing a current in a gas column, especially for nitrogen laser applications [151][152]. The optical cavity poisoning

due to electrode evaporation and the excessive heat dissipation in the vacuum tube wall by diffused plasma can lead to an unstable system. An electrodeless, confined plasma system can improve the performance of such a system. In this chapter the helicon wave excitation of nitrogen in particular and selective excitation of carbon species are discussed. The helicon wave generated plasma is compared with a conventional inductively coupled RF plasma, and the results observed are compared with theoretical predictions.

4.2 Helicon Wave Theory

A low frequency electro-magnetic wave which propagates in a highly conducting medium such as a metal at low temperature or in a gas discharged plasma in the presence of a strong magnetic field, was first named a helicon in 1960 by Aigrain [153]. In the presence of a wave field, the static magnetic field lines due to a separate source which were initially straight become helical. Such waves are found in the frequency range between electron and ion cyclotron frequencies and are known as high frequency Alfven waves or as low frequency whistler waves - named after the pitch falling audio frequency observed in ionospheric studies [146].

4.2.1 Electro-magnetic waves that propagate parallel to magnetic field

Say $\vec{B}_0$ is along z which is the direction of propagation of the wave and the electric field components of the electro-magnetic wave are on the $x-y$ plane. Such waves satisfy Maxwell's equations,

$$\begin{aligned} \vec{\nabla} \times \vec{E} &= -\frac{\partial \vec{B}}{\partial t} \\ \vec{\nabla} \times \vec{B} &= \mu_0 \vec{\vec{J}} + \mu_0 \frac{\partial \vec{D}}{\partial t} \end{aligned} \tag{4.1}$$

Ohm's law for a cold uniform plasma when $N = n_0$ and $q_e = -e$,

$$\vec{E} = \frac{1}{en_0}\vec{J} \times \vec{B} \tag{4.2}$$

When we solve equations 4.1 and 4.2, considering a medium such as plasma, for solutions of the form $e^{i(\vec{k}\cdot\vec{r} - \omega t)}$, we have, the wave equation [154],

$$-\vec{k}(\vec{k} \cdot \vec{E}_1) + k^2\vec{E}_1 = \frac{4\pi i\omega}{c^2}\vec{J}_1 + \frac{\omega^2}{c^2}\vec{E}_1 \tag{4.3}$$

Let us say $\hat{x}$, $\hat{y}$ and $\hat{z}$ are unit vectors in x,y and z directions, respectively. Since the wave propagates along z direction the propagation constant $\vec{k} = k\hat{z}$. And the composite electric field $\vec{E}_1$ in the $x - y$ plane is given by,

$$\vec{E}_1 = E_x\hat{x} + E_y\hat{y} \tag{4.4}$$

The linearised equation of motion for electrons when $kT_e \approx 0$ is,

$$-im\omega\vec{\nu}_{e1} = -e(\vec{E} + \vec{\nu}_{e1} \times \vec{B}_0) \tag{4.5}$$

Now we obtain nontrivial components on x and y given by,

$$\begin{aligned} \nu_x &= -\frac{ie}{m\omega}(E_x + \nu_y B_0) \\ \nu_y &= -\frac{ie}{m\omega}(E_y - \nu_x B_0) \end{aligned} \tag{4.6}$$

The general solutions for ν_x and ν_y in the simultaneous equation system 4.6 are,

$$\begin{aligned} \nu_x &= \frac{e}{m\omega}\left(-iE_x - \frac{\omega_c}{\omega}E_y\right)\left(1 - \frac{\omega_c^2}{\omega^2}\right)^{-1} \\ \nu_y &= \frac{e}{m\omega}\left(-iE_y - \frac{\omega_c}{\omega}E_x\right)\left(1 - \frac{\omega_c^2}{\omega^2}\right)^{-1} \end{aligned} \tag{4.7}$$

where $\omega_c = eB/m$. Since $\vec{k}$ and $\vec{E}_1$ are mutually orthogonal vectors, $\vec{k}\cdot\vec{E}_1 \rightarrow 0$, the wave equation given in 4.3 takes the form,

$$(\omega^2 - c^2k^2)\vec{E}_1 = -4\pi i\omega\vec{J}_1 = 4\pi i n_0 \omega e\vec{\nu}_{e1} \tag{4.8}$$

We can obtain components in x and y from equations 4.7 and 4.8,

$$\begin{aligned}(\omega^2 - c^2k^2)E_x &= \frac{\omega_p^2}{1-\omega_c^2/\omega^2}\left(E_x - \frac{i\omega_c}{\omega}E_y\right)\\ (\omega^2 - c^2k^2)E_y &= \frac{\omega_p^2}{1-\omega_c^2/\omega^2}\left(E_y - \frac{i\omega_c}{\omega}E_x\right)\end{aligned} \tag{4.9}$$

where $\omega_p = \sqrt{\frac{n_0 e^2}{\epsilon_0 m}}$. Now we define,

$$\alpha \equiv \frac{\omega_p^2}{1-(\omega_c^2/\omega^2)} \tag{4.10}$$

With the definition 4.10 in the set of components in 4.9, the coupled equations for E_x and E_y are given by,

$$\begin{aligned}(\omega^2 - c^2k^2 - \alpha)E_x + i\alpha\frac{\omega_c}{\omega}E_y &= 0\\ (\omega^2 - c^2k^2 - \alpha)E_y + i\alpha\frac{\omega_c}{\omega}E_x &= 0\end{aligned} \tag{4.11}$$

By making the determinant of the coefficient zero, we have,

$$(\omega^2 - c^2k^2 - \alpha)^2 = \left(\alpha\frac{\omega_c}{\omega}\right)^2 \tag{4.12}$$

Hence,

$$\omega^2 - c^2k^2 - \alpha = \pm\alpha\frac{\omega_c}{\omega} \tag{4.13}$$

Now we have,

$$\begin{aligned}\omega^2 - c^2k^2 &= \alpha\left(1 \pm \frac{\omega_c}{\omega}\right) = \frac{\omega_p^2}{1-(\omega_c^2/\omega^2)}\left(1 \pm \frac{\omega_c}{\omega}\right)\\ &= \omega_p^2\frac{1 \pm (\omega_c/\omega)}{[1+(\omega_c/\omega)][1-(\omega_c/\omega)]} = \frac{\omega_p^2}{1 \mp (\omega_c/\omega)}\end{aligned} \tag{4.14}$$

The presence of $\pm$ sign in the end result indicates that there are two possible solutions for the equation set given in 4.11 giving rise to two distinct wave types that can propagate along $\vec{\mathbf{B}}_\mathbf{0}$. The corresponding dispersion relations are given by,

$$\tilde{n}^2 = \frac{c^2k^2}{\omega^2} = 1 - \frac{\omega_p^2/\omega^2}{1-(\omega_c/\omega)} \tag{4.15}$$

which is associated with a *right-hand circularly polarised* wave propagating along $\vec{\mathbf{B}}_\mathbf{0}$. Right hand circular polarisation means, the electric field vector of the electro-magnetic wave that propagates along $\vec{\mathbf{B}}_\mathbf{0}$ rotates in a clockwise sense in time as viewed along the direction of $\vec{\mathbf{B}}_\mathbf{0}$. Likewise there is a similar wave which is *left- hand circularly polarised* given by,

$$\tilde{n}^2 = \frac{c^2k^2}{\omega^2} = 1 - \frac{\omega_p^2/\omega^2}{1+(\omega_c/\omega)} \tag{4.16}$$

The cutoffs are obtained by setting $k = 0$ in eqs. 4.15, 4.16.

Thus,

$$\omega^2 \mp \omega\omega_c - \omega_p^2 = 0 \tag{4.17}$$

Each of the two signs will give a different cutoff frequency corresponds to right-hand and left-hand circular polarised waves. The roots are,

$$\begin{aligned} \omega_R &= \frac{1}{2}\left(\omega_c + \sqrt{\omega_c^2 + 4\omega_p^2}\right) \\ \omega_L &= \frac{1}{2}\left(-\omega_c + \sqrt{\omega_c^2 + 4\omega_p^2}\right) \end{aligned} \tag{4.18}$$

The cutoff and resonance frequencies divide the dispersion diagram into regions of propagation and nonpropagation. For $\omega > \omega_L$, the left-hand circular polarised wave propagates such that $\vec{u}_\phi > c$. However, the left-hand circular wave does not propagate in the low frequency regime. Similarly, when $\omega > \omega_R$, a right-hand circular polarised wave propagates for $\vec{u}_\phi > c$. When $\omega = \omega_c$, k becomes infinite as seen in 4.15. In other words the right-hand circular polarised wave is in resonance with the cyclotron motion of the electrons in the plasma

when $\omega = \omega_c$. The sense of rotation of the plane of polarisation is the same as that of the gyration of electrons. When this mode is in action, the wave loses energy by means of continuously accelerating electrons in the plasma. Since the wave is in lossy mode, it is not in a position to propagate along. For frequencies $\omega < \omega_c$, there is a propagating band such that $\vec{u}_\phi < c$. A propagating wave in this low frequency regime is called a *whistler wave*. However, as seen in expression 4.16 there is no resonance for positive ω in left-hand circular polarised waves. There is no propagating wave of this kind for $\vec{u}_\phi < c$. Helicon waves are essentially right-hand circularly polarised waves governed by 4.15.

4.3 Collision-less Plasma Excitations via Landau Damping

In order to derive the dispersion relation for electron plasma oscillations in the zeroth order, we assume a uniform plasma with distribution $f_0(\vec{v})$, and let $\vec{B}_0 = \vec{E}_0 = 0$. The first order perturbation in $f(\vec{r}, \vec{v}, t)$ by $f_1(\vec{r}, \vec{v}, t)$,

$$f(\vec{r}, \vec{v}, t) = f_0(\vec{v}) + f_1(\vec{r}, \vec{v}, t) \tag{4.19}$$

Since $\vec{v}$ is an independent variable not to be linearised, the first order Vlasov equation for electrons is [154],

$$\frac{\partial f_1}{\partial t} + \vec{v} \cdot \vec{\nabla} f_1 - \frac{e}{m} \vec{E}_1 \cdot \frac{\partial f_0}{\partial \vec{v}} = 0 \tag{4.20}$$

Since ions are large we can assume that they are stationary and that the waves in motion are plane waves in the x direction,

$$f_1 \propto e^{i(kx - \omega t)} \tag{4.21}$$

With that, equation 4.20 becomes,

$$-i\omega f_1 + ik\nu_x f_1 = \frac{e}{m} E_x \frac{\partial f_0}{\partial \nu_x}$$

(4.22)

$$f_1 = \frac{ieE_x}{m}\frac{\partial f_0/\partial x}{\omega - k\nu_x}$$

In the unperturbated plasma, all electrons have the velocity ν_0, and the contour of constant f is a straight line. The electric field $\vec{E}_1$ causes electrons to develop a sinusoidal ripple, which travels at the phase velocity, not the particle velocity. Particles stay on the curve as they move relative to the wave. Poisson's equation gives,

$$\vec{\nabla} \cdot \vec{E}_1 = ikE_x = -4\pi e n_1 = -4\pi e \int\int\int f_1 \, d^3\nu \tag{4.23}$$

Substituting for f_1 from 4.22, we have,

$$1 = -\frac{4\pi e^2}{km}\int\int\int \frac{\partial f_0/\partial x}{\omega - k\nu_x}\, d^3\nu \tag{4.24}$$

A factor n_0 can be factored out when f_0 is replaced by a normalised function $\hat{f}_0$,

$$1 = -\frac{\omega_p^2}{k}\int_{-\infty}^{\infty} d\nu_z \int_{-\infty}^{\infty} d\nu_y \int_{-\infty}^{\infty} \frac{\partial \hat{f}_0(\nu_x,\nu_y,\nu_z)/\partial x}{\omega - k\nu_x}\, d\nu_x \tag{4.25}$$

If f_0 is a Maxwellian or some other factorable distribution, the integration over ν_y and ν_z can be carried out. Say, the remaining one dimensional distribution $\hat{f}_0(\nu_x)$ is a Maxwellian of the form,

$$\hat{f}_m(\nu_x) = \sqrt{\frac{m}{2\pi kT}}\, e^{-\frac{m\nu_x^2}{2kT}} \tag{4.26}$$

The dispersion relation is now,

$$1 = \frac{\omega_p^2}{k^2}\int_{-\infty}^{\infty} \frac{\partial \hat{f}_0(\nu_x)/\partial \nu_x}{\nu_x - (\omega/k)}\, d\nu_x \tag{4.27}$$

For the general one-dimensional case,

$$1 = \frac{\omega_p^2}{k^2}\int_{-\infty}^{\infty} \frac{\partial \hat{f}_0/\partial \nu}{\nu - (\omega/k)}\, d\nu \tag{4.28}$$

For any equilibrium distribution of $\hat{f}_0$ the equation 4.28 holds. If $\hat{f}_0$ is a Maxwellian distribution, then equation 4.26 has to be used.

Since in practice ω is almost never real, waves are usually slightly damped by collisions or are amplified by some instability mechanism, and the velocity ν in the denominator of equation 4.28 is a real quantity, the denominator never vanishes. It appears that the singularity at $\nu = \omega/k$ has no effect on the integration. But Landau was the first to point out that even if it lies off the path of the integral, its presence introduces a significant modification to the plasma wave dispersion relation. This was never predicted by the fluid theory.

To evaluate the integral consider a plasma given a sinusoidal perturbation so that k is real. When the perturbation grows or decays, ω is complex. If we take equation 4.28 as a contour integral in complex plane ν, then we have an unstable wave with $Im(\omega) > 0$ and a damped wave with $Im(\omega) < 0$. Applying the residue theorem,

$$\int_{C_1} G\, d\nu + \int_{C_2} G\, d\nu = 2\pi i R(\omega/k) \tag{4.29}$$

where G is the integrand, C_1 is the path along the real axis, C_2 is the semicircle at infinity and $R(\omega/k)$ is the residue at ω/k. Since C_2 does not vanish for a Maxwellian distribution, the contribution from C_2 cannot be neglected. As Landau showed when curve C_1 passes below the singularity the problem can be treated as an initial value problem properly. Since the analysis is complicated, we find the approximate solution when there is large phase velocity and weak damping. Now the contour becomes a straight line along the $Re(\nu)$ axis with a small semicircle around the pole at ω/k which lies near the real axis. The equation 4.28 becomes,

$$1 = \frac{\omega_p^2}{k^2}\left[P\int_{-\infty}^{\infty}\frac{\partial \hat{f}_0/\partial\nu}{\nu-(\omega/k)}\,d\nu + i\pi\left.\frac{\partial \hat{f}_0}{\partial\nu}\right|_{\nu=\frac{\omega}{k}}\right] \tag{4.30}$$

where P stands for the Cauchy principal value. When phase velocity $\nu_\phi = \omega/k$ is sufficiently large the contribution from the neglected part of the contour becomes small since $\hat{f}_0$ and $\partial\hat{f}_0/\partial\nu$ are also very small. And the integral, can now be evaluated partially,

$$\int_{-\infty}^{\infty} \frac{\partial \hat{f}_0}{\partial \nu} \frac{d\nu}{\nu - \nu_\phi} = \left[\frac{\hat{f}_0}{\nu - \nu_\phi}\right]_{-\infty}^{\infty} - \int_{-\infty}^{\infty} \frac{-\hat{f}_0 d\nu}{(\nu - \nu_\phi)^2} = \int_{-\infty}^{\infty} \frac{\hat{f}_0 d\nu}{(\nu - \nu_\phi)^2} \tag{4.31}$$

Since this is an average over the distribution, the real part of the dispersion relation is,

$$1 = \frac{\omega_p^2}{k^2} \overline{(\nu - \nu_\phi)^{-2}} \tag{4.32}$$

Given the fact that $\nu_\phi \gg \nu$ and the averaged expression of $(\nu - \nu_\phi)^{-2}$ has no odd terms, hence,

$$\overline{(\nu - \nu_\phi)^{-2}} \approx \nu_\phi^{-2} \left(1 + \frac{3\bar{\nu}^2}{\nu_\phi^2}\right) \tag{4.33}$$

For $\hat{f}_0$ of Maxwellian, the evaluation of $\bar{\nu}^2$ given that ν here is really a ν_x,

$$\frac{1}{2} m \bar{\nu}_x^2 = \frac{1}{2} k T_e \tag{4.34}$$

The dispersion relation for a system with one degree of freedom becomes,

$$\begin{aligned} 1 &= \frac{\omega_p^2}{k^2} \frac{k^2}{\omega^2} \left(1 + 3 \frac{k^2}{\omega^2} \frac{kT_e}{m}\right) \\ \omega^2 &= \omega_p^2 + \frac{\omega_p^2}{\omega^2} \frac{3kT_e}{m} k^2 \end{aligned} \tag{4.35}$$

When thermal correction is small, $\omega^2 \approx \omega_p^2$, hence we have,

$$\omega^2 = \omega_p^2 + \frac{3kT_e}{m} k^2 \tag{4.36}$$

In evaluating the imaginary part of equation 4.30, still the approximation $\omega^2 \approx \omega_p^2$ for real part holds. From equations 4.31 and 4.33 the principal value of the integral becomes $\approx k^2/\omega^2$. Now 4.30 becomes,

$$1 = \frac{\omega_p^2}{\omega^2} + i\pi \frac{\omega_p^2}{k^2} \left.\frac{\partial \hat{f}_0}{\partial \nu}\right|_{\nu = \nu_\phi}$$

$$\omega^2 \left(1 - i\pi \frac{\omega_p^2}{k^2} \left[\frac{\partial \hat{f}_0}{\partial \nu}\right]_{\nu=\nu_\phi}\right) = \omega_p^2 \tag{4.37}$$

Taking imaginary part to be small and square root by Taylor series expansion gives,

$$\omega = \omega_p \left(1 + i\frac{\pi}{2}\frac{\omega_p^2}{k^2} \left[\frac{\partial \hat{f}_0}{\partial \nu}\right]_{\nu=\nu_\phi}\right) \tag{4.38}$$

For $\hat{f}_0$ of a one-dimensional Maxwellian, we have,

$$\frac{\partial \hat{f}_0}{\partial \nu} = (\pi \nu_{th}^2)^{-1/2} \left(\frac{-2\nu}{\nu_{th}^2}\right) \exp\left(\frac{-\nu^2}{\nu_{th}^2}\right) = -\frac{2\nu}{\sqrt{\pi}\nu_{th}^3} \exp\left(\frac{-\nu^2}{\nu_{th}^2}\right) \tag{4.39}$$

The term ν_ϕ in the coefficient can be approximated by ω_p/k, but not in the exponent. From eqs. 4.38 and 4.39, we have the imaginary part of ω,

$$\begin{aligned} Im(\omega) &= -\frac{\pi}{2}\frac{\omega_p^3}{k^2}\frac{2\omega_p}{k\sqrt{\pi}}\frac{1}{\nu_{th}^3} \exp\left(\frac{-\omega^2}{k^2\nu_{th}^2}\right) \\ &= -\sqrt{\pi}\omega_p \left(\frac{\omega_p}{k\nu_{th}}\right)^3 \exp\left(\frac{-\omega^2}{k^2\nu_{th}^2}\right) \exp\left(\frac{-3}{2}\right) \end{aligned} \tag{4.40}$$

$$Im\left(\frac{\omega}{\omega_P}\right) = -0.22\sqrt{\pi} \left(\frac{\omega_p}{k\nu_{th}}\right)^3 \exp\left(\frac{-1}{2k^2\lambda_D^2}\right) \tag{4.41}$$

The negative $Im(\omega)$ indicates a collisionless damping of the plasma wave. This is called Landau damping. It is clear from expression 4.41 that this kind of damping is small when $k\lambda_D$ is small.

4.4 Instrumental set up of Helicon Wave Excited Plasma system

The schematic diagram of the helicon wave experimental set up is shown in Fig. 4.1. The plasma was generated in a 7cm diameter pyrex glass tube. In

the helicon wave excited reactor, RF power at 13. 56MHz is fed via a water cooled double loop helicon antenna placed inside the axial electromagnet. The RF power supply is capable of delivering up to 3kW. The DC magnetic field up to 0. 13T can be applied.

4.4.1 Introduction

There can be a right-hand circular polarised electro-magnetic wave launched into the plasma column in the presence of a DC axial magnetic field having a direction of propagation along the magnetic field, provided that the condition $\omega < \omega_c$ is preserved as discussed at length in section 4.2. One of the most astonishing features of plasma waves is the ability of a charged particle to exchange energy without any collision via wave interactions as first pointed out by Landau mathematically. When the imaginary part of ω is kept negative, the wave starts to lose energy into plasma. In effect the plasma gains energy without any collisions present in the medium. This phenomenon is called Landau damping, as described in section 4.3 mathematically.

The *cyclotron frequency* of an electron is given by,

$$f_c = \frac{1}{2\pi}\frac{e\vec{B}_0}{m_e} \tag{4.42}$$

where e - electron charge, $\vec{B}_0$ - magnetic field density and m_e - electron mass.

The cyclotron frequency was found to be $1.18GHz$ when a magnetic field of 42mT is present. If the plasma is excited by a RF power operated at $13.56MHz$, obviously the condition $\omega < \omega_c$ is met. It was reported previously that when the frequency of RF excitation is close to the *lower hybrid frequency* given by,

$$f_L = \frac{1}{2\pi}\sqrt{\Omega_c\omega_c} = \frac{1}{2\pi}\frac{e\vec{B}_0}{\sqrt{m_i m_e}} \tag{4.43}$$

where m_i - mass of the ion.

of the system, the energy transfer of RF coupling is in resonance [155]. If we take the excitation of N_2^*, the necessary condition is to maintain N_2^+ ions at their lower threshold energy of ≈16eV. Then the lower hybrid frequency of the

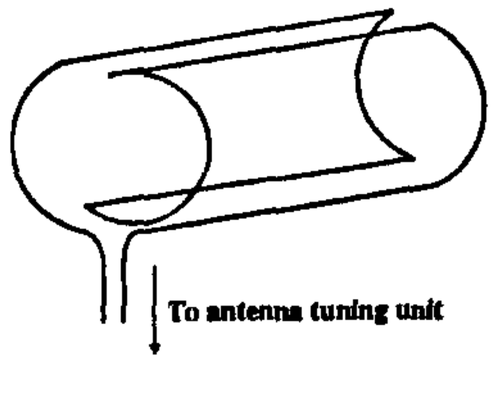

(a)

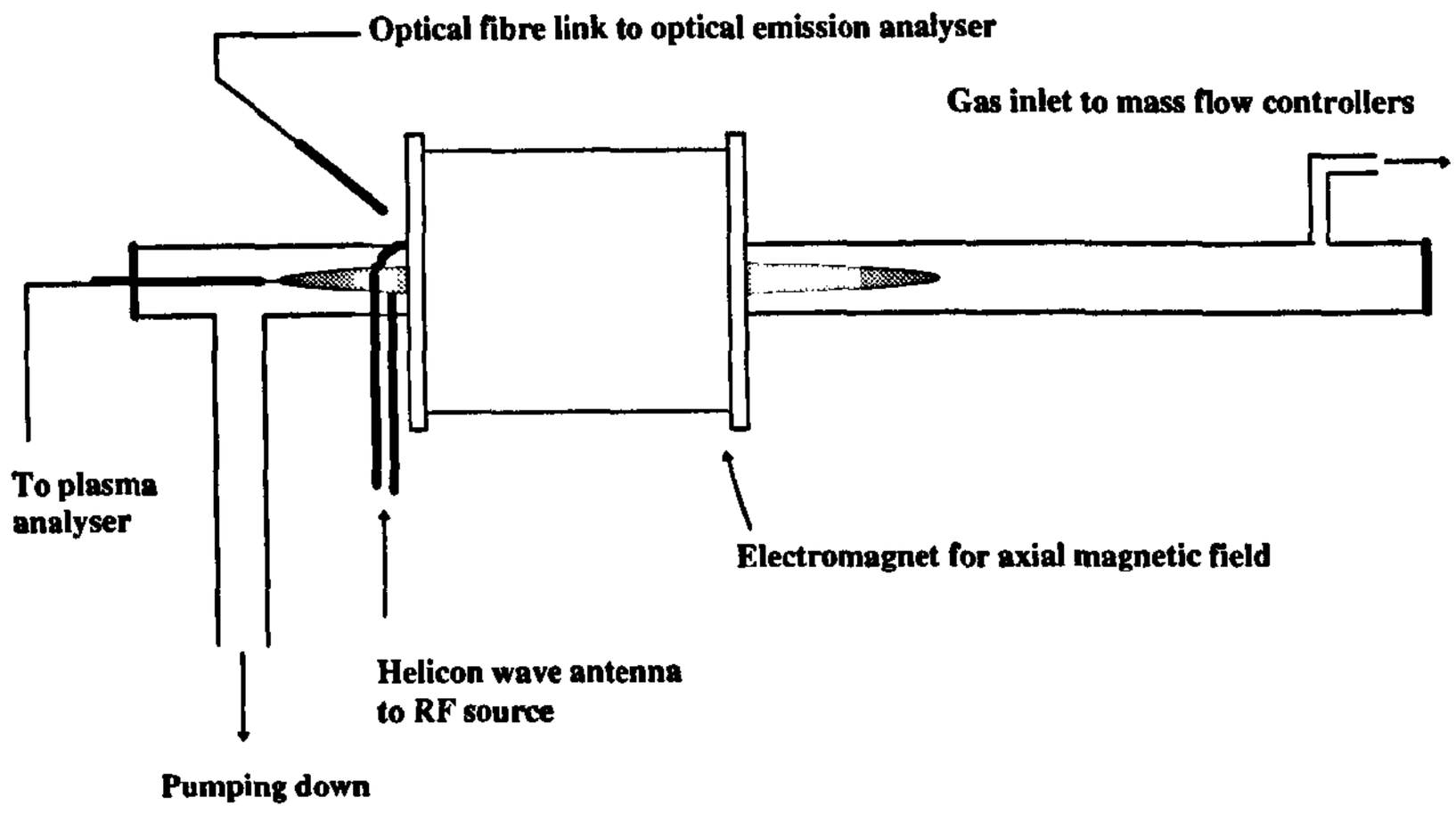

(b)

Figure 4.1: Schematic Diagram of the Helicon Wave Excited Plasma System. RF power is fed into plasma tube via double loop helicon antenna (a) which is inside the axial electromagnet.

system becomes 5.2MHz, making it necessary to have additional RF tuning to couple RF power at 13.56MHz.

Now we will look at how a plasma system capable of maintaining resonance excitations in a nitrogen plasma via Landau damping is practically implemented and the experimental observations made. The effect of resonance excitations in nitrogen on a-C:H:N films deposited is also studied.

4.4.2 RF Antenna Design

To sustain excitation from $X^1\Sigma_g^+$ to $C^3\Pi_u$ in N_2^*, it is necessary to maintain N_2^+ in $X^2\Sigma_g^+$ at its energy threshold of $\approx$16eV [156]. Now we have,

$$\Delta E_{ion} = 16eV$$

When helicon waves are in resonance such that the *energy equivalent* of the phase velocity is equal to the above energy, then

$$\Delta E_{ion} = \frac{1}{2} m_e \vec{u}_\phi^2$$

where $\vec{u}_\phi$ is the phase velocity of the plasma wave.

$$\vec{u}_\phi = \sqrt{\frac{2\Delta E_{ion}}{m_e}} = \sqrt{\frac{2 \times 1.6 \times 10^{-19} \times 16}{0.91 \times 10^{-30}}} = 2.37 \times 10^6 m\,\mathrm{sec}^{-1}$$

The phase velocity is related to the wave length by,

$$\vec{u}_\phi = f_0 \lambda_H$$

The corresponding *Helicon wavelength*

$$\lambda_H = \frac{\vec{u}_\phi}{f_0} = \frac{2.37 \times 10^6}{13.56 \times 10^6} = 17.47cm$$

An antenna having a length of multiples of $\frac{\lambda_H}{2}$ couples resonantly with the plasma wave.

4.4.3 Axial Electromagnets

The dispersion relation brings a link between the axial magnetic field and the antenna length, given by

$$\lambda_H \propto \sqrt{\frac{\vec{B}_0 a}{n f_0}}$$

where a - plasma radius and n - electron density.

For $n = 10^9 cm^{-3}$ the required magnetic field is 42mT.

The flux density of an electromagnet is given by,

$$B_{\beta_1\beta_2} = \frac{\mu \bar{n} I}{2}(\cos\beta_1 - \cos\beta_2)$$

where $\bar{n}$ - number of turns per unit length, I - current through the coil and $\beta_1 \& \beta_2$ - edge angles seen by the point of interest (see Fig. 4.2).

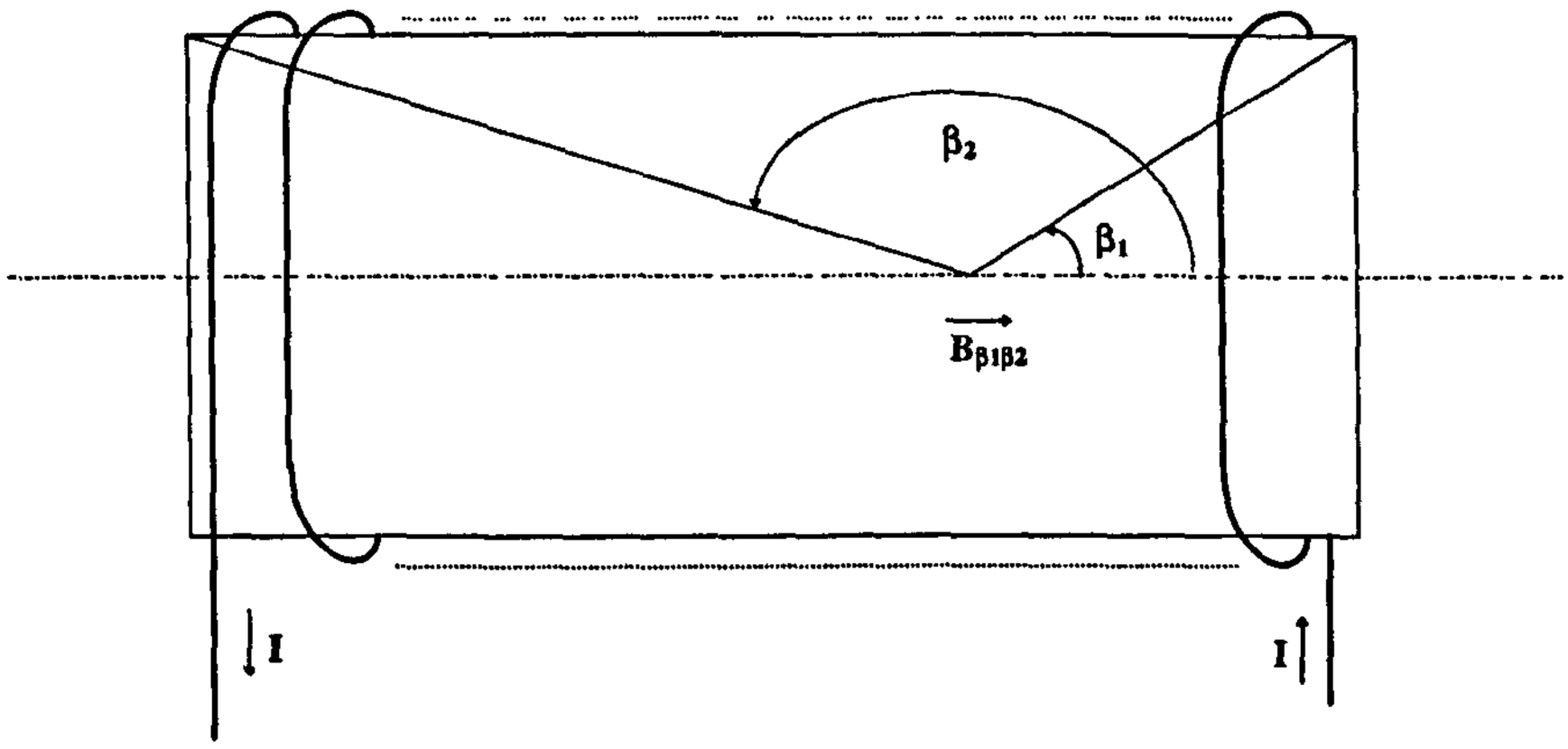

Figure 4.2: Schematic Diagram of an electromagnet. β_1 and β_2 are incident angles of edges of the coil with respect to the axis.

In a coil having a length of 300mm, outer diameter of 320mm and an inner diameter of 70mm, for 4600 turns, the average axial flux density per unit current is,

$$B_{ave} = \frac{4\pi \times 10^{-7} \times 4600}{2 \times 0.3}[\cos(31.6°) - \cos(180° - 31.6°)]$$

$$B_{ave} = 1.64 \times 10^{-2} T/A$$

An electromagnet capable of providing this field was fabricated, and had a resistance of 11Ω, the total power dissipation at the full current rating of 10A is therefore $1.1kW$. This amount of power dissipation makes it necessary to have an external cooling system (water or air).

4.4.4 Resonant Excitation of Nitrogen Plasma for 337.1nm Laser Emission

Generally, to initiate an excitation suitable for laser activity in nitrogen, a high density plasma with high electron temperature in the first few nanoseconds of the gaseous break down is necessary [157]. The main reason for the requirement of a hot dense plasma to reach laser excitations is that the energy band $C^3\Pi_u$ associated with an excited N_2^* having an energy threshold of 11.1eV is reached only via electron impact excitations (see Fig. 4.3). To generate such an impact electron in a suitable energy regime there must be sufficient N_2^+ ions at least at $X^2\Sigma_g^+$ which has an energy threshold of 15.6eV [156]. Usually this is achieved mainly by short duration DC discharges in N_2 gas, but with poor efficiency of excitation, restricting the laser operation only to pulse mode.

Figure 4.4 shows optical emission spectra collected from a N_2 plasma generated in the helicon wave reactor. When there is no DC magnetic field applied, the helicon wave antenna behaves as an inductively coupled RF electrode. However, in an inductively coupled system the RF electric field vector oscillates perpendicular to the major axis of the plasma chamber since the antenna is wound round the chamber. In this system which is excited with a helicon antenna the magnetic field vector is perpendicular.

As shown in figure 4.4(a), the emission line at 750nm, associated with $B^3\Pi_g$ to $A^3\Sigma_u^+$ transition in the N_2 *molecule* [158] and the emission at 868nm associated with $2s^22p^23p\ ^4D^0$ to $2s^22p^23s\ ^4P$ de-excitation in *atomic* N [159] can

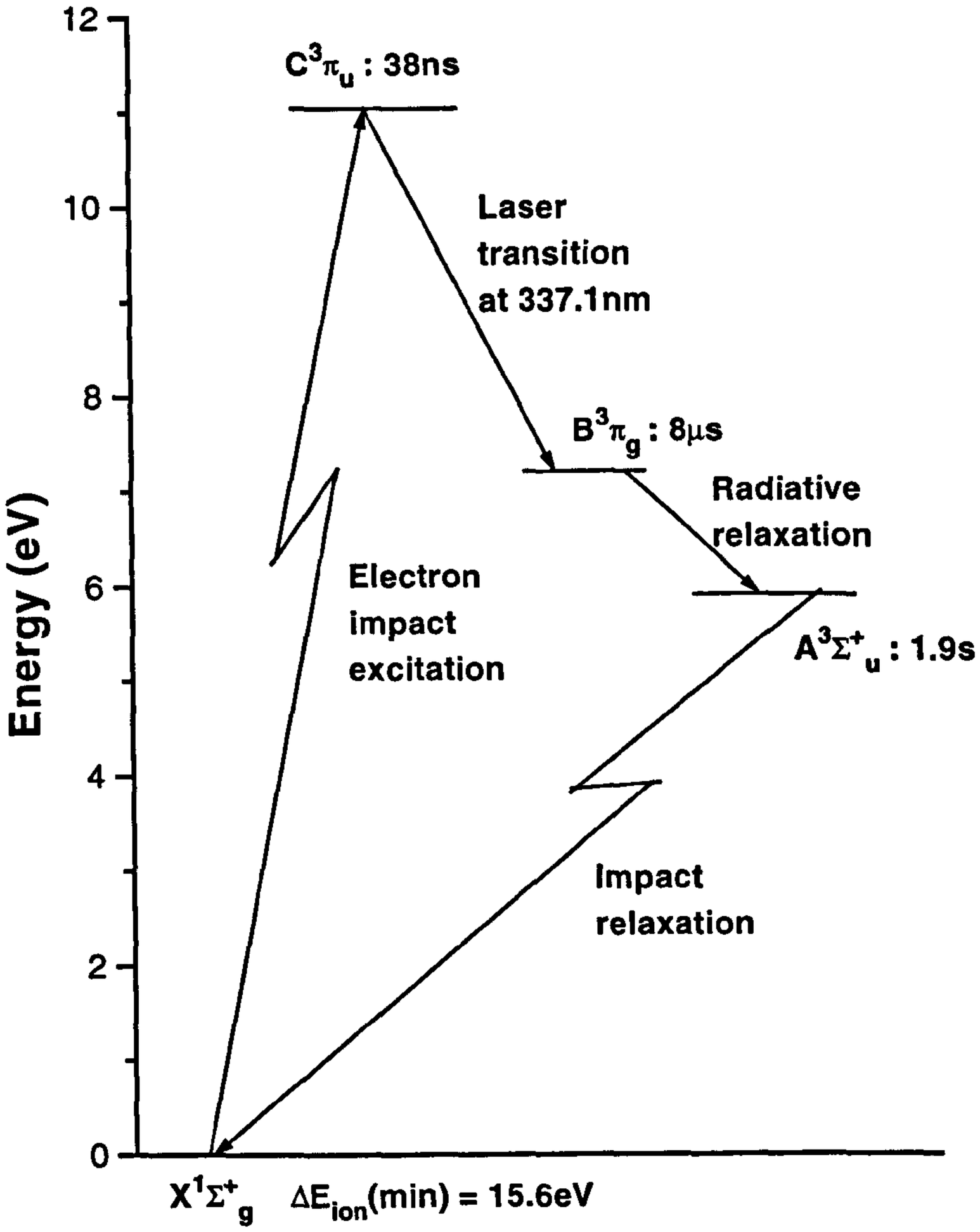

Figure 4.3: The energy transition diagram of N_2 plasma. The continuous excitation of N_2^* is restricted by the long life-time in energy level $A^3\Sigma_u^+$

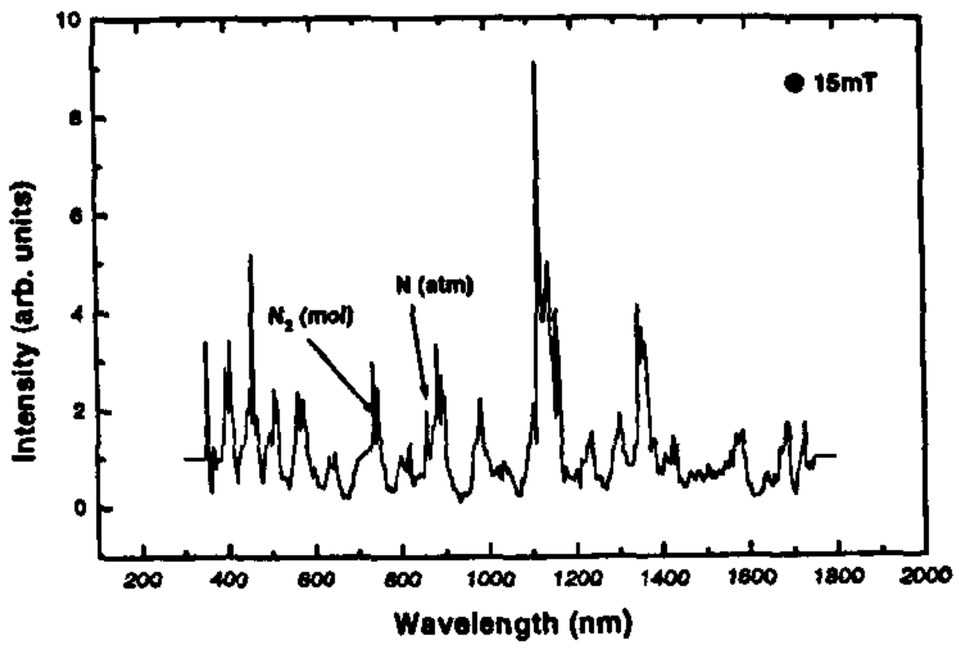

(a)

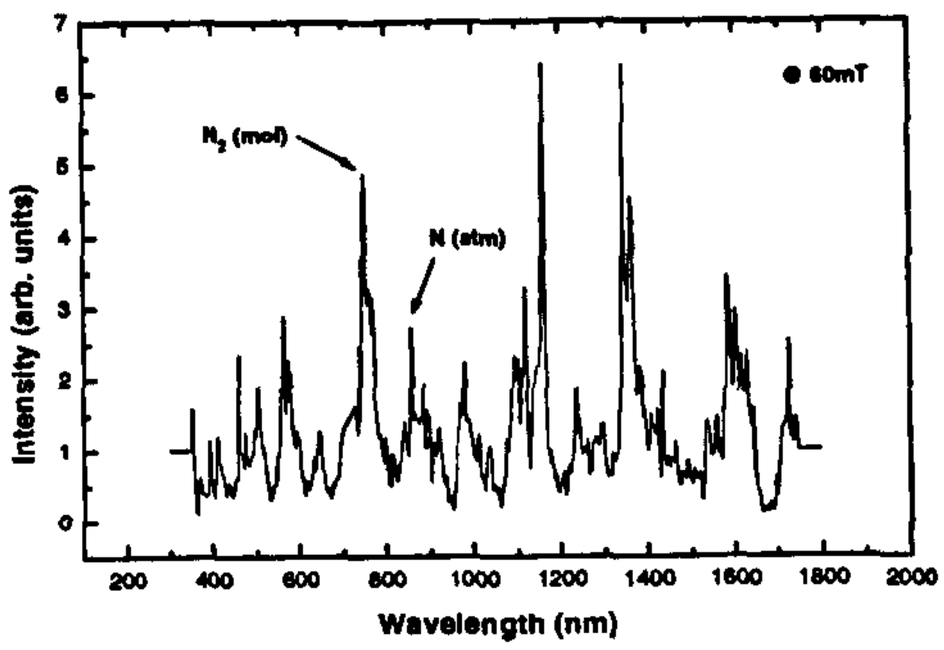

(b)

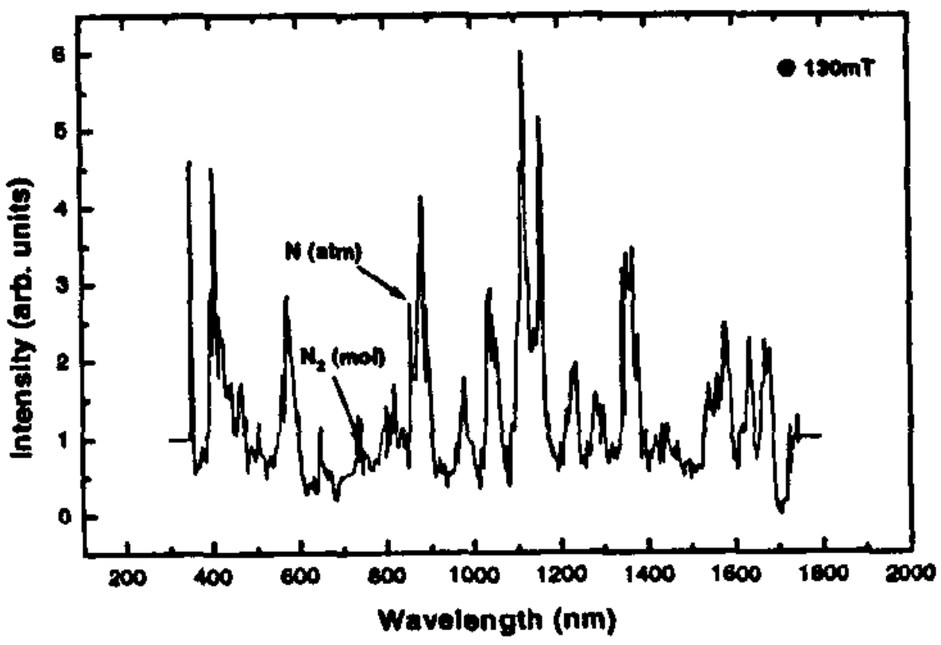

(c)

Figure 4.4: The optical emission spectra of N_2 plasma with varying axial magnetic field at 15mT, 60mT and 130mT. When the DC magnetic field is increased the emission at 750nm, originating from excited N_2 *molecules* has the largest intensity in 60mT spectrum, and then reduces again in the 130mT spectrum, In contrast the emission from *atomic* N at 868nm has increased consistently with magnetic field.

clearly be identified in the OE spectrum when an axial magnetic field of 15mT is applied. When magnetic field is increased to 60mT the emission line at 750nm has become significantly larger than it was in (a). The emission at 868nm too has increased in intensity. Further increase in magnetic field to 130mT has brought down the the intensity at 750nm while the spectral line at 868nm has increased steadily in (c).

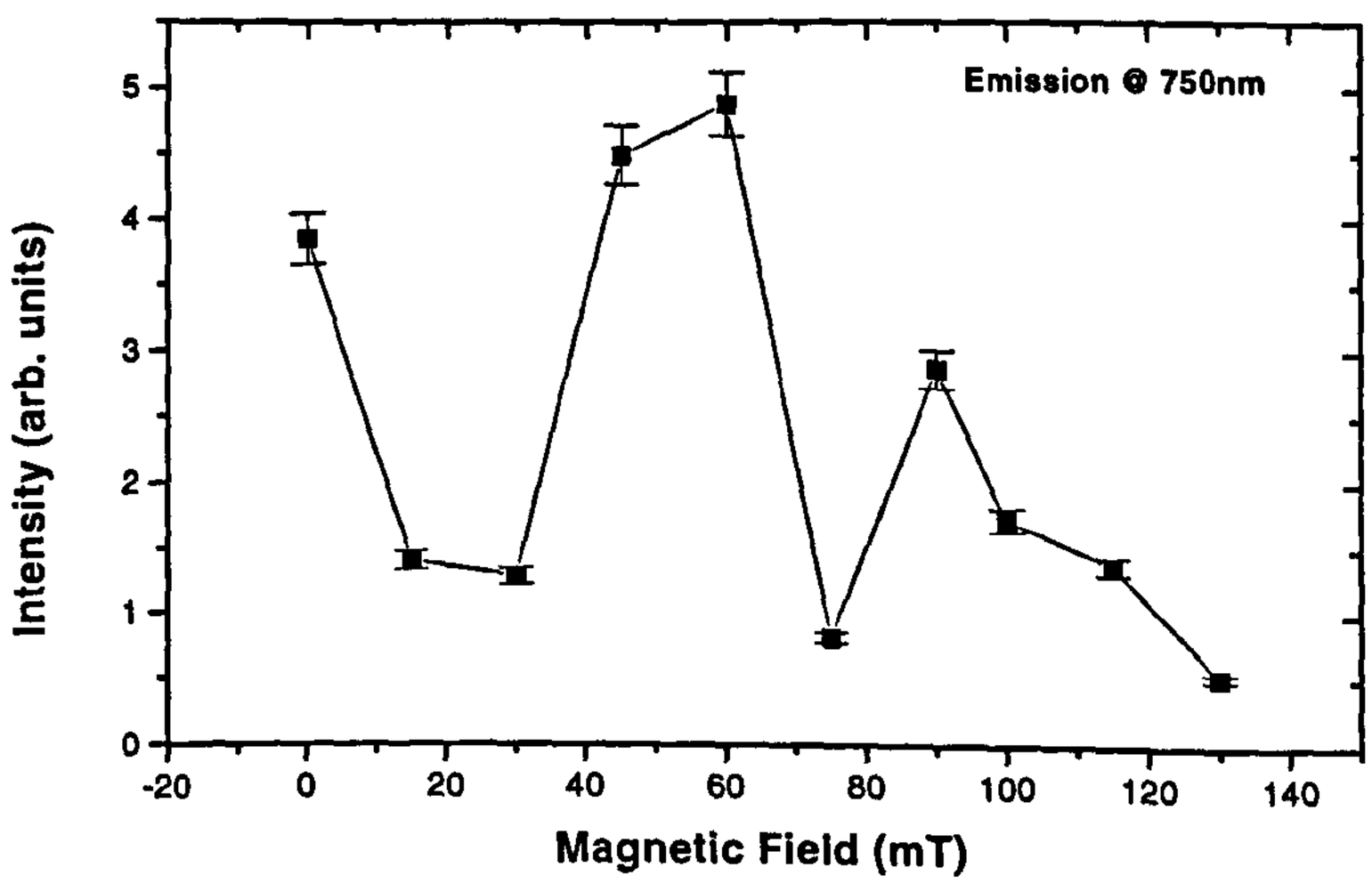

Figure 4.5: The optical emission intensity of the 750nm N_2 line with varying axial magnetic field. The intensity goes through a maximum between 40mT to 60mT.

Figure 4.5 illustrates the effect of magnetic field over the emission at 750nm. As magnetic field is increased up to 130mT, the intensity of emission goes through a peak for magnetic fields between 40mT to 60mT.

If there is sufficient population of N_2^+ in $X^2\Sigma_g^+$, the resultant electrons are in an energy regime in which an impact with an N_2 can generate N_2^* in $C^3\Pi_u$. After 38 nanoseconds (life time of the excited molecule) the N_2^* decays down to $B^3\Pi_g$ emissively. The resulting photon is the 337.1nm emission used for stimulated amplification. The life time of a $B^3\Pi_g$ nitrogen is 8μS. It then decays to $A^3\Sigma_u^+$

via radiative relaxation. The emitted photon is at 750nm, the spectral line what is being detected here which goes through a peak between 40mT to 60mT axial magnetic field. The nitrogen in the $A^3\Sigma_u^+$ state is de-excited radiatively to ground level in the absence of impact relaxation (phononic interactions), after staying in the excited state for a typical period of seconds. However phononic interactions bring down the relaxation time to the millisecond regime for high nitrogen flow rates and for high gas pressures. The N_2 in $X^1\Sigma_g^+$ is now ready to go through another cycle started with an electron impact excitation to $C^3\Pi_u$.

As seen from Fig. 4.5 the emission line at 750nm results from the transition of N_2^* from $B^3\Pi_g$ to $A^3\Sigma_u^+$ which is a part of the $C^3\Pi_u \rightarrow B^3\Pi_g \rightarrow A^3\Sigma_u^+ \rightarrow X^1\Sigma_g^+$ excitation-de-excitation cycle. The intensity of this peak goes through a maximum for axial magnetic fields between 40mT and 60mT. Since the excitation up to $C^3\Pi_u$ is only possible via collision induced energy transitions between electrons liberated from N_2^+ in $X^2\Sigma_g^+$ and N_2 in $X^1\Sigma_g^+$, the above observation indicates an increase in population of N_2^+ at $X^2\Sigma_g^+$ energies for magnetic fields of 40mT to 60mT. The phase velocity of $2.37X10^6 ms^{-1}$ in the helicon wave is kept so that the preferential energy transfer into the plasma from RF energy is at 16eV, which is just above the probable N_2^+ energy level of $X^2\Sigma_g^+$ at 15.6eV. This seems effective in maintaining a sufficient amount of electrons necessary to sustain the $X^1\Sigma_g^+$ to $C^3\Pi_u$ transition of N_2^*.

As shown in figure 4.6, the emission at 868nm shows a sharp increase around 40mT. However, the intensity of this particular line keeps increasing as the magnetic field is increased. The 868nm emission originates from atomic N de-excitations in $2s^22p^23p\ ^4D^0 \rightarrow 2s^22p^23s\ ^4P$ which has a threshold energy of 11.76eV. In usual nitrogen excitations for laser applications, the transition into the $C^3\Pi_u$ state is mainly limited by the *bottle neck* formed at the $A^3\Sigma_u^+$ long life time energy level during the de-excitation process to ground level. The processes associated with phononic interactions are highly pressure dependent. It has been necessary in the past to keep the gas pressure at several Torrs in order to maintain enough collisional interactions so that there are sufficient de-excitations from $A^3\Sigma_u^+$ to ground level in nitrogen plasmas used in a successful laser systems[152]. At such high pressures the required ionisation is achieved by

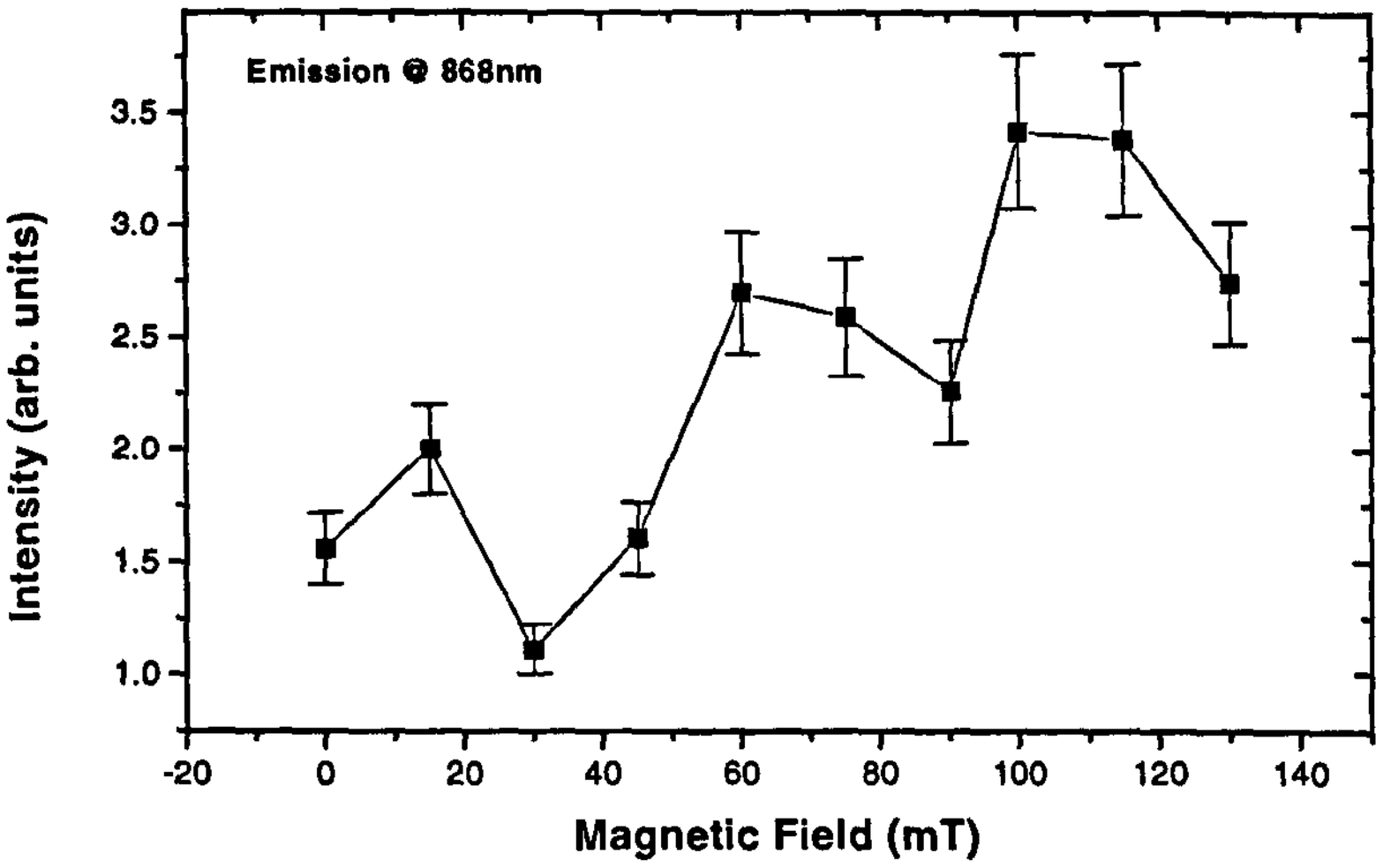

Figure 4.6: The intensity of 868nm spectral line associated with *atomic N* emissions. The graph shows an abrupt increase around 40mT and continues to increase in intensity as the magnetic fields increases further.

DC discharges. The repetition rate of the DC pulse which in effect becomes the laser pulsing rate should allow adequate time for N_2^* to relax before making any attempt to populate $C^3\Pi_u$. Even at a pressure of 50Torr the relaxation time is in the order of 15ms [156]. However in the present work when the helicon mode is activated the population in $C^3\Pi_u$ can be maintained continuously even at pressures as low as 100mTorr. As a result a 5 times increase in 750nm emission is seen in the presence of this helicon excitation. When the helicon wave allows preferential energy coupling at 16eV there are three possible transitions leading to the depopulation of the ground state. As described before the main process is the excitation of N_2^+ to $X^2\Sigma_g^+$ via direct Landau damping. The next is the transition of N_2^* from $X^1\Sigma_g^+$ to $C^3\Pi_u$ by electron impacts resulting from the above process. The last is the atomic transition of $2s^22p^23p\ ^4D^0 \rightarrow 2s^22p^23s\ ^4P$. In effect the collective de-population of the ground state, has made the de-excitation of the $A^3\Sigma_u^+$ long life time energy level more probable, thus removing

the *bottle neck* for a near continuous operation of the laser excitation cycle. This is manifested as a strong continuous emission at 750nm for the helicon mode N_2 plasma tuned for laser emission.

4.4.5 Selective Excitation of Multiple Ion Species in the Plasma

As discussed in section 4.4.2 the amount of energy transferred into the plasma resonantly from the wave is characterised by the phase velocity of the standing wave. The higher the phase velocity the higher is the amount of energy transferred. Since the excitation frequency is fixed as the energy requirement increases the helicon wavelength must also increase. When the Landau damping length is comparable with the collisional mean free path of the species, the collisionless term vanishes and energy transfer is no longer collisionless. With the experimental set up in this work, the maximum energy that can be reached is 60eV at an axial magnetic field of 0.16T (corresponding to 10A through the coils). This energy level requires a Landau damping length of ≈34cm - still outside the collision dominated regime.

With a separate set of antenna and magnetic field combinations, it is possible to excite several plasma species in the same reactor simultaneously as shown in Fig. 4.7. The RF power can be shared over different antenna regions. In a-C:H:N deposition, N can be ionised with the characteristic energy of the species of interest. Likewise from CH_4 the required species can be selectively promoted so that the energy transition necessary is in resonance at the antenna-axial magnet combination independently from that of the N system.

4.4.6 Influence of helicon waves on plasma properties

The plasma potential measured on an RF compensated Langmiur probe for axial magnetic fields up to 120mT are illustrated in figure 4.8. When no magnetic field is applied plasma potential is negatively low. As the field intensity increases that begins to grow negatively until ≈40mT and then remains constant upto

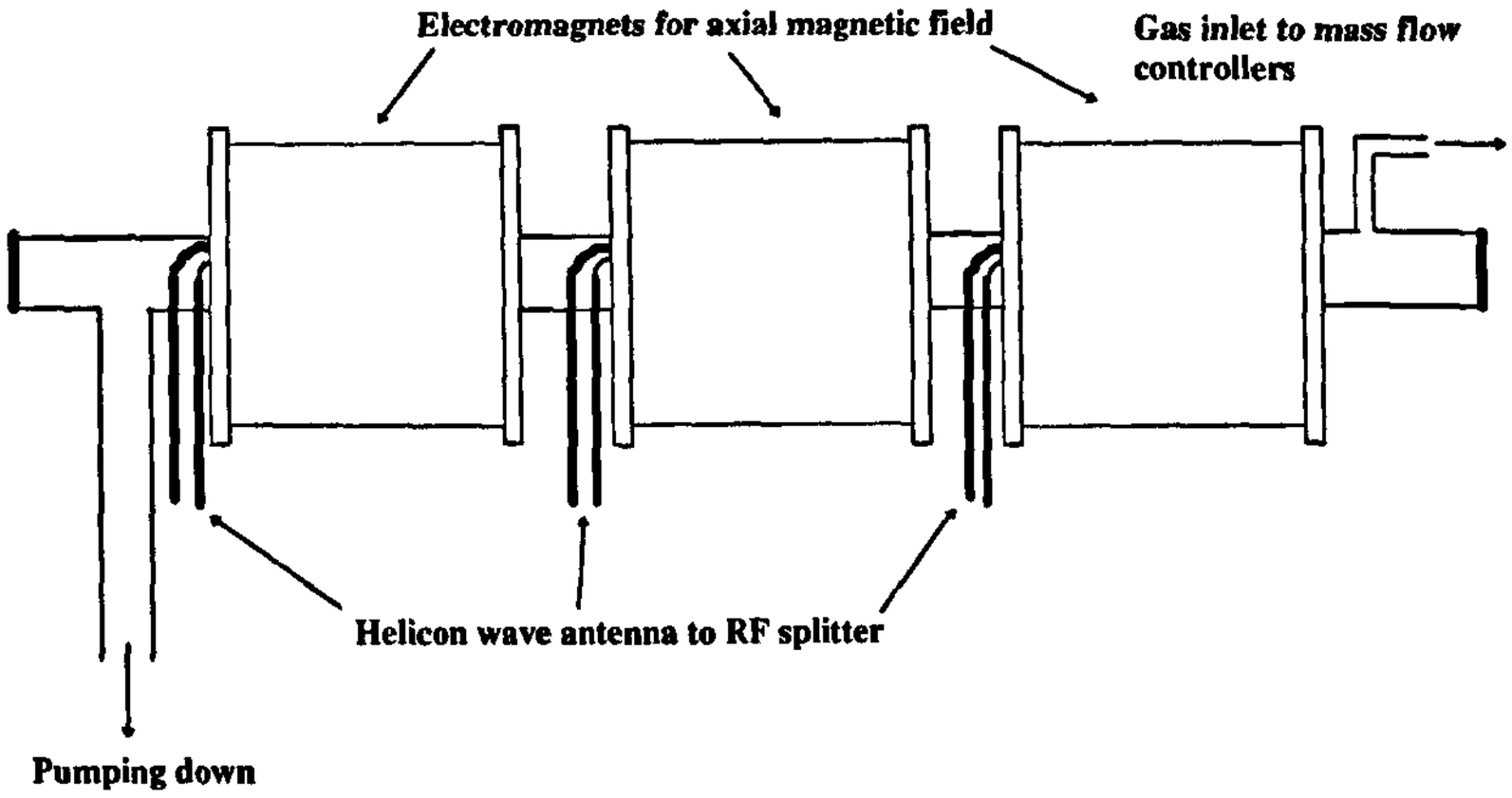

Figure 4.7: Each electromagnet and antenna combination is tuned to promote a particular energy transition in the plasma. The RF power from a single source can be shared among different antenna regions with separate matching arrangements.

80mT. As the magnetic field is further increased, that again goes low.

When a Langmiur probe is inserted into the plasma there can be a current flow through the probe even if an external potential is not applied due to the fact that there can be a potential difference between the plasma and the chamber wall. Depending upon the sign of the potential difference it is necessary to apply an external voltage on the probe in order to stop the current flow, this voltage is known as the plasma potential and it is an indication of excess charge in the plasma. The plasma potential attains a peak level in the vicinity of 40mT to 60mT indicating that the excess charge formation also goes through a peak in this regime. As discussed in section 4.4.4, in this range of magnetic fields there is a preferential energy coupling into N_2 to maintain the N_2^+ at its threshold energy level $X^2\Sigma_g^+$. Selective activation of this process has led to increase in the plasma potential.

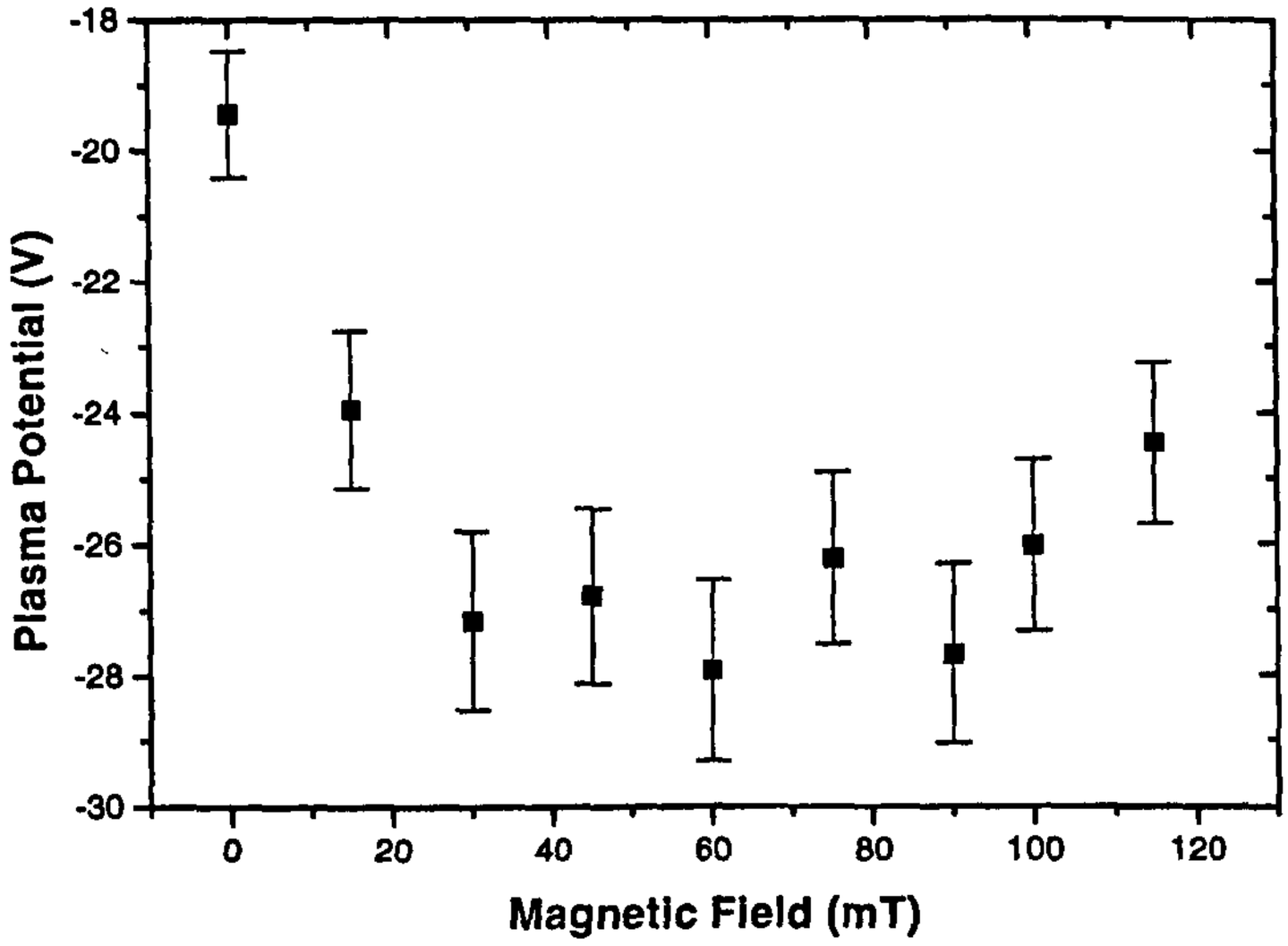

Figure 4.8: With the axial magnetic field the plasma potential of N_2 plasma goes through a peak value of -28V between 40mT and 60mT.

The electron density of the helicon plasma does not significantly vary with variations in the axial magnetic field as seen in figure 4.9. This indicates that no major ionisation activity is promoted by the selective coupling of RF power to maintain N_2^+ at the threshold level. Rather it is a matter of diverting energy into a particular process which was coupled in an average manner over a wider energy range.

4.5 Properties of a-C:H:N Films Deposited Using HW PECVD

4.5.1 Introduction

Films for electrical measurements, field emission studies and for PL measurements were deposited on Si substrates. The optical characterisation was done for films on fused quartz substrates. Prior to deposition the chamber is pumped

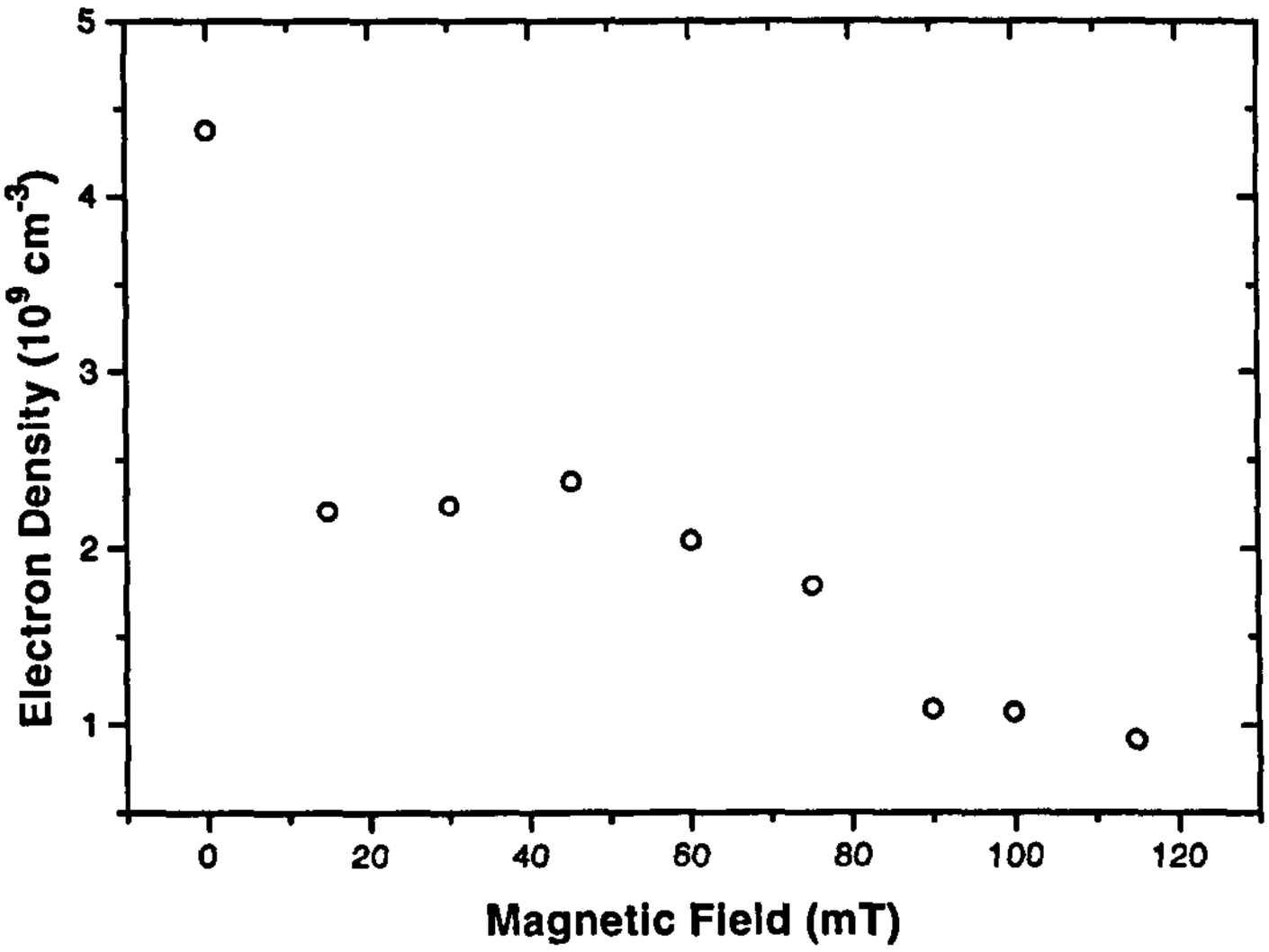

Figure 4.9: The electron density of the plasma remains steady with applied magnetic field. However there is a small peak around 40mT.

down to a base pressure of $4 \times 10^{-5} mbar$. A mixture of CH_4 and N_2 is introduced at a pressure of 300mTorr.

4.5.2 RF Power Dependence

The deposition rate of a material can be influenced by several factors. When an energetic particle reaches the surface of the substrate, the energy of the particle seen by the surface can have several forms. The kinetic energy is characterised by the impinging velocity. The difference in electrostatic potential between the particle and the surface (or the charge difference between the two) forms a differential electrostatic field leading to a potential energy component. It is possible for a particle to possess a form of energy owing to the level of excitation (*eg.* radicals, N_2^*) making it more reactive in the plasma. The eventual result, whether it is net growth or etching, is determined by the leading process between the competing etch and deposition processes occurring simultaneously at the

surface. The deposition process results from particles which lose energy and aggregate in a bound configuration. The etching process results from particles having large enough additional energy to cause bond rupture and lead to a net loss of atoms from the surface.

When the RF power input varies from 50W to 500W without applying any axial magnetic field in HW PECVD reactor, the deposition rate of $a-C:H:N$ on Si substrates goes through a peak around 150W, and then settles down to a steady deposition rate of 4nm min^{-1} as shown in Fig. 4.10. A similar behaviour in the growth with a peak at mid powers was observed for the inductively coupled system as well, but with a much higher rate of growth (see Fig. 1.5). In both cases deposition rate is lower at low RF powers mainly due to poor excitation of the plasma. As power input increases the energy gathered by the particle can increase in two ways, either as kinetic energy or as an excitation. In the capacitively coupled case the negative self bias increases with RF power, increasing potential energy which in turn converts into impinging velocity (kinetic energy) at the substrate surface. However, possible wall charging has been reported even with inductively coupled plasma [76] leading to lateral particle accelerations. This effect does not contribute to increase in the particle bombardment on the substrate as in a capacitively coupled plasma since ion and electron oscillations are parallel to the substrate as discussed elsewhere.

The optical Tauc gap for a-C:H:N films deposited using HW PECVD started from a wider value at low powers and began to reduce and then saturated at 2.8eV for powers larger than 250W, as seen in Fig. 4.11. The fact that a wider optical band gap is seen together with a small rate of deposition at lower powers indicates convincingly that the level of excitation is poor in this regime. An onset threshold of excitation around 150W is signaled by dramatic shrinking of band gap from 3.4eV (at 50W) to 2.9eV (at 150W) and by the significant rise in deposition rate from 1.5nm min^{-1} to 6nm min^{-1}. Beyond 250W things start to settle down at respective saturated levels. These results indicate that the level of excitation which can be achieved, saturates beyond RF power inputs larger than 250W in the HW PECVD system when no axial magnetic field is applied (effectively an inductively coupled excitation but with lateral magnetic

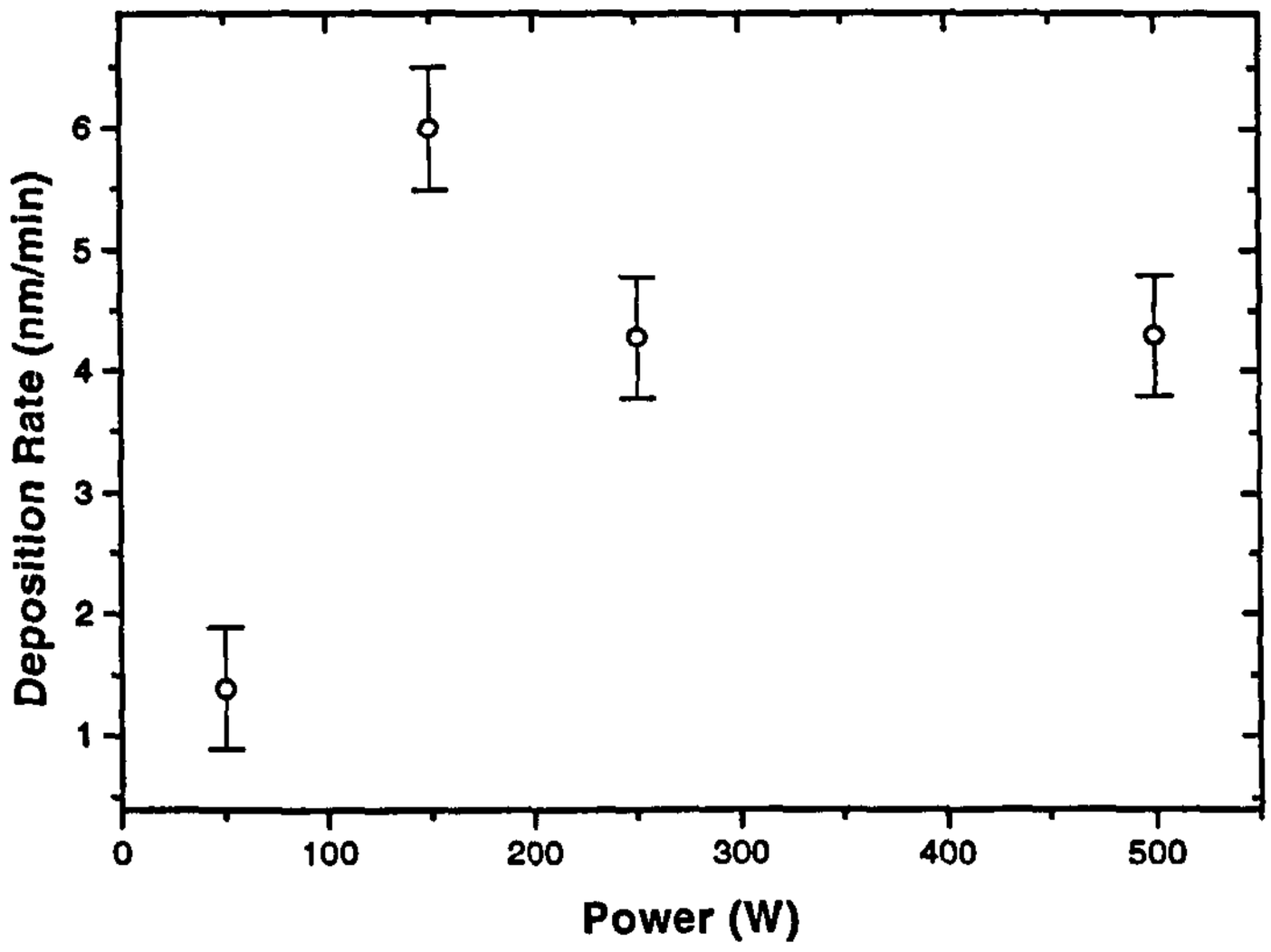

Figure 4.10: The plot of rate of deposition against RF power applied. Deposition rate goes through a peak around 150W.

field vector oscillations due to antenna orientation).

4.5.3 Axial Magnetic Field Dependence

As discussed earlier, magnetic field values between 40mT and 60mT had distinct effects on optical emission behaviour and on general plasma properties. Now we will look at the effect of axial DC magnetic field on film properties at the threshold power of 150W.

The growth rate drops to $\approx$4.5nm min^{-1} from 6nmmin^{-1} when the magnetic field exceeds 40mT as seen in Fig. 4.12, and remains at that value for further increase in magnetic field. This can either be interpreted as a density increase in the film or as a sputtering yield increment. Clay *et. al.* have attributed the decrease in growth of a-C:H:N to the sputtering of the surface by N_2^+ [158]. But the optical emission line associated with N_2^+ shows that the formation of N_2^+ has a peak between 40mT to 60mT, and that for increased magnetic fields

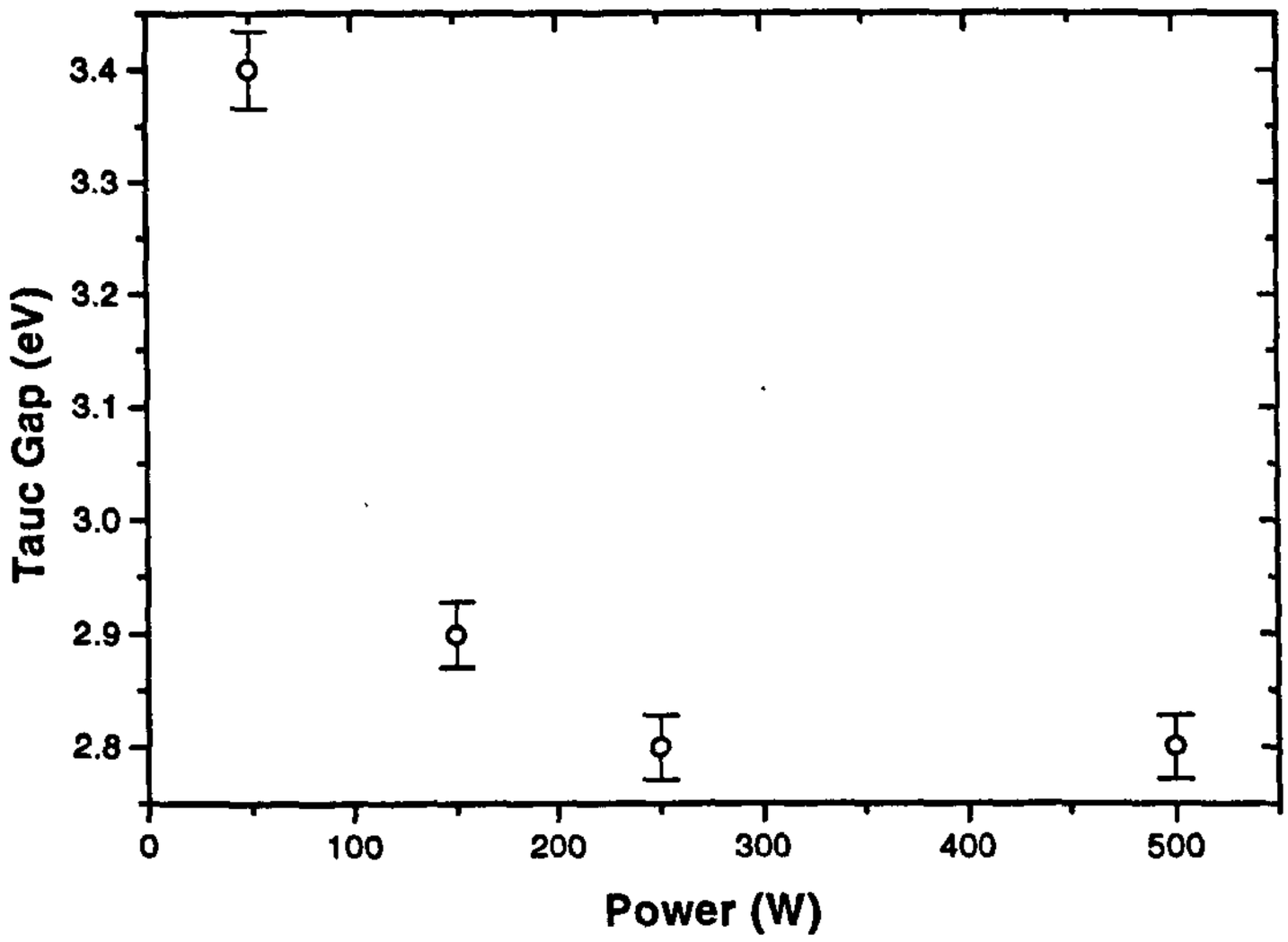

Figure 4.11: As RF power increases the optical band gap of the film decays.

diminishes (see Fig. 4.5). As seen in Fig. 4.6 the formation of atomic N increases with magnetic field, however that also does not explain the step change in growth rate and subsequent saturation at a lower rate.

The optical band gap of the films start from 2.9eV and goes through a peak (3.2eV) around 40mT, and then comes back to the original value around 115mT as seen in Fig. 4.13. The broadening of optical band gap, even at the onset of decrease of growth rate around 40mT, together with the increase of N_2^+ and N_2^* species due to helicon mode activation, suggests that the effect is in fact due to reduction in band tail defects of a-C:H:N with efficient incorporation of N into the a-C:H matrix. The defect compensation due to the incorporation of N in a-C:H:N has been reported earlier [52]. For *non-resonant* magneto-plasma excitation beyond 16eV, there are several possible reactions in the CH_4, N_2 environment. The saturation of growth rate indicates that decomposition of CH_4 is not greatly affected by the magnetic field. The steady increase in atomic N seen from the optical emission spectra suggests that the dominant reactions are,

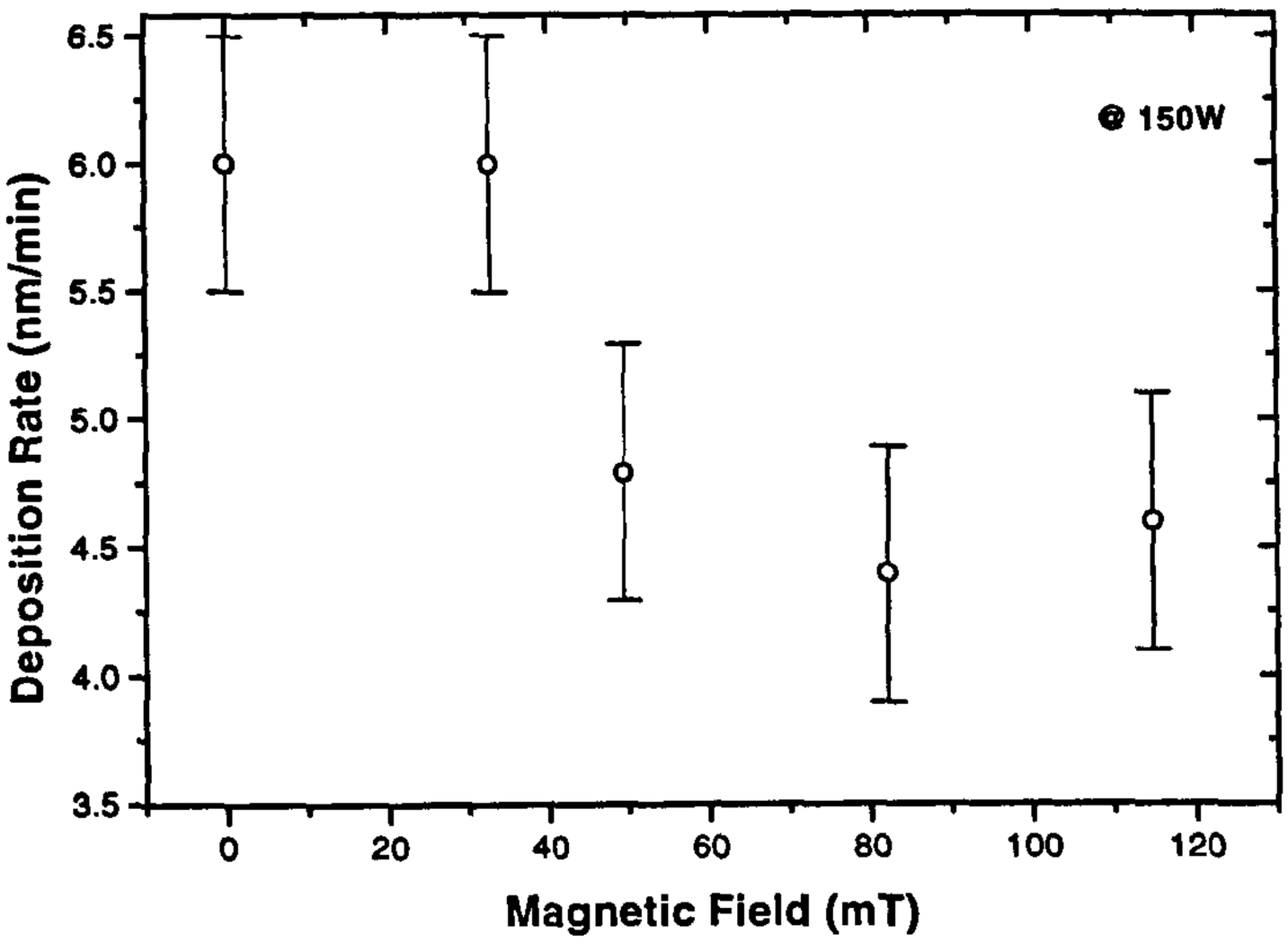

Figure 4.12: The axial magnetic field dependence of the deposition rate at 150W. There is a transition drop from 6nm/min to 4.5nm/min between 40mT and 60mT.

$$N_2^* + e \rightarrow N + N + e \tag{4.44}$$

$$CH_x^+ + N_2 \rightarrow CH_x + N^+ + N^+ + e \tag{4.45}$$

$$\begin{aligned} CH_x^* + N_2^* &\rightarrow CN^+ + N + H_y + H_z + e \\ CH_x^* + N_2^* &\rightarrow CNH_y + N^+ + H_z + e \\ CNH_y + A^* &\rightarrow CN^+ + A + H_z + H_k + e \end{aligned} \tag{4.46}$$

where A denotes a participating species in a multibody collision process, $x = y + z$ and $y = z + k$.

The further reduction in band gap beyond 40mT is more likely due to incorporation of N from one or several processes described by expressions 4.44,

4.45 and 4.46. These reactions have energy thresholds of 14.5eV, 15eV and 14eV respectively, making them all probable beyond 40mT. Even though the reactions,

$$H_2 + e \rightarrow H + H^* + e$$
$$H + e \rightarrow H^* + e \quad (4.47)$$

are also favourable, having thresholds of 17.25eV and ≈13eV respectively, the possible defect generation by energetic species bombardment is ruled out by the fact that the rate of growth saturates (absence of possible etching associated with energetic species).

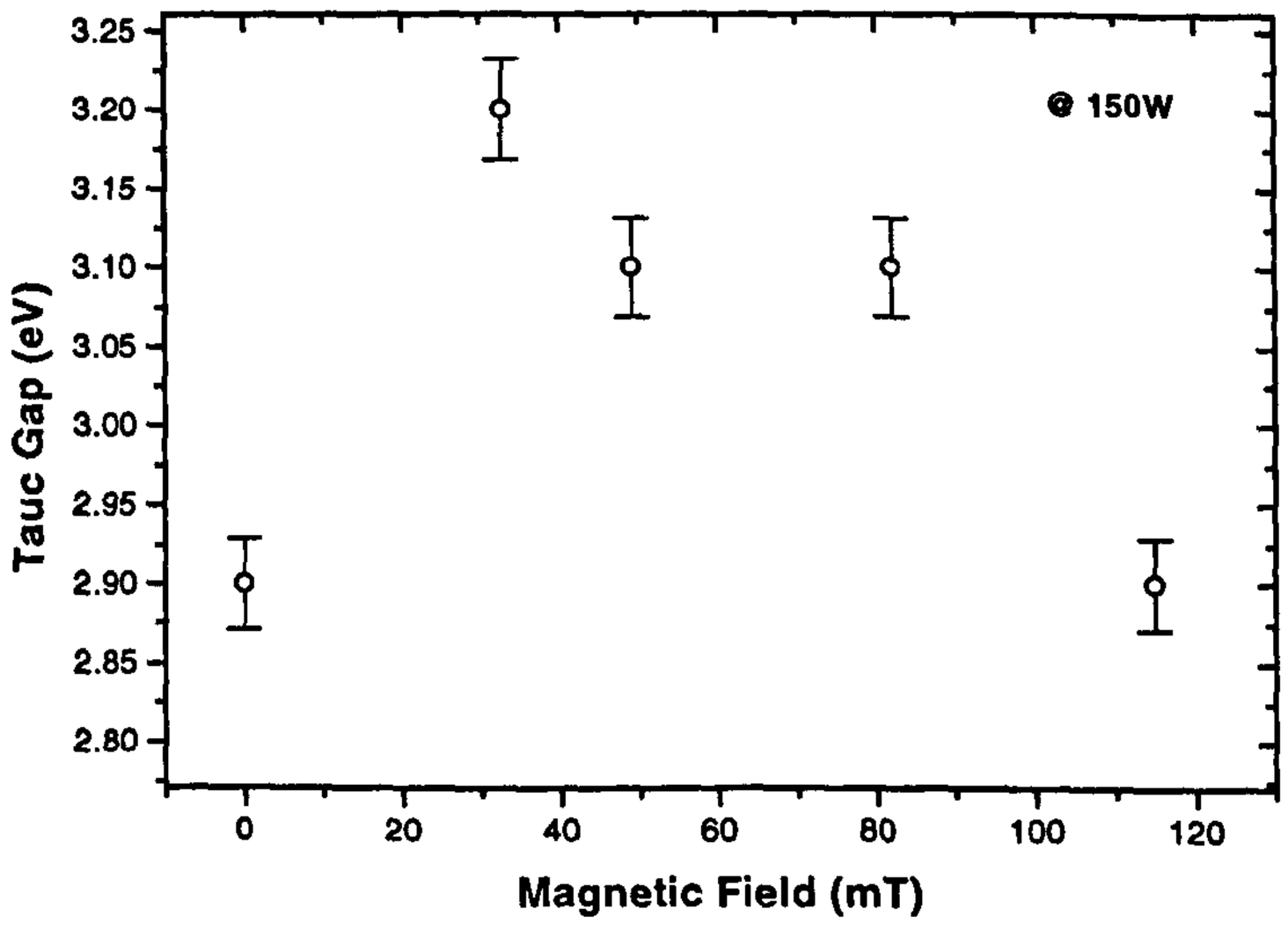

Figure 4.13: Optical Tauc gap against magnetic field shows a broad feature. There is a peak value around 40mT.

4.6 Comparison of HW PECVD with Inductively Coupled PECVD

4.6.1 Introduction

In order to compare the standard inductively coupled reactor with the helicon wave system, when the helicon mode is inactive and active, the parameters were measured from both systems under similar conditions. For plasma and optical emission spectroscopy measurements 5sccm of N_2 gas is introduced into both chambers at a pressure of 350mTorr. Plasma data were collected by a RF compensated Langmiur probe coupled with a computer controlled plasma parameter analyser (Hiden Analytical 900400). Optical emission data in the range 350nm to 1800nm were collected via a fibre optic link to the spectrum analyser (Anritsu MS9702B and MS9030A).

4.6.2 Plasma Conditions

The plasma potential was positive in an inductively coupled system while it was negative for the helicon system. When the helicon mode is attained the negative plasma potential reaches the maximum negative value. The maximum negative value recored is comparable with inductively coupled case in magnitude (see Table 4.1). However, for a He plasma both systems show positive plasma potential. When there is relatively large concentration of positively charged ions there can be a positive potential build up. The negative plasma potential indicates that even when the helicon mode is active in the N_2 plasma, the degree of positive ion generation is less than in inductive case, suggesting that the residue ion generation associated with N_2^* excitation excitation process is not excessive. Since He is more readily ionised compared to N_2, it shows positive plasma potentials in both systems.

The electron density of the plasma is $\approx$20 times in helicon system compared to that of the inductive case (see Table 4.1). However, the electron temperature shows the reverse behaviour. These two effects indicate that the energy distri-

	Inductively Coupled	Helicon Inactive	Helicon Active
Plasma Potential ± 0.05(V)	26.67	-19.44	-27.91
Electron Density ± 0.05×10^9(cm^{-3})	0.12	2.21	2.05
Electron Temperature ± 0.05(eV)	7.19	2.35	1.56

Table 4.1: The plasma potential, electron density and the electron temperature of the inductively coupled PECVD and HW PECVD are compared when helicon mode is inactive and active.

butions in the two systems are such that the inductive case has a small number of electrons, but at high energies and that the opposite is the case with helicon excitation. When the helicon mode is activated neither of parameters change significantly, which indicates that only the type of excitation has shifted, and that this contributes predominantly to the activation of the N_2^* species. This agrees well with the optical emission data. The helicon mode plasma is essentially a cold plasma with energy coupling predominantly through selected excitations.

4.6.3 Optical Emission Spectroscopy

As shown in Table 4.2 the optical emission associated with both molecular nitrogen at 750nm and atomic nitrogen at 868nm show comparable intensities in the inductively coupled and helicon activated systems when the magnetic field is such that the helicon mode is not reached. The helicon system in this mode and the inductively coupled system are fundamentally coupling the same *level*

	Inductively Coupled (arb.units)	Helicon Inactive (arb.units)	Helicon Active (arb.units)
Emission of 750nm line	3.20 ± 0.05	1.29 ± 0.05	4.87 ± 0.05
Emission of 868nm line	3.25 ± 0.05	1.11 ± 0.05	2.71 ± 0.05

Table 4.2: The molecular and atomic nitrogen emissions in inductively coupled system and HW PECVD, when helicon mode is active and inactive are compared

of power as far as the plasma excitation is concerned. With this observation in mind, it is interesting to note that the excitation of atomic N and the excitation of molecular nitrogen are of the same order in inductively coupled plasmas irrespective of the actual geometry of the reactor - note here that the physical dimensions and the antenna orientation in two systems are markedly different.

However, when the helicon mode is activated the situation changes drastically. The molecular emission begins to dominate over that of atomic emission. This is thought to be due to resonance excitation of the N_2^* species by Landau damping. The increase in the intensity of atomic emission can be due to two reasons. First, since an extra static magnetic field is applied to the helicon mode, the magnetic confinement of plasma can promote atomic N generation. Second, when N_2^+ is maintained at its threshold level, energetic *hot* electrons can promote the break up of N_2 to create N. There is a 50% increase in *amplified* molecular emission when helicon mode is active, when compared with the standard inductive plasma in similar conditions.

4.6.4 Film Properties

The optical bad gap of the films deposited with $CH_4 : N_2$ ratio of 1 : 1 using the inductively coupled system and the helicon system without a magnetic field is shown in table 4.3. Films are of the soft polymeric type and optically quite transparent. However when helicon mode is activated the films have a wide band gap. This widening of the optical band gap can be attributed to band

tail state passivation by efficient nitrogen incorporation, as discussed in section 4.5.3.

	Inductively Coupled	Helicon Inactive	Helicon Active
Band Gap (eV)	2.7 ± 0.05	2.9 ± 0.05	3.2 ± 0.05
Growth Rate ($nmmin^{-1}$)	30.0 ± 0.5	6.0 ± 0.5	4.5 ± 0.5

Table 4.3: The band gap variation and the film deposition rate variation in inductively coupled system and HW PECVD, when helicon mode is active and inactive are compared

The rate of deposition is markedly higher in the inductively coupled plasma compared to helicon system under any mode. The positive plasma potential and the high electron temperature of inductively coupled plasma is consistent with the higher growth rate observed. The overall ionisation capability is higher in the inductively coupled plasma apparatus used, even though the helicon plasma is capable of selective excitation of species. In order to compare the real ionisation capability, one should tune the helicon wave also to ionise the dominant species of a-C:H:N deposition. However, when the helicon excitation of N_2^* is activated the deposition rate decreases to $4.5 nmmin^{-1}$. As discussed in section 4.5.3 this behaviour is primarily due to dense film deposition associated with N incorporation.

4.6.5 Overview

At the beginning of this chapter we looked at the possibility of electro-magnetic waves that would propagate in a plasma column in the presence of a DC magnetic field. It was shown that, out of two possible circular polarisations, there can be a right-hand circularly polarised wave which is sustained along the magnetic field having a propagation vector parallel or anti-parallel to the axis of the magnetic field. The condition required for this wave to propagate is that the frequency of excitation is less than the cyclotron frequency of the plasma. Such

waves would possess a phase velocity $\vec{u}_\phi$ smaller than that of electro-magnetic waves which propagate in vacuum. In the plasma world such waves are referred to as either *whistler* waves, after their first observation in ionospheric studies, or *helicon* waves.

Next we established a method of utilising electro-magnetic waves travelling in plasmas to transfer energy from wave to plasma species. As Landau first pointed out mathematically, the waves can exchange energy with plasma species without any collisions via wave particle interactions. If the phase velocity of the wave is slightly larger than the velocity of the particle, then particle gains energy from the wave, and as a result the wave is damped. This phenomenon is known as Landau damping and the mathematical treatment is seen in section 4.3.

A practical implementation of the Landau damping process for plasma excitation was carried out using new apparatus designed as part of this research. The initial design work was aimed at preferentially sustaining the excitation of N_2^* in a nitrogen plasma used for laser emission at 337.1nm. A double loop helicon antenna placed inside an electromagnet capable of delivering upto 0.16T was used. The operating frequency of 13.56MHz of the RF power was well below the cyclotron frequency (1.18GHz) corresponding to the static magnetic field of 42mT. However, the lower hybrid frequency of the nitrogen plasma (5.2MHz) is well below the operating frequency, making the antenna impedance looking into the plasma, inductive. Consequently in order to achieve the matching condition with the RF power supply it was necessary to add an additional capacitor with the standard antenna matching unit.

The observations made in optical emission spectra suggest that the preferential excitations in N_2^* over atomic nitrogen excitations were possible. This was seen as a significant increase in the 750nm emission which arises as a part of $C^3\Pi_u \rightarrow B^3\Pi_g \rightarrow A^3\Sigma_u^+ \rightarrow X^1\Sigma_g^+$ process over the 868nm emission associated with atomic N. This was achieved in the vicinity of theoretically predicted magnetic field of 42mT. The demonstration of the ability to excite selectively a given species in a gas/plasma, shows that the Landau damping process can be used for selective simultaneous excitation of multiple plasma species. Such an excitation is necessary to realise a multi-species plasma source using a mixture of gases

(*e.g.* CH_4, N_2, for a-C:H:N film deposition). This can be achieved when there are separate magnet-antenna combinations tuned to couple with each energy transition.

The optical band gap variations and the rate of deposition dependence of the axial magnetic field showed that it may be possible to achieve compensation of band tail states with N, incorporated via N_2^* excitations. The films deposited at high magnetic fields where the atomic N content is high showed shrinking of band gap. This effect of band gap reduction as N in the plasma increases, cannot be attributed to ion bombardment due to the fact that there was no increase in etching associated with the energetic plasma species.

Finally the helicon wave PECVD was compared with standard inductively coupled PECVD in terms of plasma, optical emission and a-C:H:N film properties. The plasma properties and the optical emission observations suggest that the inductively coupled plasma is a *hot* plasma having broad energy distribution whereas, the helicon plasma is *cold* with selective energy transfer capability. The films properties (band gap and deposition rate) also agreed with the above conclusions.

Chapter 5

Applications of Hydrogenated Amorphous Carbon

5.1 As a field emitter

5.1.1 Introduction

When a sufficiently intense electric field is applied normal to a metal surface in vacuum, electrons are emitted from the surface boundary. This phenomenon is known as field emission. For a metal, the electric field required for electron emission is in the range of $10^3 \mathrm{V}\mu\mathrm{m}^{-1}$ to $10^4 \mathrm{V}\mu\mathrm{m}^{-1}$. To achieve such high electric fields, equipotential contour concentrations via field enhancement can be generated by using sharp metallic tips. However, in recent years semiconductor surfaces with low electron affinity have been investigated as possible field emission sources. The low electron affinity allows them to emit electrons at low fields, eliminating the need for sharp tips. These low electron affinity materials have a strong potential for flat panel display applications. The Diamond [111] surface terminated by a highly electro-positive atom shows negative electron affinity, and thus is a very interesting candidate for field emitting cold cathodes. Amorphous carbon has also shown evidence of being a flat thin film cold cathode with low electron affinity. Such thin film emitters hold a great promise for future flat panel displays based on active emission of light from the phosphor, (i.e. field

emission display (FED)). In addition, a-C films have also attracted attention in the vacuum microelectronics field due to its ability to combine the advantages of both vacuum tubes and modern semiconductor devices. The suitability of nitrogen doped a-C:H (a-C:H:N) for field emission is examined in this section. The effect of nitrogen in the amorphous carbon matrix and the dominant barrier for field emission in the *n*-Si/a-C:H:N system are also discussed.

5.1.2 Mechanisms Describing the Emission of Electron into Vacuum

When materials having different electro-positivity (or negativity) come into electrical contact, there can be an electron flow from the 'less' electro-positive material to the 'more' electro-positive material (or a hole flow in reverse the direction). Exchange of charges modifies the relative electro-positivity of the material and hence also the Fermi energy. This charge carrier flow continues until the materials in contact become electrically equal (*i.e.* the modified Fermi energy is the same).

The band diagram for a metal and a semiconductor in equilibrium is illustrated in Fig. 5.1(a)(i). However, if a positive potential is applied on an electrode placed across a vacuum gap (anode), with respect to the back metal, the electrical band diagram modifies to that shown in Fig. 5.1(a)(ii). It can be seen that if the potential on the anode increases, then the barrier at the metal-vacuum interface can be thin and tall so as to significantly increase the tunnelling probability of electrons across the barrier. The initial work on electron tunnelling through a barrier was performed by Fowler and Nordheim in 1928 and was subsequently modified by others.

In the case of thin semiconductor layers, electrons first have to be transfered from the base metal contact to the semiconductor conduction band and subsequently tunnel into vacuum. The transfer of electrons from the back metal contact to the semiconductor is readily achieved if the metal-semiconductor back interface is ohmic. However, this has the same effect as a heavily doped semiconductor. In this case the field emission is very similar to that of a metal, with

the exception that tunnelling occurs from the bottom of the conduction band rather than the Fermi level. For a very heavily doped (degenerate) semiconductor the Fermi level is in the conduction (or valence) band, and the situation is almost identical to that of a metal with regards field emission. When the semiconductor is undoped, or lightly doped, the back metal contact is of the Schottky type so that a barrier for electron transfer exists. The geometry of this back contact barrier is dependent on thermal excitation or tunnelling or a combination of the two. There are then two barriers which must be considered for field emission into vacuum.

In general, for a triangular vacuum barrier for electron emission at the Fermi level from the metal into the semiconductor, the tunnelling current density is given by,

$$\vec{J} = \frac{A^* T^2 \pi \exp(-2\alpha\phi_B^{3/2}/3q\vec{E})}{(\alpha\phi_B^{1/2}kT/q\vec{E})\sin(\pi\alpha\phi_B^{1/2}kT/q\vec{E})} \tag{5.1}$$

where α is defined as,

$$\alpha = \frac{4\pi}{h}\sqrt{2m^*}$$

A^* is given by,

$$A^* = \frac{4\pi q m^* k^2}{h^3}$$

When, T - temperature, ϕ_B - barrier seen by electrons, q - charge of an electron, $\vec{E}$ - local electric field across the barrier, k - Boltzmann constant, h - Plank constant and m^* - effective mass of an electron.

At relatively low temperatures, the expression 5.1 becomes,

$$\vec{J} = \frac{A^* T^2}{\phi_B}\left(\frac{q\vec{E}}{\alpha kT}\right)^2 \exp\left[-\frac{2\alpha\phi_B^{3/2}}{3q\vec{E}}\right] \tag{5.2}$$

At sufficiently high temperatures, electrons can overcome the vacuum barrier by thermal activation. This phenomenon is known as *thermionic emission* of electrons. However at moderate temperatures the tunnelling process occurs at energies that are higher than the Fermi energy but lower than the barrier energy.

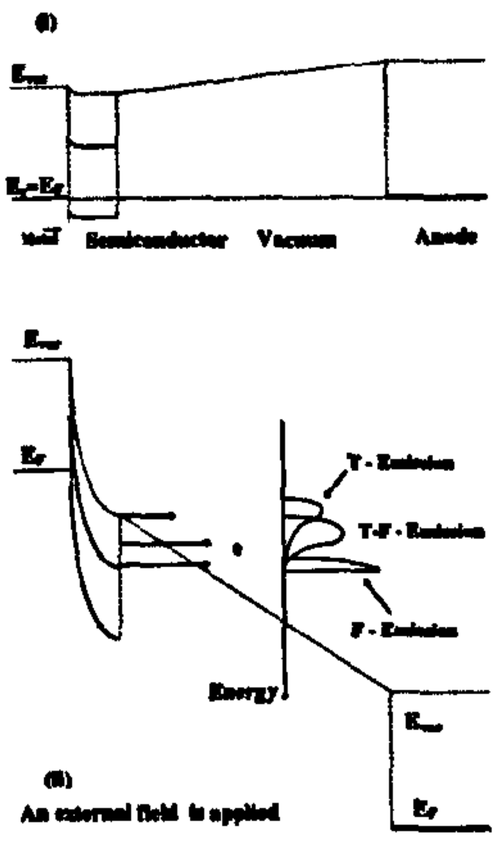

(a) Field Emission at Fermi level and Thermionic Emission.

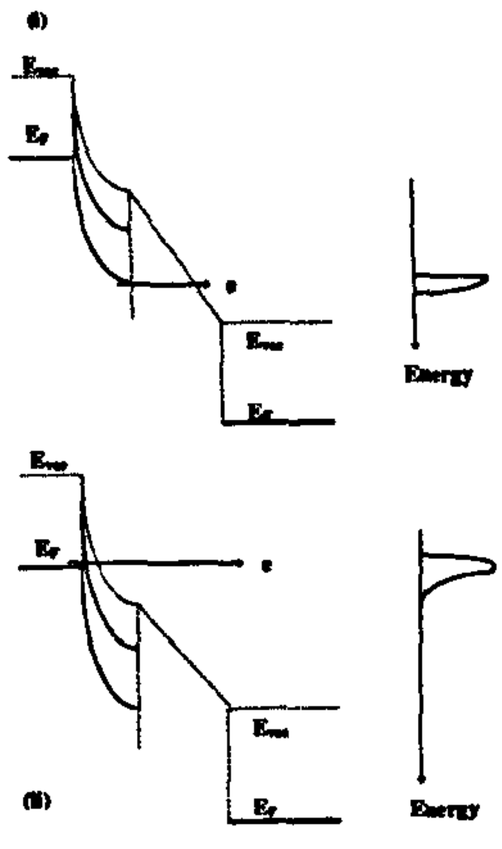

(b) (i)Emission from valance band.(ii)Ballistic Emission occurs when the film act as a thin tunnelling layer.

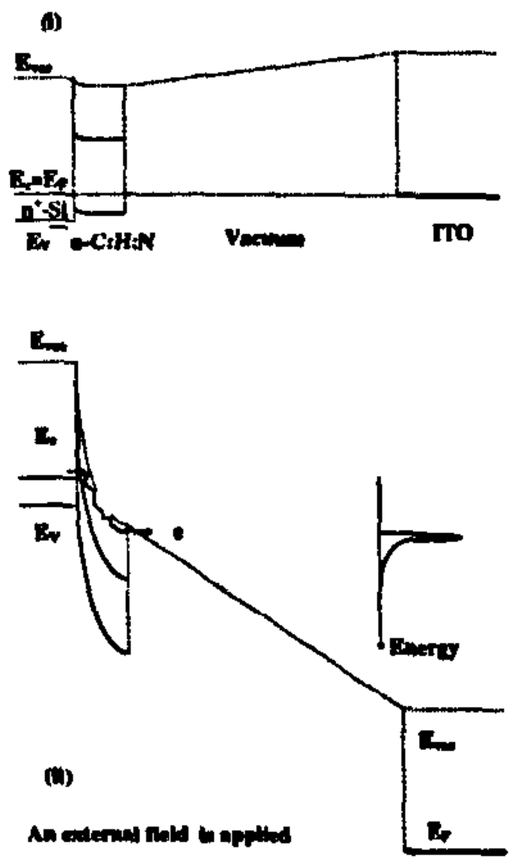

(c) Emission via hot electrons in conduction band.

Figure 5.1: As illustrated in (a), for a metal the electron emission into vacuum at low temperatures around Fermi level energies is referred to as *Field Emission.* At higher temperatures electrons can travel above the barrier and this is called *Thermionic Emission.* Generally at moderate temperatures *thermally assisted field emission* takes place. For semiconductors, field emission can take place from the conduction or the valence band. The former is more likely for an n-doped material (similar to a metal) and the latter for a p-doped material. The emission process at valence band energies is a variant of the field emission at Fermi energies - (b). When the semiconductor layer is a thin layer *ballistic emission* can occur straight from the back electrode to vacuum via the semiconductor layer. In (c), the hot electron model of electron emission for a semiconductor is illustrated where the electrons enter into the conduction band of the semiconductor via the back contact tunnelling barrier, and are then accelerated into the conduction band under a high electric field and become *hot.* The electrons are hot enough to overcome the barrier at the material-vacuum interface.

This process is referred as *thermionic field emission* or *thermally assisted field emission* - (*i.e.* T-F emission).

The T-F emitted current density is given by,

$$\vec{J} = J_S \exp\left(\frac{qV}{E'}\right) \tag{5.3}$$

where J_S is defined as,

$$J_S = A^* T^2 \left(\frac{\pi E_{00}}{k^2 T^2}\right)^{1/2} \left[qV + \frac{\phi_B}{\cosh^2(E_{00}/kT)}\right]^{1/2} \exp\left(-\frac{\phi_B}{E_0}\right)$$

$$E' = E_{00}\left[\frac{E_{00}}{kT} - \tanh\left(\frac{E_{00}}{kT}\right)\right]^{-1}$$

$$E_0 = E_{00} \coth\left(\frac{E_{00}}{kT}\right)$$

In the case of a metal-semiconductor barrier at the back contact, and thermionic field emission from the metal into the semiconductor,

$$E_{00} = \frac{2q}{\alpha}\left(\frac{N_d}{2\epsilon}\right)^{1/2}$$

The energy at which the thermally assisted field emission occurs is given by,

$$E_m = E_{Fm} + \frac{\phi_B - qV \sinh^2(E_{00}/kT)}{\cosh^2(E_{00}/kT)} \tag{5.4}$$

where V - applied potential, E_{Fm} -Fermi energy of the back contact and N_d - donor concentration.

The above result (equation 5.4) is valid only when $E_m < E_{Fm} + \phi_B$. When $E_m \geq E_{Fm} + \phi_B$, thermionic field emission becomes thermionic emission.

The electron emission into vacuum can occur at valence band energies. This possibility is illustrated in Fig. 5.1(b)(i). When the semiconductor layer acts like a thin tunnelling layer at the back metal contact, ballistic emission can occur from the back contact straight into vacuum via a thin tunnelling layer as seen in Fig. 5.1(b)(ii). When sufficiently large band bending is present in the semiconductor, the barrier to electron emission at the material-vacuum interface can be

completely overcome through electron heating in the conduction band under a high electric field. This is referred to as the hot electron model of field emission and is illustrated in Fig. 5.1(c). Even though the field emission phenomenon has been studied since 1928, the description of the emission observed from flat cathodic materials is still the subject of intense debate [160].

5.1.3 Amorphous Carbon as a Flat Cold Cathode

Amorphous carbon field emitting cathodes do not necessarily require large electric fields in order to liberate electrons into the vacuum owing to their low electron affinities compared to metals or other semiconductors. Thin film cold cathode emitters with low threshold fields of 4-10Vμm^{-1} using nitrogenated a-C:H (a-C:H:N) on Si have been reported recently [59, 109, 118]. Such cathodes may prove to be very important for the development of field emission displays.

Generally in a diode type field emitting cell, a large potential is applied on the anode with respect to the cathode in order to obtain an adequate electric field at the emitting surface. A large portion of the applied field is dropped across the vacuum, and the remainder is the effective field across the cathode. Depending on the actual mechanism of emission, the amount of field dropped across the cathode can be a vital requirement for emission. Taking 100μm as an acceptable vacuum gap for micro-vacuum devices, potential differences of the order of a few kilovolts are required to achieve meaningful emission from a practical amorphous carbon cathode. The fact that it is necessary to switch such high voltages makes it almost impossible to use a diode cell in an actual display matrix. However in a triode style pixel arrangement, the emission is triggered by a relatively small electric voltage applied on the gate electrode. The high cathode to anode voltage can be maintained without switching in order to sufficiently accelerate the emitted electrons so that they can acquire enough energy to excite the phosphor on the anode. The introduction of a gate electrode eliminates the requirement of high voltage switching making the addressed field emitting pixel feasible.

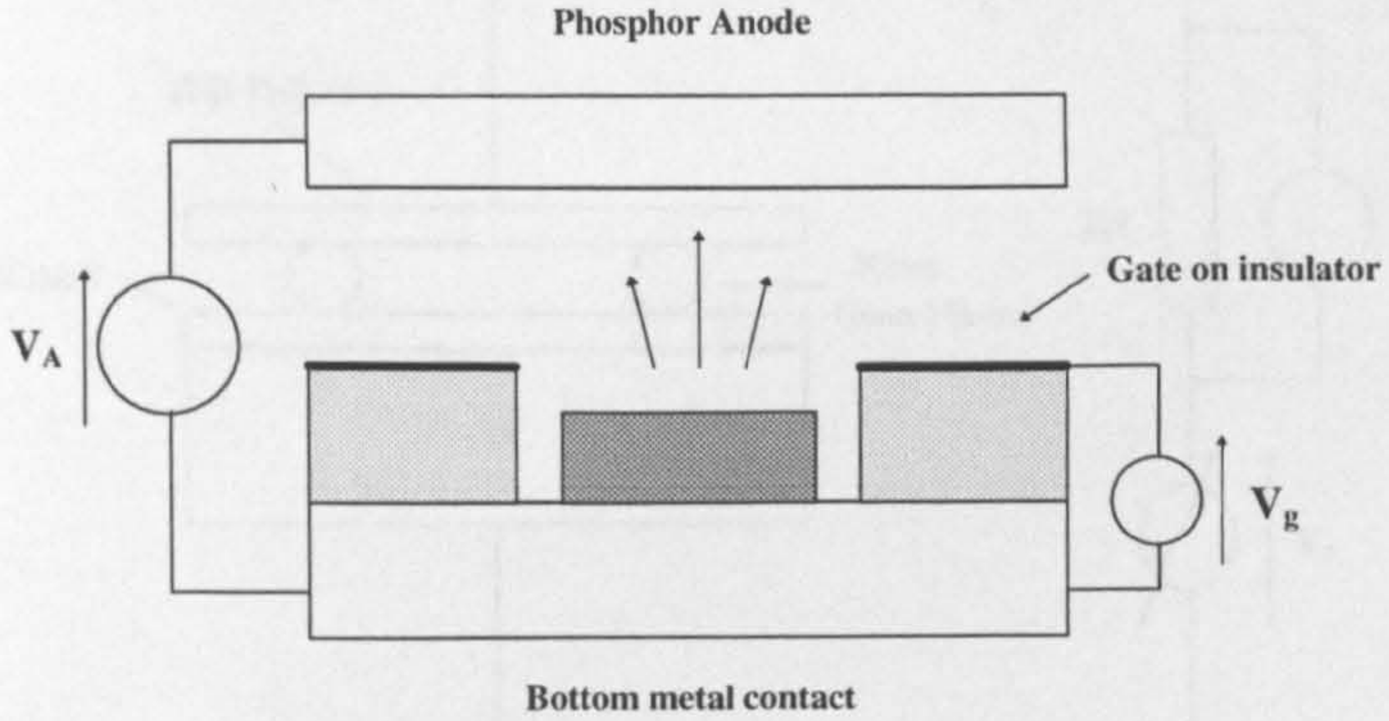

Figure 5.2: Schematic diagram of a flat panel field emitting display pixel. When a low electric field is applied on the gate electrode initially, electron emission from flat cold cathode is triggered. The emitted electrons drift in vacuum under the influence of the anode electric field to the phosphor anode. The gate arrangement enables the ability to switch the pixel on and off without switching the anode voltage.

5.1.4 Field Emission from a-C:H:N on n^+–Si

As shown in Fig. 5.3, an indium tin oxide (ITO) or aluminium coated glass was used as the anode electrode for measurements reported here. The emitting material was deposited on n^+-Si to serve as the cathode. The two electrodes were separated by thin glass fibre spacers (thickness $\approx$ 50 μm). A resistor ($\approx 1.2M\Omega$) was placed in series with the field emitting cell and variable voltage source circuitry to quantify the emitting current.

A *conditioning* sequence was necessary prior to repeatable emission for all films. That is, prior to achieving the lowest threshold field value, it was necessary to ramp the electric field up and down for several cycles. The field was

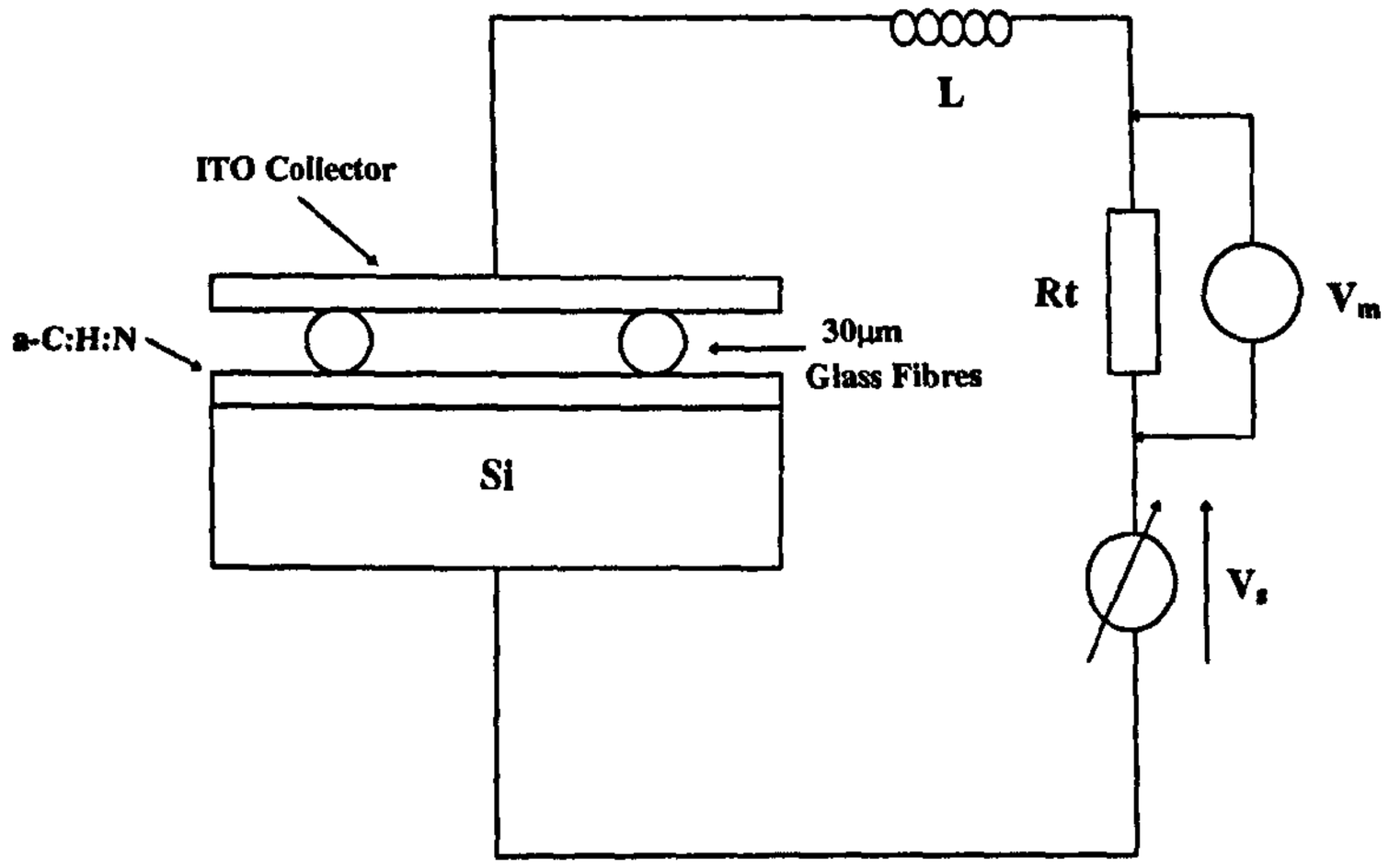

Figure 5.3: Schematic of the field emission monitoring set up. To extract the field emitting current the voltage across a resistor placed in series with the field emitting cell was measured. The inductor in series limits current surges and excludes possible microarcing during *conditioning*.

normally ramped up until electron emission was observed then reduced. After several cycles, a field value where repeatable emission occurs is achieved and this is taken as the threshold field value. This effect gives rise to a hysteresis in the conditioning I-V characteristics. Once this lowest turn on field, or the steady I-V curve is achieved, the *conditioning* process ends and the optimum state of emission is achieved. Sudden changes in the emission current can be readily observed during the emission process. These current surges may be attributed to preferential spot emission prior to removal of surface charge states via conditioning. An inductor of the order of 10mH is placed in series with the current loop in order to reduce micro-arcing. The transient potential drop across an inductor is given by

$$V_L = L\frac{di}{dt}$$

with usual notations.

so that when there is a sudden change in current (*i.e.* when $\frac{di}{dt}$ is high) the potential drop taken by the inductor increases making that across the emitting cell small. Hence the *runaway* of a current surge from a preferential emission site is suppressed.

5.1.5 Nitrogen Dependence of Turn on Threshold and Current Emitted

The field emission properties of a-C:H:N films deposited by HW PECVD with CH_4:N_2 ratio variation from 1:2 to 1:100 are shown in Fig. 5.4. It can be seen that the onset of the turn on threshold electric field reduces as the nitrogen content in the film increases. The emitted current density also increases with the nitrogen content at low fields, but saturates at high fields.

The normalised current density and applied electric field data plotted on Fowler-Nordheim axes is shown in Fig. 5.5. For low N content films the slope was found to be steep which decreased as the nitrogen content in the film was increased. The characteristics of the F-N plot in Fig. 5.5 are similar to those reported in literature [118]. As discussed in section 5.1.7, for steeper slopes, the barrier for field emission extracted from the F-N fit is highly dependent on the effective mass used in eqn. 5.2. However, the back contact barrier dominance observed in section 5.1.6 suggests that the electrons participating in emission process are *hot*, hence they are *heavy* electrons (*e.g.* $0.1m_o$), minimising the ambiguity in barrier height extraction.

The effect of nitrogen concentration on the threshold electric field for electron emission into vacuum and for the barrier seen by such electrons in a *n*-Si/a-C:H:N/vacuum/ITO is unlikely to be due to Fermi level movement across the band gap due to several reasons. First, the barrier heights were extracted assuming that the hot electron mechanism of emission are very low, so if it is dominated by Fermi level movement then the thermal effects should also be of similar orders. Second, such small changes in the Fermi level are not expected to change the band banding to such an extent that it is manifested as differ-

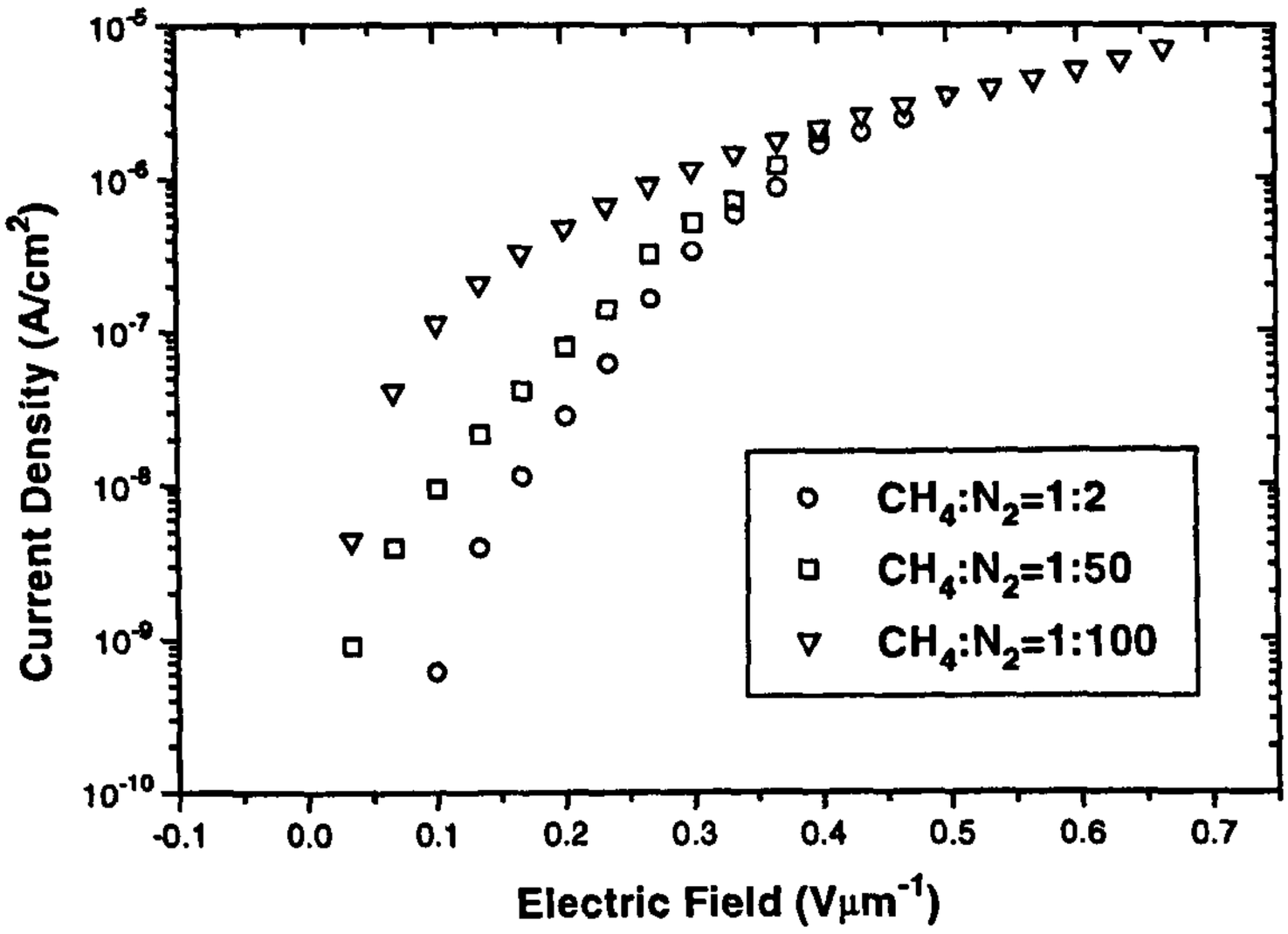

Figure 5.4: The normalised current is plotted against the applied electric field. The electric field quoted is the nominal field, calculated by dividing the applied anode-cathode voltage by the vacuum gap. For CH_4:N_2 ratios from 1:2 to 1:100, the turn on threshold electric field reduces while the high-field current density saturates.

ent threshold fields. Third, the shrinking of the band-gap for the highest N content film is not reflected greatly in any of the key parameters measured in field emission, suggesting that the observations made are not affected greatly by band structure changes. A closer look at the influence of nitrogen over changing material properties can be helpful in understanding the observations.

5.1.6 Dominant Barrier for Emission in a-C:H:N/n^+–Si system

The field emission characteristics of a-C:H:N, measured as described in section 5.4 are shown in Fig. 5.6. Films of ≈30nm were deposited on n^+-Si with CH_4 : N_2 ratio of 1 : 1. The average current density was found by taking the ratio of

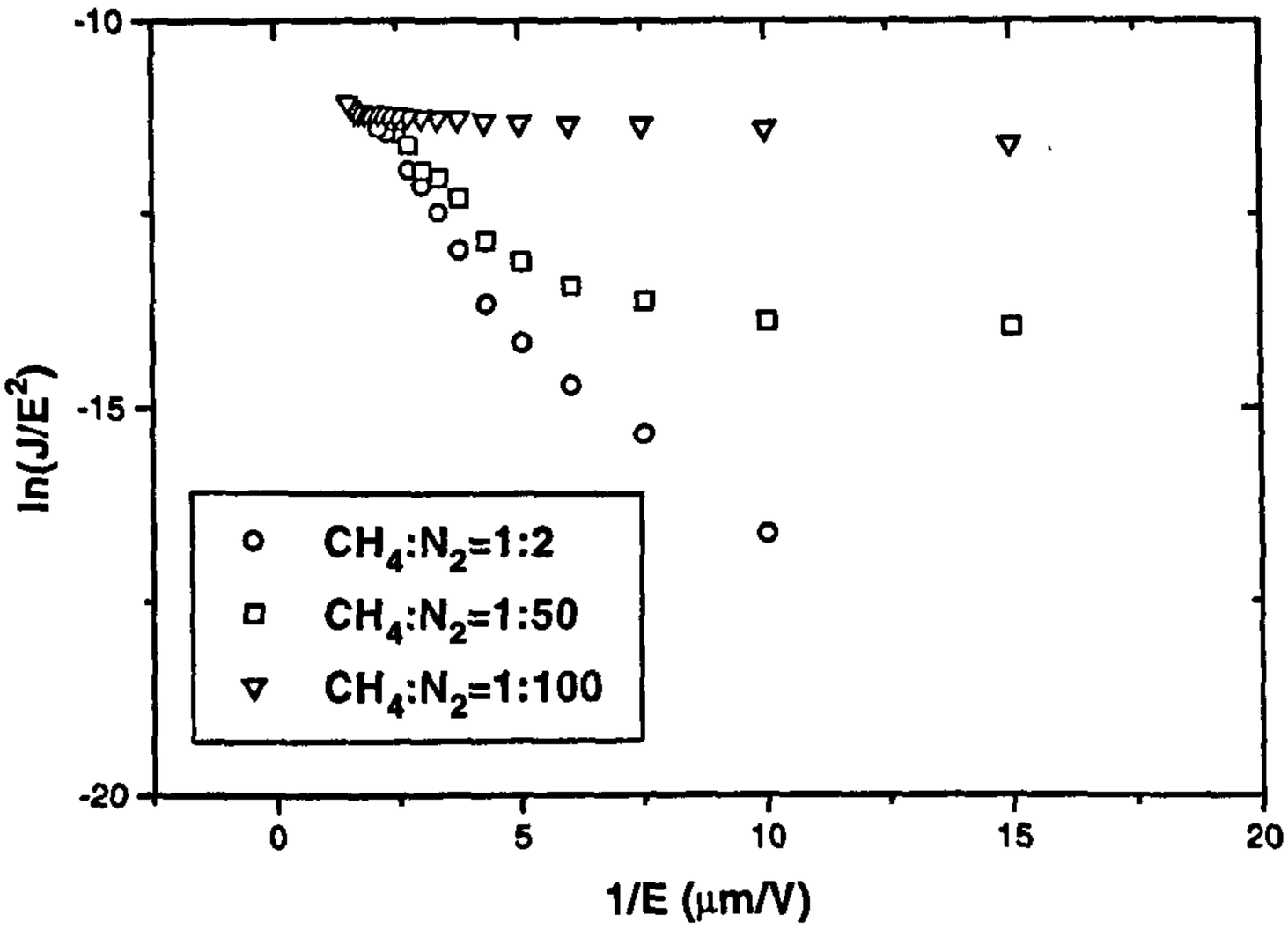

Figure 5.5: The Fowler-Nordheim behaviour of a-C:H:N films with CH_4:N_2 ratios from 1:2 to 1:100. The slope of the plot reduces with increasing N content indicating the influence of nitrogen over the dominant barrier for electron emission.

current monitored to the whole cathode-anode overlap area, assuming a uniform emission site distribution over the entire cathode. The electric field was taken to be the nominal field (*i.e.* the ratio between the applied voltage across the emitting cell to cathode-anode separation). Here it is assumed that the largest component of voltage is dropped across the vacuum gap.

When the emitted current density into vacuum from a-C:H:N and the nominal applied field are analysed according to the Fowler-Nordheim type equation, it takes the form shown in Fig. 5.7. The barrier as seen by the emitted electrons is characterised by the slope of the Fowler-Nordheim fit. When an electron effective mass of $0.1m_0$ is assumed the extracted barrier height is found to be 0.02eV. The influence of the effective mass of the electron on the barrier for emission is discussed in section 5.1.7.

When the anode is brought close to the emitting surface, the resulting struc-

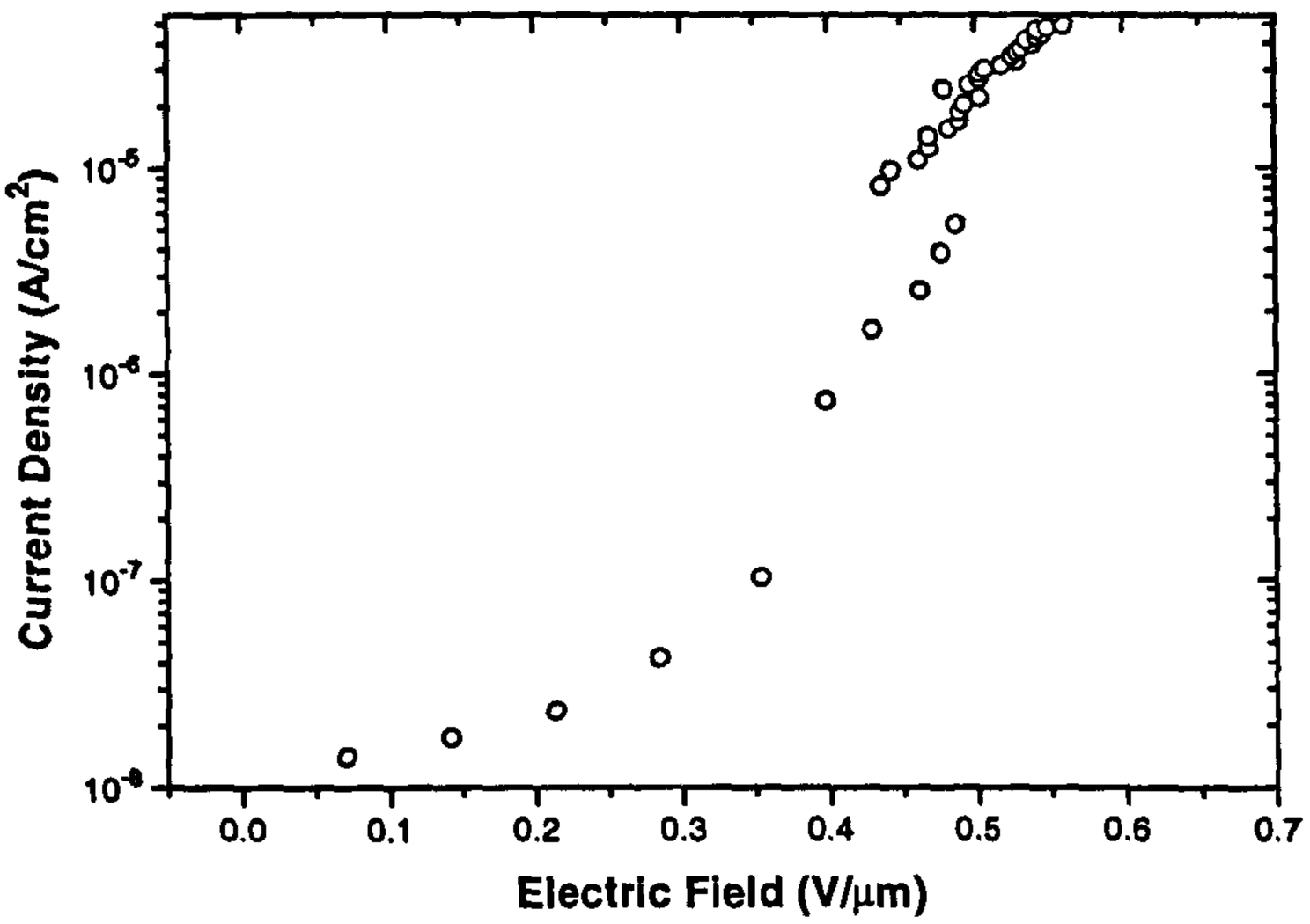

Figure 5.6: Electron emission characteristics of the *n*-Si/a-C:H:N/vacuum/ITO structure.

ture is *n*-Si/a-C:H:N/anode, so that the vacuum gap between the film surface and the anode is effectively eliminated. The structure *n*-Si/a-C:H:N/Au corresponds to this situation. The resulting current density versus electric field plot is shown in Fig. 5.8. The current density was found by taking the metal contact area as the effect area of conduction. The potential drop across the *n*-Si was neglected and the film thickness was taken to be the field separating distance.

The current in a Au/a-C:H:N/*n*-Si structure, with the Au biased positive with respect to the Si, was fitted to a Fowler-Nordheim type tunnelling mechanism as shown in Fig. 5.9. The transition barrier was found to be very low $\approx$ 0.07eV when an electron effective mass of $0.1m_0$ is assumed in the F-N equation.

When the data in Fig. 5.7 is taken together with that in Fig. 5.9, it is readily observed that the barrier seen by the electrons emitted into the vacuum from the a-C:H:N surface in first case and those collected by the gold electrode in the second case is very small and of the same order of magnitude. Given the fact that in both cases the back contact offered by *n*-Si substrate is of large

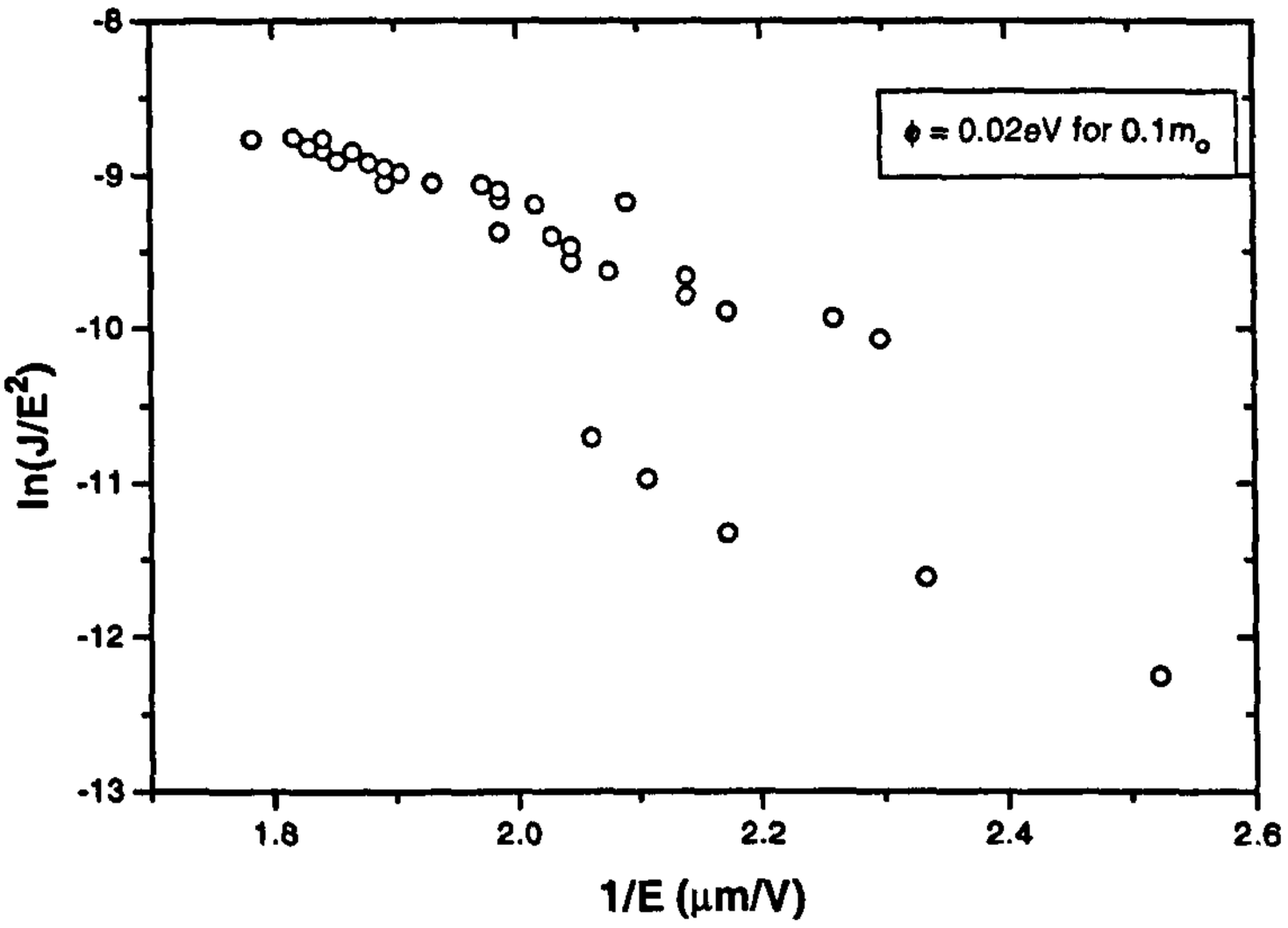

Figure 5.7: Fowler-Nordheim plot is shown. The extracted barrier height for an effective mass of 0. 1m$_o$ is 0. 02eV

area with very low contact resistance and the gold contact on top in the second case also offers ohmic contact on a-C:H:N with low contact resistance (as shown in section 2.2.4), the barrier observed should be at the *n*-Si/a-C:H:N interface. In this case the Fowler-Nordheim type characterises the tunnelling barrier at *n*-Si/a-C:H:N interface as illustrated in Fig. 5.1(c). Now the question to be answered becomes how the barrier at a-C:H:N/vacuum interface is overcome in the first case. If we take the field emission mechanism suggested in Fig. 5.1(c), then the barrier to electron emission from the a-C:H:N surface into vacuum can be almost completely overcome through electron heating in the conduction band due to the high electric field being dropped across the a-C:H:N layer. The results suggest that a high quality Si/a-C:H:N heterojunction can act as hot electron cold cathode with a minimal barrier to electron emission into vacuum from the a-C:H:N surface.

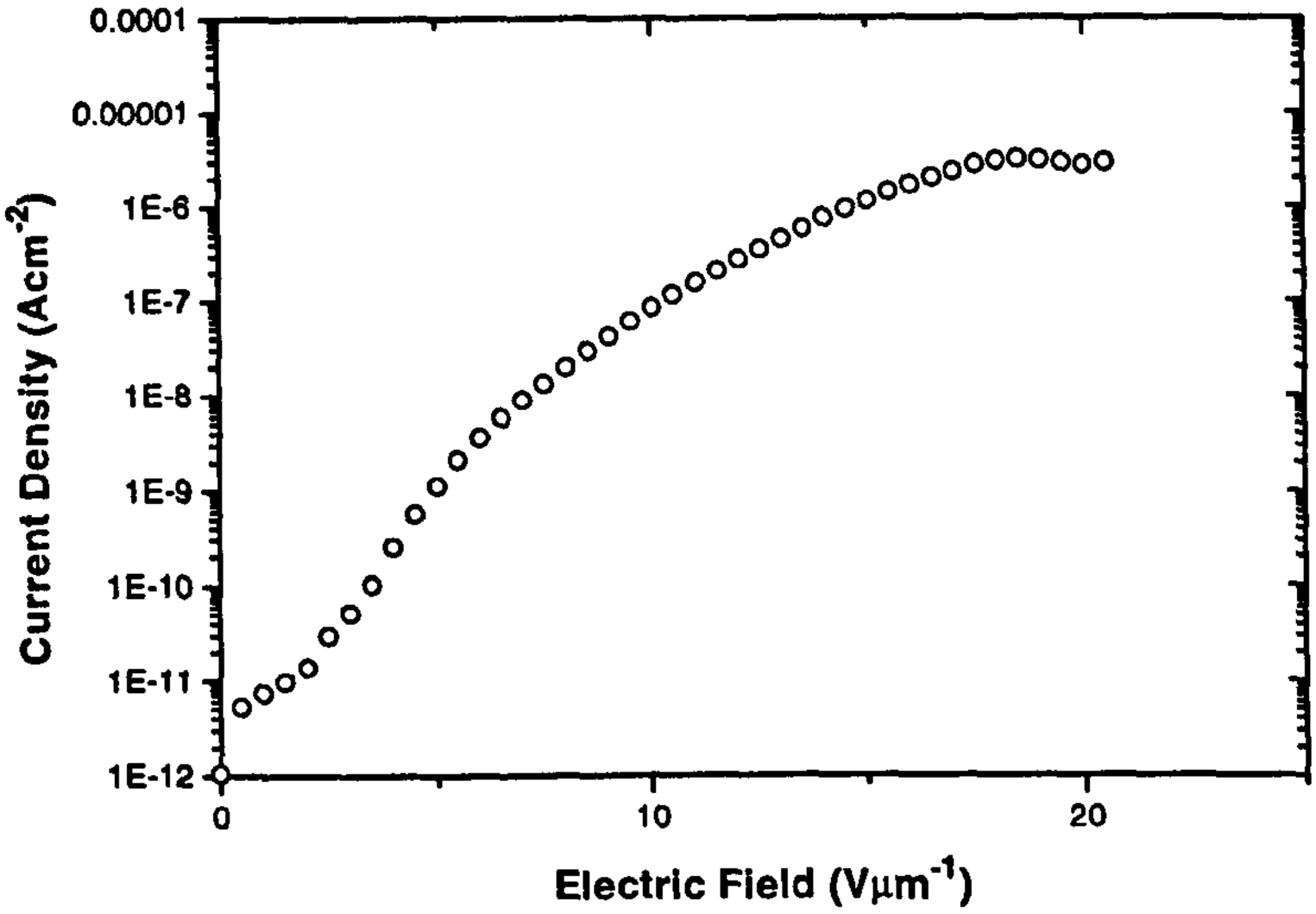

Figure 5.8: The current density versus electric field for Au/a-C:H:N/*n*-Si structure is plotted.

5.1.7 Influence of the Effective Mass of the Carrier on the Dominant Barrier

The plot of $\ln(\frac{J}{E^2})$ versus $\frac{1}{E}$ (Fowler-Nordheim type behaviour) gives a slope obtained by,

$$-\frac{4}{3\hbar}\sqrt{2m^*q}\,\phi^{3/2}$$

where m^* - the effective mass of the charge carrier, q - the charge and ϕ - the barrier seen by the carrier.

In a Fowler-Nordheim type fit, it is evident from the above expression that the barrier extracted from the slope is dependent upon the effective mass of the charge carrier among other things. In Fig. 5.10 a plot of the barrier extracted for a range of slopes against the effective mass factor of the charge carrier is shown. It can be seen that for relatively small slopes associated with conventional low barriers, the influence of the effective mass is smaller so that the barrier extracted

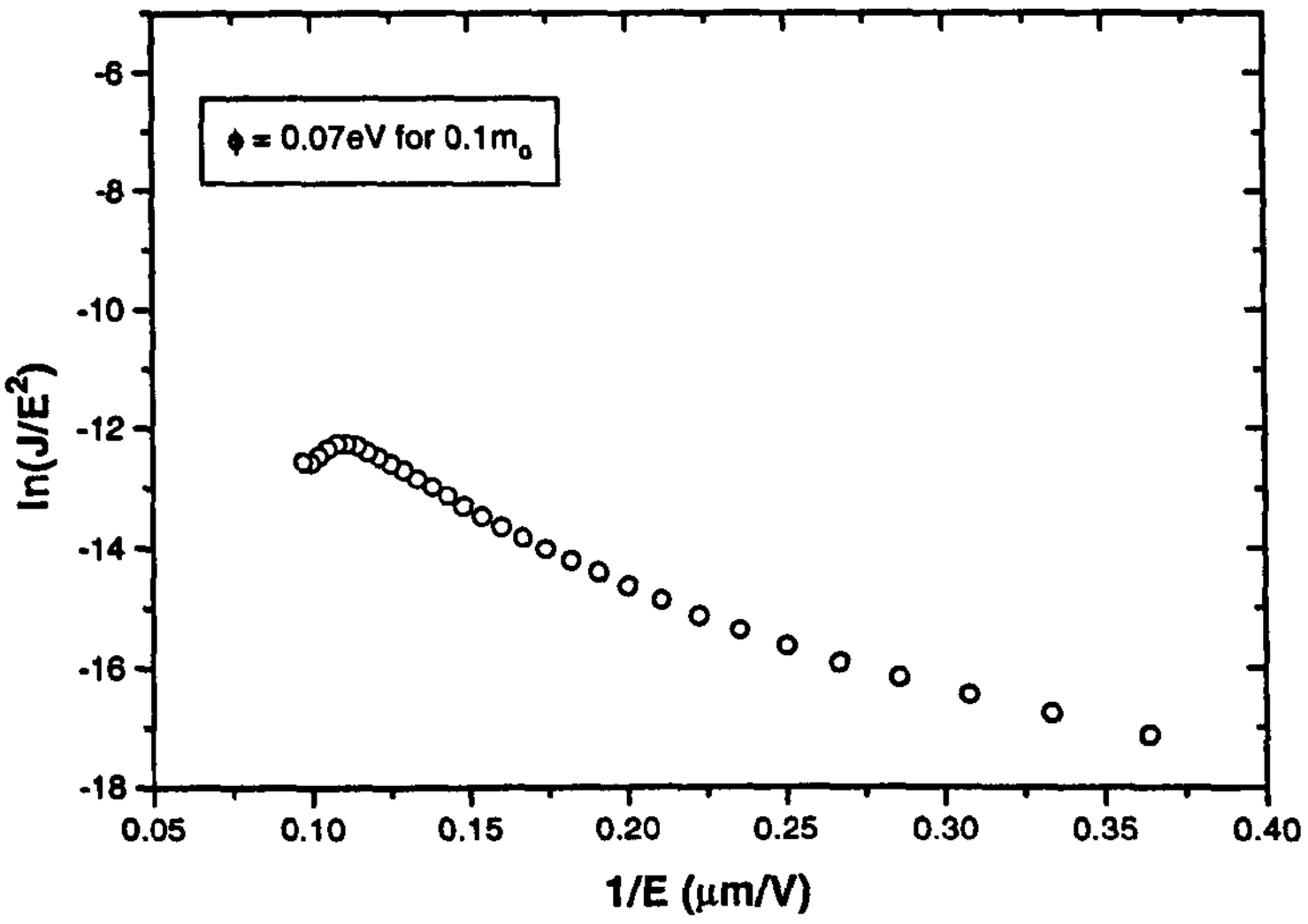

Figure 5.9: Fowler-Nordheim plot for Au/a-C:H:N/*n*-Si structure yields an extracted barrier height of 0.07eV for an effective mass of $0.1m_o$.

is almost independent of the effective mass of the carrier. However the case for the larger slope values is significantly different. The possible barrier height is heavily dependent on the value of the effective mass. As the effective mass reduces the extracted barrier height increases.

For *hot* electrons (*i.e.* electrons at energies higher than that of the bottom valley of the conduction band in the E-k diagram in the classical case), the second derivative is small, making them *heavy*. As seen in Fig. 5.10 for heavy charge carriers the deviation depending upon the value of the slope of the F-N fit is small. But if the emission process takes place from the bottom of the conduction band or from the top of the valence band, one has to be careful in extracting the barrier height since it is heavily dependent upon the effective mass of the charge carrier for such *light* particles.

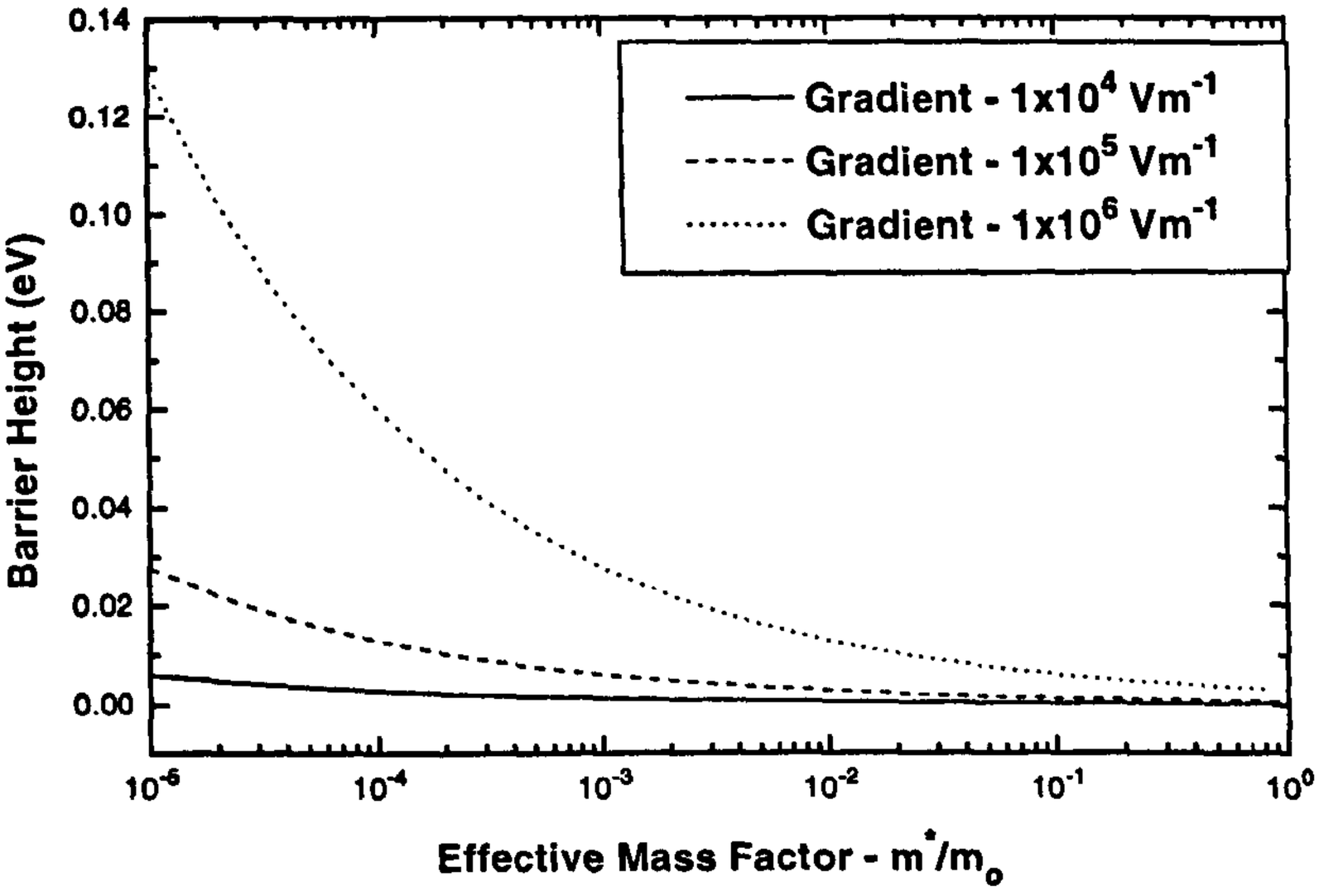

Figure 5.10: The possible barrier height extracted from three different slopes of the Fowler-Nordheim plot against the effective mass factor is illustrated. For shallower slopes effective mass dependence is negligible, but when slope is steep the deviation is large.

5.1.8 Does the Emitting Cell always Rectify ?

At times the emitting cell loses the rectifying nature expected for a vacuum diode. These instances are associated with heavy current emissions as well as deposition conditions. When such reverse conduction is detected, careful investigation of the anode under a optical microscope shows crater formation such as those illustrated in Fig. 5.11. However the cathode is free of any craters, and upon replacement with a new anode the normal rectifying operation of the cell can be resumed.

The fact that no craters are seen on the cathode, and its ability to comply with normal operation when a new anode is used suggests that the crater formation process should be on the anode itself, and no arcing has taken place between the two electrodes. The timing of this mechanism can give some insight

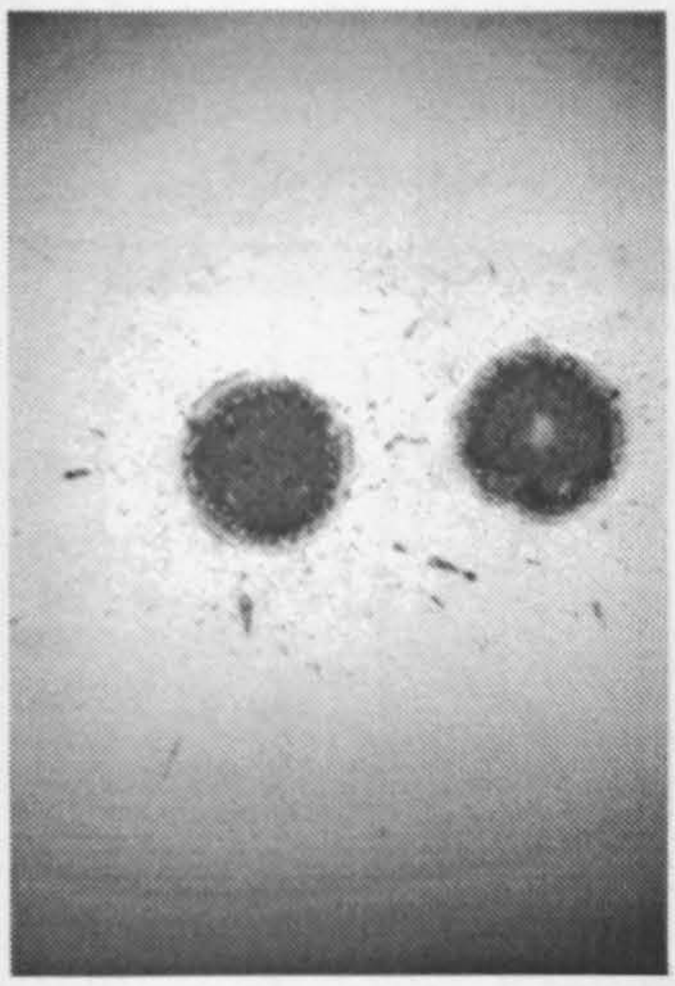

(a) The craters observed on the anode electrode of field emitting cell at the lowest magnification of X200.

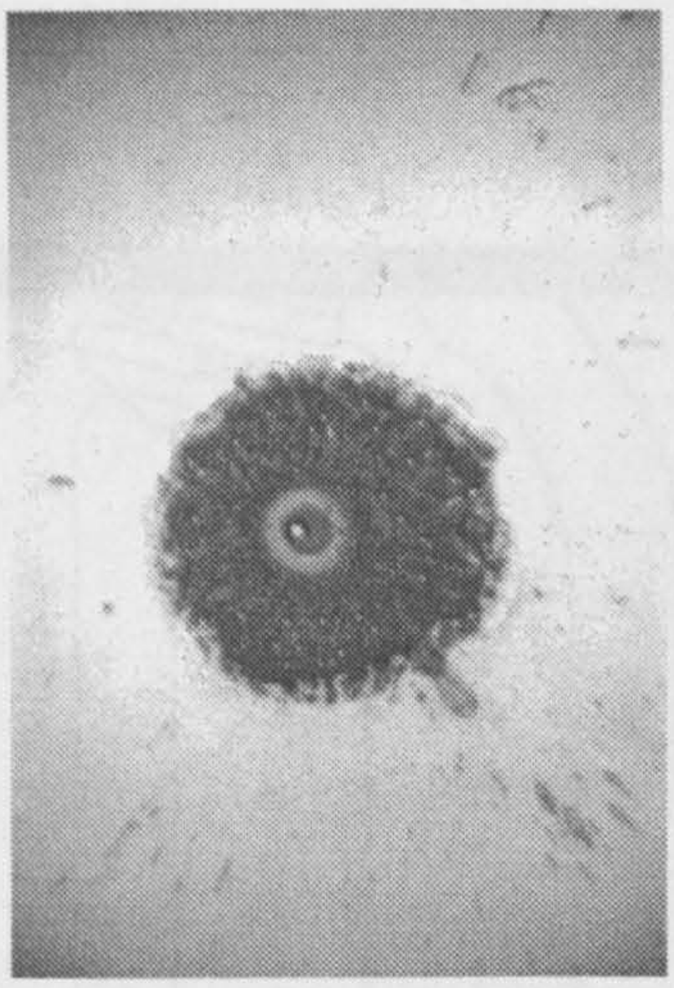

(b) A crater showing typical ridges and splash over associated with an arc.

(c) In large magnification of X630 sharp features inside and on the edge of the crater are evident.

Figure 5.11: For certain cathode types and when a large current density is drawn over a broad anode, a reverse current is observed. The loss of rectifying behaviour is associated with crater formation on the anode.

into a possible process of crater formation. If any vacuum breakdown were to occur, it is more probable during the *conditioning* phase of the measurement where the largest electric fields are applied. However, the craters were detected readily only after some emission current was seen in addition to some prolonged usage of the electrode.

As an example, consider a piece of macroparticle on the anode as shown in Fig. 5.12. The electric field line concentration on the particle can increase due to two factors. One is the geometric intensification. That is, if the macroparticle carries relatively sharp features compared to the flat anode, the potential contours concentrate together on the sharp feature. The other is the dielectric *amplification* indicated by,

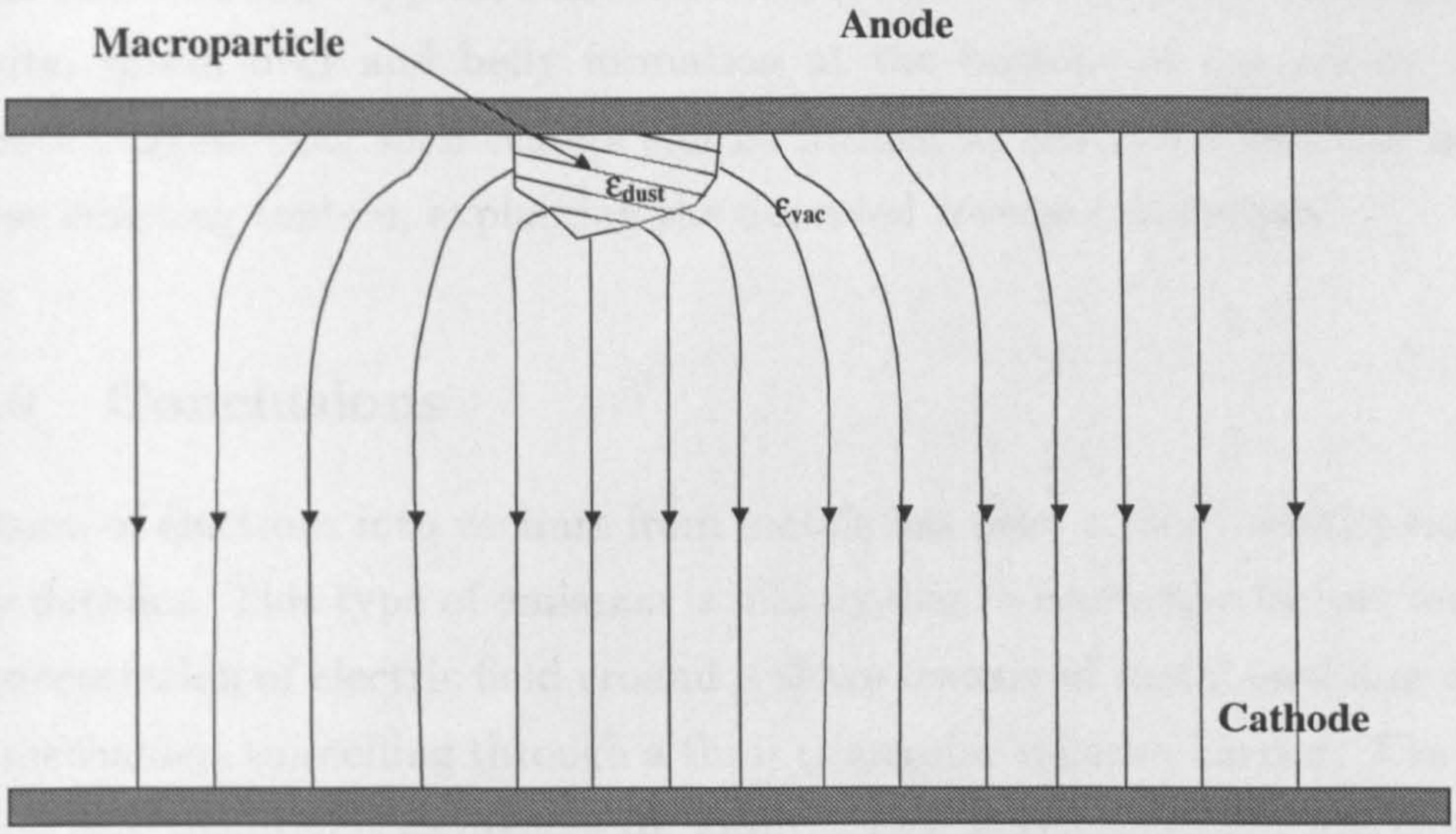

Figure 5.12: A macroparticle sitting on the anode modifies the vacuum environment for electric field lines in two ways. Due to geometric unevenness, potential contours tend to concentrate around the face of the particle causing the field lines to come together. In addition, the difference in permittivities also gather the field lines towards the particle. The combined effect brings additional emitted electrons from the cathode towards the particle.

$$\frac{\phi}{A} = \epsilon \vec{E}$$

where ϕ - flux, A - area, ϵ - permittivity and $\vec{E}$ - the electric field.

Since the macroparticle possesses a permittivity (ϵ_{dust}) higher than that of vacuum (ϵ_0) (*i.e.* $\epsilon_{dust} > \epsilon_0$) then $\phi_{dust} > \phi_0$ for the same electric field. The intensified field brings more emitted electrons onto the particle causing charge build up provided that the conduction capability is low enough. The limiting case of the charge build up is the potential increase on the particle is not large

enough to cause a discharge on to the anode in the form of a micro- arc. The craters observed show typical characteristics of micro-arcs, having ridges around the site, splash over and belly formation at the bottom of the crater. The evidence suggest that such craters can be formed as described and can act as reverse emitting centers, explaining the observed reverse conduction.

5.1.9 Conclusions

Emission of electrons into vacuum from metals has been under investigation for many decades. This type of emission is mainly due to geometric factors leading to concentration of electric field around a sharp feature of metal enabling quantum mechanical tunnelling through a thin- triangular vacuum barrier. The local electric field required is as high as $10^2 V\mu m^{-1}$. Due to the relatively low electron affinity of carbon based materials, they show field emission at low electric fields. Moreover such materials do not require sharp features to intensify the electric field, making possible their use as flat cathodes. An additional third electrode - the gate in a triode structure eliminates the high voltage switching necessary in a diode emitter when being used as a matrix addressed element in a display.

There are several models describing possible emission mechanisms. First to treat this behaviour theoretically were Fowler and Nordheim in 1928. Later their treatment was modified by others to describe different situations. When the temperature effects on field emission were understood, the concept of thermally assisted field emission was established. Even though the field emission phenomenon has been studied since 1928, which process describes the emission seen from flat cathodic materials in the most appropriate way is uncertain. A simple set up to monitor field emission from flat cathodes was illustrated.

When the anode structure is a *n*-Si/a-C:H:N heterostructurel cathode, the resulting arrangement is the same as having a metal electrode on the *n*-Si/a-C:H:N heterojunction (*i.e.* making up a *n*-Si/a-C:H:N/Au structure). The I-V characteristics measured from such an arrangement, fits into Fowler-Nordheim behaviour and the barrier height extracted from the slope of the plot is very low, 0.07eV for an electron effective mass of $0.1m_0$. The fact that a-C:H:N/Au forms

a low resistive interface as seen in section 2.2.4 and the Al back contact on *n*-Si is also of low resistivity suggest that the barrier seen is in fact between a-C:H:N and *n*-Si. The barrier extracted in a similar Fowler-Nordheim fit, electron emission in to vacuum out of *n*-Si/a-C:H:N cathode is also very low, 0.02eV for effective mass of $0.1m_0$. This leads to the deduction that the barriers measured can be those at the Si/a-C:H:N interface and that the barrier to electron emission from the a-C:H:N surface to vacuum can be almost completely overcome through electron heating in the conduction band due to the high electric field within a-C:H:N.

The influence of nitrogen in the a-C:H material was also discussed. It was seen that the field emitting threshold in the range of hundreds of millivolts per micron could be realised. As nitrogen content in the film increased the threshold field for electron emission reduced but the current density saturated almost at the same level at high fields. The slope of the F-N plot became less steep with increased nitrogen contents, in accordance with previous reports by other workers.

In addition, the influence of effective mass of the charge carrier on the emission barrier extracted from the F-N fit was discussed. It was established that the influence of the effective mass is greater for steeper slopes and for the lighter effective mass regime (*i.e.* for charge carriers in band valleys of the E-k diagram). For hot electrons the effect is less significant since they are *heavy* electrons at energy levels above the valley region.

The reverse current observed in the field emitting cell under certain film conditions and after extracting large emission currents is discussed in terms of microarcing on the anode due to macroparticle charging.

5.2 Passivation in Power Semiconductor Devices

5.2.1 Background

Unarguably the electrode is the essential bridge between the semiconductor material and the outside world as far as relatively low frequency interactions are concerned. The electrical nature of the electrode is characterised by two main parameters, namely the electrode resistance and the capacitance of the electrode. It is necessary to design the electrodes so that these parameters are suited for a given application. These parameters in general are mainly geometry dependent. For example diode structures used in microwave applications require a reduced contact capacitance in order to maintain better high frequency response. This is readily achieved by a point metal-semiconductor contact. But the trade off is that point contacts suffer from high contact resistance given by,

$$R_c = \frac{\rho}{2\pi r_0}$$

where ρ - resistivity and r_0 - the radius of the hemispherical point contact.

making it a current limiting contact. Hemispherical contacts show a better electric field distribution at the metal-semiconductor interface.

In order to incorporate mass produced electrode formation into general semiconductor fabrication, metalization is the most commonly used process. Metal-semiconductor contacts are formed by several processes such as thermal evaporation, electron-gun evaporation, chemical decomposition, sputtering and electro plating etc. Generally these electrodes are planar and the contact resistance is given by

$$R_c = \frac{nkT}{qJA_j}$$

where n - carrier density, k - Boltzmann's constant, T - temperature, q - carrier charge, J - current density and A_j - effective contact area.

Contacts formed by metal on a semiconductor to obtain an electrode have to be either a heavily doped tunnelling junction or a large area contact dominated

by interface state conduction. Depending upon the geometric shape of the electrode - especially the shape of the edge, the electric field distribution pattern penetrating into the semiconductor layer can be influenced.

The breakdown voltage of a semiconductor device can be determined by the high field breakdown occurring either within the interior of the device structure or at the edge of the device. It is important to take measures in order to minimise the breakdown at the edge of the device so that the optimum breakdown voltage for a particular device design is reached.

5.2.2 The Concept of Edge Termination and Surface Passivation

The schematic diagram of a p-n junction obtained by planar diffusion is illustrated in Fig. 5.13(a). Use of a rectangular window to perform the diffusion process results in cylindrical junctions at the straight edges and spherical junctions at corners. As shown the depletion boundary follows the profile of the junction, resulting in electric field concentration at the edge [161].

Applying the Poisson's equation in cylindrical coordinates to the cross-section of the cylindrical portion of the junction shown in Fig. 5.13(b),

$$\frac{1}{r}\frac{d}{dr}\left(r\frac{dV}{dr}\right) = -\frac{1}{r}\frac{d}{dr}\left(r\vec{E}\right) = -\frac{\rho}{\epsilon} = -\frac{qN_D}{\epsilon_s} \tag{5.5}$$

where $V(r)$ - the potential distribution, $\vec{E}(r)$ - the electric field distribution, ρ - charge concentration and N_D - donor concentration. Integration of eqn. 5.5 with the boundary condition that the electric field is zero at the depletion boundary r_d gives,

$$\vec{E}(r) = -\frac{1}{2}\frac{qN_D}{\epsilon_s}\left(\frac{r_d^2 - r^2}{r}\right) \tag{5.6}$$

For $r = r_j$, the electric field at the junction $\vec{E}(r_j)$,

$$\vec{E}(r_j) = -\frac{1}{2}\frac{qN_D}{\epsilon_s}\left(\frac{r_d^2 - r_j^2}{r_j}\right) \tag{5.7}$$

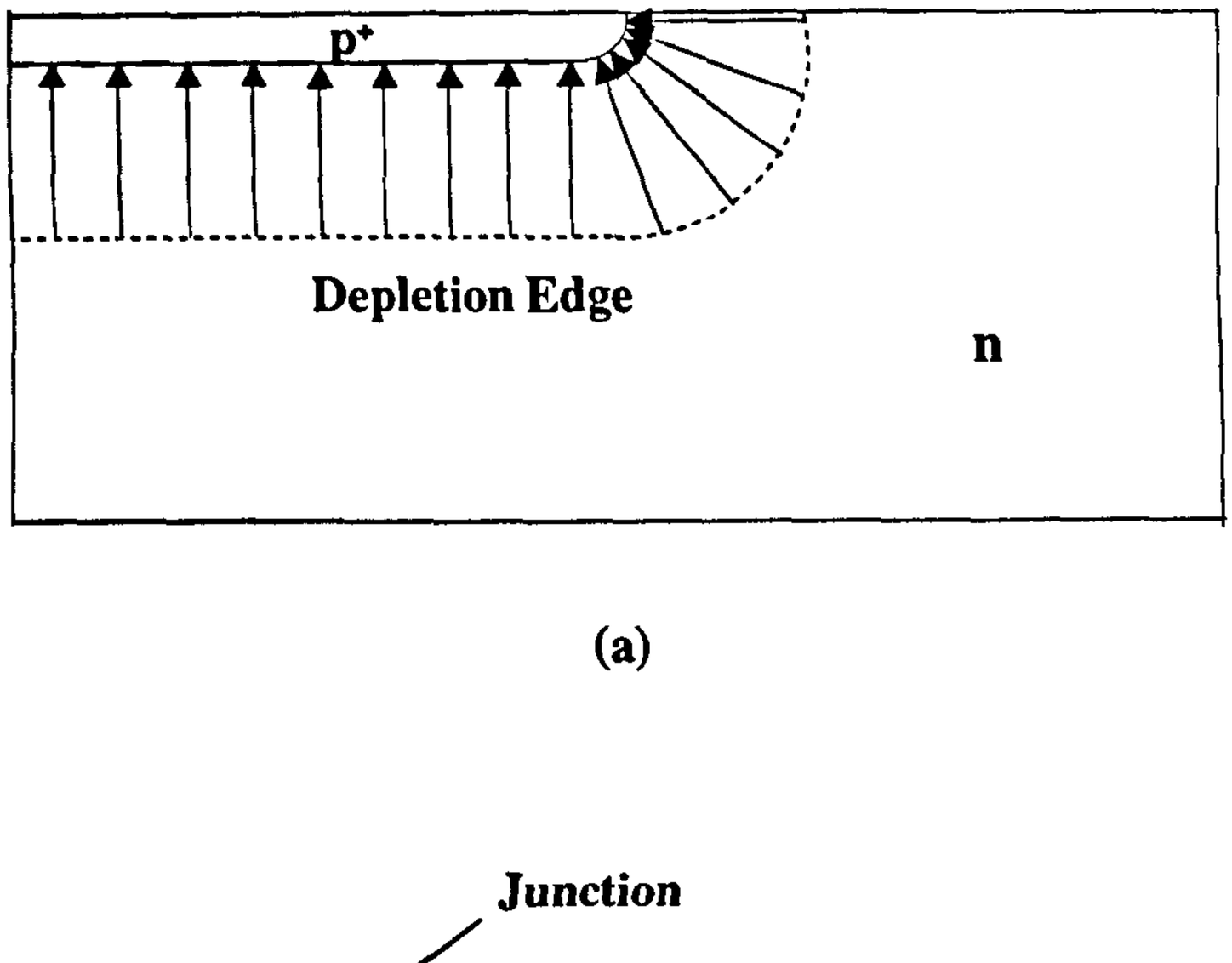

Figure 5.13: Schematic diagram of the electric field distribution of a p^+/n junction. The electric field can rise at the edge of the junction due to the depletion boundary curvature. On the cross-section of the junction, r_j and r_d are the junction radius and the depletion boundary curvature, respectively.

$\left|\vec{E}(r_j)\right|$ is the maximum electric field. When $r_j \ll r_d$, the maximum electric field at the cylindrical junction is given by,

$$\vec{E}_{Cyl} \approx -\frac{1}{2}\frac{qN_D}{\epsilon_s}\frac{r_d^2}{r_j} \tag{5.8}$$

Using the Poisson's equation in spherical coordinates, the maximum electric field at the spherical portion of the junction can be derived as follows,

$$\frac{1}{r^2}\frac{d}{dr}\left(r^2\frac{dV}{dr}\right) = -\frac{1}{r^2}\frac{d}{dr}\left(r^2\vec{E}\right) = -\frac{\rho}{\epsilon} = -\frac{qN_D}{\epsilon_s} \tag{5.9}$$

Integrating Eqn. 5.9 using the same boundary conditions as in the cylindrical case, and the maximum electric field at the junction for $r_j \ll r_d$ is given by,

$$\vec{E}_{Sph} \approx -\frac{1}{3}\frac{qN_D}{\epsilon_s}\frac{r_d^3}{r_j^2} \tag{5.10}$$

From equations 5.8 and 5.10,

$$\vec{E}_{Sph} \approx \frac{2}{3}\frac{r_d}{r_j}\vec{E}_{Cyl} \tag{5.11}$$

When $r_j \ll r_d$, it can be seen from Eqn. 5.11 that the maximum electric field occurs at the spherical portion of the junctions. *i.e.* at the corners of the p^+ region. The electric field in the planar region of the junction, $\left|\vec{E}_p\right| = qN_D r_d/\epsilon_s$ is the lowest.

The rise in electric field due to crowding of potential lines is characterised by the curvature of the depletion boundary as seen in Fig. 5.13(a). There are two basic types of processes involved in modifying the depletion boundary curvature. First, the *planar termination* techniques, based upon masked diffusion processes are used.

One such process is to deploy another p^+ diffusion region around the junction, known as the *floating field ring*. As the name implies the p^+ ring induces an additional depletion layer by means of the floating potential acquired. When such a ring is placed at the optimal distance away from the main junction, it is possible to planarise the depletion boundary curvature of the main junction, by means of the merger of two depletion regions as illustrated in Fig. 5.14(a).

In practice, a number of such rings are used based on the voltage rating of the device.

Part of this approach is to modify the depletion boundary curvature by applying an appropriate voltage on an additional electrode, placed next to the edge of the junction, separated by an oxide later. This technique is known as the use of a *field plate*. Generally field plates are employed in conjunction with floating field rings to enhance the stability of the breakdown voltage (see Fig. 5.14b).

The other process is to remove the material in the vicinity of the junction in a selective manner so as to maintain charge balance. The depletion layer in the low doped side of the junction is extended away from the interface, manifesting a reverse curvature in the depletion boundary. Since it is necessary to remove material to form a taper, the technique is known as the *beveled termination*.

To use any of these techniques effectively, the surface of the device must be kept free of residual surface charge. Especially since the the charge density of stray surface charge can be comparable with that of the lightly doped region in which the depletion layer extends in high voltage semiconductor devices. The effect of the depletion region modified by the edge termination technique tends to cease under influence of the surface charge. To overcome the surface charging effect, a layer of another material is deposited on the surface. This is known as a *passivation* layer. The most common materials used are, rubberised materials, organic polymers, silicon dioxide and silicon nitride. It has been found that by introducing a semi-insulating coating such as semi-insulating polycrystalline silicon film on the surface, the potential on the p^+ diffused region can be extended beyond the junction via ohmic current flow in the SIPOS layer [162].

5.2.3 Passivation from a-C:H and a-C:H:N films

The growth process of a-C:H and a-C:H:N films in inductively coupled PECVD process can be seen as a layer by layer deposition based on the the nature of energy possessed by the active species participating in growth. Inductively coupled plasmas carry predominantly *state* energy of the particular species rather

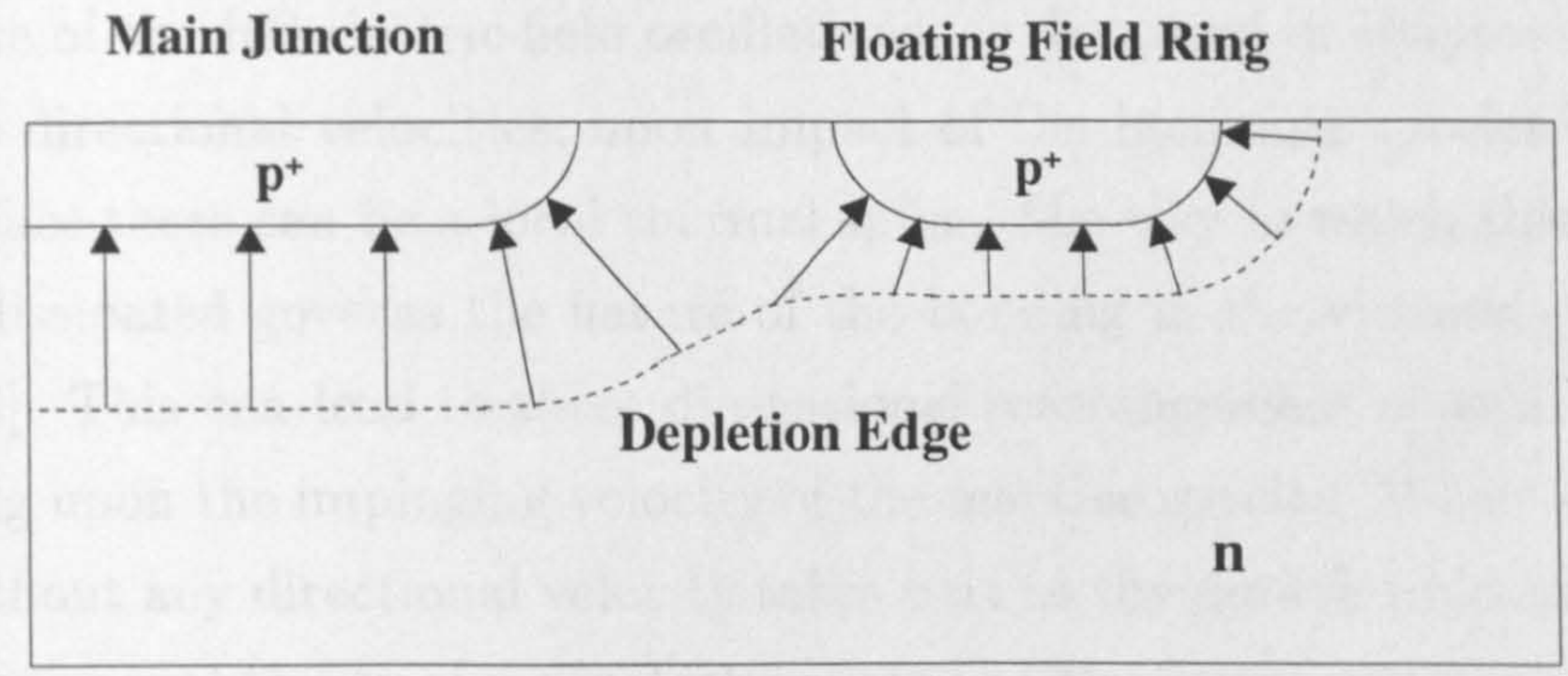

(a)

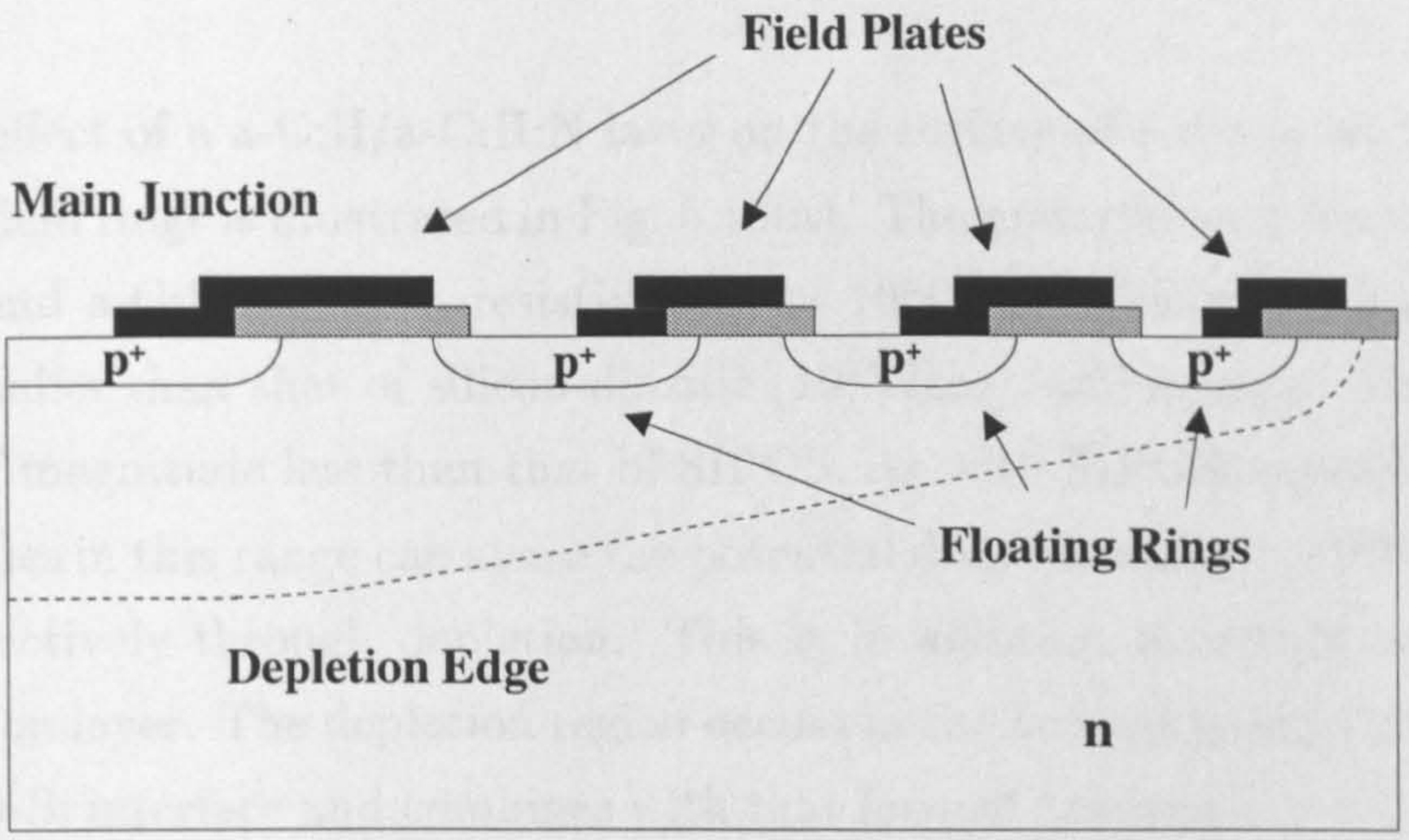

(b)

Figure 5.14: The placement of a diffused floating field ring can reduce the field concentration at the edge of the junction. Use of multiple floating field rings in conjunction with field plates results in a smooth depletion edge.

than kinetic energy as in the arc plasma or potential energy which is subsequently converted to kinetic as in the capacitively coupled case. This is due to the nature of the RF electric field oscillations, as discussed in chapter 1. When there are directional velocities, upon impact of the incoming species with the fresh surface there can be a local thermal spike. The way in which this thermal spike is dissipated governs the nature of the bonding in the vicinity of the impact [163]. This can lead to three dimensional rearrangement of local bonding depending upon the impinging velocity of the reactive species. When a reactive agent without any directional velocity takes part in the growth process, there is much smaller probability of a penetration into the film, and bondings take place beneath the surface. In ICPECVD, the growth process is on the surface leading to clustering of sp^2 sites as proposed by Robertson *et. al.* [136]. The resulting a-C:H (a-C:H:N) is highly resistive even though the sp^2 (graphitic) content is $\approx 50\%$.

The effect of a a-C:H/a-C:H:N layer on the surface of a diode with multiple floating field rings is illustrated in Fig. 5.15(a). The material used for passivation (a-C:H and a-C:H:N) has a resistivity of $> 10^8 \Omega$cm. This resistivity value is much smaller than that of silicon dioxide ($10^{14}\Omega$cm), and is approximately two orders of magnitude less than that of SIPOS. As with SIPOS, materials having resistivities in this range can share the potential drop around p^+- diffused region more effectively through depletion. This is in addition to acting as a charge passivation layer. The depletion region occurs in the heterojunction formed at a-C:H:N/*n*-Si interface and combines with that formed between the substrate and the field ring. The over all effect is the efficient distribution of electric field along the combined depletion region minimising the undesired field concentration.

The behaviour of the bevel terminated diode with a-C:H/a-C:H:N passivation layer is shown in Fig. 5.15(b). In this case also the combination of the heterojunction formed at the a-C:H:N/Si interface and the potential distribution across the a-C:H/a-C:H:N layer, introduces a smooth depletion boundary formation.

The residual charge density measured at the a-C:H:N/Si interface is negligible compared to the typical doping density of 10^{14}cm^{-3} in Si used for high

voltage devices [164]. In addition to act as an effective field distributing layer, a-C:H/a-C:H:N has been found to act as a very effective barrier to surface charge compared to the usual passivation materials. The films studied here (a-C:H and a-C:H:N) have a breakdown fields of $\approx 2.7 \times 10^6 \mathrm{Vcm}^{-1}$, in contrast that for Si is $3 \times 10^5 \mathrm{Vcm}^{-1}$. Which gives further stability in the breakdown process.

The table 5.1 shows the breakdown voltages and leakage currents for high voltage diodes designed to operate at 4.5kV when a-C:H or a-C:H:N is used for electrode passivation. These diodes have been fabricated by GCE-Plessy Power Semiconductors, and the a-C:H/a-C:H:N was deposited by the author on the complete device structure. Three types of films act well as passivation layers at 25°C. Out of these the film deposited with CH_4:N_2 = 1:4 survives only upto 4kV at 125°C. The film deposited with CH_4:N_2 = 1:1 fails. The reverse leakage current is in the range of ≈60mA for both operating temperatures indicating that the passivation layer of these CH_4:N_2 compositions do not contribute significantly to the enhancement of reverse leakage current. However, this level of leakage current suggests that the passivation layer may not be completely depleted, and may have some current flowing through it. The leakage currents for other compositions are less than 10mA at 25°C (The forward current rating of the diode is >1kA!). The film with highest nitrogen concentration shows the least leakage after continuous voltage stressing at 4.6kV and 125°C in a 100% humidity atmosphere for 72 hours. All the other passivation layer materials tested by the diode manufacturer failed the test at 125°C in 100% humidity. The measured film properties do not offer clear insight strong enough to differentiate among different growth parameters. However it should be noted that with certain types of a-C:H:N and a-C:H, the device exceeds the design limits for the diodes.

5.2.4 Conclusions

At the beginning of this section we looked at the different techniques used in device passivation and termination. It is seen that the use of a depleted semiconductor type dielectric layer in the vicinity of the junction provides the most

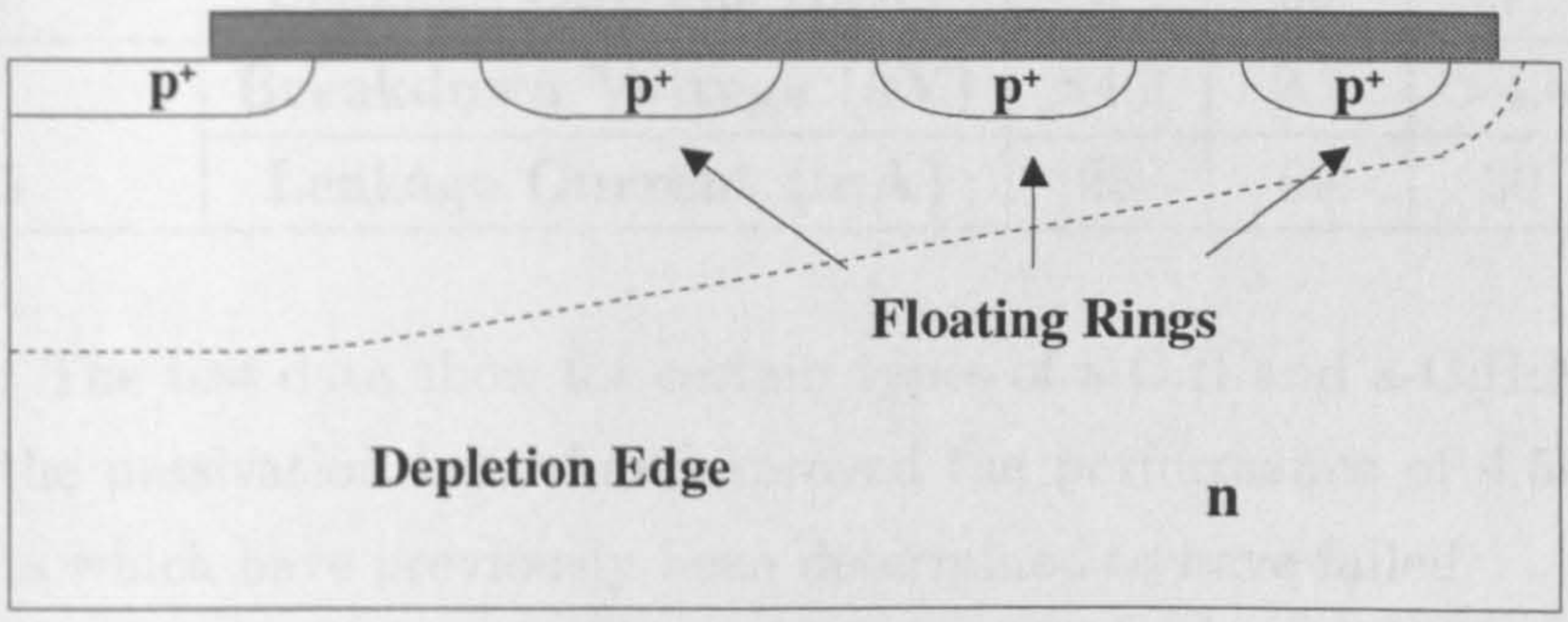

(a)

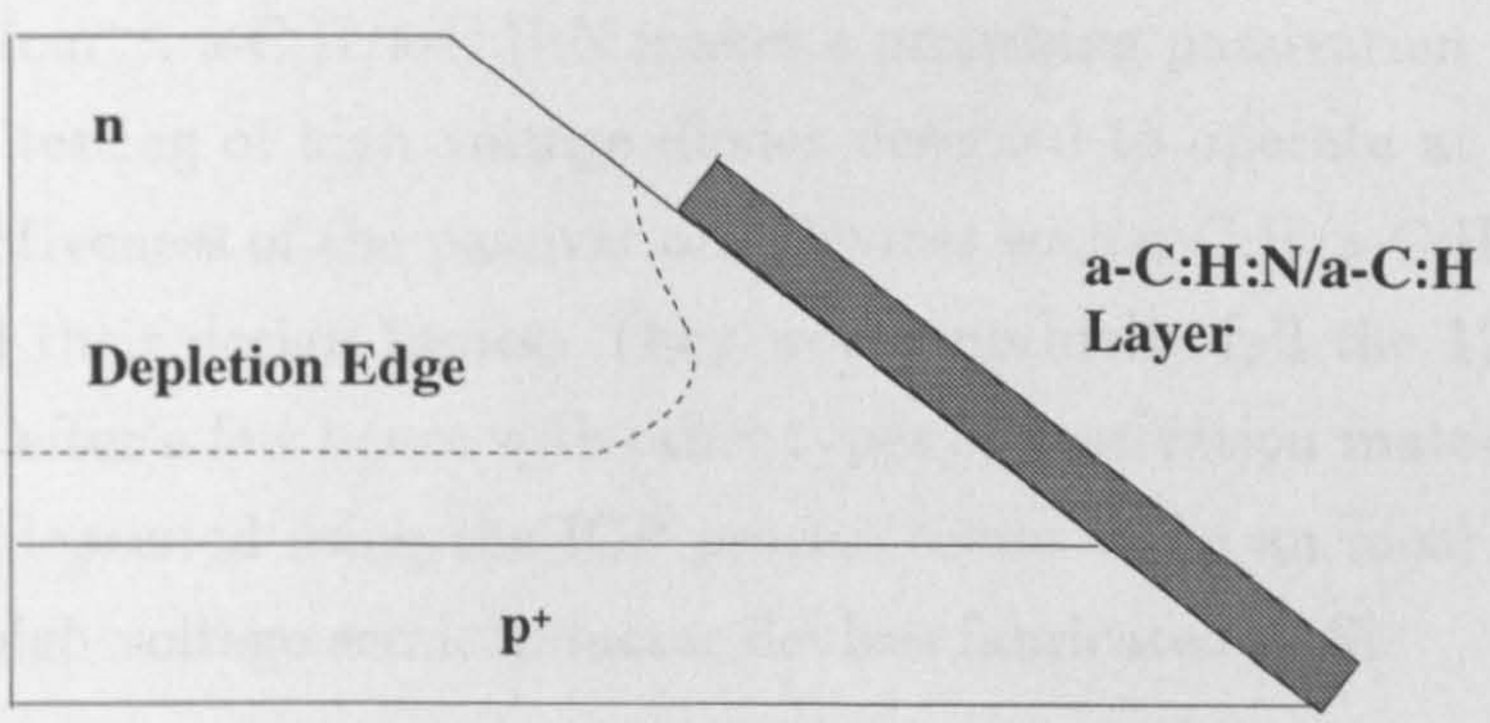

(b)

Figure 5.15: The effect a-C:H/a-C:H:N layer on the curvature of the depletion boundary in planar termination is in (a). That on a beveled termination is shown in (b)

Test Temperature (°C)		Precursor Ratio CH_4:N_2:He			
		1:0:0	1:1:0	1:1:1	1:4:0
25	Breakdown Voltage (kV)	6.0	3.7	>4.6	>4.6
	Leakage Current (mA)	8	60	7	4
125	Breakdown Voltage (kV)	>4.6	2.7	>4.6	4.0
	Leakage Current (mA)	25	60	30	8

Table 5.1: The test data show for certain types of a-C:H and a-C:H:N employment as the passivation layer has improved the performance of 4.5kV power diode units which have previously been determined to have failed.

efficient method of passivation and termination.

a-C:H and a-C:H:N grown in inductively coupled PECVD having resistivities of the order $\approx 10^8 \Omega$cm are suitable semiconducting dielectric materials for high voltage device passivation. Taken together with the breakdown threshold field of $\approx 2.7 \times 10^6 \mathrm{Vcm}^{-1}$, a-C:H/a-C:H:N makes a promising passivation material.

Industrial testing of high voltage diodes designed to operate at 4.5kV confirms the effectiveness of the passivation. Devices with a-C:H/a-C:H:N passivation exceeded their design limits. They would normally fail the 125°C, 100% humidity test after a few hours with other types of passivation materials. a-C:H and a-C:H:N deposited using the ICP process seems to be an ideal passivation material for high voltage semiconductor devices fabricated in Si.

Chapter 6

Conclusions and Suggestions for Future Work

In this chapter, the conclusions drawn out of present work and directions for future work to follow in order to gain a better understanding of ICPECVD and HWPECVD deposited a-C:H and a-C:H:N, and for better utilisation of the unique ability of resonant energy transfer in a helicon wave excited plasma, are presented.

The electronic properties and optical properties of a-C:H and a-C:H:N, deposited in inductively coupled PECVD and in helicon wave excited plasma are presented in this thesis. The design and the implementation of the helicon wave excited plasma system is also presented.

Towards the beginning of the study the properties of heterojuctions formed on Si were investigated to understand the nature of the interface. It was found by analysis of C-V characteristics, that by optimising plasma conditions, almost ideal interface behaviour can be accomplished in ICPECVD. Heterojunction conduction was dominated by Fowler-Nordheim type electron tunnelling in the a-C:H:N/n-Si structure and hole tunnelling in the a-C:H:N/p-Si structure. The temperature dependence of bulk conductivity revealed localised tail state conduction originating from deep π_N states at low temperatures, and the thermal activation of relatively delocalised extended states associated with shallow π_N and π_C states at high temperatures. Gold was identified as a suitable electrode

material on a-C:H:N. The frequency dependence of Au/a-C:H:N/p-Si followed the existing MCS model with slight modification to polarisation parameter. The highest frequency response, known to date, for a-C, 13MHz, was recorded. This was the limit of the measuring apparatus.

The temperature dependence of absorption gave further evidence to thermal activation from relatively deep states. The change in absorption occurred at the same temperature at which the electrical conduction transition took place. The investigation of the low optical absorption region gave evidence for optically inactive band gap states. The nitrogen and the optical band gap dependencies of PL indicated the existence of N associated recombination centres. A twin recombination mechanism at localised tails and N associated centres was suggested to understand the observed behaviour. Lack of electric field quenching of PL indicates that the recombination centres are highly localised, and that they do not interact with each other.

The feasibility of sustained N_2 excitation as predicted theoretically, in $X^1\Sigma_g^+ \rightarrow C^3\Pi_u$ transition was successfully demonstrated by optical emission analysis and also by plasma properties. This gave convincing evidence for the capability of selective energy transitions in a helicon wave plasma. It was seen that the film properties also have strong changes at the predicted resonant energy transfer point owing to selective excitation of N_2.

Passivation of high power Si devices and the electron field emission are identified as potential areas where a-C:H and a-C:H:N are useful. It was suggested that the dominant barrier for electron emission into vacuum is at the a-C:H:N/n-Si interface. The high resistivity and the low charge density shown by ICPECVD deposited films were proposed as the key features which lead to the superior passivation properties measured.

In the future, the following points should be considered,

- In the present study, the upper limit of the frequency response was limited by the instruments capability. It would be interesting to find out the *real* cut-off frequency of Si/a-C:H:N heterojunction diodes using a C-V measurement beyond 13MHz.

- The optical band-gap did not change significantly with RF power. This suggests the non-directional energy of plasma species in ICPECVD does not influence significantly the densification of the material. However, this leads to a material relatively free of charged defects as indicated by the C-V behaviour. In order to change the densification, a grid type electrode biased negative and placed just above the substrate can be used.

- The presence of N related deep electronic states is indicated by its temperature dependence of conductivity. The N dependence of PL peak energy, and the redshift in PL peak energy with band gap can be further verified by the use of a suitable source that can excite above band gap energies.

- A weak *visible* electroluminescence was observed in a *p*-Si/a-C:H:N/Au-*transparent-contact* structure when *p*-Si was biased positive with respect to Au. This is thought to be due to hole injection from *p*-Si and electron injection from the Au into the a-C:H:N. To understand the origin of EL in this structure, a more efficient method of photon collection and analysis is necessary. A multichannel OES with CCD photo-collectors would be suitable.

- The continuous excitation of N_2 in $X^1\Sigma_g^+ \rightarrow C^3\Pi_u$ energy transition demonstrated can be utilised in an optical cavity tuned for 337.1nm UV laser emission. Two quartz windows set at the Brewster angle on either end of the plasma tube and two aligned UV mirrors are necessary.

- As suggested in chapter 4, three separate resonant excitations can be employed in the same plasma chamber in order to achieve selective energy transfer in different plasma species simultaneously - in this case say CH_2^+, N^+ and N_2^*. The helicon antenna lengths and the intensity of the axial magnetic field will be different. A RF power splitter is necessary to feed all antenna using the same source.

Appendix A

Publications

1. Production of large metallic clusters by thermal evaporation, O.Buiu, J.L.Leclerc, S.H.Yan, A.Munindradasa, R.Murray, S.Taylor, *Applied Surface Science*, **145**, 668-671, (1999).

2. Performance of thin film carbon materials and carbon nanotubes as cold cathodes, G.A.J.Amaratunga, M.Baxendale, N.Rupesinghe, D.A.I. Munindradasa, M.Chhowalla, T.Butler, *Proceedings of the IEEE International Vacuum Microelectronics Conference, IVMC*, **184-185** (1998).

3. Ultra-low-threshold field emission from conjugated polymers, I.Musa, D.A.I.Munindradasa, G.A.J.Amaratunga, W.Eccleston, *Nature*, **395**, 6700, 362-365, (1998).

4. Photoluminescence and optical characteristics of a-C:H:N, D.A.I.Munindradasa and G.A.J.Amaratunga, *9th European Conference on Diamond, Diamond-like and Related Materials (Diamond '98) , Crete, Greece,* (1998).

5. Electron field emission studies from amorphous carbon thin films, S.R.P.Silva, R.D.Forrest, D.A.Munindradasa, G.A.J.Amaratunga, *Diamond and Related Materials*, **7**, 2-5, 645-650, (1998).

6. Electronic properties of tetrahedral amorphous carbon (ta-C) films containing nanotube regions, G.A.J.Amaratunga, M.Chhowalla, K.G.Lim,

D.A.I.Munindradasa, S.D.Pringle, M.Baxendale, I.Alexandrou, C.J.Kiely, B.Keyse, *Carbon*, **36**, 5-6, 575-579, (1998).

7. Electronic behaviour and field emission of a-C:H:N/Si heterojunctions, D.A.I.Munindradasa, M.Chhowalla, G.A.J.Amaratunga, S.R.P.Silva, *Journal of Non-Crystalline Solids*, **230**, PtB, 1106-1112 , (1998).

8. Photoluminescence characteristics of nitrogen containing hydrogenated amorphous carbon, D.A.I.Munindradasa and G.A.J.Amaratunga, *Submitted to Applied Physics Letters.*

9. Helicon wave excited nitrogen plasma, D.A.I.Munindradasa and G.A.J.Amaratunga, *Asia-Pacific Conference on Plasma Science and Technology (APCPST98) , Sydney, Australia,* (1998).

10. Optical properties of carbon thin films containing nanoparticles, M.Chhowalla, A.I.Munindradasa, K.G.Lim, G.A.J.Amaratunga, C.J.Kiely, *Materials Research Society Symposium - Proceedings*, **498**,115-120, (1997).

11. Fullerene and nanoparticle formation in carbon cathodic arc deposition, M.Chhowalla, A.I.Munindradasa, G.A.J.Amaratunga, *Applied Physics Letters*, **70**, 24, 3233-3235, (1997).

Appendix B

Mathematical background of plasmas

B.1 Lumped macroscopic parameters involved in plasmas

Consider a plasma to be a mixture of electrons, ions and neutrals. Say the particle number densities, N_e - electrons, N_i - ions and N_n - neutrals are present. The fact that there is a macroscopic charge neutrality is given by $N_e = N_i = N$. This charge neutrality is maintained by the would be electrostatic forces if there were any significant charge separation. We define the degree of ionisation, α

$$\alpha = \frac{N}{N + N_n} \tag{B.1}$$

When $\alpha = 0$ means an ordinary gas without and ionisation and $\alpha = 1$ is a fully ionised plasma without any neutrals in it.

Let us take a fully ionised plasma ($\alpha = 1$) for further treatment, where there is a set of hydro-dynamical equations corresponding to each particle species. The macroscopic variables $\mathbf{N_e}$ - the number density, $\vec{\mathbf{v}}_\mathbf{e}$ - the average velocity and $\vec{\psi}_\mathbf{e}$ - the kinetic pressure dyad are for electrons, there is a similar set of variables distinguished by subscript **i** for ions. To understand the plasma as a whole it is logical to lump some macroscopic variables associated with the individual

electron and ion components, and generate a new lumped set of variables which describe the governing equations for a plasma as whole. The mass and the electric charge densities, the mass current and the electric current densities, and the kinetic and electro-kinetic pressure dyads are the newly introduced six lumped variables [165].

The mass density,

$$\rho_{\mathbf{m}} = N_e m_e + N_i m_i \tag{B.2}$$

where m - particle mass.

The charge density,

$$\rho = N_e q_e + N_i q_i \tag{B.3}$$

where q - particle charge.

The mass current density,

$$\vec{\mathbf{J}}_{\mathbf{m}} = N_e m_e \vec{v}_e + N_i m_i \vec{v}_i \tag{B.4}$$

The electric current density,

$$\vec{\mathbf{J}} = N_e q_e \vec{v}_e + N_i q_i \vec{v}_i \tag{B.5}$$

The total kinetic pressure dyad,

$$\vec{\psi} = \vec{\psi}_e + \vec{\psi}_i \tag{B.6}$$

The total electro-kinetic pressure dyad,

$$\vec{\psi}_{\mathbf{E}} = \frac{q_e}{m_e}\vec{\psi}_e + \frac{q_i}{m_i}\vec{\psi}_i \tag{B.7}$$

Now we have the mass velocity $\vec{V}$ defined by

$$\vec{\mathbf{V}} = \frac{\vec{J}_m}{\rho_m} = \frac{N_e m_e \vec{v}_e + N_i m_i \vec{v}_i}{N_e m_e + N_i m_i} \tag{B.8}$$

If the plasma is partially ionised, equations B.2, B.4 and B.6 should be modified so that they accommodate the contribution from neutral particles in corresponding terms. The hydrodynamic equations B.6 - B.8 governing the lumped

macroscopic variables are deduced from the corresponding set of equations satisfied by the macroscopic variables pertaining to the constituent particles. In general these equations are nonlinear, making it complicated to solve. However for most applications it is sufficient to consider the linearised version as discussed below.

B.2 Plasmas in motion

The general equation of continuity for the electrons,

$$\frac{\partial N_e}{\partial t} + (\vec{v}_e \cdot \vec{\nabla}) N_e + N_e(\vec{\nabla} \cdot \vec{v}_e) = 0 \tag{B.9}$$

For our linearisation, it is taken that the average velocity, the electric field and the kinetic pressure are first-order perturbations and that the second-order terms resulting from the product of two perturbations are negligible. The first order perturbations N and $\vec{B}$ are very small compared to their ambient values N_0 and $\vec{B}_0$ respectively. With that we have,

$$N \to N_0 + N \quad \vec{B} \to \vec{B}_0 + \vec{B} \tag{B.10}$$

The assumption in B.10 applies to both electrons and ions alike. When we put conditions described in B.10 into B.9 and the second-order terms neglected,

$$\frac{\partial N_e}{\partial t} + N_{e0}(\vec{\nabla} \cdot \vec{v}_e) = 0 \tag{B.11}$$

The linearised form of continuity equation for the electrons in plasma. Similarly a linearised equation for the ions can also be derived.

$$\frac{\partial N_i}{\partial t} + N_{i0}(\vec{\nabla} \cdot \vec{v}_i) = 0 \tag{B.12}$$

When equation B.11 is multiplied by m_e and equation B.12 by m_i are added, and using equations B.2 and B.8 gives,

$$\frac{\partial}{\partial t}\rho_m + \vec{\nabla} \cdot (\rho_{m0}\vec{V}) = \frac{\partial}{\partial t}\rho_m + \rho_{m0}(\vec{\nabla} \cdot \vec{V}) = 0 \tag{B.13}$$

ρ_{m0} is the ambient density whereas ρ_m is the perturbation and $\vec{V}$ is the linearised form of mass velocity given by,

$$\vec{V} = \frac{\vec{J}_m}{\rho_{m0}} = \frac{N_{e0}m_e\vec{v}_e + N_{i0}m_i\vec{v}_i}{N_{e0}m_e + N_{i0}m_i} \tag{B.14}$$

Similarly multiplication of equation B.11 by q_e and equation B.12 by q_i and summing them gives,

$$\frac{\partial}{\partial t}\rho + \vec{\nabla}\cdot\vec{J} = 0 \tag{B.15}$$

where $\vec{J}$ is the linearised form of electric current density described by,

$$\vec{J} = N_{e0}q_e\vec{v}_e + N_{i0}q_i\vec{v}_i \tag{B.16}$$

It is now possible to describe the mass velocity $\vec{V}$ in expression B.13 and the electric current density $\vec{J}_m$ in expression B.14 by linearised forms. The linearised form of the momentum transfer equation for electrons in the plasma is given by,

$$N_{e0}m_e\frac{\partial}{\partial t}\vec{v}_e = -\vec{\nabla}\cdot\vec{\psi}_e + N_{e0}q_e[\vec{E} + \vec{v}_e\times\vec{B}_0] + \vec{P}_{ei} \tag{B.17}$$

where $\vec{P}_{ei}$ is the total momentum transferred to the electrons per unit volume per unit time by the collisional interactions with the ions, whereas $\vec{P}_{ie}$ denotes the reverse process. Similarly the linearised momentum transport equation for the ions is given by,

$$N_{i0}m_i\frac{\partial}{\partial t}\vec{v}_i = -\vec{\nabla}\cdot\vec{\psi}_i + N_{i0}q_i[\vec{E} + \vec{v}_i\times\vec{B}_0] + \vec{P}_{ie} \tag{B.18}$$

From equations B.14, B.6 and B.16 together with summation of equations B.17 and B.18, expression,

$$\rho_{m0}\frac{\partial\vec{V}}{\partial t} = -\vec{\nabla}\cdot\vec{\psi} + \rho_0\vec{E} + \vec{J}\times\vec{B}_0 \tag{B.19}$$

can be obtained. The fact that the total momentum transfer in collisions between the electrons and the ions must be conserved follows,

$$\vec{P}_{ei} + \vec{P}_{ie} = 0 \tag{B.20}$$

The ambient electric charge density in a plasma is given by,

$$\rho_0 = N_{e0}q_e + N_{i0}q_i \tag{B.21}$$

Since the plasma is electrically neutral in macroscopic scale, $\rho_0 = 0$, hence equation B.19 becomes,

$$\rho_{m0}\frac{\partial \vec{V}}{\partial t} = -\vec{\nabla}\cdot\vec{\psi} + \vec{J}\times\vec{B}_0 \tag{B.22}$$

the equation of motion in a conducting fluid.

B.3 Generalised Ohm's law applied to helicon plasmas

The summation of equations B.17 and B.18 multiplied by q_e/m_e and q_i/m_i respectively together with equations B.16 and B.6 yields,

$$\frac{\partial}{\partial t}\vec{J} = -\vec{\nabla}\cdot\vec{\psi}_E + \left(\frac{N_{e0}q_e^2}{m_e} + \frac{N_{i0}q_i^2}{m_i}\right)\vec{E} + \left(\frac{N_{e0}q_e^2}{m_e}\vec{v}_e + \frac{N_{i0}q_i^2}{m_i}\vec{v}_i\right)\times\vec{B}_0 + \frac{q_e}{m_e}\vec{P}_{ei} + \frac{q_i}{m_i}\vec{P}_{ie} \tag{B.23}$$

From equation B.14,

$$\rho_{m0} = N_{e0}m_e + N_{i0}m_i \tag{B.24}$$

solutions for N_{e0} and N_{i0} from simultaneous equation system B.21 and B.24 are,

$$\begin{aligned} N_{e0} &= \frac{m_i\rho_0 - q_i\rho_{m0}}{q_e m_i - q_i m_e} \\ N_{i0} &= \frac{-m_e\rho_0 + q_e\rho_{m0}}{q_e m_i - q_i m_e} \end{aligned} \tag{B.25}$$

which gives,

$$\frac{N_{e0}q_e^2}{m_e} + \frac{N_{i0}q_i^2}{m_i} = \left(\frac{q_e}{m_e} + \frac{q_i}{m_i}\right)\rho_0 - \frac{q_e q_i}{m_e m_i}\rho_{m0} \tag{B.26}$$

For a macroscopically neutral plasma ($\rho_0 = 0$), and equation B.26 becomes,

$$\frac{N_{e0}q_e^2}{m_e} + \frac{N_{i0}q_i^2}{m_i} = -\frac{q_e q_i}{m_e m_i}\rho_{m0} \tag{B.27}$$

Similarly for $\vec{v}_e$ and $\vec{v}_i$, the simultaneous set of equations B.14 and B.16 can be solved to give,

$$\begin{aligned} \vec{v}_e &= \frac{\rho_{m0}}{m_e m_i N_{e0}\left(\frac{q_e}{m_e} - \frac{q_i}{m_i}\right)}\left[\frac{m_i}{\rho_{m0}}\vec{J} - q_i\vec{V}\right] \\ \vec{v}_i &= \frac{\rho_{m0}}{m_e m_i N_{i0}\left(\frac{q_e}{m_e} - \frac{q_i}{m_i}\right)}\left[-\frac{m_e}{\rho_{m0}}\vec{J} + q_e\vec{V}\right] \end{aligned} \tag{B.28}$$

B.28 can be used to get,

$$\frac{N_{e0}q_e^2}{m_e}\vec{v}_e + \frac{N_{i0}q_i^2}{m_i}\vec{v}_i = \left(\frac{q_e}{m_e} + \frac{q_i}{m_i}\right)\vec{J} - \frac{q_e q_i}{m_e m_i}\rho_{m0}\vec{V} \tag{B.29}$$

The substitution of B.20, B.27 and B.29 in equation B.23 gives,

$$\begin{aligned} \frac{\partial}{\partial t}\vec{J} = -\vec{\nabla}\cdot\vec{\psi}_E &+ \left(\frac{N_{e0}q_e^2}{m_e} + \frac{N_{i0}q_i^2}{m_i}\right)[\vec{E} + \vec{V}\times\vec{B}_0] \\ &+ \left(\frac{q_e}{m_e} + \frac{q_i}{m_i}\right)\vec{J}\times\vec{B}_0 + \left(\frac{q_e}{m_e} - \frac{q_i}{m_i}\right)\vec{P}_{ei} \end{aligned} \tag{B.30}$$

In general the mass of an ion m_i is always very much larger than that of an electron m_e which results in,

$$\frac{q_e}{m_e} \pm \frac{q_i}{m_i} \approx \frac{q_e}{m_e} \tag{B.31}$$

and

$$\frac{N_{e0}q_e^2}{m_e} + \frac{N_{i0}q_i^2}{m_i} \approx \frac{N_{e0}q_e^2}{m_e} \tag{B.32}$$

Generally a plasma is not far from being in thermodynamic equilibrium. Under such conditions the partial pressure of the electrons is expected to be in the same order of magnitude that of ions. This leads to,

$$\vec{\psi}_E = \frac{q_e}{m_e}\vec{\psi}_e + \frac{q_i}{m_i}\vec{\psi}_i \approx \frac{q_e}{m_e}\vec{\psi}_e \tag{B.33}$$

With equations B.31 - B.33, equation B.30 reduces to,

$$\frac{\partial}{\partial t}\vec{J} = -\frac{q_e}{m_e}\vec{\nabla}\cdot\vec{\psi}_e + \frac{N_{e0}q_e^2}{m_e}[\vec{E} + \vec{V}\times\vec{B}_0] + \frac{q_e}{m_e}\vec{J}\times\vec{B}_0 + \frac{q_e}{m_e}\vec{P}_{ei} \tag{B.34}$$

Since ambient charge density $\rho_0 = 0$, it follows from equations B.16 and B.21 that,

$$\vec{J} = N_{e0}q_e(\vec{v}_e - \vec{v}_i) \tag{B.35}$$

The collision associated momentum term $\vec{P}_{ei}$ has yet to be expressed in lumped macroscopic terms. It is not unreasonable to expect that the total momentum transfer to the electrons per unit volume in unit time $\vec{P}_{ei}$, is proportional to the relative average velocity $(\vec{v}_e - \vec{v}_i)$ and to the mass of the electrons per unit volume, hence we have,

$$\vec{P}_{ei} = -N_{e0}m_e\nu_{ei}(\vec{v}_e - \vec{v}_i) \tag{B.36}$$

It can be seen from equation B.36 that ν_{ei} has the dimensions of frequency. It is called the *collision frequency* of momentum transfer from ions to electrons. With equation B.35 equation B.36 can be rewritten as,

$$\vec{P}_{ei} = -\frac{m_e\nu_{ei}}{q_e}\vec{J} \tag{B.37}$$

Now we can introduce the parameter η_0 which has the dimensions of *resistivity*. When σ_0 is *conductivity*,

$$\eta_0 = \frac{m_e\nu_{ei}}{N_{e0}q_e^2} = \frac{1}{\sigma_0} \tag{B.38}$$

Hence B.37 becomes,

$$\vec{P}_{ei} = -N_{e0} q_e \eta_0 \vec{J} \tag{B.39}$$

In B.39, both $\vec{P}_{ei}$ and $\vec{J}$ are first order perturbations, and they are linearly related too. The most general form can be,

$$\vec{P}_{ei} = -N_{e0} q_e \vec{\eta} \vec{J} \tag{B.40}$$

where η is known as the dyadic resistivity. Comparison of equation B.39 with B.40 indicates that the former is a special case of the latter. From equations B.40 and B.34,

$$\frac{\partial}{\partial t}\vec{J} = -\frac{q_e}{m_e}\vec{\nabla} \cdot \vec{\psi}_e + \frac{N_{e0} q_e^2}{m_e}[\vec{E} + \vec{V} \times \vec{B}_0] + \frac{q_e}{m_e}\vec{J} \times \vec{B}_0 - \frac{N_{e0} q_e^2}{m_e}\vec{\eta} \cdot \vec{J} \tag{B.41}$$

Helicon waves exist in media where conductivity is high, *ie* $\eta = 0$ and in the presence of static magnetic fields. Consider a steady current in such a uniform plasma, the equation B.41 becomes,

$$\vec{E} + \vec{V} \times \vec{B}_0 + \frac{1}{N_{e0} q_e}\vec{J} \times \vec{B}_0 = 0 \tag{B.42}$$

The term $\frac{1}{N_{e0} q_e}\vec{J} \times \vec{B}_0$ arises from the *Hall effect* associated with magneto-hydrodynamic flows. In most practical helicon situations, the perturbation term ρ_m in eqn. B.8 is small, and when plasma is steady, Hall effect can be neglected. Hence the Ohm's law for helicon media becomes,

$$\vec{E} + \vec{V} \times \vec{B}_0 = 0 \tag{B.43}$$

Bibliography

[1] S. M. Sze, *Physics of Semiconductor Devices*, 2nd ed. (John Wilwy & Sons, Canada., 1981).

[2] R. A. Street, *Hydrogenated amorphus silicon* (Cambridge University Press, Cambridge., The Pitt Buliding, Trumpington Street, Cambridge CB2 1RP, 1991).

[3] S. N. Mott, Review of Modern Physics **50**, 203 (1978).

[4] P. W. Anderson, Review of Modern Physics **50**, 191 (1978).

[5] M. Shimazu, Photonics Spectra **26**, 62 (1992).

[6] J. L. Crowley, Solid State Technology **35**, 94 (1992).

[7] T. P. Brody, Photonics Spectra **26**, 16 (1992).

[8] Y. Hamakawa, *Renewable* Energy **8**, 10 (1996).

[9] N. Gonzalez, J. J. Gandia, J. Carabe, and M. T. Gutierrez, *Solar Energy* Materials and Solar Cells **45**, 175 (1997).

[10] C. Hebling, S. W. Glunz, C. Schetter, J. Knobloch, and A. Rauber, Solar Energy Materials and Solar Cells **48**, 335 (1997).

[11] S. J. Townsend, T. J. Lenosky, D. A. Muller, C. S. Nichols, and V. Elser, Physical Review Letters **69**, 921 (1992).

[12] D. A. Drabold, P. Stumm, and P. A. Fedders, Physical Review Letters **72**, 2666 (1994).

[13] C. Z. Wang and K. M. HO, Physical Review Letters **72**, 2667 (1994).

[14] C. Z. Wand and K. M. HO, Physical Review Letters **71**, 1184 (1993).

[15] D. A. Drabold, P. A. Fedders, and P. Stumm, Physical Review B **49**, 16415 (1994).

[16] M. Vogel, O. Stenzel, and W. Grunewald, Thin Solid Films **209**, 195 (1992).

[17] G. A. J. Amaratunga, V. S. Veerasamy, W. I. Milne, C. A. Davis, S. R. P. Silva, and H. S. Mackenzie, Applied Physics Letters **63**, 370 (1993).

[18] S. B. Hwang, Y. K. Fang, K. H. Chen, C. R. Liu, and L. C. Kuo, Electronics Letters **27**, 2043 (1991).

[19] S. R. P. Silva, G. A. J. Amaratunga, C. N. Woodburn, M. E. Welland, and S. Haq, Japanese Journal of Applied Physics **33**, 6458 (1994).

[20] R. Berman and F. Simon, Electrochem **59**, 338 (1955).

[21] A. Olborska, M. Swider, R. Wolowiec, P. Niedzielski, A. Rylski, and S. Mitura, Diamond and Related Materials **3**, 899 (1994).

[22] B. Bhushan and V. N. Koinkar, Surface and Coatings Technology **76-77**, 655 (1995).

[23] R. G. Pregliasco, G. Zampieri, H. Huck, E. B. Halac, M. A. R. DeBenyacar, and R. Righini, Applied Surface Science **103**, 261 (1996).

[24] F. L. Freire and D. F. Franceschini, Thin Solid Films **293**, 236 (1997).

[25] J. Fink, T. MuellerHeinzerling, J. Pflueger, A. Bubenzer, P. Koidl, and G. Crecelius, Solid State Communications **47**, 687 (1983).

[26] B. Dischler and G. Brandt, Industrial Diamond Review **45**, 131 (1985).

[27] K. Kobayashi, K. Yamamoto, N. Mutsukura, and Y. Machi, Thin Solid Films **185**, 71 (1990).

[28] E. Marotta, N. Bakhru, A. Grill, V. Patel, and B. Meyerson, Thin Solid Films **206**, 188 (1991).

[29] J. L. Lauer, T. A. Blanchet, and Q. Ng, STLE Tribology Transactions **37**, 566 (1994).

[30] D. F. Franceschini, C. A. Achete, and F. L. Freire, Applied Physics Letters **60**, 3229 (1992).

[31] K. Yase, S. Horiuchi, M. Kyotani, K. Yamamoto, A. Yaguchi, Y. Futaesaku, T. Suwa, M. Kakimoto, and Y. Imai, Japanese Journal of Applied Physics **35**, L657 (1996).

[32] S. L. Heidger, Materials Research Society Symposium Proceedings **383**, 319 (1995).

[33] J. Robertson, Journal of Non-Crystalline Solids **137**, 825 (1991).

[34] J. Robertson, Philosophical Magazine B - Physics of Condensed Matter **66**, 199 (1992).

[35] H. W. Kroto, J. R. Heath, S. C. Obrien, R. F. Curl, and R. E. Smalley, Nature **318**, 162 (1985).

[36] G. A. J. Amaratunga, M. Chhowalla, C. J. Kiely, I. Alexandrou, R. Aharonov, and R. M. Devenish, Nature **383**, 321 (1996).

[37] K. Yamamoto, Y. koga, S. Fujiwara, and M. Kubota, Applied Physics Letters **69**, 4174 (1996).

[38] M. Chhowalla, D. A. I. Munindradasa, and G. A. J. Amaratunga, Applied Physics Letters **70**, 3233 (1997).

[39] G. Stenberg, M. Boman, and J. O. Carlsson, Diamond and Related Materials **6**, 1143 (1997).

[40] O. I. Konkov, I. N. Kapitonov, I. N. Trapeznikova, and E. I. Terukov, Technical Physics Letters **23**, 9 (1997).

[41] E. Vainonen, J. Likonen, T. Ahlgren, P. Haussalo, J. Keinonen, and C. H. Wu, Journal of Applied Physics **82**, 3791 (1997).

[42] F. Fujimoto, M. Tanaka, Y. Iwata, A. Ootuka, K. Komaki, M. Haba, and K. Kobayashi, Nuclear Instruments and Methods in Physics Research B **33**, 792 (1988).

[43] R. Stief, J. Schafer, J. Ristein, L. Ley, and W. Beyer, Journal of Non-Crystalline Solids **200**, 639 (1996).

[44] N. Ohtani, M. Katsuno, T. Futagi, Y. Ohta, H. Mimura, and K. Kawamura, Japanese Journal of Applied Physics **30**, L1539 (1991).

[45] C. A. Davis, Y. Yin, D. R. McKenzie, L. E. Hall, E. Kravtchinskaia, V. Keast, G. A. J. Amaratunga, and V. S. Veerasamy, Journal of Non-Crystalline Solids **170**, 46 (1994).

[46] C. Ronning, U. Grisemeier, M. Gross, H. C. Hofsass, R. G. Downing, and G. P. Lamaze, Diamond and Related Materials **4**, 666 (1995).

[47] M. Chhowalla, Y. Yin, G. A. J. Amaratunga, D. R. McKenzie, and T. Frauenheim, Diamond and Related Materials **6**, 207 (1997).

[48] A. Y. Liu and M. L. Cohen, Physical Review B **41**, 10727 (1990).

[49] J. Haggin, Chemical and Engineering News **70**, 20 (1992).

[50] C. M. Niu, Y. Z. Lu, and C. M. Lieber, Science **261**, 334 (1993).

[51] J. Robertson and C. A. Davis, Diamond and Related Materials **4**, 441 (1994).

[52] S. R. P. Silva, J. Robertson, G. A. J. Amaratunga, B. Rafferty, L. M. Brown, J. Schwan, D. F. Franceschini, and G. Mariotto, Journal of Applied Physics **81**, 2626 (1997).

[53] L. A. Bursill, J. L. Peng, V. N. Gurarie, A. V. Orlov, and S. Prawer, Journal of Materials Research **10**, 2277 (1995).

[54] J. H. Kaufman, S. Metin, and D. D. Saperstein, Physical Review B **39**, 13053 (1989).

[55] X. Wang and P. J. Martin, Applied Physics Letters **68**, 1177 (1996).

[56] P. Stumm, D. A. Drabold, and P. A. Fedders, Journal of Applied Physics **81**, 1289 (1997).

[57] X. Shi, H. Fu, J. R. Shi, L. X. Cheah, B. K. Tay, and P. Hui, Journal of Physics **10**, 9293 (1998).

[58] R. Kalish, O. Amir, R. Brener, R. A. Spits, and T. E. Derry, Applied Physics A **52**, 48 (1991).

[59] G. A. J. Amaratunga and S. R. P. Silva, Applied Physics Letters **68**, 2529 (1996).

[60] Rusli, Ph.D. thesis, University of Cambridge, 1996.

[61] B. Meyerson and F. W. Smith, Solid State Communication **41**, 68 (1982).

[62] W. Jacob and W. Moller, Applied Physics Letters **63**, 1771 (1993).

[63] M. Weiler, S. Sattel, K. Jung, H. Ehrhardt, V. S. Veerasamy, and J. Robertson, Applied Physics Letters **64**, 2797 (1994).

[64] T. Mori and Y. Namba, Journal of Applied Physics **55**, 3276 (1984).

[65] K. Suzuki, A. Sawabe, H. Yasuda, and T. Inuzuka, Applied Physics Letters **50**, 728 (1987).

[66] T. Mori and Y. Namba, Journal of Vacuum Science and Technology **1**, 23 (1983).

[67] Y. Namba, Journal of Vacuum Science and Technology **10**, 3368 (1992).

[68] P. B. Lukins, D. R. McKenzie, A. M. Vassallo, and J. V. Hanna, Carbon **31**, 569 (1993).

[69] C. Wyon, R. Gillet, and L. Lombard, Thin Solid Films **122**, 203 (1984).

[70] J. Kulik, G. D. Lempert, E. Grossman, D. Marton, J. W. Rabalais, and Y. Lifshitz, Physical Review B **52**, 15812 (1995).

[71] L. K. Cheah, S. Xu, and B. K. Tay, Electronics Letters **33**, 1339 (1997).

[72] A. A. Benmassaoud and R. W. Paynter, Thin Solid Films **287**, 125 (1996).

[73] M. Schiller and W. Kulisch, Surface and Coating Technology **98**, 1590 (1998).

[74] I. M. El-Fayoumi, I. R. Jones, and M. M. Turner, Journal of Physics D **31**, 3082 (1998).

[75] J. Schafer, J. Ristein, and L. Ley, Journal of Non-Crystalline Solids **166**, 1123 (1993).

[76] C. Charles and R. Boswell, Journal of Vacuum Science Technology. **13**, 2805 (1995).

[77] N. S. Yoon, S. S. Kim, C. S. Chang, and D. I. Choi, Physical Review E **54**, 757 (1996).

[78] B. Dischler, Proceedings of European Materials Research Symposium **17**, 18 (1987).

[79] S. R. P. Silva, G. A. J. Amaratunga, and C. P. Constantinu, Journal of Applied Physics **72**, 1149 (1992).

[80] F. F. Chen and C. D. Decker, Plasma Physics and Controlled Fusion **34**, 635 (1992).

[81] F. F. Chen, Jurnal of Vacuum Science and Technology **10**, 1389 (1992).

[82] C. W. Jurgensen, R. S. Hutton, and G. N. Taylor, Journal of Vacuum Science and Technology **10**, 2542 (1992).

[83] R. Petri, B. Kennedy, D. Henry, N. Sadeghi, and J. P. Booth, Journal of Vacuum Science and Technology **12**, 2970 (1994).

[84] M. Koike, M. Chiwaki, I. H. Suzuki, and N. Kobayashi, Review of Scientific Instruments **66**, 2141 (1995).

[85] Y. Nishimoto, N. Tokumasu, and K. Maeda, Japanese Journal of Applied Physics **34**, 762 (1995).

[86] K. Endo and T. Tatsumi, Applied Physics Letters **68**, 2864 (1996).

[87] I. V. Kamenski and G. G. Borg, Computer Physics Communications **113**, 10 (1998).

[88] Y. Mouzouris and J. E. Scharer, IEEE Transactions on Plasma Science **24**, 152 (1996).

[89] J. E. Stevems, M. J. Sowa, and J. L. Cecchi, Journal of Vacuum Science and Technology **13**, 2476 (1995).

[90] J. Robertson, Diamond and Related Materials **6**, 212 (1997).

[91] S. V. Chernyskov, E. I. Terukov, V. A. Vassilyev, and A. S. Volkov, Journal of Non-Crystalline Solids **134**, 218 (1991).

[92] K. C. Kao and W. Hwang, *Electrical Transport in Solids* (Pergamon Press Inc., Maxwell House, Fairview Park, Elmsford, New York 10523, U.S.A., 1981).

[93] J. Frenkel, Physics Review **54**, 647 (1938).

[94] G. Amaratunga, W. Milne, and A. Putnis, IEEE Electron Device Letters **11**, 32 (1990).

[95] N. Konofaos and C. B. Thomas, Applied Physics Letters **61**, 2805 (1992).

[96] J. P. Donnelly and A. G. Milnes, Proceedings IEE (London) **113**, 1468 (1966).

[97] K. Kadas and S. Kugler, Solid State Communications **102**, 721 (1997).

[98] J. Robertson, Diamond and Related MAterials **5**, 797 (1996).

[99] S. Logothetidis, E. Evangelou, and N. Konofaos, Journal of Applied Physics **82**, 5017 (1997).

[100] S. Lin, B. J. Feldman, D. Min, and M. T. Jones, Solid state Communications **80**, 101 (1991).

[101] M. Chhowalla, Ph.D. thesis, University of Cambridge, 1998.

[102] K. K. Chan, S. R. P. Silva, and G. A. J. Amaratunga, Thin Solid Films **212**, 232 (1992).

[103] S. R. P. Silva and G. A. J. Amaratunga, Thin Solid Films **253**, 146 (1994).

[104] B. Kleinsorge, A. Ilie, M. Chhowalla, W. Fukarek, W. I. Milne, and J. Robertson, Diamond and Related Materials **7**, 472 (1998).

[105] P. Hammer, A. Helmbold, K. C. Rohwer, and D. Meissner, Materials Science and Engineering **A139**, 334 (1994).

[106] K. K. Chan, Ph.D. thesis, University of Cambridge, 1992.

[107] K. K. Chan, G. A. J. Amaratunga, S. P. Wong, and V. S. Veerasamy, Solid State Electronics **36**, 345 (1993).

[108] J. Seth, M. I. Chaudhry, and S. V. Babu, Journal of Vacuum Science and Technology **10**, 3125 (1992).

[109] V. S. Veerasamy, G. A. J. Amaratunga, C. A. Davis, W. I. Milne, and P. Hewitt, Solid-States Electronics **37**, 319 (1994).

[110] J. Wanger and Lautenschlager, Journal of Applied Physics **59**, 2044 (1986).

[111] Rusli, J. Robertson, and G. A. J. Amaratunga, Journal of Applied Physics **80**, 2998 (1996).

[112] J. H. Kim, D. H. Ahn, Y. H. Kim, and H. Baik, Journal of Applied Physics **82**, 658 (1997).

[113] H. Nakaue, T. Mitani, H. Kurakawa, and T. Yonezawa, Thin Solid Films **212**, 240 (1992).

[114] B. Dischler, A. Bubenzer, and P. Koidl, Applied Physics Letters **42**, 636 (1983).

[115] J. Robertson, Advance Physics **35**, 317 (1986).

[116] D. Kruangam, T. Endo, M. Deguchi, W. Guang-Pu, H. Okamoto, and Y. Hamakawa, Optoelectronics **1**, 67 (1986).

[117] Y. Hamakawa, T. Toyama, and H. Okamoto, Journal of Non-Crystalline Solids **115**, 180 (1989).

[118] G. A. J. Amaratunga and S. R. P. Silva, Journal of Non-crystaline Solids **198-200**, 661 (1996).

[119] Z. Vardeny, E. Ehrenfreund, J. Shinar, and F. Wudl, Physical Review B **32**, 2498 (1987).

[120] S. Schuhtte, S. Will, H. Mell, and W. Fuhs, Diamond Related Materials **2**, 1360 (1993).

[121] S. R. P. Silva, J. Robertson, Rusli, and G. A. J. Amaratunga, Philosophical Magazine B **74**, 369 (1996).

[122] F. W. Smith, Journal of Applied Physics **55**, 764 (1984).

[123] A. Durandet and D. R. McKenzie, Journal of Applied Physics **80**, 4707 (1996).

[124] S. R. P. Silva, Ph.D. thesis, University of Cambridge, 1993.

[125] E. A. Davis, Journal of Non-Crystalline Solids **4**, 107 (1970).

[126] R. H. Klazes, M. H. L. M. Broek, J. Bezemer, and S. Radelar, Philosophical Magazine B. **45**, 377 (1982).

[127] A. R. Forouhi and I. Bloomer, Physical Review B. **34**, 7018 (1986).

[128] F. Urbach, Physical Review **92**, 1324 (1953).

[129] J. D. Dow and D. Redfield, Physical Review **B1**, 3358 (1970).

[130] B. T. Kolomiets, T. N. Mamontova, and A. A. Babaev, Journal of Non-Crystalline Solids **4**, 289 (1970).

[131] M. H. Cohen, H. Fritzche, and S. R. Ovshinsky, Physical Review Letters **22**, 1065 (1969).

[132] R. Fischer, U. Heim, F. Stern, and K. Weiser, Physical Review Letters **26**, 1182 (1971).

[133] H. Fritzche, *Electronic and Structural Properties of Amorphous Semiconductors* (Academic Press, New York., 1973).

[134] R. A. Street, T. M. Searle, L. G. Austin, and R. A. Sussmann, Journal of Physics **7**, 1582 (1974).

[135] R. A. Street, Advances in Physics **25**, 379 (1974).

[136] J. Robertson, Diamond and Related Materials **4**, 297 (1995).

[137] N. F. Mott and E. A. Davis, *Electronic Processes in Non-Crystalline Materials*, 2nd ed. (Clarendon Press, Oxford., Oxford University Press, Walton Street, Oxford OX2 6DP., 1979).

[138] I. Watanabe, S. Hasegawa, and Y. Kurata, Japanese Journal of Applied Physics **21**, 856 (1982).

[139] H. X. Han and B. J. Feldman, Solid States Communications **65**, 921 (1988).

[140] S. Liu, S. Gangopadhyay, G. Sreenivas, S. Ang, and H. Naseem, Journal of Applied Physics **82**, 4508 (1997).

[141] K. Fabisiak, J. Rozploch, J. Szatkowski, and P. Targowski, Journal of Physics. D **21**, 995 (1988).

[142] I. Watanabe, M. Inoue, and T. Atoji, Journal of Non-Crystalline Solids **59-60**, 377 (1983).

[143] A. Reyes-Mena, J. Gonzalez-Hernandez, and R. Asonoza, Journal of Vacuum Science Techonology. A **7**, 2328 (1989).

[144] R. R. Koropecki, L. R. Tessler, J. A. Sanjurjo, and F. Alvarez, Journal of Non-Crytalline Solids **137**, 835 (1991).

[145] G. H. Kim, J. H. Lee, and J. S. Chang, Solid State Communication **89**, 529 (1994).

[146] J. P. Klozenberg, B. McNamara, and P. C. Thonemann, Journal of Fluid Mechanics **21**, 545 (1965).

[147] R. W. Boswell, Physics Letters **33**, (1970).

[148] P. Zhu and R. W. Boswell, Physical Review Letters **63**, (1989).

[149] A. Durandet, C. A. Davis, and R. W. Boswell, Applied Physics Letters **70**, (1997).

[150] A. Ganguli, R. K. Jarwal, R. D. Tarey, and M. K. Akhtar, IEEE Transactions on Plasma Science **25**, (1997).

[151] A. V. Martinez and V. Aboites, IEEE Journal of Quantum Electronics **29**, (1993).

[152] V. P. Tzolov, K. A. Grozdanov, and P. A. Atanasov, Journal of Applied Physics **75**, (1994).

[153] P. Aigrain, Proceedings of International Conference on Semiconductor Physics, Prague 224 (1960).

[154] F. F. Chen, *Introduction to Plasma Physics* (Plenum Press, New York and London, 227 West 17th Street, New York, N.Y. 10011, 1977).

[155] P. Zhu and R. W. Boswell, Journal of Applied Physics **68**, 1981 (1990).

[156] J. Neukum, J. Heber, H.-J. Haschka, U. Umhofer-Strobel, and T. Xiao, Measurement Science and Technology. **3**, 1198 (1992).

[157] H. Golnabi, IEEE Journal of Quantum Electronics. **29**, 1192 (1993).

[158] K. J. Clay, S. P. Speakman, G. A. J. Amaratunga, and S. R. P. Silva, Journal of Applied Physics **79**, 7227 (1996).

[159] S. C. Snyder and A. M. LeRoux, IEEE Transactions on Plasma Science **25**, 824 (1997).

[160] J. Robertson, Journal of Vacuum Science and Technology B **17**, 659 (1999).

[161] B. J. Baliga, *Power Semiconductor Devices* (PWS Publishing Company, Boston., 20 Park Plaza, Boston, MA 02116., 1987).

[162] T. Matsushita, T. Aoki, T. Ohtsu, H. Yamoto, H. Hayashi, M. Okayama, and Y. Kawana, IEEE Transactions of Electron Devices **ED-23**, 826 (1976).

[163] D. R. McKenzie, D. Muller, and B. A. Palthorpe, Physical Review Letters **67**, 773 (1991).

[164] D. A. I. Munindradasa, M. Chhowalla, G. A. J. Amaratunga, and S. R. P. Silva, Journal of Non-Crystalline Solids **227-230**, 1106 (1998).

[165] S. R. Seshadri, *Fundamentals of Plasma Physics* (American Elsevier Publishing Company Inc., New York, 52, Vanderbilt Avenue, New York, N.Y.10017, 1973).